Linking NDE Data and Bridge Deck Performance

February 2025

Publication No. FHWA-HRT-25-029

U.S. Department of Transportation
Federal Highway Administration

Research, Development, and Technology
Turner-Fairbank Highway Research Center
6300 Georgetown Pike McLean, VA 22101-2296

Turner-Fairbank
Highway Research Center

FOREWORD

Accelerated bridge testing provides a unique opportunity to simulate the behavior of bridge components under real-world structural and environmental loads within a significantly shorter timeframe. This report presents a comprehensive analysis of nondestructive evaluation (NDE) data collected at the accelerated bridge testing facility at Rutgers University. The study examines the relationship between the results of accelerated testing exposure and bridge deck deterioration, as characterized by a suite of NDE methods. The findings highlight the role of NDE in assessing bridge deck conditions and supporting advanced performance modeling of bridge structures.

This report provides guidance for engineers, researchers, and bridge asset owners to leverage NDE technologies to make data-driven decisions. By integrating NDE data into service life and deterioration modeling, this work contributes to improving the safety and management of highway bridge infrastructure.

Jean A. Nehme, Ph.D., P.E.
Director, Office of Infrastructure
Research and Development

Recommended citation: Federal Highway Administration, *Linking NDE Data and Bridge Deck Performance* (Washington, DC: 2025) https://doi.org/10.21949/1521625

TECHNICAL REPORT DOCUMENTATION PAGE

<table>
<tr><td>1. Report No.
FHWA-HRT-25-029</td><td>2. Government Accession No.</td><td colspan="2">3. Recipient's Catalog No.</td></tr>
<tr><td colspan="2" rowspan="2">4. Title and Subtitle
Linking NDE Data and Bridge Deck Performance</td><td colspan="2">5. Report Date
February 2025</td></tr>
<tr><td colspan="2">6. Performing Organization Code:</td></tr>
<tr><td colspan="2">7. Author(s)
Saeed Nejad, Glenn Washer, Richard Walther, Elizabeth Wagner, Stephen Garrett, and Hoda Azari</td><td colspan="2">8. Performing Organization Report No.</td></tr>
<tr><td colspan="2" rowspan="2">9. Performing Organization Name and Address
Wiss, Janney, Elstner Associates, Inc. (WJE)
330 Pfingsten Road
Northbrook, IL 60062</td><td colspan="2">10. Work Unit No.</td></tr>
<tr><td colspan="2">11. Contract or Grant No.
693JJ319D000054</td></tr>
<tr><td colspan="2" rowspan="2">12. Sponsoring Agency Name and Address
Office of Infrastructure Research and Development
Federal Highway Administration
6300 Georgetown Pike
McLean, VA 22101-2296</td><td colspan="2">13. Type of Report and Period
Final Report, October 2022–March 2024</td></tr>
<tr><td colspan="2">14. Sponsoring Agency Code
HRDI-20</td></tr>
<tr><td colspan="4">15. Supplementary Notes
The contracting officer's representative was Hoda Azari (HRDI-20; ORCID: 0000-0002-7340-0035).</td></tr>
<tr><td colspan="4">16. Abstract
The researchers and the University of Missouri collaborated to complete a comprehensive analysis of nondestructive evaluation (NDE) data collected from the first phase of accelerated testing performed at the Bridge Evaluation and Accelerated Structural Testing facility at Rutgers University in New Jersey. The research team evaluated the use of data from predictive NDE (PNDE) and defect NDE (DNDE) techniques in bridge deck performance models to offer recommendations for incorporating NDE data to accurately predict the actual performance of the deck specimen subject to accelerated testing. The NDE data reliability analysis for assessing bridge deck conditions incorporated several techniques, including time-lapsed analyses to assess the temporal consistency of data collected over the lifespan of the accelerated testing, chronological comparison studies of PNDE and DNDE techniques throughout the accelerated testing experimentation, and a detailed evaluation of each technology's effectiveness in predicting bridge conditions through NDE condition indexing and the use of receiver-operator characteristic (ROC) analysis. In addition, the researchers used a mechanistic service life modeling technique to characterize the bridge deck condition throughout the accelerated testing, from original construction to corrosion initiation to visible damage detection. The team used the collected NDE data as model inputs to enhance the model agreement to observed performance. Additionally, the team applied the service life modeling technique to two in-service bridges in Iowa to further explore potential integrations between NDE data and deck performance. Deterioration models developed in consultation with NDE data were also studied and compared with condition indexes, defect indexes, and deck condition ratings to ascertain the quantitative correlations between NDE and deck performance measures. The data from bridge accelerated testing served as a pivotal demonstration in this analysis, illustrating how NDE data integration not only refines and enhances model predictions but also provides a more nuanced understanding of bridge deck health over time.</td></tr>
<tr><td colspan="2">17. Key Words
Non-destructive evaluation, reliability analysis, predictive NDE, defect NDE, conventional condition data, service life modeling, deterioration modeling</td><td colspan="2">18. Distribution Statement
No restrictions. This document is available to the public through the National Technical Information Service, Springfield, VA 22161.
https://www.ntis.gov</td></tr>
<tr><td>19. Security Classif. (of this report)
Unclassified</td><td>20. Security Classif. (of this page)
Unclassified</td><td>21. No. of Pages
187</td><td>22. Price
N/A</td></tr>
</table>

Form DOT F 1700.7 (8-72) Reproduction of completed page authorized.

SI* (MODERN METRIC) CONVERSION FACTORS

APPROXIMATE CONVERSIONS TO SI UNITS

Symbol	When You Know	Multiply By	To Find	Symbol
		LENGTH		
in	inches	25.4	millimeters	mm
ft	feet	0.305	meters	m
yd	yards	0.914	meters	m
mi	miles	1.61	kilometers	km
		AREA		
in^2	square inches	645.2	square millimeters	mm^2
ft^2	square feet	0.093	square meters	m^2
yd^2	square yard	0.836	square meters	m^2
ac	acres	0.405	hectares	ha
mi^2	square miles	2.59	square kilometers	km^2
		VOLUME		
fl oz	fluid ounces	29.57	milliliters	mL
gal	gallons	3.785	liters	L
ft^3	cubic feet	0.028	cubic meters	m^3
yd^3	cubic yards	0.765	cubic meters	m^3
		NOTE: volumes greater than 1,000 L shall be shown in m^3		
		MASS		
oz	ounces	28.35	grams	g
lb	pounds	0.454	kilograms	kg
T	short tons (2,000 lb)	0.907	megagrams (or "metric ton")	Mg (or "t")
		TEMPERATURE (exact degrees)		
°F	Fahrenheit	5 (F-32)/9 or (F-32)/1.8	Celsius	°C
		ILLUMINATION		
fc	foot-candles	10.76	lux	lx
fl	foot-Lamberts	3.426	candela/m^2	cd/m^2
		FORCE and PRESSURE or STRESS		
lbf	poundforce	4.45	newtons	N
lbf/in^2	poundforce per square inch	6.89	kilopascals	kPa

APPROXIMATE CONVERSIONS FROM SI UNITS

Symbol	When You Know	Multiply By	To Find	Symbol
		LENGTH		
mm	millimeters	0.039	inches	in
m	meters	3.28	feet	ft
m	meters	1.09	yards	yd
km	kilometers	0.621	miles	mi
		AREA		
mm^2	square millimeters	0.0016	square inches	in^2
m^2	square meters	10.764	square feet	ft^2
m^2	square meters	1.195	square yards	yd^2
ha	hectares	2.47	acres	ac
km^2	square kilometers	0.386	square miles	mi^2
		VOLUME		
mL	milliliters	0.034	fluid ounces	fl oz
L	liters	0.264	gallons	gal
m^3	cubic meters	35.314	cubic feet	ft^3
m^3	cubic meters	1.307	cubic yards	yd^3
		MASS		
g	grams	0.035	ounces	oz
kg	kilograms	2.202	pounds	lb
Mg (or "t")	megagrams (or "metric ton")	1.103	short tons (2,000 lb)	T
		TEMPERATURE (exact degrees)		
°C	Celsius	1.8C+32	Fahrenheit	°F
		ILLUMINATION		
lx	lux	0.0929	foot-candles	fc
cd/m^2	candela/m2	0.2919	foot-Lamberts	fl
		FORCE and PRESSURE or STRESS		
N	newtons	2.225	poundforce	lbf
kPa	kilopascals	0.145	poundforce per square inch	lbf/in^2

*SI is the symbol for International System of Units. Appropriate rounding should be made to comply with Section 4 of ASTM E380.
(Revised March 2003)

TABLE OF CONTENTS

LIST OF FIGURES

LIST OF TABLES

ACRONYMS AND ABBREVIATIONS

AASHTO	American Association of State Highway and Transportation Officials
ACI	American Concrete Institute
ADT	average daily traffic
ADTT	average daily truck traffic
AI	artificial Intelligence
AUC	area under the curve
BEAST®	Bridge Evaluation and Accelerated Structural Testing
BMS	bridge management system
CASLE™	Corrosion Assessment and Service Life Estimation
CIP	cast in place
CR	condition rating
CS	condition state
CSE	copper-copper sulfate electrode
C_s	concentration of chloride at the surface of the element
C_t	chloride threshold
D_{28}	28-d diffusion coefficient of the concrete
D_a	apparent diffusion coefficient
dB	decibel
DNDE	defect nondestructive evaluation
DOT	department of transportation
ER	electrical resistivity
ESAL	equivalent single-axle load
FHWA	Federal Highway Administration
FN	false negative
FP	false positive
FPR	false positive rate
GPR	ground penetrating radar
HCP	half-cell potential
HD	high definition
IE	impact echo
IHRB	Iowa Highway Research Board
IRT	infrared thermal imaging
kΩ	kilohm
ksi	kilopounds per square inch
LCC	life-cycle cost
LEF	load equivalency factor
LTBP	Long-Term Bridge Performance (Program)
MBEI	*Manual for Bridge Element Inspection*
ML	machine learning
NBI	National Bridge Inventory
NBIS	National Bridge Inspection Standards
NDE	nondestructive evaluation
NHS	National Highway System
NJDOT	New Jersey Department of Transportation

OPC	ordinary portland cement
PHM	proportional hazards model
PNDE	predictive nondestructive evaluation
POD	probability of detection
POFA	probability of false alarm
PPC	polyester polymer concrete
ppm	parts per million
psi	pounds per square inch
RC	reinforced concrete
ROC	receiver-operator characteristics
SCM	supplementary cementitious materials
t_i	initiation time
TN	true negative
t_p	propagation time
TP	true positive
TPR	true positive rate
UC	uncracked sample
USW	ultrasonic surface wave
VI	visual inspections
WIM	weigh in motion
Δ_x	transfer function

CHAPTER 1. INTRODUCTION AND ORGANIZATION

In 2021, the Federal Highway Administration (FHWA) completed phase I testing of a bridge deck specimen at the Bridge Evaluation and Accelerated Structural Testing (BEAST®) facility at Rutgers University in Piscataway, NJ. This work was funded through FHWA's Long-Term Bridge Performance (LTBP) Program to study the performance of full-scale bridge decks subjected to accelerated aging and loading conditions. The Rutgers University team collected nondestructive evaluation (NDE) data, visual observations, and material data throughout a separate research study; however, the data from that project formed the basis for the present study. This study sought to demonstrate how NDE data can be analyzed and interpreted to further the industry's understanding of bridge deck performance.

The research team and the University of Missouri led the present study, which is organized in the following four chapters:

- Chapter 2—Collection and Analyses of NDE Data from Bridge Accelerated Testing.
- Chapter 3—Integration of NDE Data with Conventional Condition Data.
- Chapter 4—Service Life Modeling.
- Chapter 5—Deterioration Modeling.

Chapter 2 focuses on the reliability assessment and analyses of NDE data collected periodically throughout the phase I accelerated testing of a bridge deck specimen at the BEAST facility. This chapter describes the purpose and methodology behind collecting and analyzing NDE data, highlighting the importance of various NDE methods, such as impact echo (IE) and half-cell potential (HCP), among others, in assessing bridge deck conditions. The chapter discusses the facility's capabilities in simulating real-world deterioration mechanisms on bridge decks and the comprehensive data analysis performed by the research team to evaluate the reliability and validity of the NDE technologies used. Key findings include the assessment of NDE data through time-lapsed analysis, multisensor NDE stacks, and the development of an NDE condition index to quantify bridge deck conditions. The chapter also includes a receiver-operator characteristics (ROC) analysis to further validate the effectiveness of NDE technologies in detecting defects and for use in later investigations of the present research study.

The ROC analysis revealed significant insights into the reliability of the different NDE techniques used in the bridge accelerated testing. The team used the ROC analysis to compare the effectiveness of each different NDE method in a quantitative, point-by-point comparison, relative to an assumed ground truth, in detecting sound or otherwise defective concrete. Since no destructive verification of the deck condition at each data collection stage occurred, the researchers selected each NDE method to serve as the ground truth and then compared them against the other NDE techniques to evaluate their comparative reliability. The team assessed six different scenarios, each linked to one of the six NDE techniques used during bridge accelerated testing. The team initially assumed the IE data to be the ground truth due to its high area-under-the-curve (AUC) values in previous studies (Sultan and Washer 2018), suggesting robustness in detecting subsurface delamination. The researchers observed consistency among predictive NDE (PNDE) technologies, suggesting that each demonstrated comparable reliability. Among defect NDE (DNDE) technologies, subjectively, the IE data are most likely to present accurate and reliable results. Previous research also illustrated the high reliability of IE and sounding technologies (Sultan and Washer 2018; Sultan 2017).

The conclusion of chapter 2 suggests several areas for improvement and further research for accelerated testing. The chapter recommends additional physical sampling and destructive analysis to improve the evaluation of NDE techniques and service life models (described in chapter 3 and chapter 4). The need for more uniform chloride exposure to closely simulate real-world conditions is also identified. Additionally, the research reveals that test methods are sensitive to a range of concrete properties beyond just damage, thus indicating that variations in moisture and chloride ion content can profoundly influence the outcomes of HCP, electrical resistivity (ER), and ground penetrating radar (GPR) tests. This insight opens avenues for adjusting test protocols to better account for these factors in accelerated aging studies. A key recommendation is to expose structures to brine or deicing salt in a manner more reflective of in-service conditions, despite the challenge posed to the accelerated testing paradigm. Additionally, the researchers suggest extending the structure age before testing to mitigate issues related to concrete curing and associated early-age material changes.

Chapter 3 presents an evaluation of the collected NDE data alongside other conventional performance indicators and demonstrates how NDE technologies can transcend the limitations of traditional visual inspection (VI) by providing detailed insights into subsurface and material-level deteriorations not visible to the naked eye. The study investigated the correlation between NDE data and reported component condition rating (CR) and element-level condition state (CS) using both qualitative and quantitative assessments. The results of this analysis demonstrate how data from accelerated testing can be used within the broader context of component CR and element-level CS performance reporting.

Chapter 4 and chapter 5 focus on assessing NDE data integration into bridge deck service life modeling using mechanistic and deterioration modeling approaches, respectively. The chapters present an analysis of the bridge performance from accelerated testing relative to these two modeling approaches. The chapters also explore a comparison field study of similar in-service bridges that leverage NDE techniques to assess how NDE can be used to enhance the accuracy of performance evaluations and service life predictions.

Chapter 4 describes the fundamentals of a mechanistic service life model and its various components. The chapter describes the chloride-induced corrosion of reinforcing steel and how the corrosion is modeled within the context of a service life model. CASLE™ (Corrosion Assessment and Service Life Estimation), the contractor’s proprietary in-house service life modeling software (CASLE 2024), is then introduced with an explanation of how NDE data can be incorporated into service life models. The chapter explains the mathematical and computational approaches used to simulate the deterioration mechanisms in bridge decks, highlighting the role of chloride-induced corrosion and how NDE data provide critical information necessary to define the model attributes (i.e., corrosion initiation timing and damage propagation).

The service life model is calibrated against the data from the accelerated test, both NDE and material data, to showcase the mechanistic model capabilities for predicting deck performance in accelerated, aging testing programs. The bridge accelerated testing case study plays a pivotal role throughout this chapter, as it serves as a critical component for validating the integration of NDE data into service life modeling. The bridge accelerated testing framework is used to simulate accelerated deterioration mechanisms in a controlled environment, allowing for a direct comparison between predicted outcomes using NDE-informed models and actual observed degradation.

Chapter 4 concludes that the service life model, developed within the CASLE framework for the accelerated test, successfully models chloride ion ingress and subsequent corrosion initiation and damage in conventionally reinforced bridge decks. NDE techniques, specifically GPR for concrete cover determination and IE for corrosion propagation time (t_p) estimation, play crucial roles in refining model inputs that lead to better predictive outcomes. Furthermore, the use of HCP measurements validates the predicted percentage of the surface area with corrosion initiation, pinpointing NDE's importance in the propagation stage where traditional mechanistic models fall short.

The bridge accelerated aging and exposure protocol does not accelerate concrete cement hydration but does introduce unique materials degradation behaviors that ultimately affect chloride ingress rates. This degradation, manifesting as surface scaling and spalling, is distinct from that observed in more mature conventional bridge decks. To account for this behavior, the report suggests adding a materials degradation factor to the service life model, enhancing its predictive accuracy for decks exposed to accelerated testing conditions. With these refinements and comparison with the independent NDE data taken from the bridge, the developed service life models in chapter 4 have been shown to successfully predict the behavior observed in accelerated testing.

Chapter 4 explores the validity of the proposed framework through field studies of two in-service bridges in Iowa. The chapter specifically leverages NDE evaluations and service life models developed for these structures to examine potential correlations between NDE data and National Bridge Inspection Standards (NBIS) data (Office of the Federal Register 2022). These studies demonstrate the application of NDE data in real-world scenarios, validating the proposed modeling approach against observed conditions.

The listed conclusions and recommendations in chapter 4 stress the importance of NDE in defining model inputs, validating model predictions, and identifying areas for future refinement. The findings underscore the significant impact of NDE integration on improving service life predictions. The data from NDE techniques allow for more precise identification of deterioration stages and rates, which would enable timely, targeted maintenance interventions. The chapter also suggests improvements to testing protocols and modeling approaches, aiming to better predict the service life of bridge decks by accounting for various factors influencing corrosion and deterioration.

Chapter 5 investigates the integration of NDE techniques in bridge deck deterioration modeling. By systematically comparing traditional deterioration models with those incorporating NDE data, the analysis highlights the significant improvement in predictive accuracy and reliability that NDE data offer. The study leverages a variety of analytical methods, including deterministic and probabilistic models, alongside advanced artificial intelligence (AI)/machine learning (ML) techniques. Bridge accelerated testing serves as a pivotal demonstration in this analysis, highlighting how NDE data integration not only refines model predictions but also provides a more nuanced understanding of bridge deck health, thereby supporting more informed maintenance and rehabilitation decisions. This chapter concludes by detailing the qualitative correlations between NDE condition indexes, NDE defect indexes, and deck CRs. These correlation studies serve as an initial framework for the application of NDE data to a wider variety of bridge types encompassing varying deck types, geometries, and environmental conditions.

The findings of chapter 4 and chapter 5 advocate for the adoption of NDE-enhanced models in bridge management systems (BMS), emphasizing their role in predicting bridge performance to optimize repair and maintenance strategies. Through a detailed procedure and analysis, coupled with the introduction of NDE-based performance indexes, these chapters highlight the transformative potential of NDE for more advanced structural care that can lead to a pragmatic approach for bridge management that prioritizes efficiency and accuracy.

CHAPTER 2. COLLECTION AND ANALYSES OF NDE DATA FROM BRIDGE ACCELERATED TESTING

INTRODUCTION

The construction and commissioning of the first specimen at the BEAST facility is subject to two experimental phases. In phase I, the research team at Rutgers University built and tested an untreated concrete deck until widespread deterioration was evident and characterized. In phase II, the research team at Rutgers University treated the deck with two types of overlays (ultra high-performance concrete and latex modified concrete). The team will continue to test these overlay types until conditions indicate the end of service life has been reached.

The scope of the current project is limited to the data collected through phase I of this accelerated testing experiment, which includes periodically collected visual-based and NDE data. Other collected data include chloride and moisture application rates; load and temperature histories; structural health monitoring (girder deflection and rotation, girder principal stresses, internal deck stress profile); photographs; VI reports; CRs; materials sampling and testing; and information associated with the specimen construction, such as drawings, specifications, concrete mix design, and materials testing during fabrication. This chapter evaluates the validity and reliability of NDE data collected from the various methods over the full extent of the accelerated testing. The remainder of the collected data, such as material sampling, is assessed in chapter 4 and chapter 5.

BEAST FACILITY

The BEAST laboratory at Rutgers University (figure 1) is a unique facility that, for the first time, meets these primary challenges for full-scale bridge structure testing. The BEAST facility is the first facility in the Nation capable of applying controlled and accelerated live load, environmental loading, and maintenance demands on full-scale bridge superstructures. Currently, the facility is examining the performance of a composite multigirder bridge specimen primarily sponsored by FHWA. The 30-ft-by-50-ft specimen is constructed with four wide-flange beam W27x84 rolled beams, spaced at 7 ft 6 inches on center, that act compositely with a cast-in-place (CIP) reinforced concrete (RC) deck. The deck is 8 inches thick, with uncoated black ASTM Grade 60 reinforcement set to have a 2-inch cover from the top surface and a 1-inch cover from the soffit (A615/A615M (ASTM International 2020)). Due to the details of the live-load mechanism, no longitudinal or cross slope was applied to the deck. An ordinary portland cement (OPC) ASTM class A concrete mix with nominal compressive strength of 4,000 lbs/in^2 (psi) with 6-percent air entrainment and a maximum size aggregate of three-fourths of an inch was used for the concrete (C150/C150M-21 (ASTM International 2021)). No pozzolans or superplasticizer were used in the concrete mix. The deck surface was tined transverse to the direction of the moving load.

Figure 1. Photo. BEAST facility at Rutgers University, Piscataway, NJ.

During the first experimental phase (untreated concrete deck), the specimen was exposed to more than 2 million cycles of live loading (50 kilo pounds (kips)), more than 85 freeze–thaw cycles (less than and greater than 32 degrees Fahrenheit), as well as the application of deicing agents (maximum of 6-percent brine solution (sodium chloride by weight)) to simulate common winter maintenance practices. The live loading was applied in the longitudinal direction, parallel to the specimen's longitudinal girders.

SUMMARY OF NDE METHODS

The Rutgers University's team deployed multiple NDE techniques periodically to assess bridge deck conditions over the full range of accelerated testing, including the following techniques:

- IE.
- HCP.
- Ultrasonic surface wave (USW).
- GPR.
- ER.
- High-definition (HD) imaging.
- Infrared thermal imaging (IRT).

Table 1 shows the common NDE methods applicable to bridge deck assessment, with those technologies used in the accelerated testing research marked with an asterisk. The technologies in table 1 can be grouped into the following two categories:

1. Technologies that detect physical conditions consisting of subsurface delamination or cracking and surface-presenting anomalies such as cracking and spalling (referred to as DNDE).

2. Other technologies that attempt to characterize the corrosive environment surrounding the subsurface reinforcement and are focused on predicting potential areas of future damage (referred to as PNDE).

Table 1. Common NDE technologies for concrete bridge decks.

DNDE	PNDE
HD images*	GPR attenuation measurements*
IRT*	HCP*
Mobile sounding or automated chain drag	ER*
IE*	Galvanic pulse
Hammer sounding	Cover meter or pachometer
Time-lapse IR*	—
Ultrasonic pulse	—
USW*	—
GPR rebar depth measurements*†	—

—No data.
*Technologies used in the accelerated testing research.
†This technique does not necessarily detect defects; however, it can identify the gradual decrease in cover depth due to scaling. Alternatively, it can serve a predictive purpose as input for diffusion modeling, which will be discussed in chapter 4.

The researchers reviewed the PNDE and DNDE technology outputs from accelerated testing to assess the reliability of the NDE data and its viability for use in the subsequent research efforts presented in chapter 3 through chapter 5. The researchers assessed the chronology of data collection, along with the processing methodologies employed to form the final datasets. This assessment allowed further data analysis for both reliability and utility in performance modeling. The team assessed the reliability of the different NDE technologies by comparing the NDE results with an assumed ground truth, analyzed the variability of NDE results collected at different times, and assessed the correlation between results from different technologies. The results offer insights that might improve future experimental investigations and long-term studies for NDE data validation.

The following subsections summarize the NDE methods used in the accelerated testing.

IE

The IE method is a seismic or stress-wave-based method that measures element thickness and detects defects in concrete members. IE testing consists of a surface transducer and an impact source. For the test, the transducer is placed on the surface, an impact is made, and the ultrasonic wave traveling through the specimen is recorded. A more detailed description of the IE method can be found at the FHWA InfoTechnology™ web platform (FHWA n.d.c.). For a complete research-level data collection procedure, refer to ASTM International C1383 (2022b) standard and the LTBP protocol, FLD-DC-NDE-004: Impact Echo Testing (FHWA n.d.b.).

IE results are commonly presented in two forms. The first form is a map of dominant frequency as a metric for describing the position of back reflectors and internal defects. In essence, the fundamental frequencies of the wave are analyzed and can be correlated to element thickness, the presence of subsurface defects, or both. The second form is a map of condition levels related to delamination (good, fair, poor, or serious), which are assigned to each data collection location based on an interpretation of the shape of the frequency spectrum (FHWA InfoTechnology (FHWA n.d.c.)). In this approach, the overall shape of the resulting frequency spectrum is analyzed and correlated to damage severity. In this study, the first and second interpretations of IE results are identified as IE-dominant frequency and IE-index, respectively. The following subsections give a brief description of each processing approach.

Dominant Frequency

In this approach, the time-history response for each testing point is first passed through a fast Fourier transform analysis, and then a band-pass filter (2–20 kHz) is applied to clean the frequency response from noise. Next, the research team picked the frequency corresponding to the highest amplitude as the governing dominant frequency. Depending on the condition of the deck, the dominant peak frequency could be correlated with the bottom of the deck (i.e., no delamination) or any potential delamination present in the deck (figure 2).

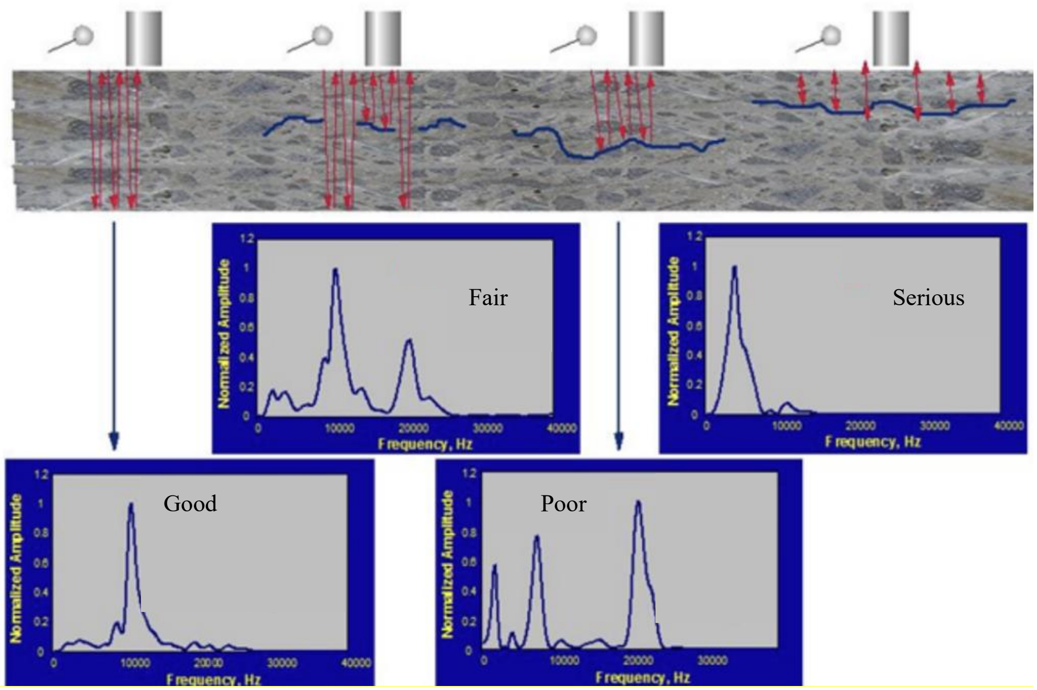

Figure 2. Graph. Physical principle of IE.

Delamination Condition Index Score

In this approach, the researchers categorized the frequency response into four subjective grades of good, fair, poor, and severe conditions (figure 2). A "good" condition is assigned to a frequency response with a single dominant peak associated with the thickness of the bridge deck. For responses that exhibit two peaks (one associated with the thickness of the deck and one associated with shallow delamination), a condition of "fair" is assigned in cases in which the deck thickness produces the dominant peak. In cases in which the peak associated with the shallow delamination is the dominant peak, a condition of "poor" is assigned. Finally, in cases in which a significant low-frequency response is observed (which is associated with the flexural mode of the delamination), a condition of "serious" is assigned (Gucunski et al. 2013; FHWA n.d.c.). Table 2 provides a description of each rating.

Table 2. Condition indexes (FHWA n.d.c.).

Index	Condition	Description
1	Good	This condition is sound. The deck thickness mode peak is dominant in the frequency spectrum.
2	Fair	The deck thickness mode peak is dominant in the frequency spectrum. However, secondary peaks of an amplitude of >50 percent of the dominant peak amplitude exist, indicating early signs of delamination formation.
3	Poor	The dominant peak is at a frequency higher than the full deck thickness mode peak.
4	Serious	The response is dominated by flexural oscillations of the delaminated deck section. The dominant frequency is significantly lower than one of the deck thickness mode, typically between 1 and 5 kHz.

For the present study, Rutgers University provided the delamination condition index scores. The research team performed the dominant frequency determination as a secondary interpretation of IE results.

HCP

HCP testing provides an indication of corrosion potential for reinforcing steel in concrete. HCP surveys are performed by establishing an electrical connection (ground) to the reinforcement and placing a reference electrode on the surface of the concrete (figure 3). Highly negative potential (voltage) readings indicate a high probability that active corrosion is occurring. HCP measurements do not locate spalls, delamination, or other damage sites. However, these conditions are often associated with corrosion and thus usually coincide with more negative potential readings. This technique can identify anodic (corroding) regions that have not yet caused delamination or spalls, and thus HCPs can be used as an indicator of regions likely to become damaged by corrosion in the near future.

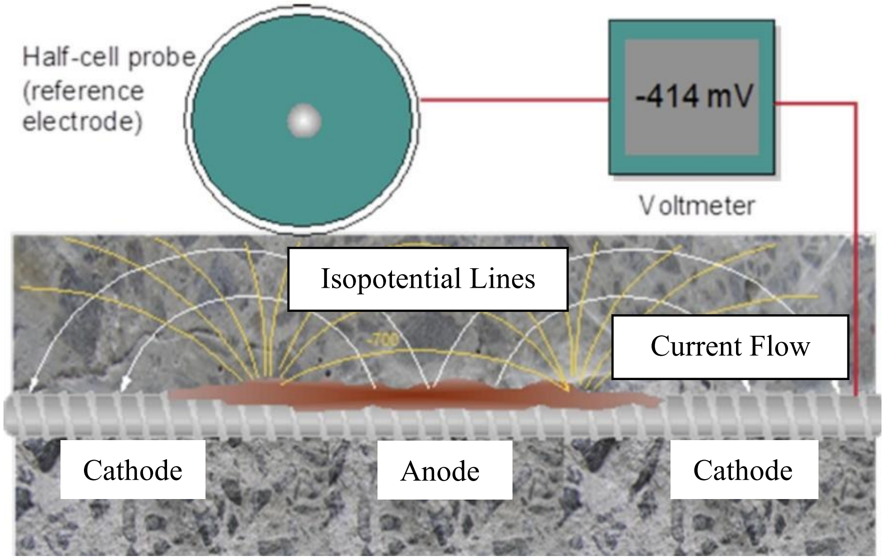

Figure 3. Illustration. Principle of HCP measurement (Gucunski et al. 2013).

USW

The USW technique derives from the spectral analysis of the surface waves method, which assesses material properties (elastic moduli) in the immediate surface area. USW test results are commonly displayed as distributions of the dynamic concrete modulus. A notably low modulus usually signals the existence of delamination or cracking, rather than reflecting the genuine concrete modulus at the specific testing site (figure 4). A more detailed description of the USW method of assessment can be found at the FHWA InfoTechnology website (FHWA n.d.c.). For a complete research-level data collection procedure, refer to American Concrete Institute (ACI) 228.2R-13 standard (ACI Committee 228 2013) and the LTBP protocol, FLD-DC-NDE-007: Ultrasonic Surface Wave Testing—Concrete (FHWA n.d.b.).

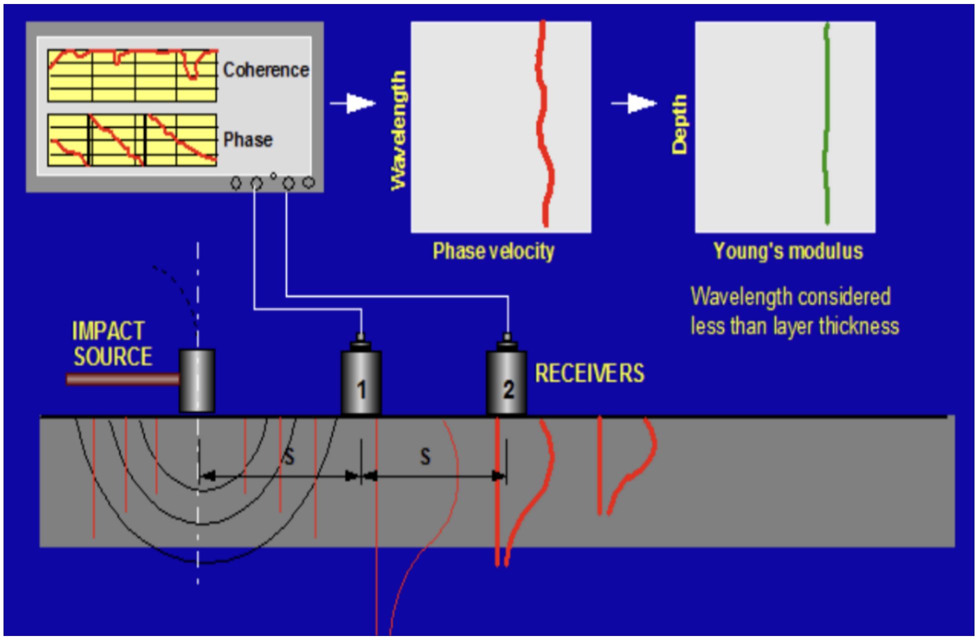

Original image: © 2013 National Academy of Sciences. Modified by FHWA (see Acknowledgments section).

Figure 4. Illustration. Evaluation of a layer modulus by the USW method (Gucunski et al. 2013).

GPR

The GPR test method is an electromagnetic-based nondestructive testing technique commonly used to identify embedded elements in concrete, including steel reinforcing (figure 5). In particular, this method can identify and map areas with a high likelihood of corrosion-based deterioration, assess construction quality, determine structural reinforcement layout, and estimate the thickness of the deck, overlays, and reinforcement cover. The technique involves the use of a high-frequency antenna that transmits electromagnetic radar pulses into the concrete as the antenna is scanned along a longitudinal path over the surface of the deck. The antennas collect electromagnetic signals reflected from material interfaces within the concrete element, amplify them, and display them for subsequent interpretation or further analysis. The signal travel time can measure the depth of embedded items, and the amplitude of the returning signal can be analyzed for changes that may be related to material properties. A more detailed description of the GPR method of assessment can be found at the FHWA InfoTechnology website (FHWA n.d.c.). For a complete data collection procedure, refer to ASTM International (2008) D6087-08 standard and the LTBP protocol FLD-DC-NDE-002: Ground Penetrating Radar Testing for Bridge Decks (FHWA n.d.b.).

GPR results are commonly presented in two forms: as a map of depth-corrected amplitude attenuation as a metric for describing the position of deterioration in the deck, and as a map of cover depth.

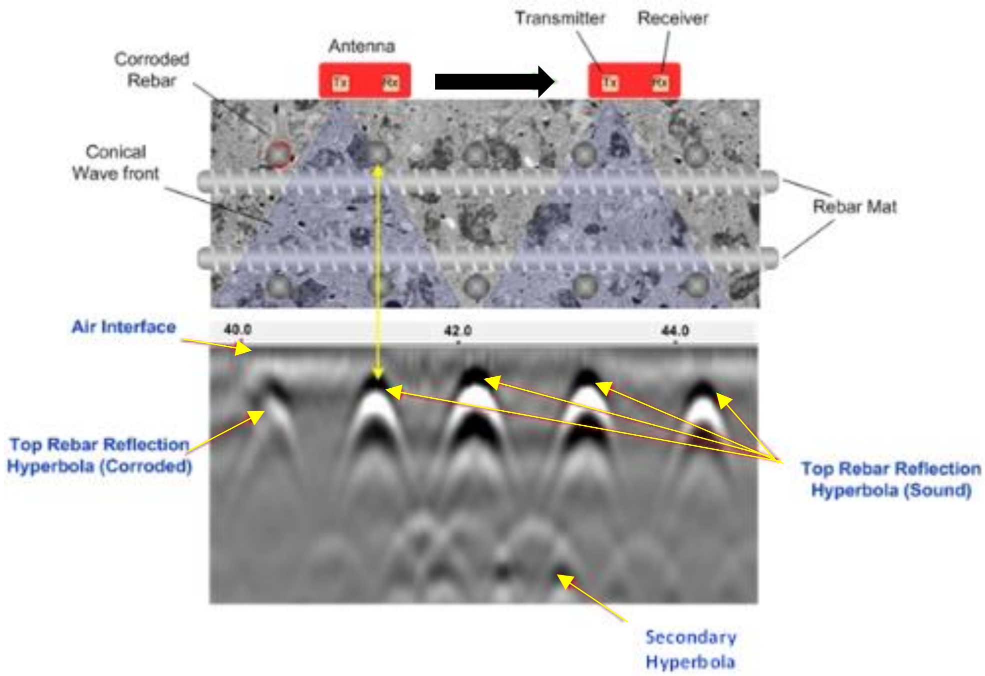

Figure 5. Illustration. Physical principle of GPR (Gucunski et al. 2013).

ER

Concrete surface resistivity is typically measured with a four-pin Wenner-type probe, whereby two probes impart a current into the concrete and the other two probes measure the voltage change. Concrete resistivity can be correlated with the corrosion activity in concrete structures (figure 6). As resistivity increases, the corrosion rate decreases at the locations where corrosion is occurring. Resistivity is affected by carbonation, with an expected trend of higher resistivity in more heavily carbonated concrete. Resistivity measurements are also affected significantly by the presence of moisture. In general, resistivity values that are greater than 100 kilohm-centimeter (kΩ·cm) indicate a low risk of corrosion, and values of 100 kΩ·cm or less indicate a corrosion risk that increases as values are reduced. The lower the ER of the concrete, the higher the current passing between anodic and cathodic areas of the reinforcement steel will be. Resistivity is also affected by material properties such as moisture and ionic content of the pore solution. A more detailed description of the ER method of assessment can be found at the FHWA InfoTechnology website (FHWA n.d.c.). Currently, no ASTM standards for in situ measuring the resistivity of concrete using a Wenner array exist. ASTM G57-06 and American Association of State Highway and Transportation Officials (AASHTO) T 358 are similar applications to concrete testing, with some differences (ASTM International 2012; AASHTO 2019b). For a complete data collection procedure, refer to the LTBP protocol, FLD-DC-NDE-001: Electrical Resistivity Testing (FHWA n.d.b.).

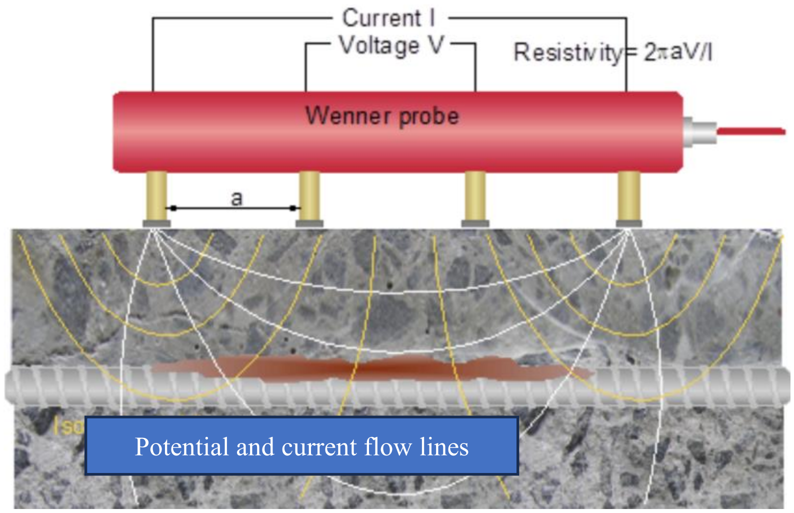

Original image: © 2013 National Academy of Sciences. Modified by FHWA (see Acknowledgments section).
V = voltage; I = current.

Figure 6. Graph. Physical principle of ER measurement (Gucunski et al. 2013).

HD Imaging

The team captured HD images of the deck surface from the accelerated testing to assess the deck condition in terms of cracking or any surface delamination or spalling. For some testing rounds, these images were also stitched together to create a wider view of the deck area.

IRT

IRT is an NDE technology used to detect defects and deterioration, thermal and gas leaks, and so on. Defect detection by IRT is based on assessing thermal anomalies on the surface of an element produced at areas where subsurface damage is present. Thermal anomalies result from the interruption of uniform heat flow through the material caused by subsurface damage such as areas of delamination. Maps of surface temperature (thermograms) are generated from data captured by infrared cameras that measure the infrared radiation emitted from the surface of the material under test. Figure 7 illustrates the physical principle of IRT in detecting defects in concrete decks. Diurnal temperature variations and solar radiation induce a thermal gradient in the concrete. Areas of delamination, voids, and other anomalies in the material interrupt the heat flow through the concrete and have a different thermal capacity compared with areas of sound concrete. Therefore, the surface above areas of delamination will heat up faster after sunrise and cool down more quickly during and after unset compared to sound concrete. As a result, these areas develop surface temperatures anomalies up to several degrees Fahrenheit different than the surrounding sound concrete areas when ambient conditions are favorable. The two main techniques in IRT are passive and active methods, with passive IRT being the most commonly used for bridge deck assessments. A more detailed description of the IRT method of assessment can be found at the FHWA InfoTechnology website (FHWA n.d.c.). For a complete data collection procedure, refer to ASTM International (2013) D4788-03 standard.

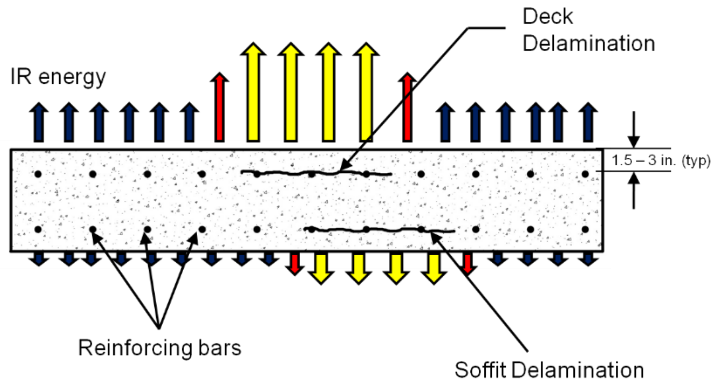

Typ = typical.

Figure 7. Illustration. IRT with the thermal radiation captured by an infrared camera (Washer et al. 2015).

SUMMARY OF THE BRIDGE ACCELERATED TESTING DATA

NDE Data

Figure 8 shows the concrete slab specimen at the BEAST facility in its after-cast condition. In the first phase of experimentation, the Rutgers University researchers subjected the structure to a combination of live loading, brine application, and environmental cycling. Environmental cycling included thermal gradients below freezing and up to 100 °F, as well as wetting and drying cycles. Figure 9 shows the cumulative plots of live-load passes and brine application.

Figure 8. Photo. BEAST deck after construction.

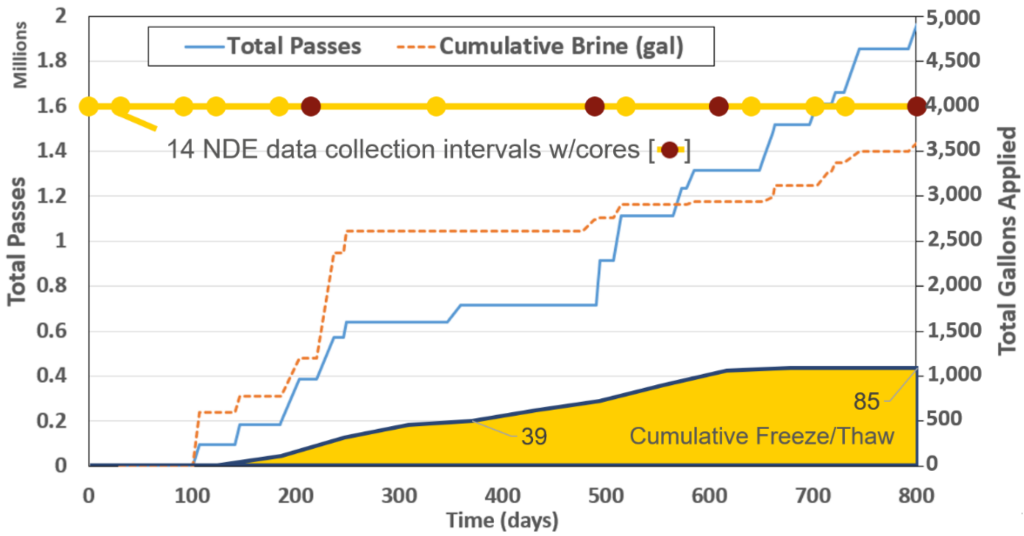

Source: FHWA.

Figure 9. Graph. Summary of live loading and brine application.

Table 3 shows the data collection intervals. In total, the Rutgers University team collected 14 NDE datasets. For each date of data collection, the cumulative live-load cycles and cumulative freeze-thaw cycles are reported. The first date of data collection was July 2, 2019, referred to as "day zero" and corresponds to the initial cast date. The first three collection intervals were during the curing process, and as such no live or environmental loading or brine application occurred. Rutgers University performed all data collection, preprocessing, and assembly, with final NDE datasets provided to the research team in 2022. The team further assembled, analyzed, and reviewed the data for reliability and validity with results presented in this report.

An NBIS-certified inspector conducted a VI of the phase I deck twice. Table 3 also reports when concrete core samples for chloride testing were extracted. The team also performed HD imaging starting in October 2019 and performed IRT intermittently.

Table 3. Summary of data collection intervals.

Data Collection Date	Cumulative Live Load Cycle (No.)	Cumulative Freeze-Thaw Cycles (No.)	Deck CR VI	Chloride Cores	NDE*	Visual	
						HD	IR
07/2019	—	—	—	—	✓	—	✓
08/2019	—	—	—	—	✓	—	—
10/2019	—	—	—	—	✓	✓	—
11/2019	185,000	8	9**	—	✓	✓	✓
01/2020	385,000	24	—	—	✓	✓	✓
02/2020	572,000	35	—	✓	✓	✓	—
06/2020	717,000	39	—	—	✓	✓	—
11/2020	914,000	48	—	✓	✓	✓	✓
12/2020	1,114,000	56	—	—	✓	✓	✓
03/2021	1,323,000	70	6	✓	✓	✓	✓
04/2021	1,527,000	83	—	—	✓	✓	✓
06/2021	1,672,000	85	—	—	✓	✓	✓
07/2021	1,867,000	85	5	—	✓	✓	✓
10/2021	2,022,000	85	4**	✓	✓	✓	✓

—No data.
*NDE includes IE, USW, GPR, ER, and HCP techniques.
**The assigned rating was not performed by an onsite certified inspector.
✓ = yes.

Other Data (Construction, Structural Monitoring, Material Testing)

At the conclusion of the deck placement, the team noticed that the profile of the deck was slightly concave. Following a detailed investigation, the Rutgers research team determined that the cause of this deviation from the design was due to the method of deck screeding and finishing. Figure 10 provides a schematic illustrating this issue. As is common practice, the deck of the specimen was constructed with the aid of a paving machine (figure 11). This machine was supported by rails that were mounted via brackets to the exterior girders and to which were imparted a rotational effect. The resulting deck profile resulted in variable concrete cover in both the transverse and longitudinal directions, described in the section titled NDE Data Assessment.

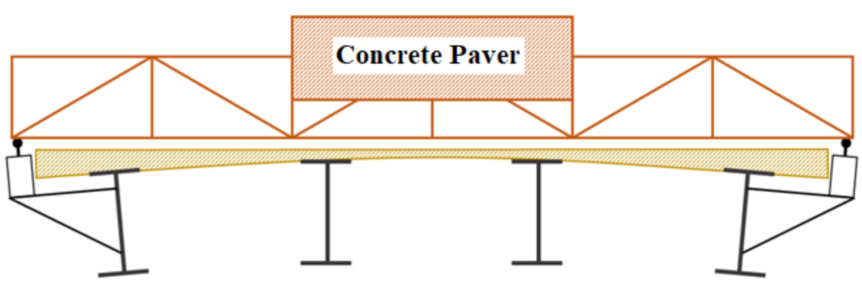

Figure 10. Illustration. Diagram of support and resulting deformation.

Figure 11. Photo. Paving machine during the deck placement.

New Jersey Institute of Technology personnel collected more than 100 fresh concrete material samples during the deck placement. The researchers carried out material tests to estimate fresh concrete properties, compression strength, modulus of elasticity, splitting tensile strength, modulus of rupture, and ER after various curing durations to document properties.

The team collected core samples from the structure at four intervals, as shown in table 3. The samples were prepared and tested for acid soluble chloride concentration, which was used for durability assessment and numerical service life modeling, as described in chapter 4.

The Rutgers team installed several sensors and gauges on the deck specimen to collect real-time information. This information included girder deflections, shear strain, flexural strain, and acceleration at quarter spans and midspans. The horizontal deflection at the open joint along with the vertical strain at pedestals were also collected. The internal strain, temperature, and humidity inside the concrete deck were measured using embedded sensors. The humidity sensors were reported to malfunction at the early stages of specimen age. The ambient temperature was also measured in a continuous manner.

NDE DATA ASSESSMENT

To successfully track the progression of corrosion before delamination, PNDE techniques such as ER or HCP are typically used. For later phases of corrosion when physical damage has manifested, DNDE techniques, such as USW, IE, and IRT imaging, are commonly used. Despite the obvious advantages, deployment of multiple complementary NDE technologies still has not gained widespread use for informed maintenance and replacement decisionmaking. Issues such as measurement inconsistency among multiple NDE technologies, lack of temporal and spatial correlations for multiple datasets, lack of repeatability between multiple vendor products for a given technology, reliability of a given method, and different measurement resolution limit the capabilities of many NDE techniques in being integrated in the routine practice.

The reliability of an NDE technology is a measure of the technology's ability to perform its intended function under a given set of operating conditions. Evaluating the reliability of an NDE technology used to detect damage that is not visually observable can be difficult (Sultan and Washer 2018). Several different approaches have been used to assess the reliability or capability of NDE technologies for bridge decks. One method is to compare the results from one NDE technology with the results of another NDE technology that works by a different physical phenomenon. Comparing the PNDE techniques to a DNDE technology is an example of this approach. The second technique includes the evaluation of NDE technologies for bridge decks based on cores removed from the deck. Removing a core at a single location only determines if the result is correct or incorrect at that particular point; this practice does not assess whether the correct spatial extent of the damage has been effectively represented by the NDE data. Both cores and spatial comparison between NDE technologies are often analyzed using some form of an accuracy index. An accuracy index presents the ratio of correct results to the total number of test points (i.e., samples). The accuracy index is highly susceptible to sampling bias because of the limited number of samples and the inability to characterize all possible outcomes (e.g., false positives (FPs) and false negatives (FNs)).

The NDE data collected from the accelerated testing were subjected to multiple reliability assessments, including the following:

- Time-lapsed analysis to assess temporal consistency of each NDE technology.
- NDE stack evaluations where multiple corrosion and damage stacks are presented to investigate correlation among different NDE technologies at a given time.
- Quantification of NDE results through determination of condition indexes.
- ROC analysis.

The following subsections discuss the results of each assessment approach.

Time-Lapsed NDE Assessment

Multiround data collection allows the monitoring of bridge decks over time (i.e., evaluating the progression of both the corrosion and damage phases). Proper analysis of time-lapsed contours requires repeatability and consistency of the periodic NDE data. One primary challenge is the environmental variations that could cause significant variations in the NDE measurements, especially for electrical or electromagnetic-based technologies such as ER, HCP, and GPR. These technologies are affected by humidity content of the deck after rainfall or snowfall and the presence of residual roadway salt. Environmental sensitivity is less for stress-wave-based NDE techniques (such as IE or USW) where the measurement depends more on mechanical properties.

In total, the team collected 14 datasets from the NDE survey of the deck. For brevity, the chronological progression at four intermittent periods throughout the experiment are presented in figure 12 through figure 20 for each method. The contours for all 14 datasets are provided in appendix A for completeness. Activity appeared to be detected by each method starting at around the eighth or ninth collection interval, and the activity was generally located in the center of the specimen.

IE

Figure 12 and figure 13 show the contour plots of IE for both interpretation methods described in the dominant frequency and delamination condition index section of this chapter. In summary, the data show elevated readings at the supports and along girder lines. For later ages of testing, the team detected a region of elevated "damage" in the center of the specimen.

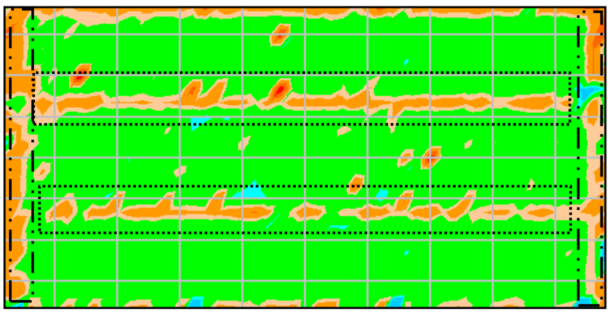

Source: FHWA.

A. First collection—July 2019.

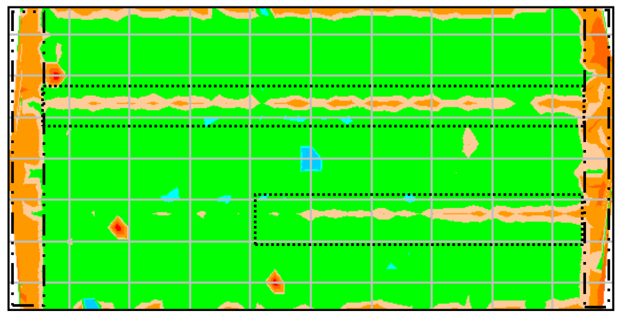

Source: FHWA.

B. Fourth collection—November 2019.

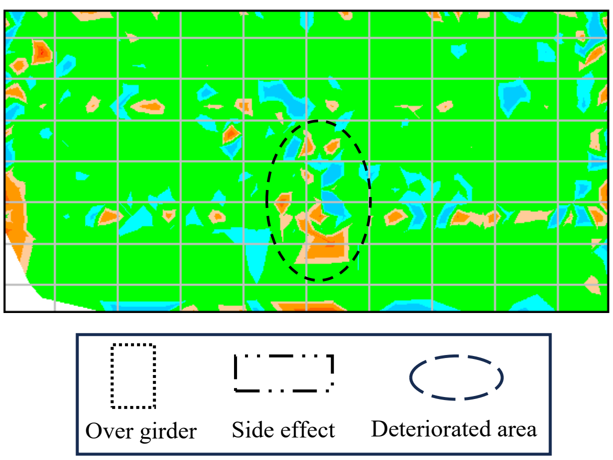

Source: FHWA.

C. Ninth collection—December 2020.

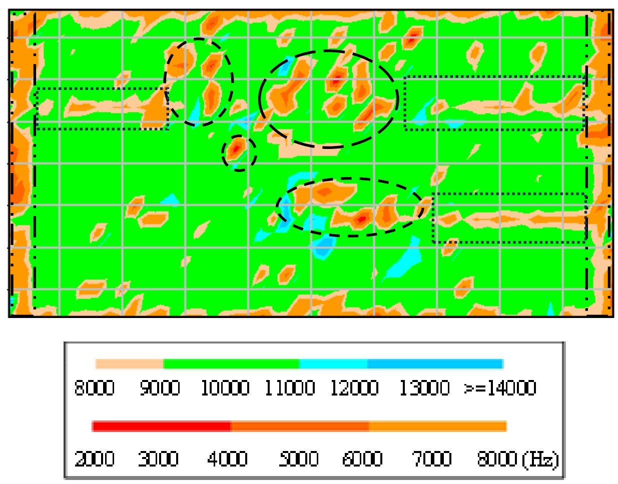

Source: FHWA.

D. 14th collection—October 2021.

Figure 12. Heat maps. IE-dominant frequency (Hz).

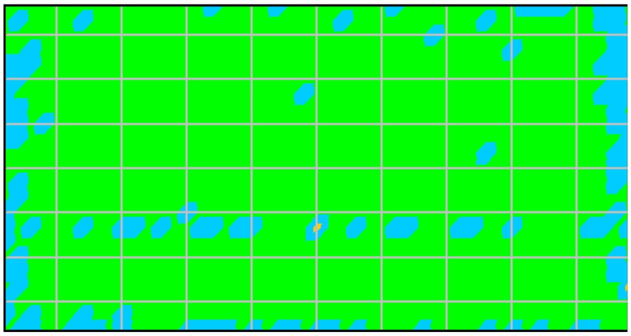

Source: FHWA.

A. First collection—July 2019.

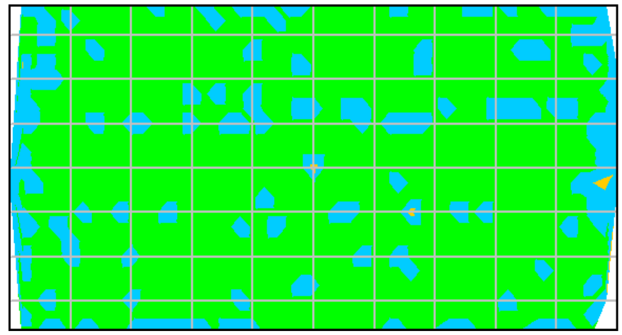

Source: FHWA.

B. Fourth collection—November 2019.

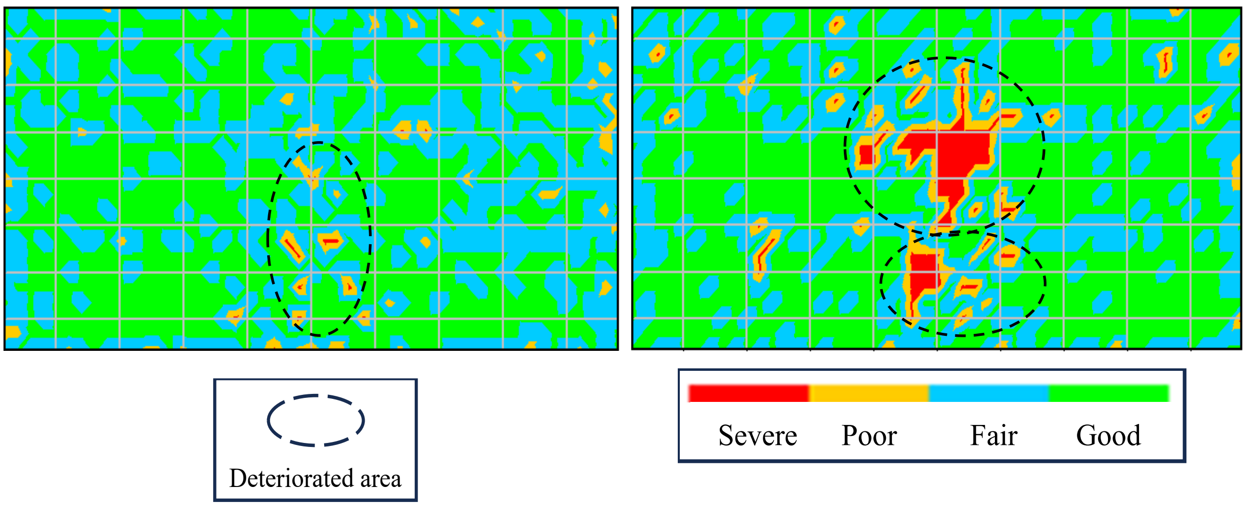

Source: FHWA.

C. Ninth collection—December 2020.

Source: FHWA.

D. 14th collection—October 2021.

Figure 13. Heat maps. IE-index score.

HCP

Figure 14 presents HCP plots. The HCP readings at early collection intervals were likely affected by curing and surface moisture related to the original construction. Note that during the construction of the deck specimen, only the top bay (between the first two longitudinal girders) was made of stay-in-place forms, while the other bays were removable. Therefore, the part of the deck above the stay-in-place formwork imposed higher electrical connection to the reinforcement, resulting in highly negative potential (voltage) readings. This section is indicated by red and yellow regions (circled) in figure 14-A. At later collection intervals, the researchers identified elevated corrosion activity near the center of the slab.

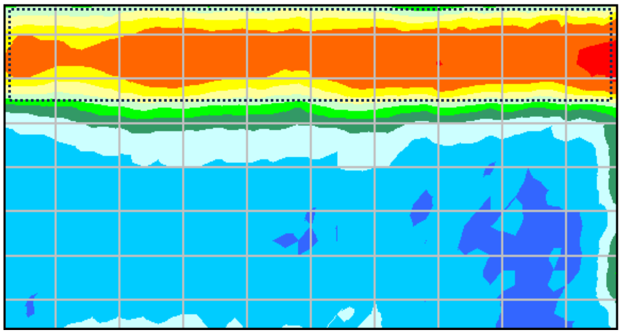

Source: FHWA.

A. First collection—July 2019.

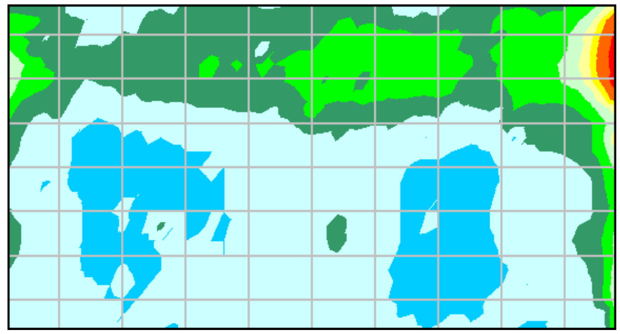

Source: FHWA.

B. Fourth collection—November 2019.

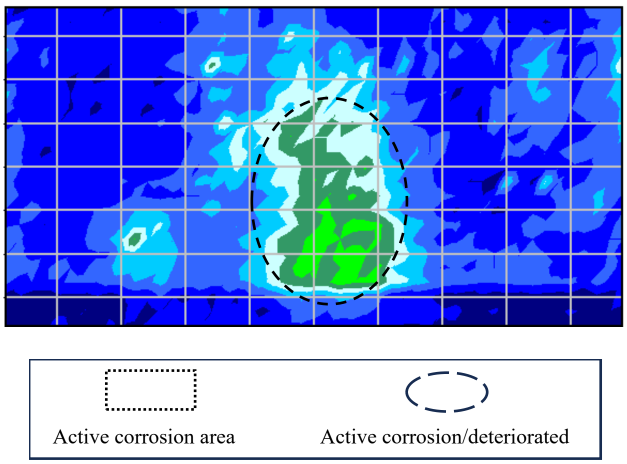

Source: FHWA.

C. Ninth collection—December 2020.

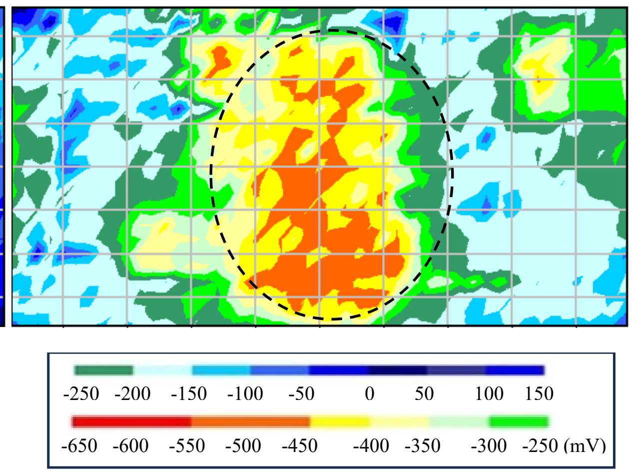

Source: FHWA.

D. 14th collection—October 2021.

Figure 14. Heat maps. HCP (mV).

USW

Figure 15 shows the changes in concrete quality described by the elastic modulus measurement using USW. A review of the contour plots derived for early stages of the experiment indicates a consistent elastic modulus across the deck. For later ages of testing, the team detected a region of elevated “damage” subsequently with lower elastic modulus in the center of the specimen.

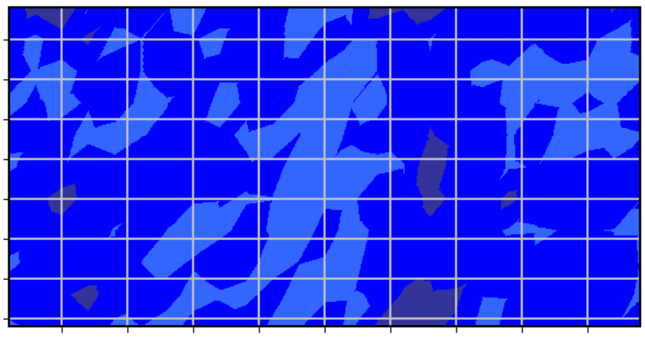

Source: FHWA.

A. First collection—July 2019.

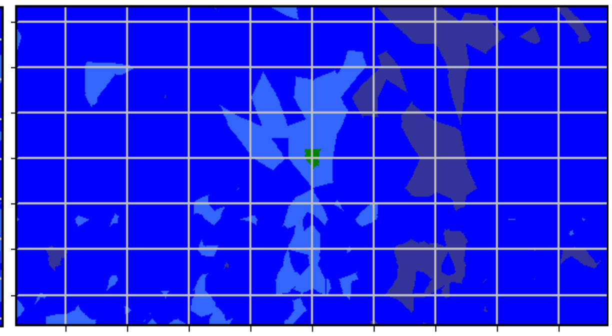

Source: FHWA.

B. Fourth collection—November 2019.

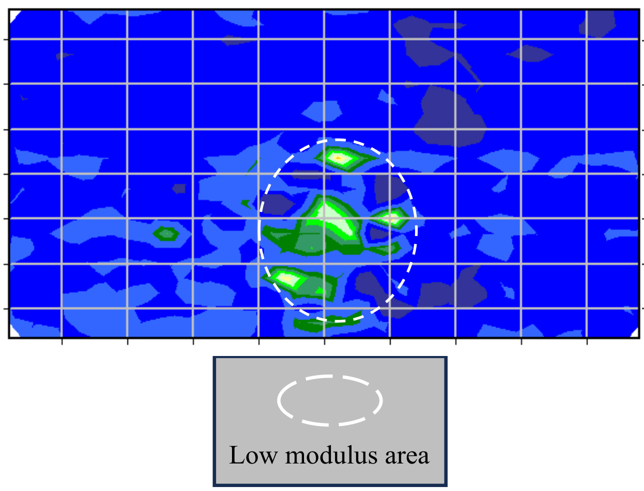

Source: FHWA.

C. Ninth collection—December 2020.

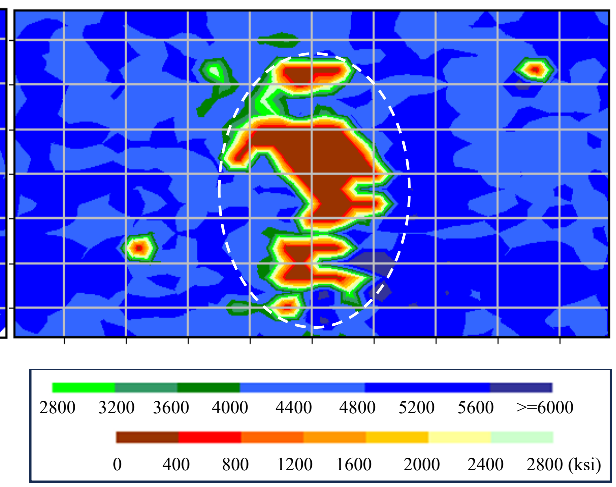

Source: FHWA.

D. 14th collection—October 2021.

Figure 15. Heat maps. USW (ksi).

GPR

Figure 16 and figure 17 show the contour plots of GPR measurements in terms of depth-corrected amplitude and cover depth. The GPR amplitude analysis resulted in generally consistent results until the 10th interval, after which an elevated region of amplitude change was identified in the center of the slab. Furthermore, the team noted a similar change in GPR cover in the same region at the same collection interval. Dielectric changes due to either corrosion product buildup or other effects from chloride ingress have likely affected both GPR-based measurements.

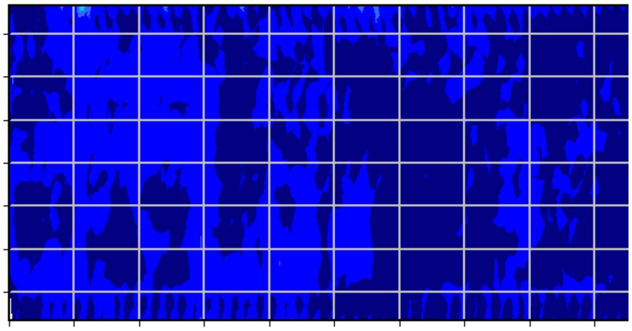

Source: FHWA.

A. First collection—July 2019.

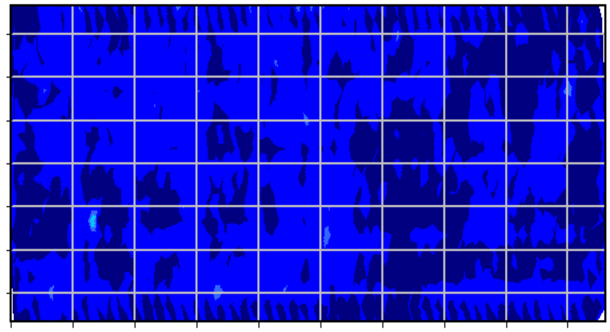

Source: FHWA.

B. Fourth collection—November 2019.

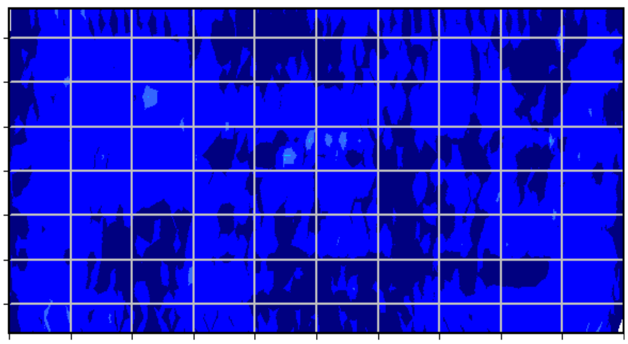

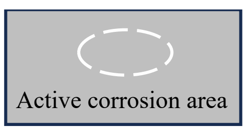

Source: FHWA.

C. Ninth collection—December 2020.

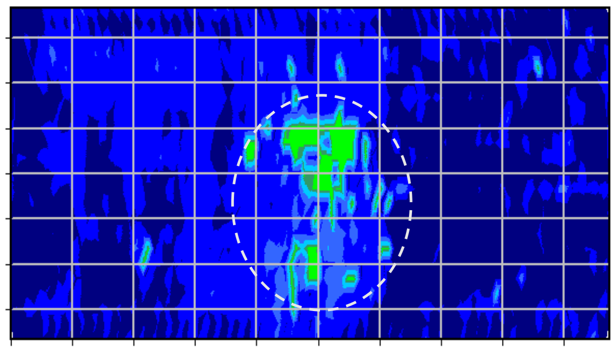

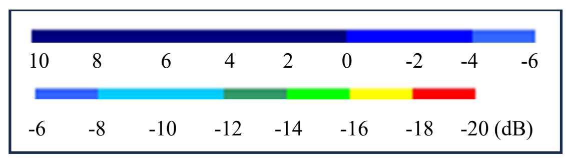

Source: FHWA.

D. 14th collection—October 2021.

Figure 16. Heat maps. GPR depth-corrected amplitude (dB).

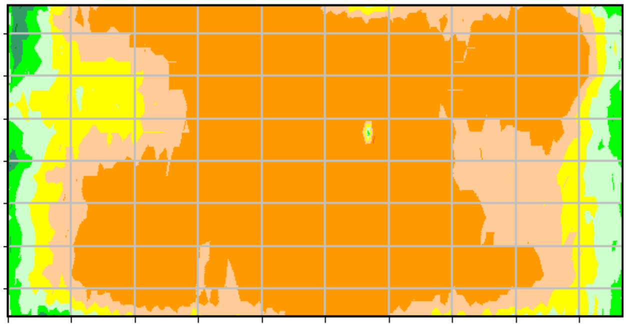

Source: FHWA.

A. First collection—July 2019.

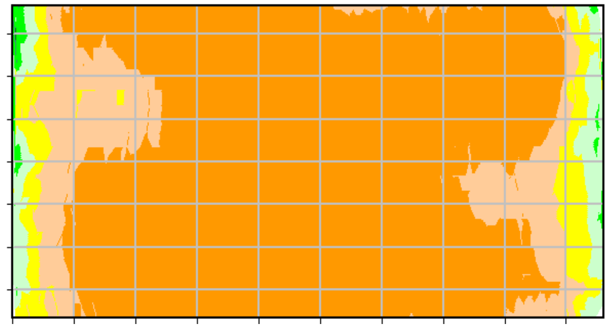

Source: FHWA.

B. Fourth collection—November 2019.

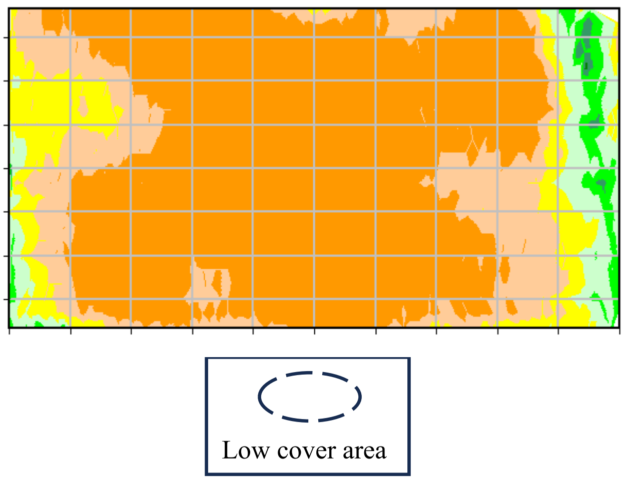

Source: FHWA.

C. Ninth collection—December 2020.

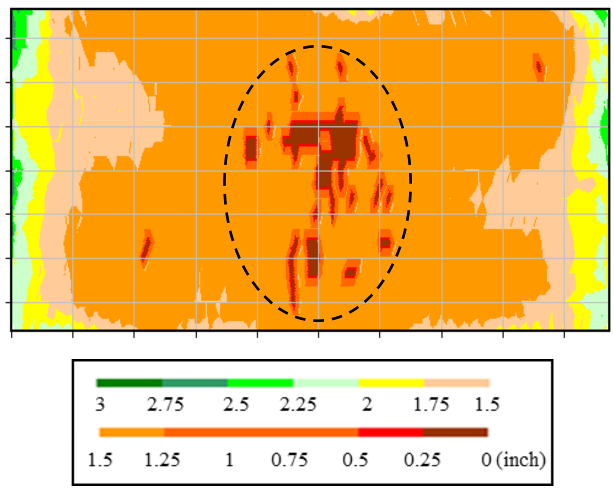

Source: FHWA.

D. 14th collection—October 2021.

Figure 17. Heat maps. GPR cover depth (inch).

ER

As shown in figure 18, the ER data show a trend of slight increasing concrete resistivity with time, as would be expected as the concrete cured. That said, ER readings were consistently low throughout the testing regime, indicating highly permeable concrete. However, corrosion activity in the reinforcing steel was minimal. ER data do not provide much insight into the condition of the structure but rather provide an indication of the concrete maturity and ability to conduct electrical charge.

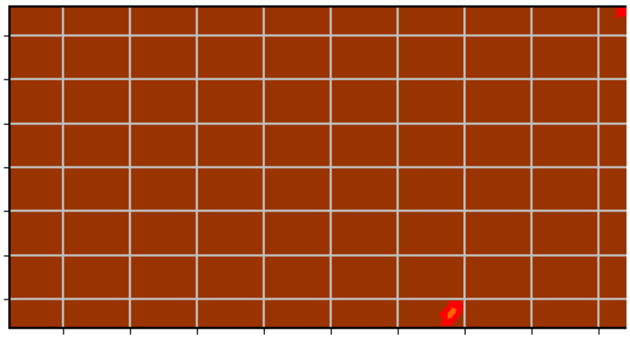

Source: FHWA.

A. First collection—July 2019.

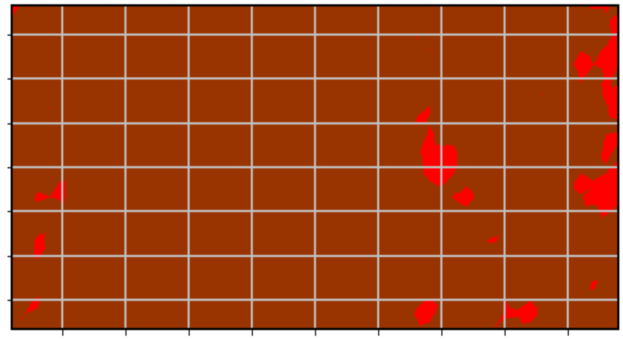

Source: FHWA.

B. Fourth collection—November 2019.

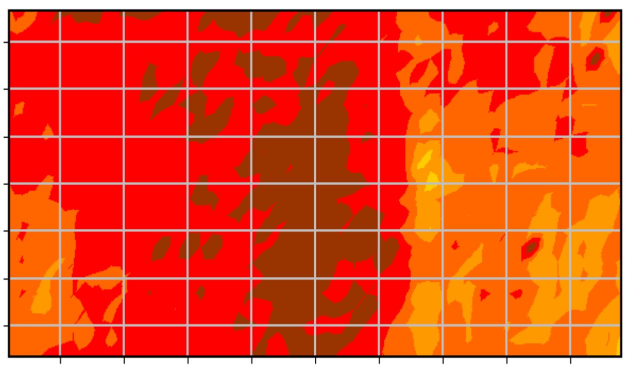

Source: FHWA.

C. Ninth collection—December 2020.

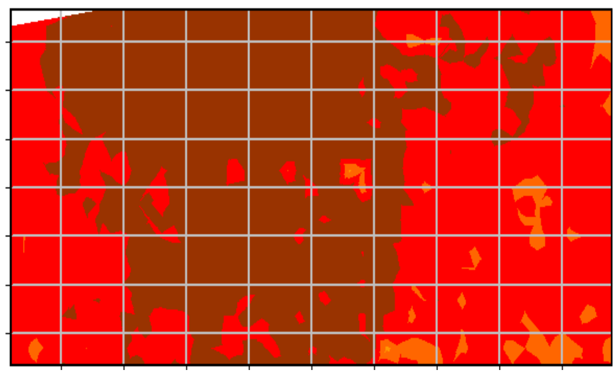

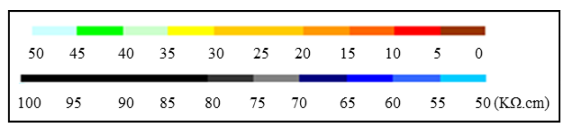

Source: FHWA.

D. 14th collection—October 2021.

Figure 18. Heat maps. ER (KΩ·cm).

HD Imaging

As seen in figure 19, the surface images clearly show a trend of increasing deck surface damage in the center of the span.

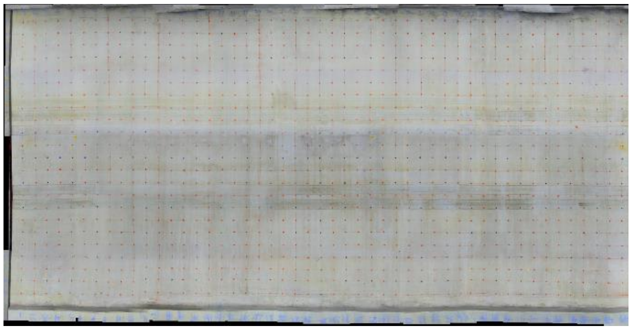

A. Third collection—October 2019.

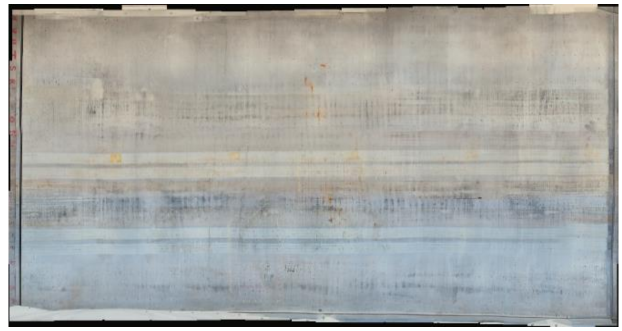

B. Seventh collection—June 2020.

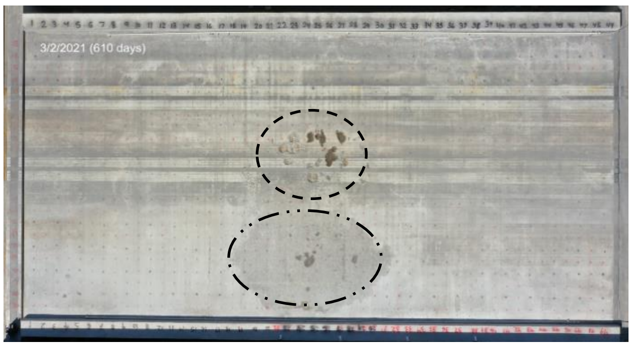

C. 10th collection—March 2021.

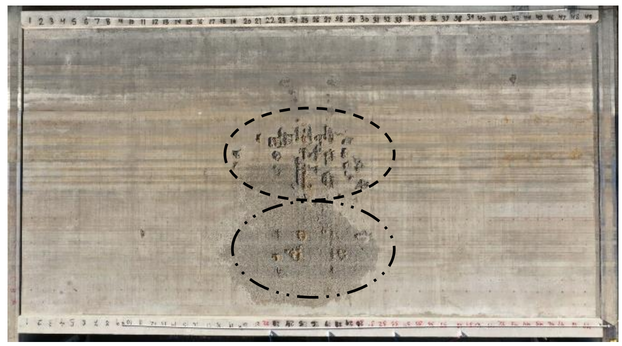

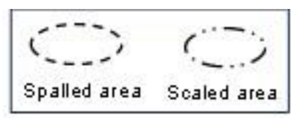

D. 14th collection—October 2021.

Figure 19. Photos. HD Imaging.

IRT

As seen in figure 20, the infrared images taken from the deck clearly show a trend of increasing deck surface or subsurface damage in the center. The selected images were taken around 2 p.m.

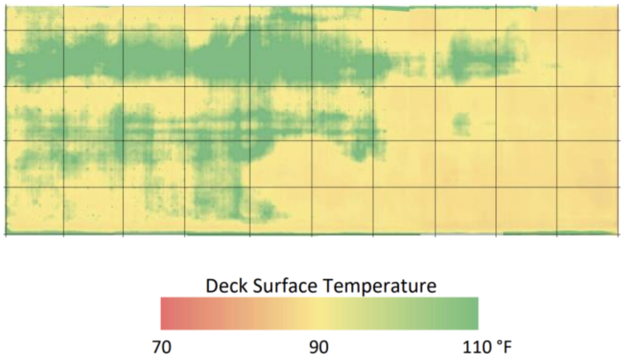

Source: FHWA.

A. First collection—July 2019.

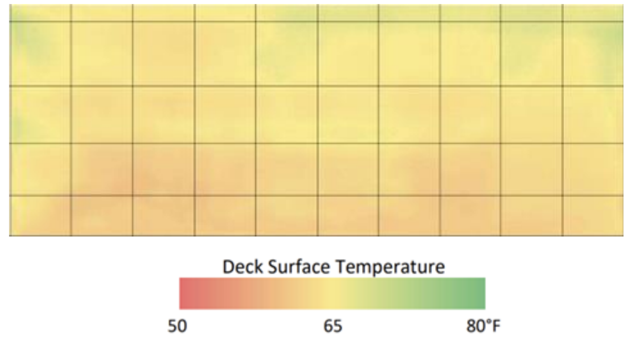

Source: FHWA.

B. Fourth collection—November 2019.

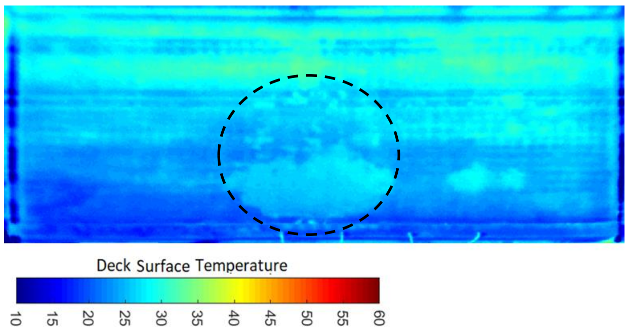

Source: FHWA.

C. Ninth collection—December 2020.

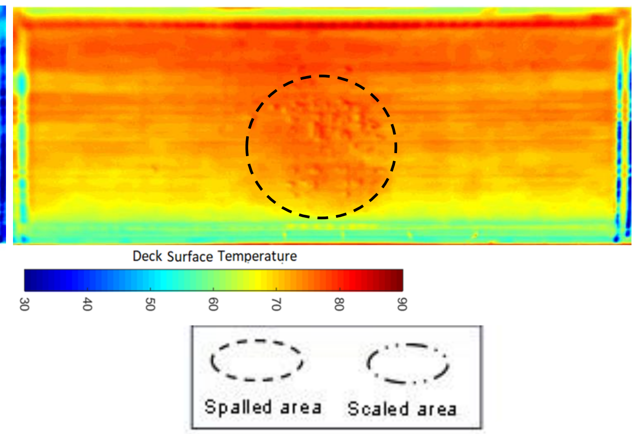

Source: FHWA.

D. 14th collection—October 2021.

Figure 20. Heat maps. IRT.

Multisensor NDE Stacks

To assess the service life of the bridge deck, being able to infer the condition of a bridge deck at all stages of a particular type of deterioration would be of interest. In principle, the deterioration process is initiated through corrosion of embedded reinforcement, which initially produces a cracking plane or delamination within the body of the deck produced from the expansive forces associated with the buildup of corrosion byproducts. As the cracking and corrosion worsen, the delamination extends to the concrete surface, causing the concrete to disengage from the deck producing a spall. Accordingly, PNDE technologies that characterize the corrosive environment surrounding the subsurface reinforcement and are more focused on predicting potential areas of future damage are expected to capture changes at early stages of deck life. On the other side, DNDE techniques that detect physical conditions consisting of subsurface delamination or cracking and surface-presenting anomalies such as cracking and spalling will be picked up at later stages of deck life. To that extent, the research team examined further the images discussed in the previous section titled Time-Lapsed NDE Assessment and compared the different methods side by side to evaluate whether any clear correlations were present between methods at various times.

Corrosion-Based Measurements

Figure 21 through figure 24 compare the results from ER, HCP, GPR amplitude, and HD at four intervals. Stitched HD images associated with some data collection periods were not available. When this situation occurred, stitched images taken from the closest data collection period were used.

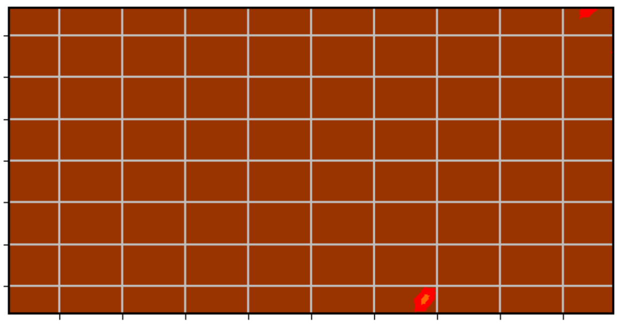

Source: FHWA.

A. ER—July 2019.

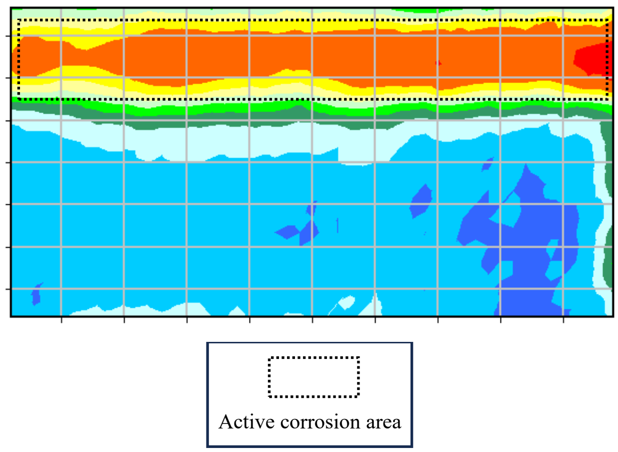

Source: FHWA.

B. HCP—July 2019.

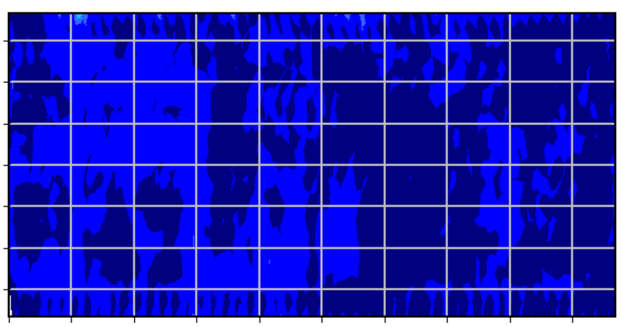

Source: FHWA.

C. GPR amplitude—July 2019.

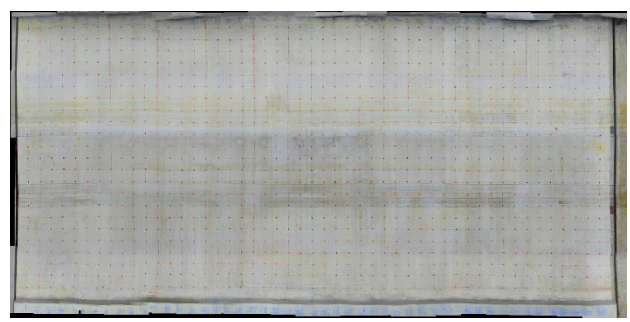

Source: FHWA.

D. HD—September 2019.

Figure 21. Heat maps. Contour plots of ER, HCP, GPR, and HD image in mid-2019 (first interval).

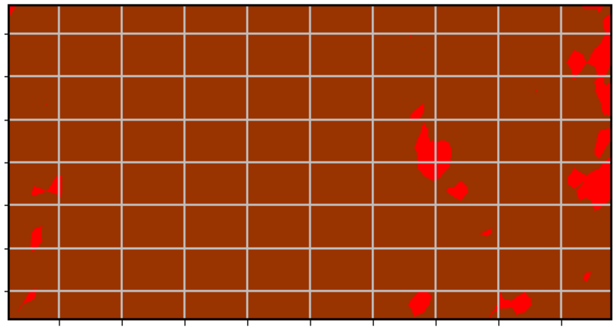

Source: FHWA.

A. ER—November 2019.

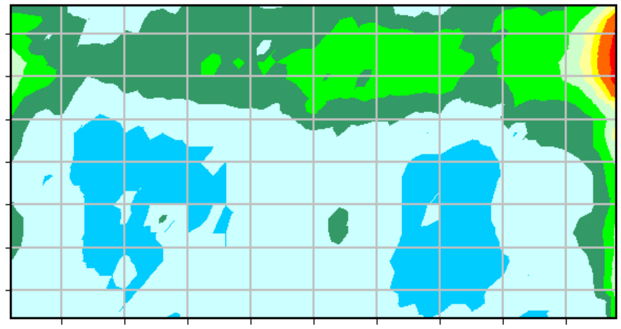

Source: FHWA.

B. HCP—November 2019.

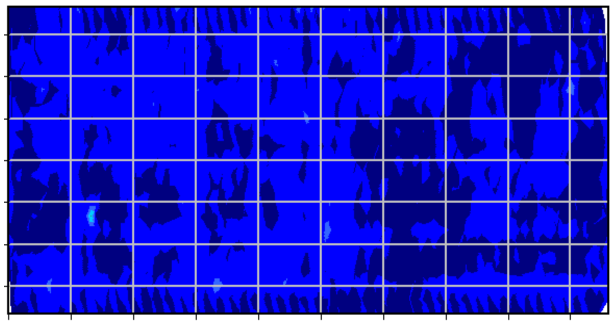

Source: FHWA.

C. GPR amplitude—November 2019.

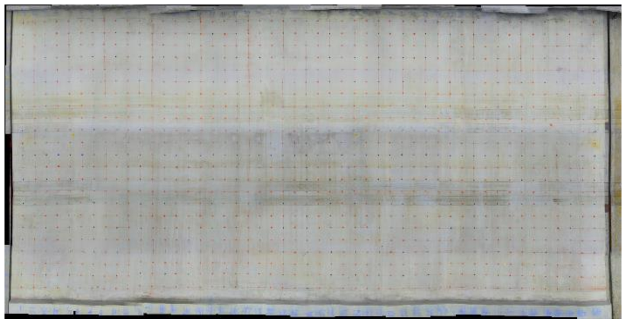

Source: FHWA.

D. HD—September 2019.

Figure 22. Heat maps. Contour plots of ER, HCP, GPR, and HD image in late-2019 (fourth interval).

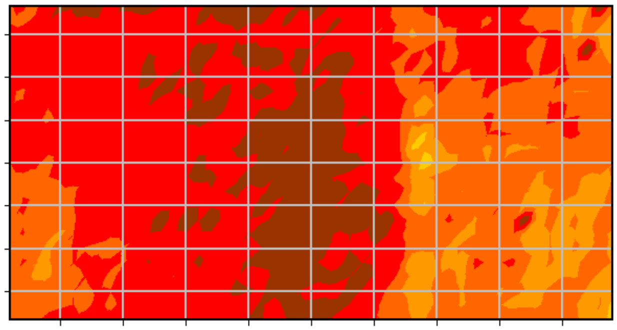

Source: FHWA.

A. ER—December 2020.

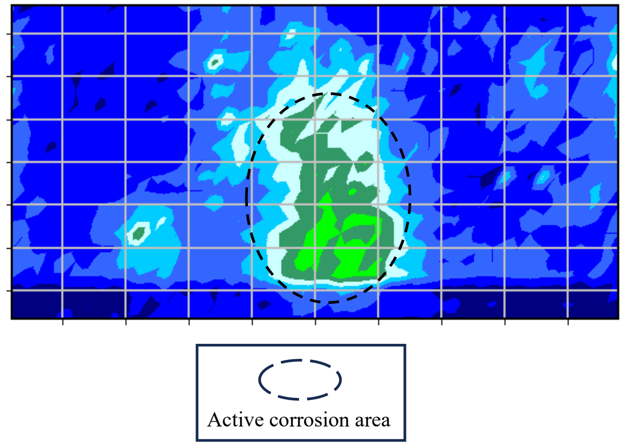

Source: FHWA.

B. HCP—December 2020.

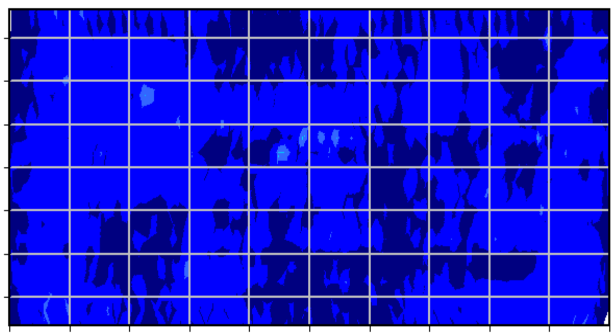

Source: FHWA.

C. GPR amplitude—December 2020.

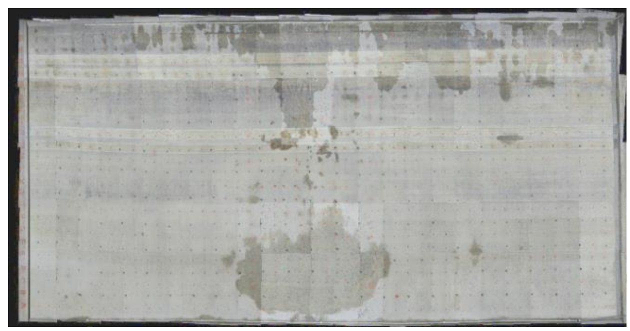

Source: FHWA.

D. HD—December 2020.

Figure 23. Heat maps. Contour plots of ER, HCP, GPR, and HD image in December 2020 (ninth interval).

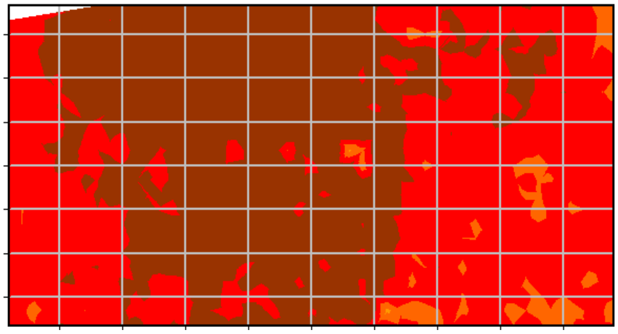

Source: FHWA.

A. ER—October 2021.

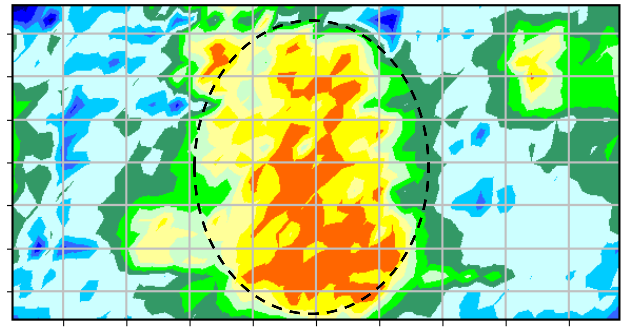

Source: FHWA.

B. HCP—October 2021.

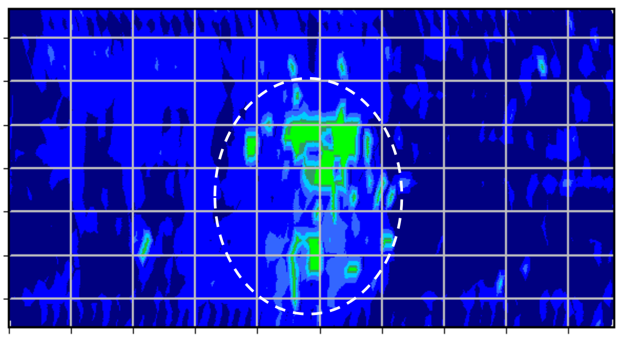

Source: FHWA.

C. GPR amplitude—October 2021.

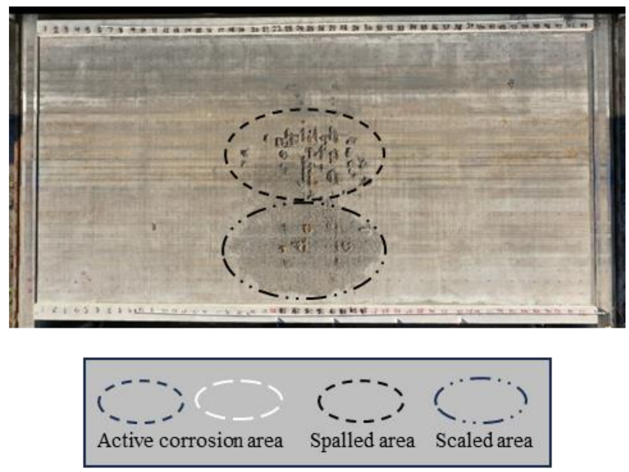

Source: FHWA.

D. HD—October 2021.

Figure 24. Heat maps. Contour plots of ER, HCP, GPR, and HD image in October 2021 (14th interval).

Damage-Based Measurements

Figure 25 through figure 28 compare the results from IE-dominant frequency, IE-index, USW, cover, IR, and HD images at four intervals. Except for IRT, all other NDE techniques follow consistent contour scales.

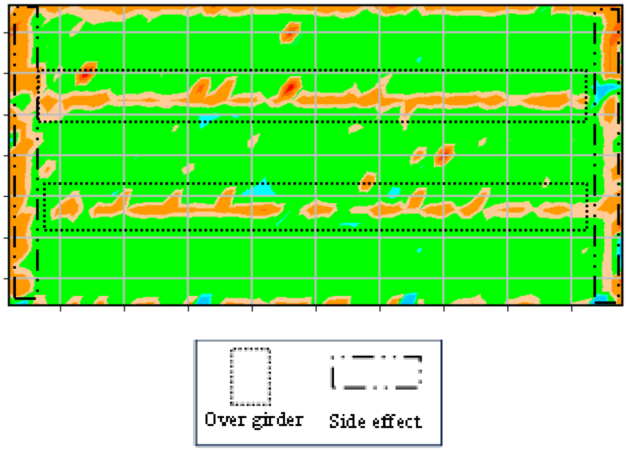

Source: FHWA.

A. IE-dominant frequency—July 2019.

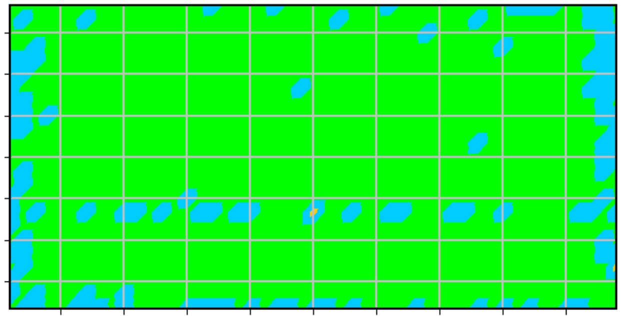

Source: FHWA.

B. IE-index—July 2019.

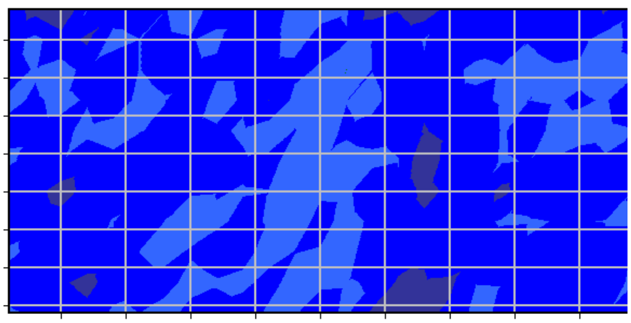

Source: FHWA.

C. USW—July 2019.

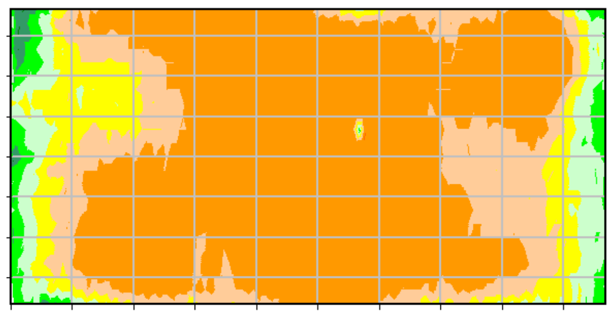

Source: FHWA.

D. GPR cover—July 2019.

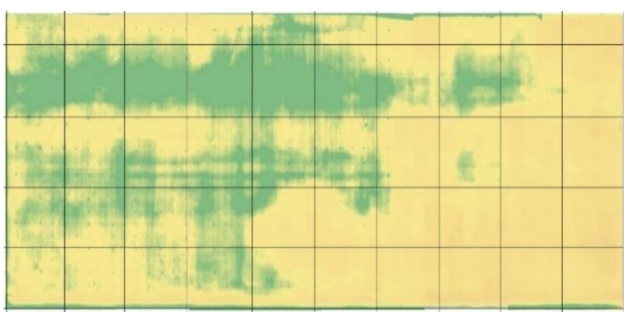

Source: FHWA.

E. IRT—July 2019.

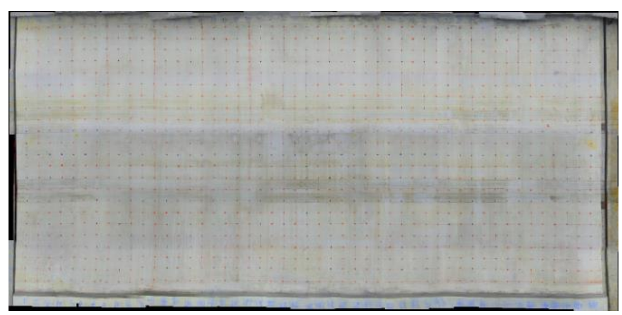

Source: FHWA.

F. HD—September 2019.

Figure 25. Heat map. Contour plots of IE-dominant frequency, IE-index, USW, GPR cover, IRT, and HD image in July 2019 (first interval).

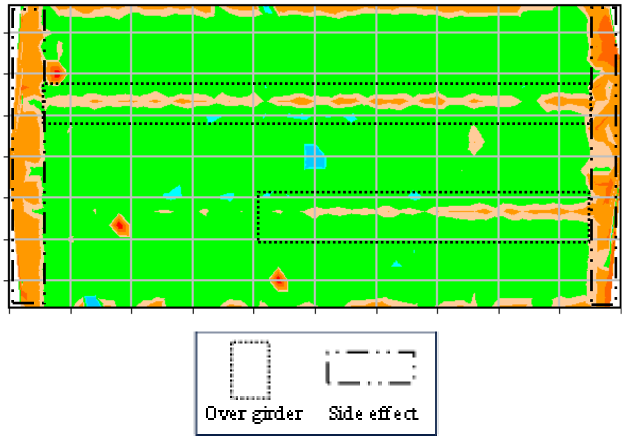

Source: FHWA.

A. IE-dominant frequency—November 2019.

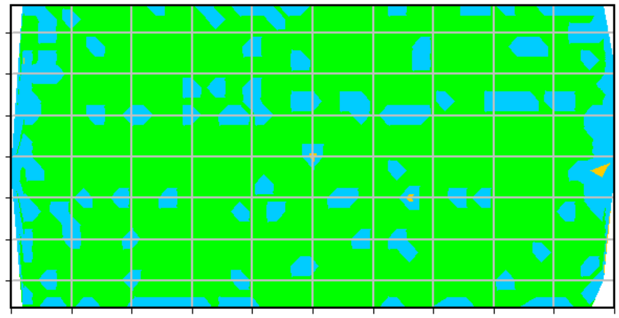

Source: FHWA.

B. IE-index—November 2019.

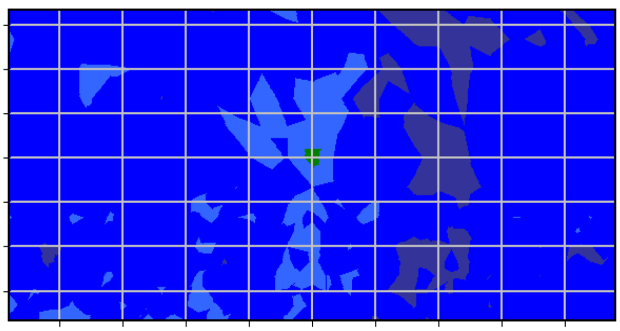

Source: FHWA.

C. USW—November 2019.

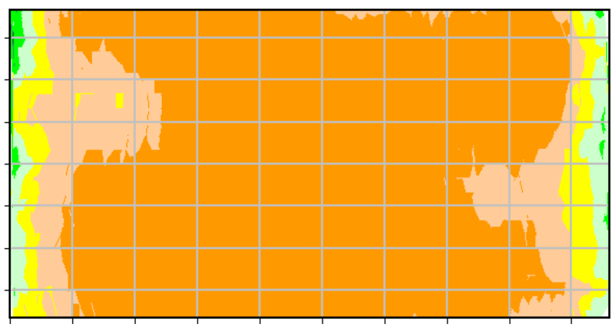

Source: FHWA.

D. GPR cover—November 2019.

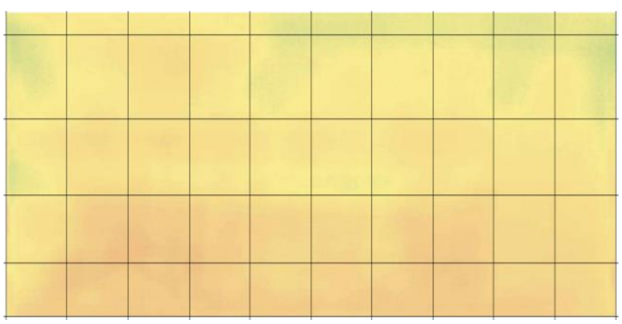

Source: FHWA.

E. IRT—November 2019.

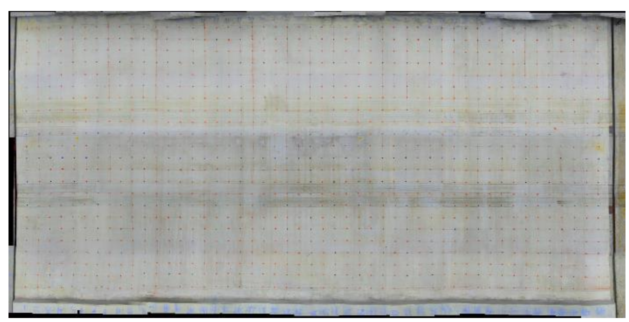

Source: FHWA.

F. HD—September 2019.

Figure 26. Heat maps. Contour plots of IE-dominant frequency, IE-index, USW, GPR cover, IRT, and HD image in November 2019 (fourth interval).

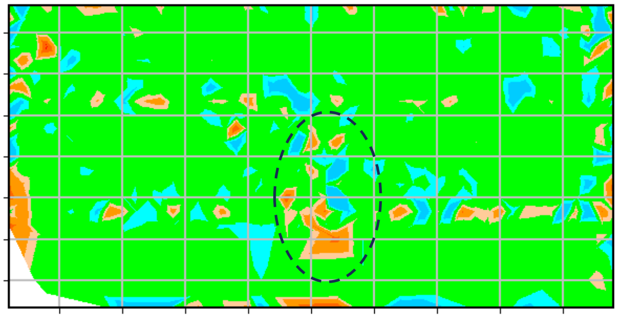

Source: FHWA.

A. IE-dominant frequency—December 2020.

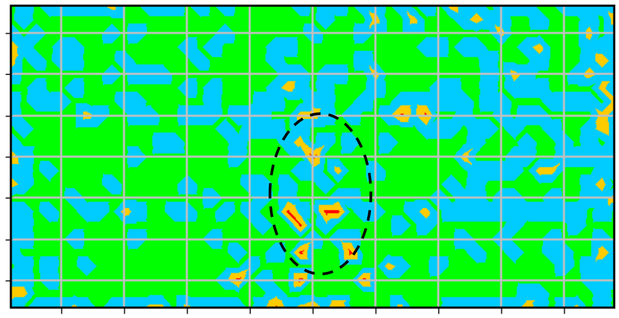

Source: FHWA.

B. IE-index—December 2020.

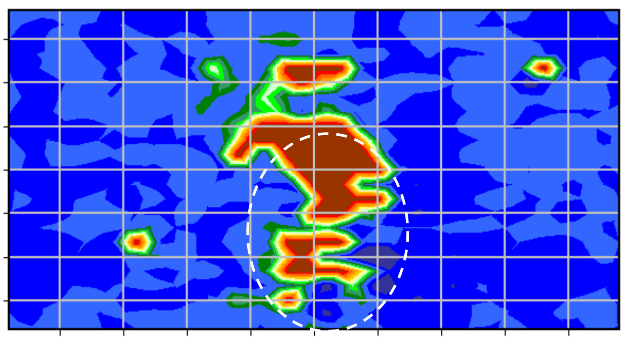

Source: FHWA.

C. USW—December 2020.

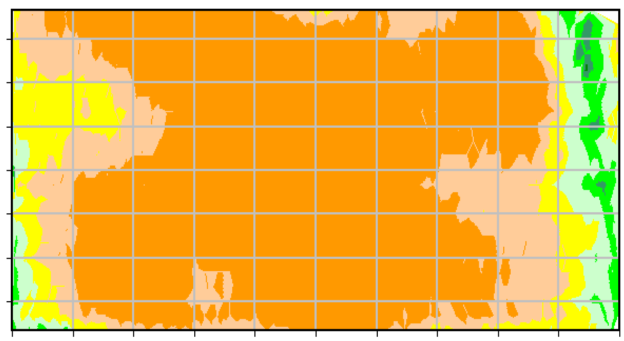

Source: FHWA.

D. GPR cover—December 2020.

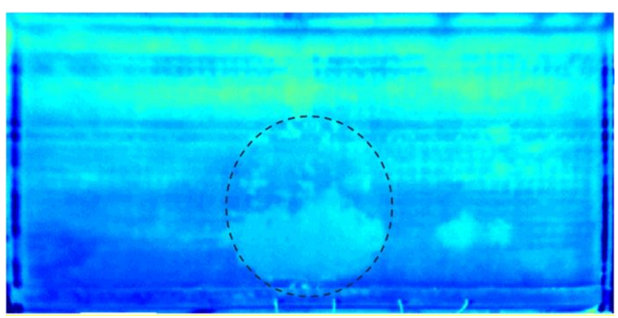

Source: FHWA.

E. IRT—December 2020.

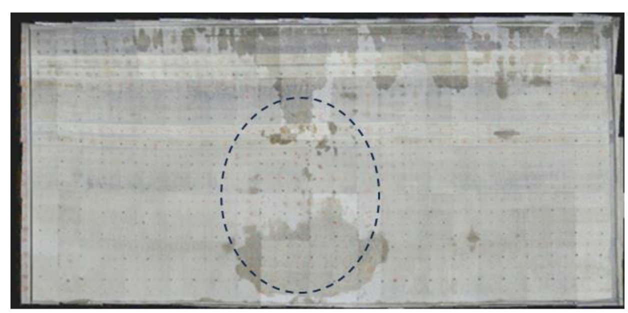

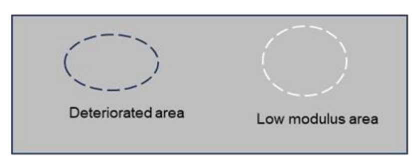

Source: FHWA.

F. HD—December 2020.

Figure 27. Heat maps. Contour plots of IE-dominant frequency, IE-index, USW, GPR cover, IRT, and HD image in December 2020 (ninth interval).

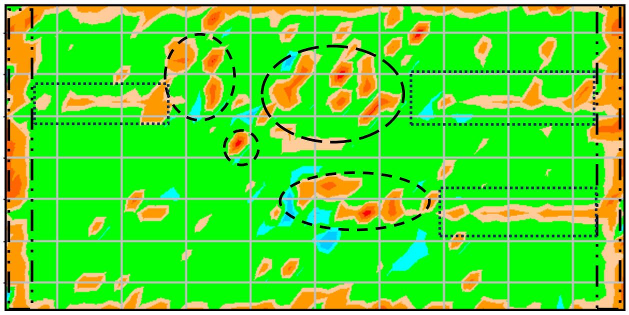
Source: FHWA.

A. IE-dominant frequency—October 2021.

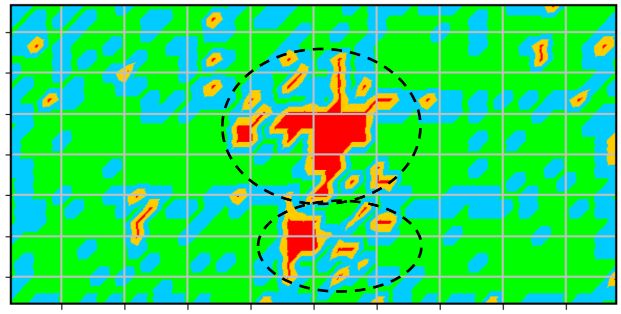
Source: FHWA.

B. IE-index—October 2021.

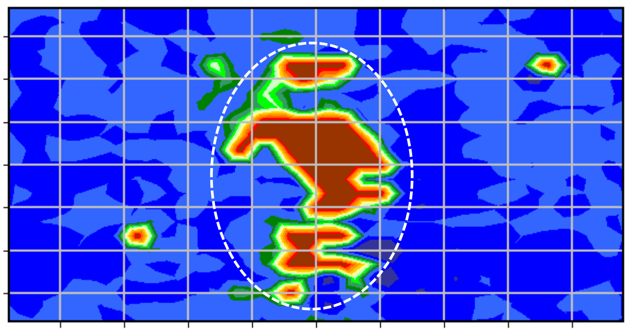
Source: FHWA.

C. USW—October 2021.

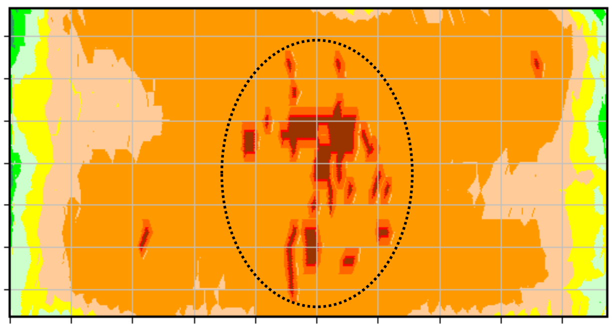
Source: FHWA.

D. GPR cover—October 2021.

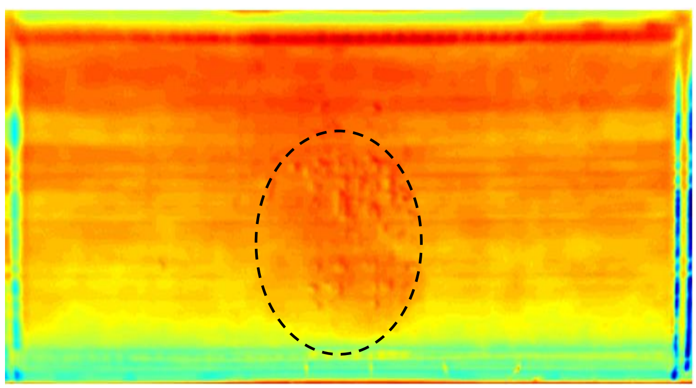
Source: FHWA.

E. IRT—October 2021.

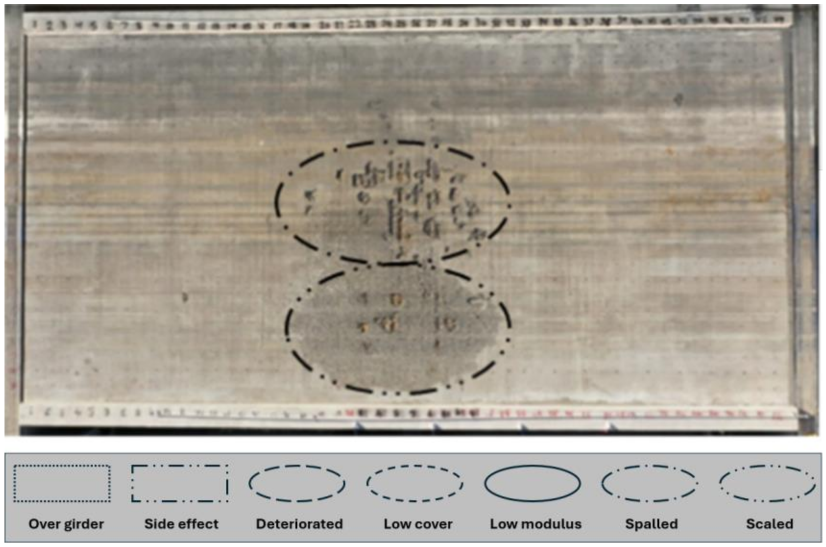

Source: FHWA.

F. HD—October 2021.

Figure 28. Heat maps. Contour plots of IE-dominant frequency, IE-index, USW, GPR cover, IRT, and HD image in October 2021 (14th interval).

Although the review of contour plots for corrosion-based NDE techniques reveals some corrosion activities in the ninth datasets collected in December 2020, the contours for damage-based NDE techniques did not imply any considerable activities. With the progression of degradation on the deck, the damage-based contours presented significant damage in the central parts of the deck.

NDE Condition Index

Inferring deck condition changes from interpretation of contour maps can be the basis for the development of more realistic bridge deterioration models for project-level decisionmaking. As such, developing approaches capable of quantifying the condition of the bridge deck in terms of condition maps and indexes is vital.

Based on the condition index methodology proposed by Gucunski et al. (2016), which was successfully validated through extensive NDE data collected from an in-service bridge, this methodology was adapted on the NDE data collected from the deck. The methodology was applied to the NDE data based on the ranges provided in table 4.

Table 4. Condition index ranges for various NDE methods (Gucunski et al. 2016).

Method	Good	Fair-Poor	Serious
IE-index	1	2 to 3	4
ER (kΩ·cm)	>70	40−70	<40
HCP (mV)	≥ −200	−200 to −350	≤−350
GPR amplitude (dB)	≥ −15	−15 to −20	≤−20

The following equations yield the relationships used to determine the condition indexes proposed by Gucunski et al. (2016). The calculated indexes are reported on the scale of 0 (worst) to 100 (best).

$$ER = \frac{A_{Low} \times 100 + A_{Moderate} \times 50 + A_{High} \times 0}{A_{Total}} \tag{1}$$

Where:

A_{Low} = low-corrosive area; ER of >70 kΩ·cm.
$A_{Moderate}$ = moderate-corrosive area; ER of 40–70 kΩ·cm.
A_{High} = high-corrosive area; ER of <40 kΩ·cm.
A_{Total} = total area surveyed.

$$GPR = \frac{A_{Good} \times 100 + A_{Fair} \times 70 + A_{Poor} \times 40 + A_{Serious} \times 0}{A_{Total}} \tag{2}$$

Where:

A_{Good} = good area; GPR signal attenuation (normalized dB) of ≥ −15 dB.
A_{Fair} = fair area; GPR signal attenuation (normalized dB) of –15 to –17 dB.
A_{Poor} = poor area; GPR signal attenuation (normalized dB) of –17 to –20 dB.
$A_{Serious}$ = serious area; GPR signal attenuation (normalized dB) of ≤ –20 dB.

$$HCP = \frac{A_{90\%\ sound} \times 100 + A_{transition} \times 50 + A_{90\%\ corrosion} \times 0}{A_{Total}} \tag{3}$$

Where:

$A_{90\%\ sound}$ = 90-percent sound area; HCP of ≥ −200 mV.
$A_{transition}$ = transition area; HCP of –350 to –200 mV.
$A_{90\%\ corrosion}$ = 90-percent corrosion area; HCP of ≤ –350 mV.

$$IE - Index = \frac{A_{Good} \times 100 + A_{Fair} \times 50 + A_{Poor} \times 50 + A_{Serious} \times 0}{A_{Total}} \tag{4}$$

Where A_{Good}, A_{Fair}, A_{Poor} and $A_{Serious}$ are defined using the method discussed in Table 2.

Figure 29 shows the results of accelerated testing NDE data analysis using the formulation described in the preceding paragraphs. The average cover and concrete elastic modulus are also provided for reference in figure 30.

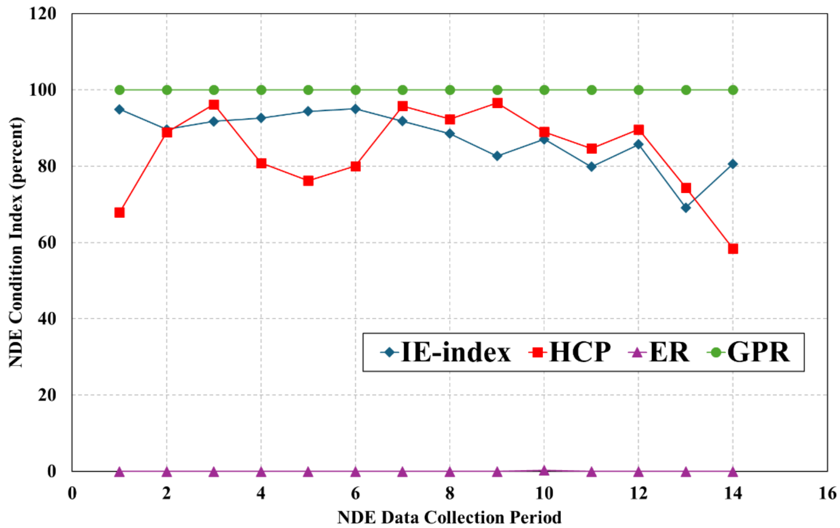

Source: FHWA.
Note: The *x*-axis represents the round of data collection, ranging from 1 to 14.

Figure 29. Graph. NDE condition index for IE, HCP, ER, and GPR amplitude.

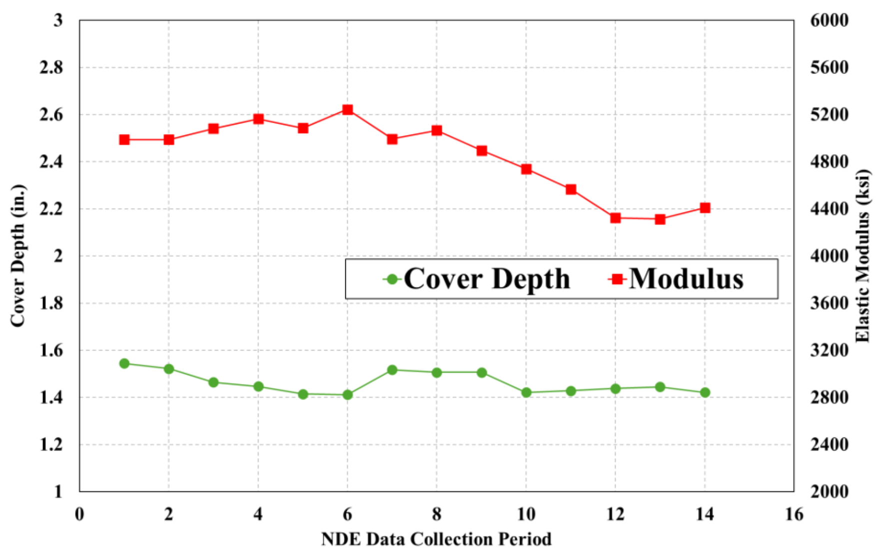

Source: FHWA.
ksi = kilopounds per square inch.
Note: The *x*-axis represents the round of data collection, ranging from 1 to 14.

Figure 30. Graph. Comparison of cover depth and concrete elastic modulus.

Based on the findings of the condition index approach, no significant correlation between the methods is evident. The GPR amplitude indicates a condition index of 100 percent, whereas the ER indicates an index of 0 percent. This finding suggest that either these methods show low sensitivity to changes in condition index within the framework of this experiment and the NDE data collected, or the criteria in Table 4 needed to be readjusted to better reflect the observed changes in both the ER and GPR techniques. The other methods (HCP, IE, GPR) vary with the data collection interval. These condition indexes followed similar trends, where an initial increase was observed during the early stages of specimen service life followed by an expected decline in later stages. Assuming that the condition of the deck worsens with time, then some weak correlation between condition index and NDE measurements is present.

Except for a few interim data collection periods, the average cover values provided in figure 30 generally indicated a constant cover depth across the data collection periods. The review of the cover depth variations shown in figure 30 reveals some fluctuations between rounds 6 and 10. Since the reported cover depth is an average of the apparent cover depths across the specimen, accurate GPR determination of cover depth requires ground-truth comparison and calibration against physical measurements. Cover depth measurements should remain consistent over time, unless accounting for scaling or spalling, in which case the cover depth should only decrease. Given the absence of physical measurements for cover depth, such variations (ranging between 5 and 10 percent) could be anticipated. Unlike the cover depth, the average elastic modulus values indicated a consistent decline in the overall modulus of the deck with the age of the specimen.

ROC Analysis

In addition to basic correlation and the NDE condition index analysis, the researchers performed a more comprehensive reliability analysis on the processed NDE data using a ROC analysis methodology. Herein, reliability refers to the degree to which an NDE method consistently produces accurate and repeatable measurements under similar conditions. In brief, ROC analysis is a statistical basis for quantitatively assessing the reliability of an inspection or diagnostic system to determine the presence of a defect (Metz 1978). Electrical and radar engineers originally developed this technique during World War II to assess the ability of radar systems and operators to correctly identify enemy aircraft. The National Aeronautics and Space Administration used a similar concept for NDE of flaw detection on metallic materials. Used by Nockemann, Heidt, and Thomsen (1991), Shin and Grivas (2003), Martino et al. (2014), and Sultan and Washer (2018), this technique was first introduced to civil engineering, primarily for bridge deck NDE evaluation. Basic principles of ROC analysis can be found elsewhere (Metz 1978). More recently, Sultan and Washer (2018) used this technique in assessing the reliability of GPR and IRT technologies.

For the current accelerated testing study, the researchers used the ROC analysis to compare the effectiveness of each different NDE method in a quantitative point-by-point comparison, relative to the ground truth, in detecting unsound or otherwise defective concrete.

ROC Methodology

ROC analysis addresses many of the limitations of accuracy-based approaches for assessing the reliability of NDE results. ROC analysis includes all the practical thresholds to provide a more objective and comprehensive analysis of reliability. The ROC analysis is less susceptible to sampling bias and explicitly represents the probability of detection (POD) and the probability of false alarm (POFA). In this way, the accuracy index for any practical threshold can be determined.

An ROC analysis considers all the possible outputs from the comparison of the ground truth and the NDE data (figure 31). This analysis includes the following results:

- True-positive (TP) results: Both NDE and the ground truth indicated delamination.
- True-negative (TN) results: Both NDE and the ground truth indicated no delamination.
- FP results: NDE indicated delamination, but ground truth indicated no delamination.
- FN results: NDE indicated no delamination but the ground truth indicated delamination.

For a given threshold setting, these indexes can calculate the POD or TP rate (TPR): TPR=TP=n^+, where n^+ is the total number of positive test points. The POFA or FP rate (FPR) is also determined: FPR=FP=n^-, where n^- is the total number of negative test points. This process is repeated across the range of practical threshold settings. This range extends from a value at which the entire deck would be indicated as sound, such that the POFA is 0 percent, to a value at which the entire deck would be indicated as delaminated and the POFA is therefore 100 percent (i.e., all the sound areas are indicated as delaminated) (Sultan and Washer 2018). On sweeping a range of threshold, an ROC curve is plotted, where the vertical and horizontal axes denote the POD and POFA, respectively.

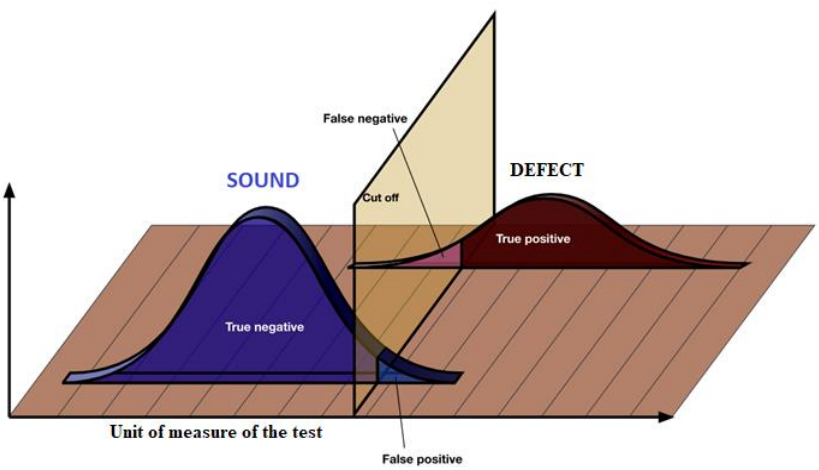

Figure 31. Illustration. Test result values (TP, TN, FN, FP) (Wikimedia Commons 2021).

As shown in figure 32, the AUC of the resulting ROC curve is considered by Sultan (2017), as well as by industry experts, to be a global measure of reliability. AUC is equivalent to the probability of correctly identifying and ranking a random pair of positive and negative test points. Larger AUC values generally indicate better performance of the diagnostic system. An AUC of 1.0 represents an ideal (perfect) diagnostic system. An AUC of 0.5 represents a diagnostic system of no ability to differentiate positive and negative test points. An AUC of 0 represents the opposite of an ideal diagnostic system.

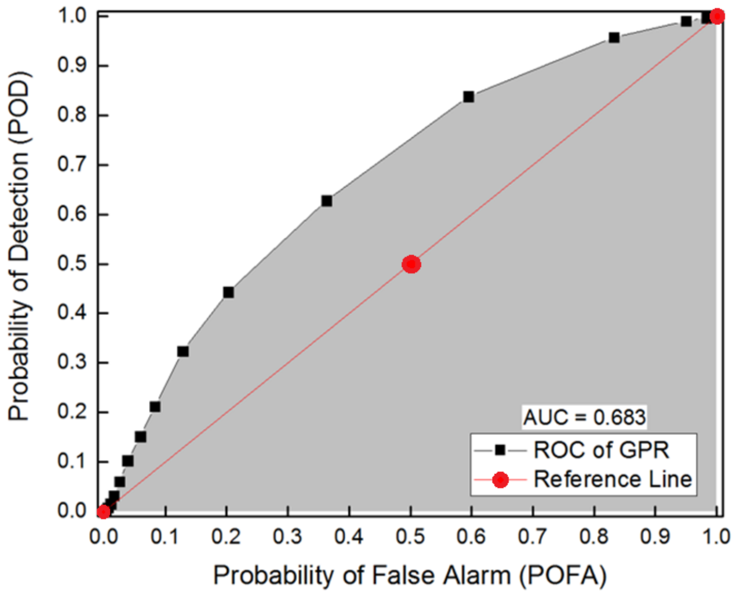

Figure 32. Graph. Typical conventional ROC curve (Sultan 2017).

To successfully implement ROC, the ground truth needs to be defined so that the measurements from each NDE technology are compared point by point with the actual condition of the deck (whether sound or defective). Ground truth is therefore established to accurately represent the location and extent of areas of delamination. Lack of a true "ground truth" significantly limits the applicability of the entire dataset for use with in-service structures.

Unfortunately, no destructive verification of the NDE data from the experimentation occurred, and the datasets themselves were severely limited by the lack of consistent exposure and therefore lack of deterioration. To overcome this limitation for the present study, the team first used the IE-index results as the ground truth and then performed an ROC analysis. Using IE results as ground truth for the study was supported by a previous study by Sultan (2017). The study showed an IE approach AUC value of greater than 0.9 for laboratory samples with simulated subsurface areas of delamination, with values of 1.0 obtained for areas with depths of 4 inches or less. A separate section titled Reliability Assessment of IE Data is dedicated to investigating if IE data are reliable and consistent enough to establish the ground truth. The team then performed additional analyses using other NDE measurements as the ground truth.

Before analyzing the data using the ROC approach, the team found it necessary to develop a consistent point-by-point data comparison between different NDE technologies. The following subsection describes the sampling approach taken to address this issue.

NDE Data Interpolation and Down-sampling

The team collected the NDE data on a regular grid across the surface of the deck; however, the measurement spacing varied slightly between measurements. To effectively compare the NDE data on a point-by-point basis, the team required interpolation and averaging between the data grids. Figure 33 through figure 36 provide the sample data grids. HCP and IE were performed on a 1-ft-by-1-ft grid, and data from the other methods were processed into a consistent format.

USW was collected inconsistently on a 1-ft-by-1-ft or 1-ft-by-2-ft grid, and adjacent data points were averaged to obtain intermediate points on the 1-ft-by-1-ft grid. GPR scanning was performed on a 1-ft-by-6-inch grid and sometimes smaller, and therefore data were down-sampled (averaging of adjacent points) on a 1-ft-by-1-ft grid. The team then used the final, processed datasets in the ROC analysis.

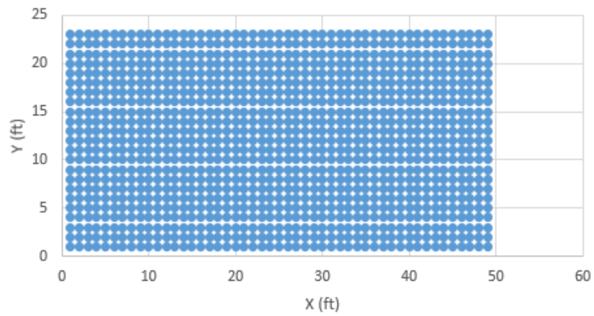

Source: FHWA.

Figure 33. Graph. IE data—1-ft-by-1-ft grid.

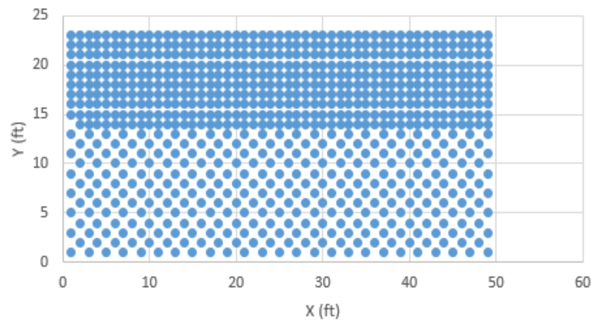

Source: FHWA.

Figure 34. Graph. USW data—variable grid, lower density.

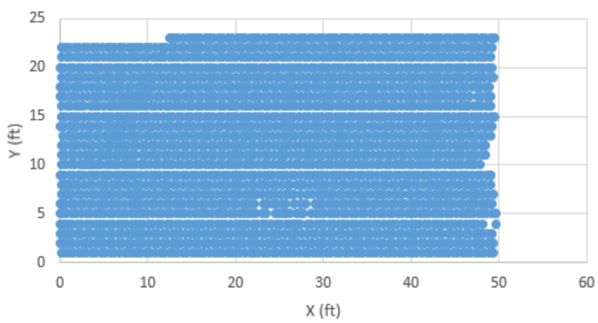

Source: FHWA.

Figure 35. Graph. GPR data—variable grid, higher density.

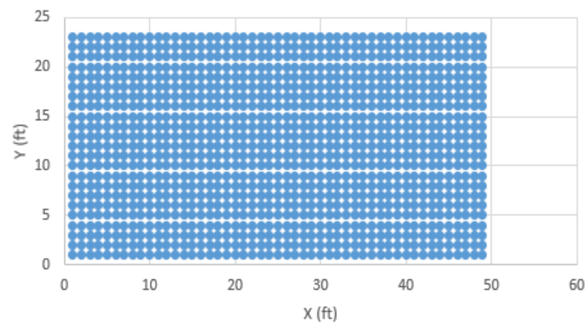

Source: FHWA.

Figure 36. Graph. HCP data—1-ft-by-1-ft grid.

The processing of IRT data needed additional efforts to convert the infrared images to a 1-ft-by-1-ft grid. Before November 2019, the entirety of the deck was covered with several images. These images were stitched together into a single image. After November 2019, a new lens permitted the entire deck to be captured in a single image when mounted atop a telescoping pole. As shown in figure 37-A, the images taken with the wide-angle lens have a fair amount of distortion. This issue was corrected in processed IRT images using postprocessing techniques, as shown in figure 37-B. Some of the image files associated with the early data collection periods were not available in a sufficient quality to the researchers; therefore, they were eliminated from the reliability analysis. At the end, as shown in figure 38, the temperature data were interpolated in a 1-ft-by-1-ft grid to consistently compare with other NDE test data.

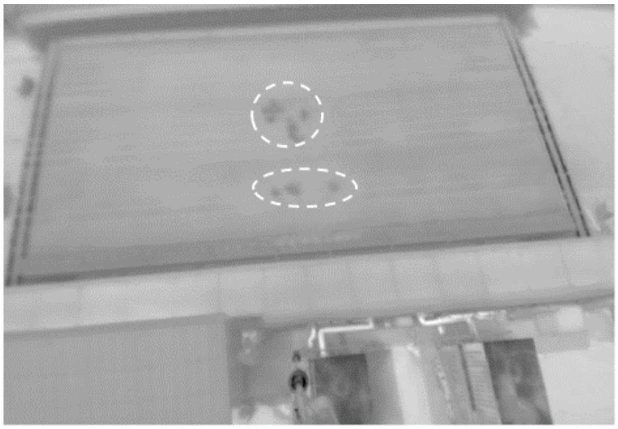

Source: FHWA.

A. View from infrared camera mounted atop a telescoping pole.

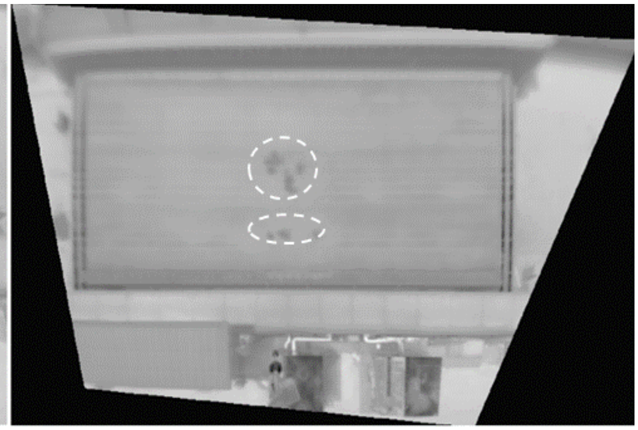

Source: FHWA.

B. Processed to rectangular shape.

Figure 37. Photos. IRT image taken from an infrared camera mounted atop a telescoping pole and postprocessed to rectangular shape.

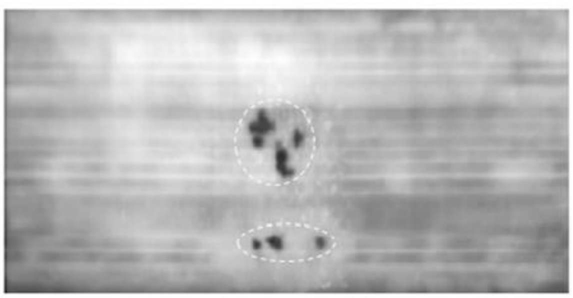

Source: FHWA.

A. Gray scale.

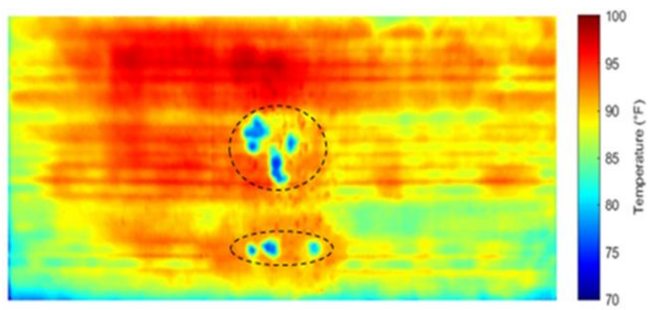

Source: FHWA.

B. Colored contour.

Figure 38. Heat maps. Postprocessed IRT data.

Reliability Assessment of IE Data Interpretation Using Indexing and Dominant Frequency Techniques

The first step in assessing the reliability of IE data was to investigate if the successive time-lapsed contours followed a temporal consistency. In other words, if an improved condition was observed, the accuracy of data collection procedure and/or data processing steps had to be revisited. That being said, the point-by-point comparison should have included some levels of tolerance due to averaging and interpolation steps embedded in developing contour plots.

Appendix A presents the time-lapsed contour plots for both IE-index and IE-dominant frequency. The review of these contours indicates a reasonable consistency in both sets of contours.

The second assessment included the point-by-point comparison of IE-index and IE-dominant frequency data. For this assessment, the dominant frequency for each measurement was plotted against the index assigned to that measurement. Figure 39 includes more than 15,000 data points from all 14 data collection periods, where each data point corresponds to a unique IE measurement from one location of the deck at a given time. The vertical and horizontal axes show the IE-dominant frequency and assigned IE-index, respectively. The average and 1 standard deviation of the IE-dominant frequencies for each IE-index rating are shown using red solid and dashed lines, respectively. In the transition from good to fair, the presence of small delamination is often identified by a secondary peak in the frequency spectrum (figure 2), rather than a shift in the dominant frequency peak. This situation does not necessarily indicate a descending or ascending trend, as shown in figure 39. Furthermore, during the transition from fair to poor, an ascending trend is expected because moderate to deep discontinuities generate a higher dominant frequency than the resonant frequency associated with the deck thickness. Subsequently, in the transition from poor to severe, a descending trend is anticipated as shallow discontinuities cause the cover to vibrate like a drum, resulting in a much lower dominant frequency.

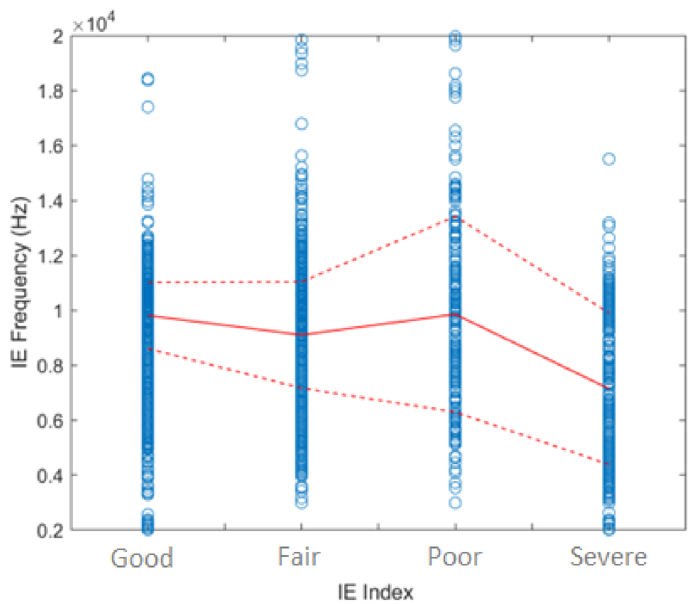

Source: FHWA.

Figure 39. Graph. Correlation of IE measurements in terms of dominant frequency and condition index.

The primary purpose of establishing the ground truth is to accurately represent the location and extent of areas of delamination. If IE is opted to be the ground truth, ensuring the IE data accurately represents the condition of deck is essential. For the current study, the first step in fulfilling this requirement was to determine whether sufficient correlation existed between different interpretations of IE data (i.e., dominant frequency and index). Figure 40 presents several different scenarios that correlate the IE-dominant frequency measurements with the IE-index for each period of data collection. In this figure, these two measurements were compared if they both detected the same spot on the deck as sound or delaminated. Shown in table 5, four different scenarios were considered by the researchers to ensure all possible interpretation of sound/delamination that could be taken from both dominant frequency and index measurements were covered. Unlike the general expectation that these two measurements should lead to highly correlated results (R^2 >0.8), the researchers' assessment did not concur. In fact, the resulting correlations fell to a very low range, where very small agreement could be concluded between these two interpretations of IE measurements. Note that this assessment is not a representation of the reliability of the IE method itself, but of the interpretation criteria.

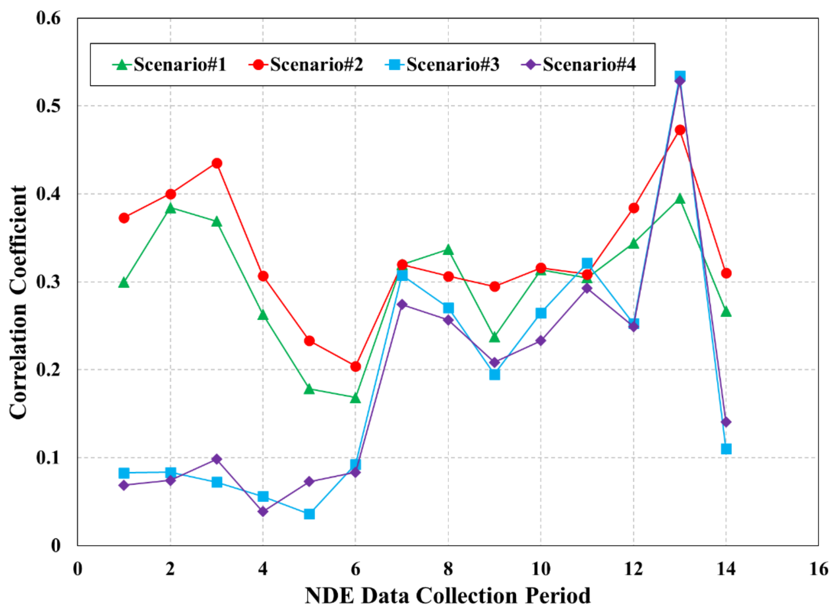

Source: FHWA.
Note: The x-axis represents the round of data collection, ranging from 1 to 14.

Figure 40. Graph. Correlation coefficient of IE-dominant frequency and IE-index measurements.

Table 5. Definition of proposed scenarios.

Case	IE-Index		IE-Dominant Frequency (kHz)	
	Delamination	Sound*	Delamination	Sound*
Scenario 1	Fair, poor, serious	Good	<8 and >11	8 to 11
Scenario 2	Fair, poor, serious	Good	<9 and >11	9 to 11
Scenario 3	Poor, serious	Good, fair	<8 and >11	8 to 11
Scenario 4	Poor, serious	Good, fair	<9 and >11	9 to 11

*No delamination.

Ground Truth—IE-index

Figure 41 demonstrates multiple ROC plots associated with the NDE data collected during the fourth data collection period. Each subplot corresponds to a unique NDE technology, where its results were compared point-by-point against the established ground truth data (herein called IE-index data). First, IE-index was essentially selected over the IE-dominant frequency given that IE-index was assigned by an NDE expert (using the methodology described in figure 2 and table 2) at Rutgers University. The estimated AUC for each subplot is also indicated in the caption of each subplot. To be clear, the IE-index data from the same round of data collection was assumed by the research team to be the ground truth for the other NDE measurements taken during that period. Given the primary objective behind setting the ground truth was to accurately represent the location and extent of areas of delamination, the areas with an assigned "good" rating based on the IE-index measurement were considered sound. The areas with assigned "fair," "poor," and "serious" ratings were considered delaminated.

Figure 42 presents a few more ROC plots associated with the last NDE data collection round performed in October 2021. Except for HCP and IE-dominant frequency, the AUC for the remainder of the NDE techniques increased from less than 0.5 to greater than 0.5. For HCP and IE-dominant frequency, the AUC slightly decreased but still remained greater than 0.5.

To summarize the ROC analysis results, figure 43 plots all the AUCs calculated for different NDE techniques (two subplots: one for PNDE and one for DNDE techniques) collected in multiple data collection periods with establishing IE-index as the ground truth. The vertical and horizontal axes denote the calculated AUC and the period of data collection (1st, 2nd, …, 14th), respectively. To verify the AUC calculations, the team compared the IE-index data against itself in every round of data collection, and all comparisons resulted in an AUC equal to 1.0. The review of results also revealed that IE-dominant frequency and HCP had the highest AUC (always ≥0.5) across all data collection periods. The other techniques have resulted in lower AUC values, but in general, they have shown improvement as the bridge deteriorated further. These techniques probably started picking up delamination after such defects passed a minimum threshold as the bridge deteriorated more and more.

Among the NDE techniques deployed in the accelerated testing, IE probably provided the best indication of delaminated versus sound areas. The testing would have been better if other direct sounding methods, such as hammer sounding or a chain drag, were used to accurately determine the location and extent of areas of delamination. In essence, using sounding as a measure of ground truth would have been more rational, since this method is primarily implemented by bridge owners and, therefore, forms a conventional comparison. Another excellent testing method would be to perform physical sampling by extracting cores and drilling holes into the deck and using a borescope to observe the subsurface cracking that formed the delamination to confirm the sounding results.

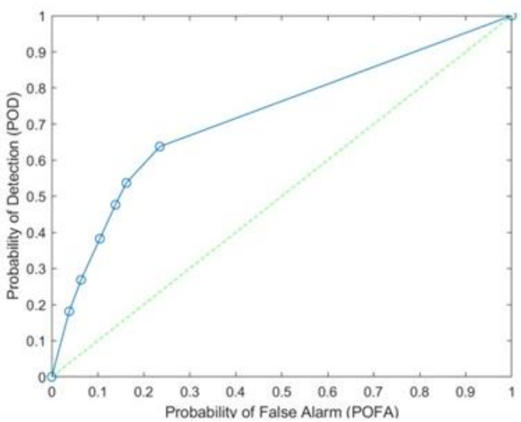

Source: FHWA.

A. IE-dominant frequency (AUC=0.72).

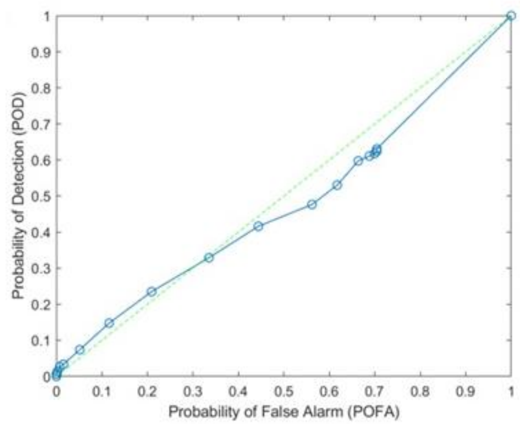

Source: FHWA.

B. USW (AUC=0.48).

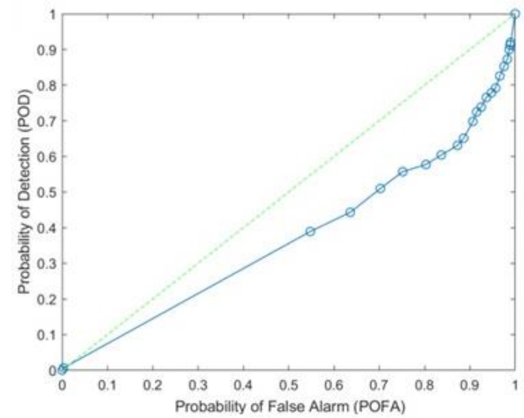

Source: FHWA.

C. Cover depth (AUC=0.37).

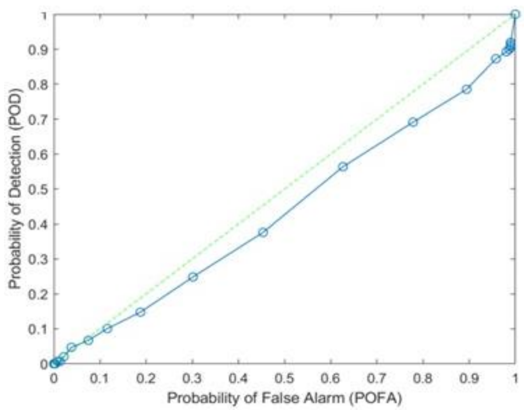

Source: FHWA.

D. GPR-amplitude (AUC=0.44).

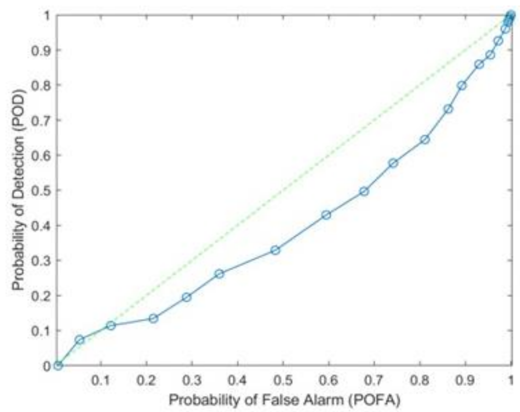

Source: FHWA.

E. ER (AUC=0.40).

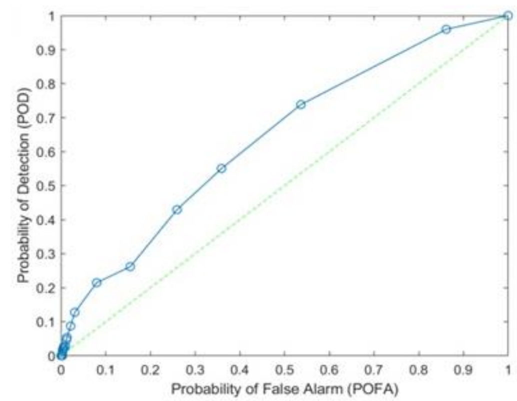

Source: FHWA.

F. HCP (AUC=0.64).

Note: The ground truth dataset was assumed to be defined based on IE-index.

Figure 41. Graphs. ROC curves for different NDE datasets collected during the fourth data collection period (November 2019).

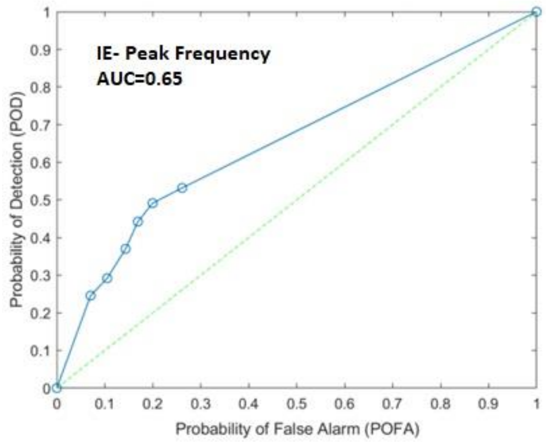

Source: FHWA.

A. IE-dominant frequency (AUC=0.65).

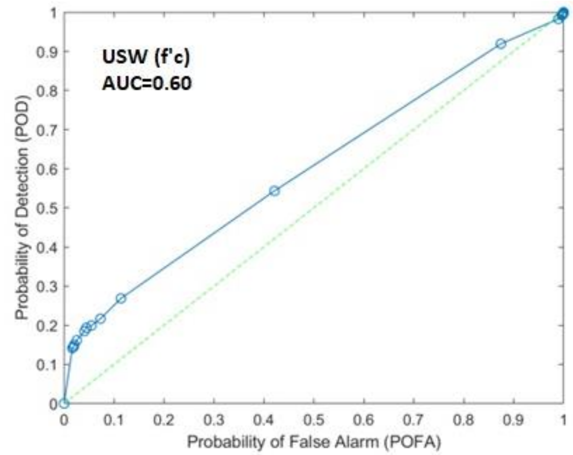

Source: FHWA.

B. USW (AUC=0.60).

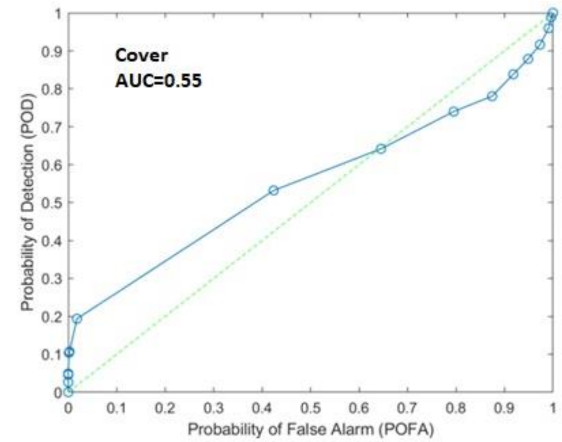

Source: FHWA.

C. Cover depth (AUC=0.55).

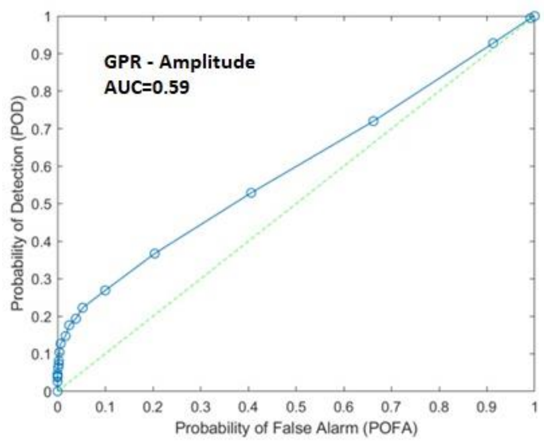

Source: FHWA.

D. GPR-amplitude (AUC=0.59).

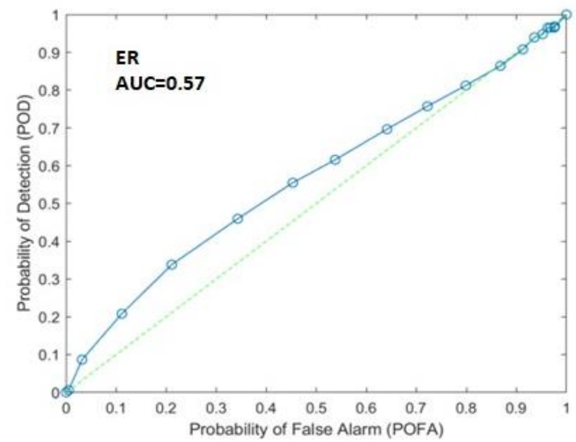

Source: FHWA.

E. ER (AUC=0.57).

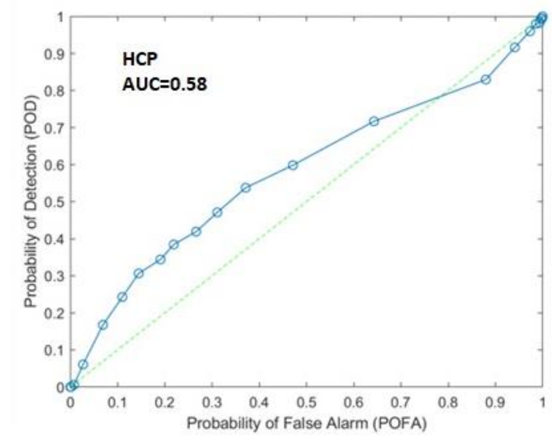

Source: FHWA.

F. HCP (AUC=0.58).

Note: The ground truth dataset was assumed to be defined based on IE-index.

Figure 42. Graphs. ROC curves for different NDE datasets collected during the 14th data collection period (October 2021).

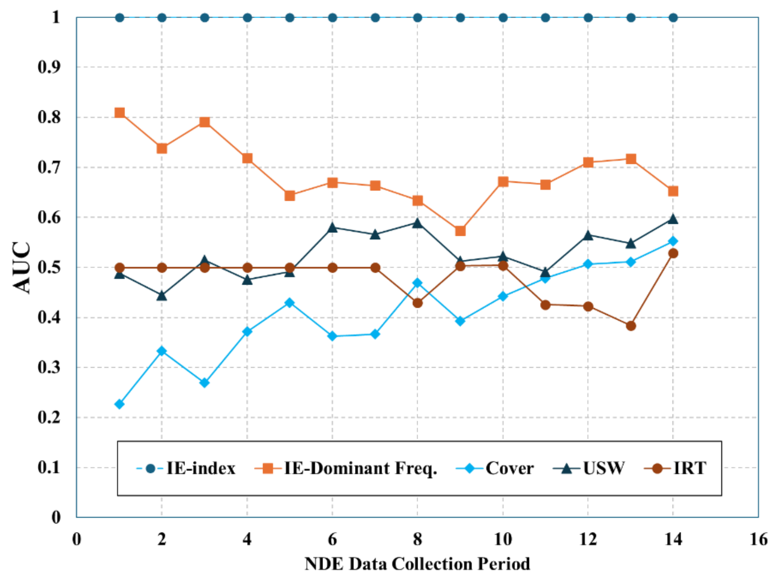

Source: FHWA.
Freq. = frequency.

A. DNDE technique.

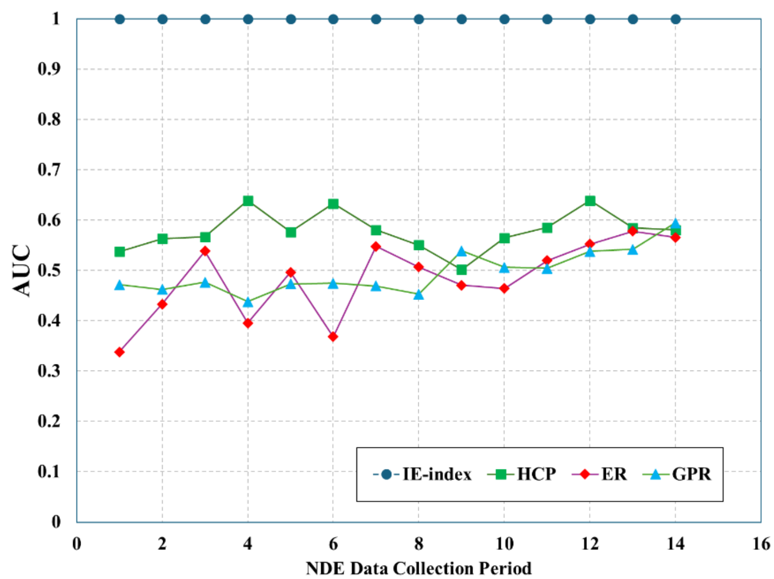

Source: FHWA.

B. PNDE technique.

Note: The x-axis represents the round of data collection, ranging from 1 to 14.

Figure 43. Graphs. ROC analysis using IE-index as the ground truth.

Ground Truth—Reminder of NDE Techniques

Since the establishment of ground truth at the current accelerated testing study was not conducted by independent physical sampling, the researchers performed a full array of analysis, where each NDE technique was once considered as the ground truth and the remainder of the techniques were compared against that technique. For brevity, only the calculated AUCs were plotted for each analysis, which are shown in figure 44 through figure 50.

Figure 44 presents the calculated AUCs for different NDE techniques where IE-dominant frequency was established as the ground truth. In defining the ground truth, if the dominant frequency fell between 9 kHz and 11 kHz, it would be considered sound (depicting the full thickness of deck). Any dominant frequency out of this range was, therefore, considered as delaminated. A slightly different range between 8 kHz and 11 kHz was also considered; however, the AUC results did not significantly change. For brevity, the plot was not provided in this report.

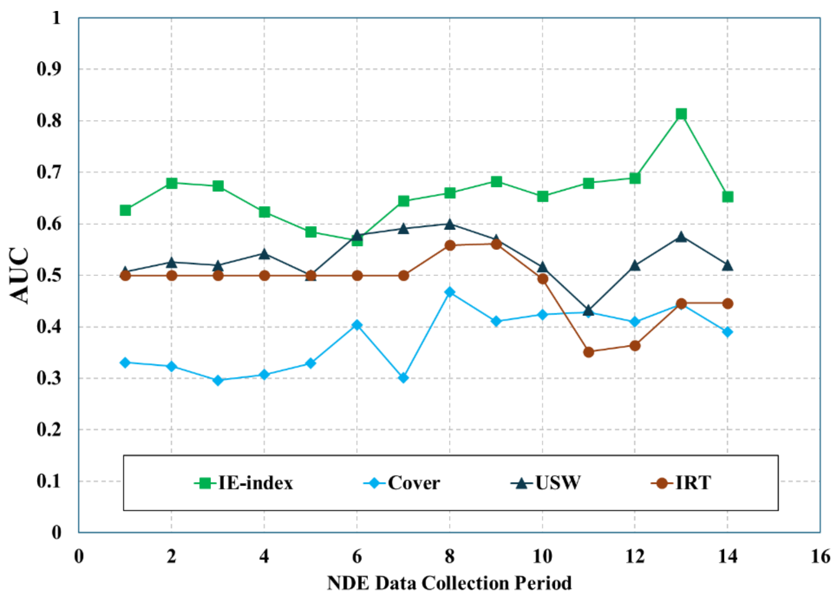

Source: FHWA.

A. DNDE technique.

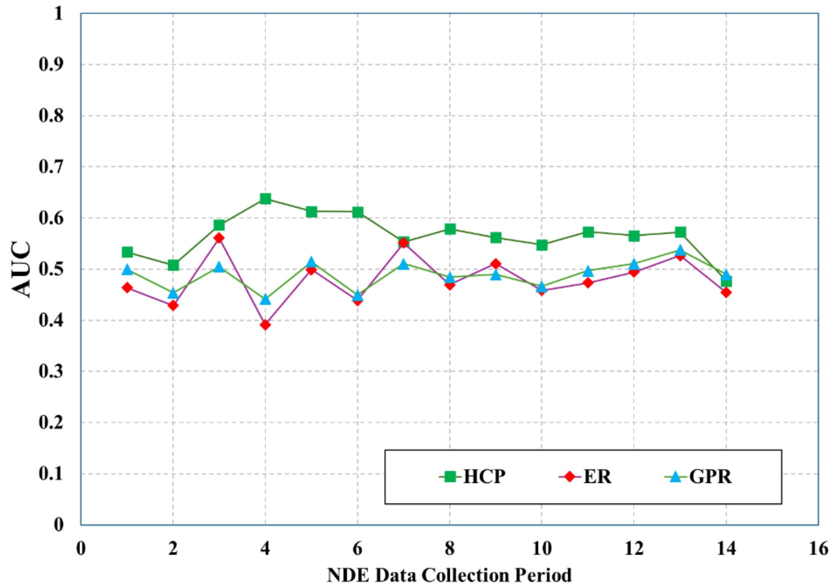

Source: FHWA.

B. PNDE technique.

Note: The *x*-axis represents the round of data collection, ranging from 1 to 14.

Figure 44. Graphs. ROC analysis using IE-dominant frequency as the ground truth.

Similarly, figure 45 presents the calculated AUCs for different NDE techniques where HCP was established as the ground truth. In defining the ground truth, the researchers used the table adapted from ASTM International (2015) C876 standard to establish the relationship between potential HCP values and corrosion probability. According to table 6, if the HCP value was greater than −200 mV, it was considered sound (no corrosion). Any value less than −200 mV was, therefore, considered corroded. Other ranges (such as ≤ −250, or ≤ −300, or ≤ −350 mV) were also considered; however, the AUC results did not significantly change. For brevity, the plots were not provided in this report.

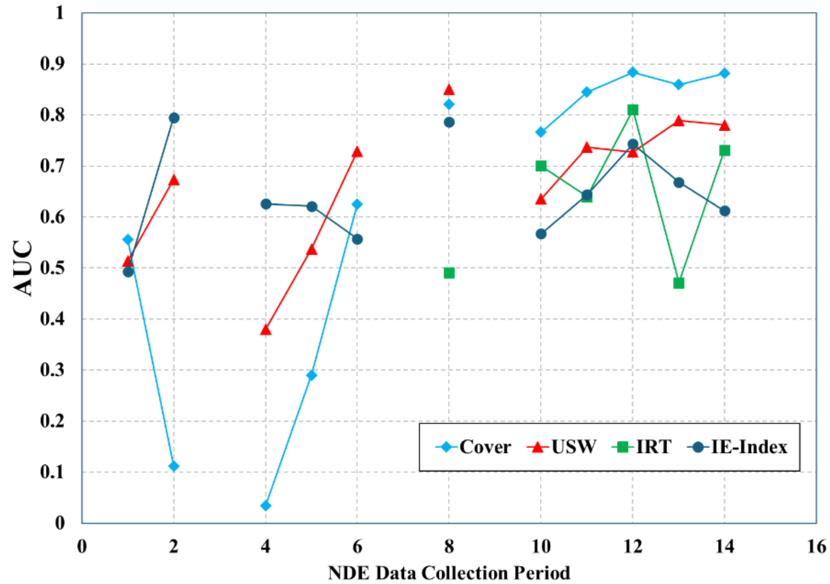

Source: FHWA.

A. DNDE technique.

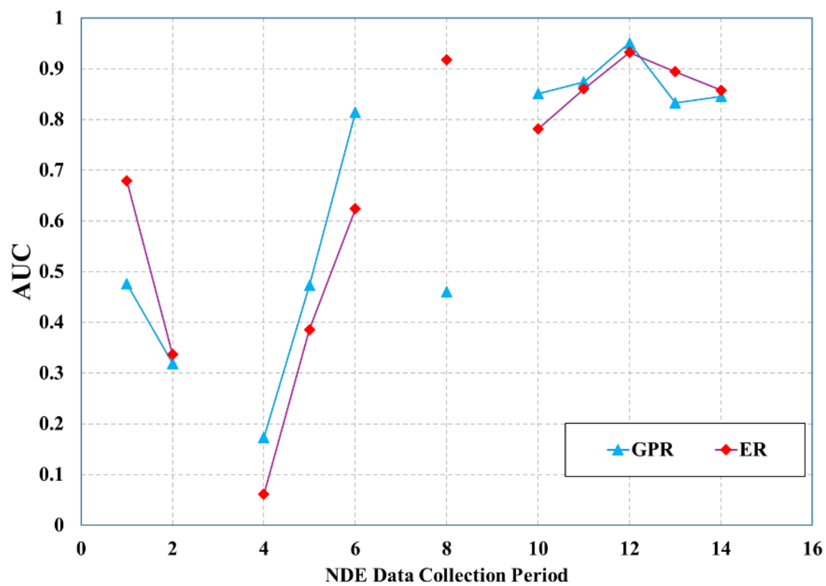

Source: FHWA.

B. PNDE technique.

Note: The *x*-axis represents the round of data collection, ranging from 1 to 14.

Figure 45. Graphs. ROC analysis using HCP as the ground truth.

Table 6. Relationship between the potential values and corrosion probability (ASTM International (2015) C876).

Measured Potential (mV CSE)	Probability of Steel Corrosion Activity (percent)
≥ –200	<10
–200 to –350	Uncertain
≤ –350	>90

CSE = copper-copper sulfate electrode.

Figure 46 presents the calculated AUCs for different NDE techniques where ER was established as the ground truth. In defining the ground truth, table 7, which was adapted from Broomfield (2007) was used to establish the relationship between resistivity values and corrosion rate. According to table 7, if the ER value was more than 10 kΩ·cm, it was considered sound (no corrosion). Any value less than 10 kΩ·cm was, therefore, considered as corroded. For some data collection periods, since the ground truth (herein ER) results were always less or more than the sound/delamination threshold (herein 10 kΩ·cm), no ROC analysis was conducted. Other ranges (such as <20 kΩ·cm, or <30 kΩ·cm) were also considered for the ground truth threshold; however, the AUC results did not significantly change. For brevity, the plots were not provided in this report.

Note that ER only indicates whether the concrete is sufficiently conductive to support active corrosion. ER does not indicate if corrosion is occurring, and it would not be expected to correlate to damage (cracks and delamination).

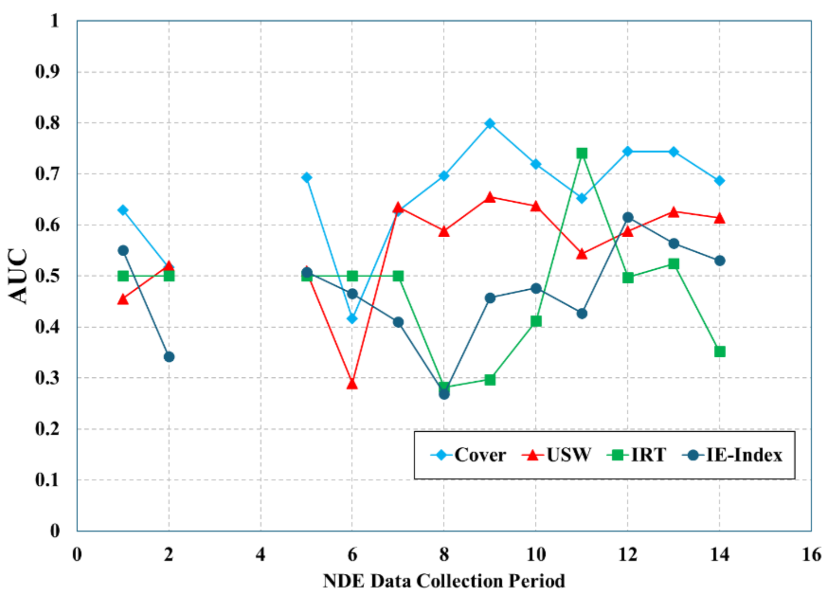

Source: FHWA.

A. DNDE technique.

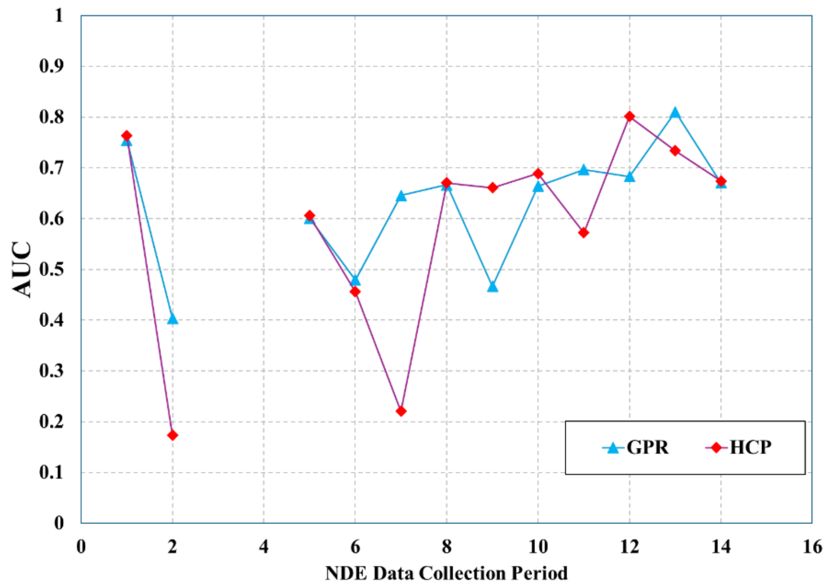

Source: FHWA.

B. PNDE technique.

Note: The *x*-axis represents the round of data collection, ranging from 1 to 14.

Figure 46. Graphs. ROC analysis using ER as the ground truth.

Table 7. Interpretation of resistivity measurements (Broomfield 2007).

Resistivity (kΩ·cm)	Corrosion Rate
>100	Negligible—Cannot distinguish between active and passive steel.
50 to 100	Low—Corrosion rates likely to be low.
10 to 50	Moderate—Moderate to high corrosion rates possible in active areas.
<10	High—Resistivity is not the controlling factor in corrosion rates.

Figure 47 presents the calculated AUCs for different NDE techniques where GPR amplitude was established as the ground truth. If the amplitude was greater than –5 dB, it was considered sound by the research team. Otherwise, it would be assumed to be delaminated. Other ranges (such as < –10 dB or < –15 dB) were also considered; however, the AUC results did not significantly change. For brevity, the plots were not provided in this report.

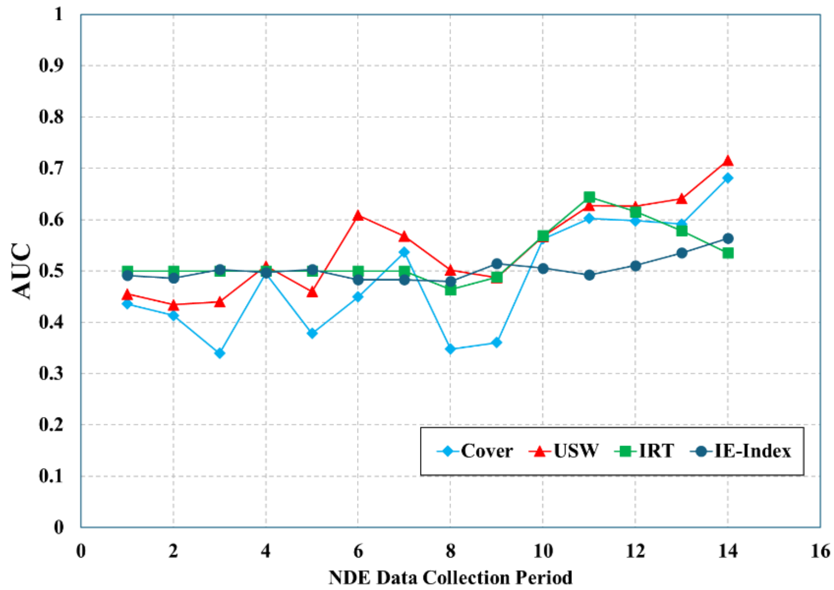

Source: FHWA.

A. DNDE technique.

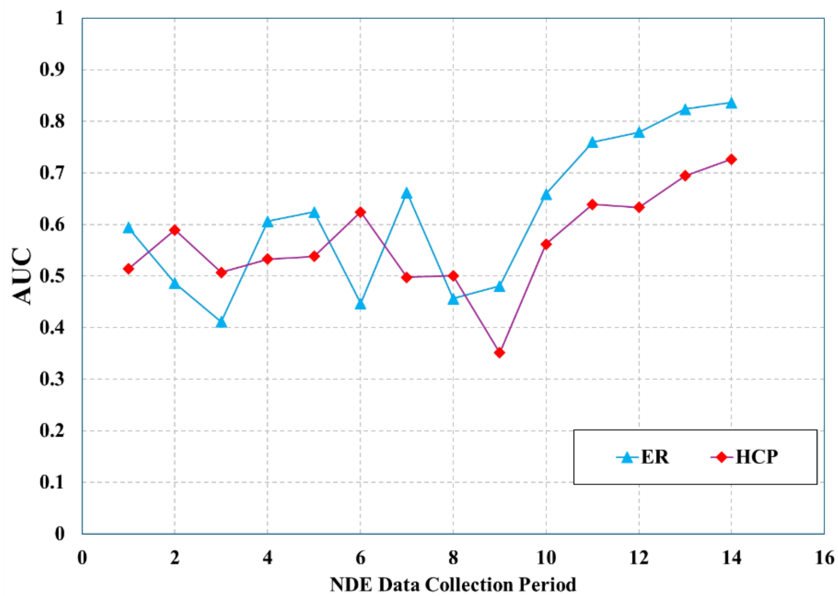

Source: FHWA.

B. PNDE technique.

Note: The *x*-axis represents the round of data collection, ranging from 1 to 14.

Figure 47. Graph. ROC analysis using GPR-amplitude as the ground truth.

Similarly, figure 48 presents the calculated AUCs for different NDE techniques where GPR-cover depth was established as the ground truth. If the cover was more than 1.5 inch, it was assumed to be sound. Otherwise, it would be assumed to be delaminated. Other ranges (such as 1.25 inches, 1.75 inches, and 2 inches) were also considered. For brevity, the plots were not provided in this report.

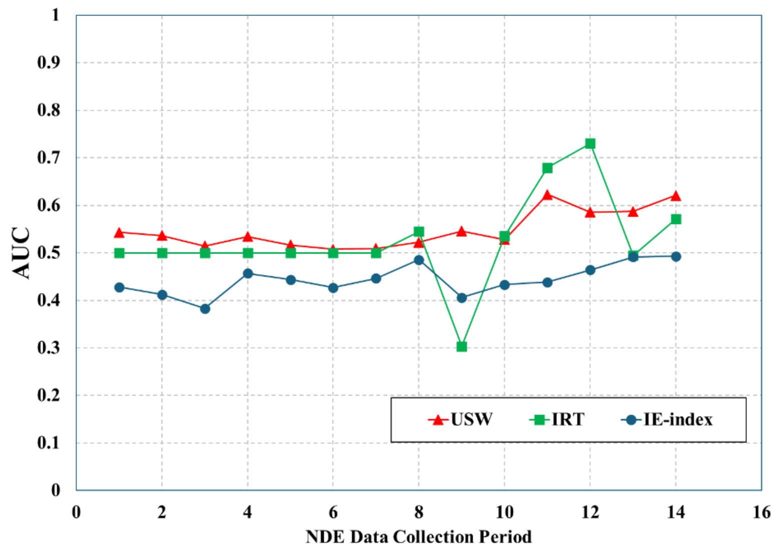

Source: FHWA.

A. DNDE technique.

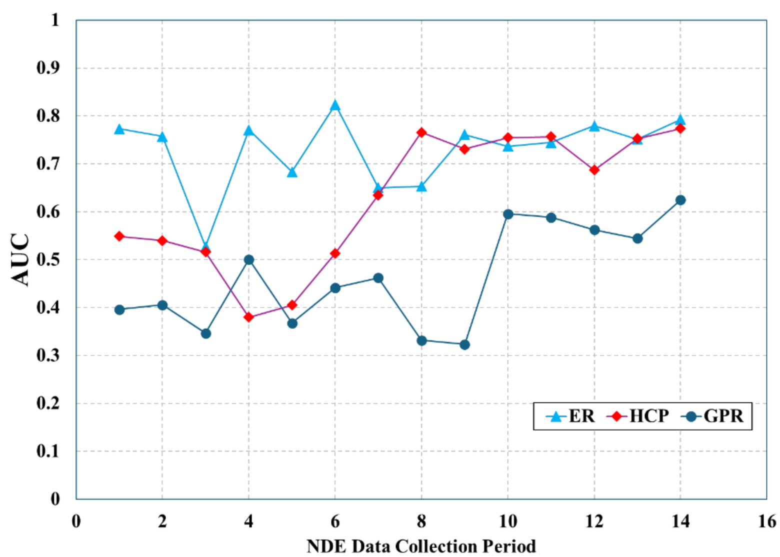

Source: FHWA.

B. PNDE technique.

Note: The *x*-axis represents the round of data collection, ranging from 1 to 14.

Figure 48. Graphs. ROC analysis using cover depth as the ground truth.

Figure 49 shows the calculated AUCs assuming USW (elastic modulus) to serve as the ground truth. If the modulus was more than 3 kilopounds/in^2 (ksi), it was assumed to be sound. Otherwise, it was assumed to be delaminated. For the early data collection periods, since the ground truth results were always more than the sound/delamination threshold (herein 3 ksi), no ROC analysis was conducted. Other ranges (such as 2 ksi and 4 ksi) were also considered; however, the AUC results did not significantly change. For brevity, the plots were not provided in this report.

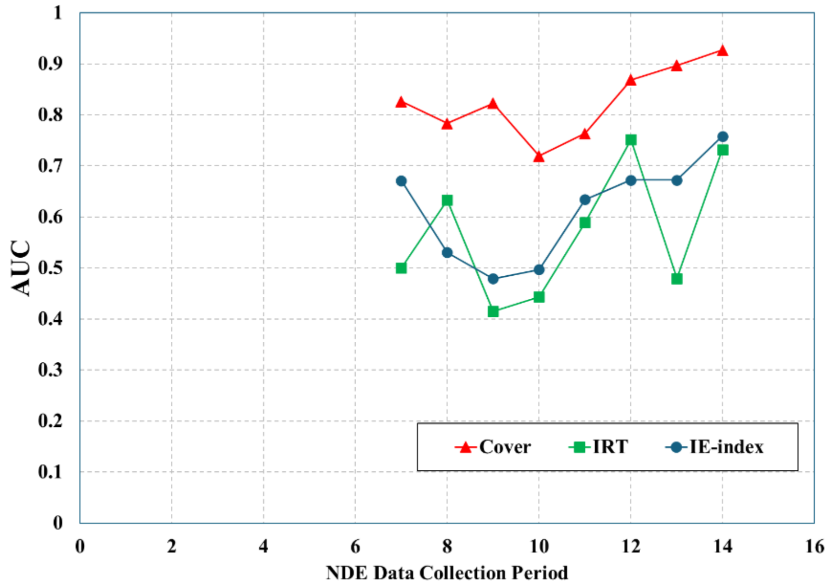

Source: FHWA.

A. DNDE technique.

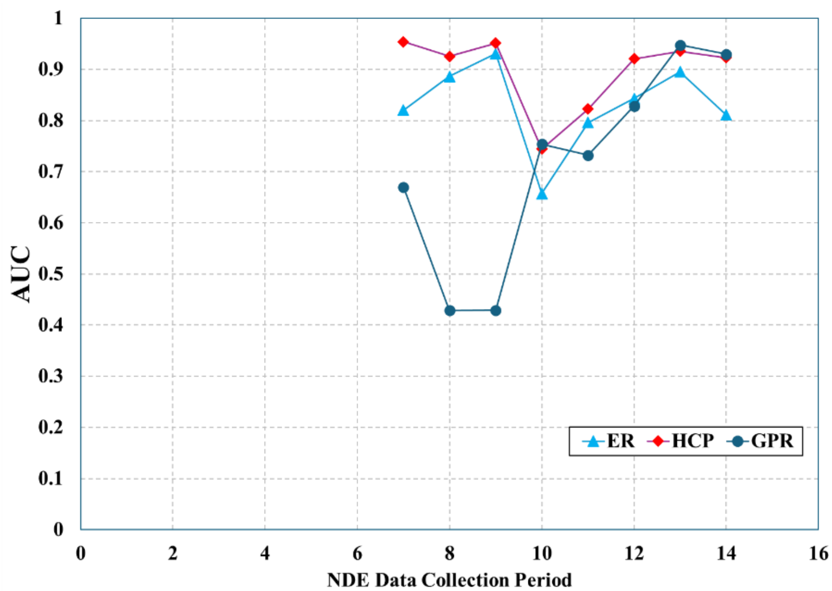

Source: FHWA.

B. PNDE technique.

Note: The *x*-axis represents the round of data collection, ranging from 1 to 14.

Figure 49. Graphs. ROC analysis using USW (elastic modulus) as the ground truth.

At the end, figure 50 shows the calculated AUCs assuming IRT to be the ground truth. If the IRT-measured temperature was more than the average temperature of the deck surface, it was assumed to be sound. Otherwise, it was assumed to be delaminated. For the early data collection periods, no reliable IRT data were collected.

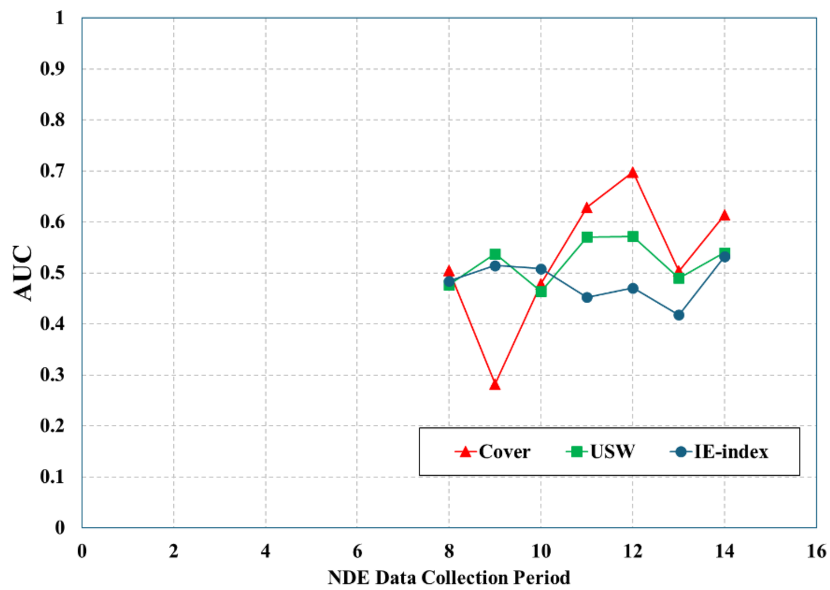

Source: FHWA.

A. DNDE technique.

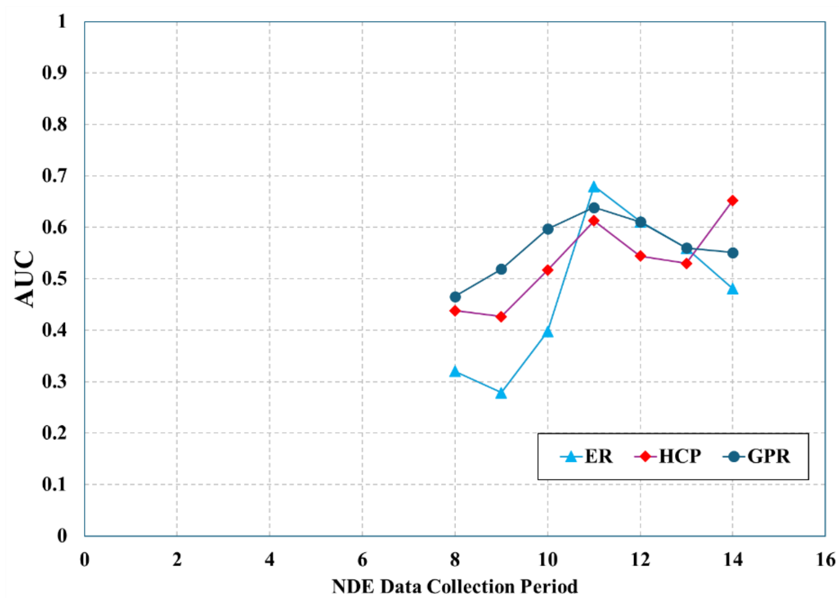

Source: FHWA.

B. PNDE technique.

Note: The *x*-axis represents the round of data collection, ranging from 1 to 14.

Figure 50. Graphs. ROC analysis using IRT as the ground truth.

Summary of ROC Analysis

Table 8 presents the summary of ROC analysis based on the AUC values calculated for different ground truth scenarios. In this table, each row represents a unique scenario where one NDE was established as the ground truth, and the remaining NDE techniques (shown in columns) were compared against this ground truth. If the calculated AUC was greater than 0.5, then the technique was marked as reliable. Otherwise, the technique was marked as not reliable. The corrosion- (PNDE) and damage-based techniques (DNDE) were evaluated separately. For each NDE technique (listed by individual column), the number of its reliable cases versus different ground truth cases were summed and ranked. Consequently, a technique(s) with the highest rank indicated that the technique is the most reliable when assessed against several different ground truths. Among the corrosion-based techniques, all three (HCP, GPR, and ER) were ranked equal. Alternatively, USW (elastic modulus) was ranked highest among the damage-based techniques. In a combined look, HCP and USW were ranked the highest among all NDE techniques deployed in accelerated testing.

Table 8. Summary of ROC analysis results.

	NDE Techniques							
Ground Truth	**ER**	**HCP**	**GPR**	**IE-Index**	**IE-Frequency**	**USW**	**Cover**	**IRT**
Corrosion								
ER	—	✓	✓	×	×	✓	✓	×
HCP	✓	—	✓	✓	✓	✓	✓	✓
GPR	✓	✓	—	✓	×	✓	✓	✓
NDE ranking (corrosion)	1	1	1	N/A				
Damage								
IE-index	×	✓	×	—	✓	✓	×	×
IE-frequency	×	✓	×	✓	—	✓	×	×
USW	✓	✓	✓	✓	✓	-	✓	✓
Cover	✓	✓	×	×	×	✓	—	✓
IRT	×	✓	✓	×	×	✓	✓	—
NDE ranking (damage)	N/A			2	2	1	2	2

—No data.
✓The technique has AUC greater than 50 percent.
×The technique has AUC less than 50 percent.
N/A = not applicable.
Note: Numbers are the rankings.

AUC equal to 0.5 represents a diagnostic system of no ability to differentiate positive and negative test points. Like the probability of coin flip, AUC equal to 0.5 means the system functions as a random system where, for 50 percent of cases, the system would correctly detect the delamination and for the remainder of cases, the system would not detect the delamination. In the area of concrete NDE assessment, no previous study developed an AUC reliability threshold, where a technique could be identified as reliable or not. Sultan and Washer (2018) expected to have AUC values between 0.5 and 1.0, but did not specify whether a 0.6, 0.7, or 0.8 value, or any specific value greater than 0.5, would be the acceptance threshold or not. Limited field testing that compared IRT with GPR showed IRT results with AUC values of 0.8–0.85 and GPR results with AUC of 0.67–0.78.

Results from the analysis of the bridge accelerated testing data, focusing on the final data (14th) collection period, showed that that AUC values in the range of 0.67 or greater (0.86) were found when PNDE technologies were compared with a different PNDE technology used as ground truth. These technologies included ER, GPR, and HCP. Given that the electromagnetic techniques (ER, GPR, and HCP) are affected by the conductivity of the material, the researchers were not surprised that some consistency would occur between results from these technologies and with the areas of low concrete cover. For example, when GPR was assumed as the ground truth, ER and HCP showed AUC values of approximately 0.84 and approximately 0.73, respectively. However, the experimental conditions surrounding the testing resulted in a high moisture level in the concrete, which had a significant effect on results. Consequently, the results may not be representative of actual field testing on bridges. Additionally, none of these technologies measures the damage in the deck that would affect a CR or CS reported during inspection.

Compared with DNDE technologies, focusing on the final data (14th) collection period, the AUC values were low (between 0.53 and 0.60) for the IE technique. Values were significantly higher (0.73 and greater) when USW was assumed as the ground truth. However, the procedure for obtaining USW values requires launching a wave from one location on the surface of the deck to a second location some distance away. The low cover (compared to design value) in the middle portion of the deck and the spalling of the concrete surface in the area are likely to affect the USW results significantly and are not representative of a typical field condition. As a result, determining if these results are meaningful or simply an experimental artifact is not possible.

Among the DNDE technologies, the IRT measurements are also affected by irregular surface conditions. Also, the high moisture level in the deck and surface staining that appears in the HD images affect these results. IRT technologies depend on the surrounding environmental conditions both during and preceding the time images were captured. The nature of the BEAST's facility environment and inability to suspend testing to secure a suitable environment for IRT testing needs to be considered when reviewing results.

The IE results are also affected by the irregular surface conditions in the area of the deck where cover was low, and spalling occurred. Compared with USW, IE launches and receives a wave from a single point on the surface of the deck and, therefore, may be affected less than USW by nearby surface spalling. The best IE data would have been collected on sound deck surfaces where the effects of spalling would be minimized.

The bridge accelerated testing study offered a unique opportunity to explore the complexities of analyzing NDE results under challenging experimental conditions. The presence of areas with low concrete cover provided insights into how NDE results can be influenced by damage. Furthermore, the deck's exposure to higher than usual moisture levels compared to an in-service bridge deck has indicated the impact such conditions have on PNDE technologies. Despite these constraints, the following valuable conclusions have been drawn from the study:

- Among the PNDE technologies, the researchers observed consistency, suggesting that each demonstrated comparable reliability. Among the PNDE technologies, HCP showed an AUC of approximately 0.6 when IE-index was assumed as the ground truth, suggesting some reliability in detecting physical damage. Qualitatively, HCP appeared to show the most consistent results with DNDE technologies, albeit focused on the area of the deck with low cover and surface spalling.

- Among DNDE technologies, the IRT results (taken from the current accelerated testing) are of low quality and likely provide little insight regarding the condition of the deck or the effectiveness of the technology. USW results show some correlation with PNDE technologies, but experimental conditions (i.e., surface spalling) raised questions regarding the reliability of these results. The IE results were also affected by the experimental conditions. However, subjectively, the IE data are most likely to present accurate and durable results because the effect of surface spalling is smaller compared with USW, and previous research has illustrated high reliability of IE and sounding technologies (Sultan and Washer 2028, Sultan 2017).

- Of the PNDE technologies, HCP results showed some degree of reliability compared to IE-index assessments of physical damage. Of the DNDE technologies, the IE-index presented the best representation available of physical damage to the deck. For this reason, the comparison of HCP and IE-index provides the best overall representation of the effectiveness of NDE technologies to use for linking NDE results to bridge deck performance.

CONCLUSIONS AND RECOMMENDATIONS FOR FUTURE WORK

The data from the bridge accelerated testing experimentation have yielded a comprehensive analysis, revealing both challenges and opportunities for enhancement in future research. Key research suggestions are as follows:

- Continue to explore the benefits of accelerated testing for a variety of structural systems such as overlay types and different maintenance activities, among others.

- Develop a testing protocol that considers concrete curing and material evolution issues throughout the accelerated aging process.

- Simulate brine or deicing salt exposure more closely to real-world conditions.

- Consider the influence and interplay of moisture and ion content on test results for HCP, ER, and GPR.

- Develop a testing protocol that considers concrete curing and material evolution issues throughout the accelerated aging process.

CHAPTER 3. INTEGRATION OF NDE DATA WITH CONVENTIONAL CONDITION DATA

INTRODUCTION

To conform with the requirements of the 2012 Moving Ahead for Progress in the 21st Century Act (Office of the Federal Register 2012), State departments of transportation (DOTs) have begun to establish modern data-driven transportation asset management plans, which typically used deterioration models to predict future condition and forecast maintenance, repair, and replacement needs.

Relatively few indicators are available that assess and report the performance of bridge components (i.e., deck, superstructure, and substructure). Two primary data sources for this purpose are the component CR and element-level CS, which are derived from typically biennial bridge inspections according to the NBIS and recorded in the National Bridge Inventory (NBI) (FHWA 2022).

CR assesses the general location, extent, and severity of deterioration and its effect on the strength or performance of a bridge component and is summarized in a single numerical rating per component on a scale from 1 to 9 (FHWA 2022). In contrast, CS focuses primarily on the quantification of types of damage to elements. Both indicators rely on VI and limited manual sounding techniques to assess the current condition of a bridge component or element and, as such, only report damage that has progressed sufficiently to be observable on the surface of the component.

Subsurface damage that develops, typically as a result of corrosion of embedded reinforcing bars in concrete, is not typically part of the assessment, although hammer sounding is used to a limited extent to gain insight on this emerging damage. Because VI is the primary tool used for assigning the appropriate CR and CS, these indicators do not provide comprehensive insights into the actual performance of a bridge component. For example, corrosion-related distress of a concrete bridge deck is only detectable using VI when the damage has already propagated in the bridge deck surface, typically manifesting as cracks and spalling of the cover concrete.

As data-driven asset management systems continue to evolve and integrate more sophisticated deterioration models, the need to incorporate objective and quantitative condition assessment data into these systems is growing. To address this gap, the research team investigated the correlation between NDE data and reported component CR and element-level CS. The team's focus was to explore how this valuable NDE data can be effectively integrated into deterioration models.

LITERATURE REVIEW

Through an extensive examination of State DOT technical manuals, the researchers derived several significant findings regarding the use of NDE for bridge performance evaluation and its potential integration with conventional performance measurements. The conclusions from the examination of these technical manuals are as follows:

- States primarily rely on the NBI component CRs as their main bridge performance measure. The performance is categorized as good (CR: ≥7), fair (CR: 5 or 6), or poor (CR: ≤4) based on discrete ranges of NBI CRs for the primary bridge components or deck, superstructure, and substructure. Some States have also adopted their own performance measures specific to their agencies. While a few years ago, element-level CS data were collected to varying degrees across the country, the data are now being collected by all bridge owners on bridges that are part of the National Highway System (NHS). The required collection of element-level inspection data on NHS bridges started in 2014 and as such is still in its early stages.

- Most State DOTs do not have comprehensive policies, formal procedures, or guidelines for the collection and implementation of NDE data. The existing policies primarily recommend basic NDE assessments during fabrication (e.g., weld quality inspections), field inspection of certain problematic details such as pin and hanger connections, and quantification of deck surface damage. These specifications mainly focus on the specific technology used without addressing data collection standards, data analysis methods, calibration and verification of the NDE tools, or data management at either the project or network level.

- Few systematic approaches are currently implemented for integrating NDE information into routine or indepth bridge inspection procedures. One State (Wisconsin) has initiated statewide IRT inspection for bridge decks, with policies developed regarding different levels of assessment and timing during the service life of bridge decks. Certain other States have implemented GPR systematically during the construction to assess quality through measurement of the reinforcing steel cover depth and deck thickness.

- The team's review of State technical manuals indicates that the applicability of NDE techniques is not directly correlated with NBI deck CRs or element-level CSs. In cases where State DOT guidelines mention the application of NDE, the results are typically linked to intervention actions rather than adjustments to performance indicators for asset management purposes. Essentially, NDE data are often used at the project level to facilitate immediate actions, where some States have defined criteria for specific actions related to bridge maintenance and repair. For example, New Jersey DOT (2016) has set the following thresholds to be a trigger for removal and replacement of deteriorated and chloride-contaminated concrete and application of membrane with asphalt overlay or concrete thin overlay (<1 inch): 5 percent of deck spalling, or up to 40 percent of total deck area with spalls, delamination, HCP less than −350 mV CSE, or up to 40 percent of the deck containing greater than 2.0 lb chloride/yd^3 concrete at the level of the top rebars. In cases involving defects such as delamination, spalling, or corrosion, multiple NDE techniques may be employed to provide more accurate quantification compared to traditional VI and engineering judgment.

- Furthermore, the researchers, during a literature review and other project endeavors, identified two studies that proposed the integration of NDE (whether direct or indirect) with the condition assessment of bridge components. Each study will be briefly introduced in the following subsections, and further details can be found elsewhere (Babanajad et al. 2018; Hearn and Shim 1998).

Service Life Assessment Module Developed Under the LTBP Program

Within the framework of the LTBP sponsored by FHWA, Babanajad et al. (2018) developed a series of data-driven deterioration and service life assessment models. A novel life expectancy modeling framework was developed to estimate the remaining service life of reinforced concrete decks for the U.S. bridge inventory. The methodology was established on the basis of a semiprobabilistic approach to inherently maintain the advantages of both deterministic and probabilistic techniques (adopted from Wenzel, Veit-Egerer, and Widmann 2013). The model was organized in a stepwise structure to incorporate the associated uncertainties.

A basic model was first developed to reflect the general life expectancy without specific information about a bridge, which was defined by the 5th, 50th, and 95th percentiles of the service lives of the entire inventory. The model was then improved through the incorporation of external attributes (i.e., data on environmental conditions and traffic loading) that influence structure life. Ultimately, a more refined model was developed by incorporating performance-specific information obtained through VI and specific NDE methods. The refined model can incorporate other NDE methods, including IE, GPR, and ER.

The proposed model facilitated the incorporation of sophisticated bridge performance information, such as NDE, directly into the estimation of the bridge's life expectancy to effectively reduce uncertainties in predicting the service life. However, the integration of NDE data into the deterioration model, which was established based on NBI CRs as a measure of bridge performance, was formulated using a linear conversion profile, and no validation was conducted using real-world bridge data to verify the accuracy and reliability of this approach. In the new release of LTBP InfoBridge™, this model was substituted with several newer models and is no longer available (FHWA. n.d.a.). The modeling scheme is briefly published in Babanajad et al. (2018).

Assimilation of BMS and NDE Through the Determination of Integrated CSs

Hearn and Shim (1998) proposed and implemented a systematic approach for the direct use of NDE data within management systems. Instead of relying solely on current CRs, such as NBI CR or element-level CS, they introduced a framework that defines a new set of condition stages to integrate NDE data into the management system. These condition stages, illustrated in Figure 51, represent different phases of the service life.

The progression starts from the "protected" stage, indicating elements that have been safeguarded with concrete sealers, paints, coatings, or effective treatments to impede the impact of aggressive agents. If the protective measures fail or are absent, the elements are classified as "exposed." When conditions allow the initiation of deterioration mechanisms, the elements are considered "vulnerable," and as deterioration progresses, they are labeled as "attacked." Finally, when visible distress is evident, the elements are classified as "damaged." This comprehensive categorization allows for a more nuanced assessment of bridge conditions based on the presence or absence of protective measures and the level of deterioration observed (Hearn and Shim 1998).

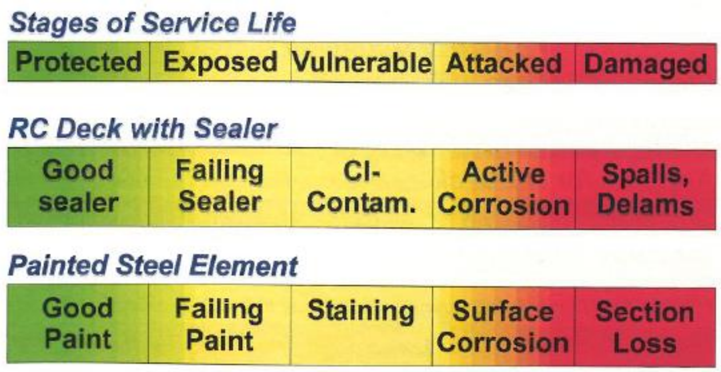

© 1998 American Society of Civil Engineers.
Cl = chloride; Contam = contamination; Delams = delaminations.

Figure 51. Illustration. Stages of service life (Hearn and Shim 1998).

By employing this methodology, quantifying NDE data and incorporating these data as a CS within a BMS becomes feasible, thus facilitating further management and analysis of lifecycle costs (LCCs). Building on the initial work by Nogueira (1998) and Rens, Nogueira, and Transue (2005), the team introduced an extended framework to optimize the integration of NDE data into a BMS. While the proposed methodology establishes a comprehensive framework for incorporating NDE data into the BMS, its practical applicability has not been substantiated through case studies. Successful implementation of this methodology requires a profound understanding of NDE testing, data analytics, and maintenance procedures.

FUNDAMENTAL DIFFERENCES

A bridge's condition can be expressed in various ways, such as using CRs like those found in the NBI, element-level CS, or sufficiency ratings. Currently, CRs play a vital role in State asset management systems, and the researchers anticipate that they will remain the dominant metrics in the foreseeable future. Consequently, NDE data must complement these CRs by modifying them accordingly. The key lies in developing an equivalency factor that allows VI findings to be refined through the application of various NDE methods.

However, the development of NDE performance indicators has faced certain challenges. First, comprehensive and periodic NDE data from a group of bridges are lacking, making the assessment of the potential use and value of these data for condition assessment difficult. Secondly, NDE techniques are sensitive to environmental factors, require expert interpretation, or are proprietary in nature, making their performance difficult to generalize. Third, these techniques provide information specific to the condition of an element rather than the entire structure or component, and their results are not performance based. In other words, unlike CRs, NDE results typically cannot assess the impact of damage on the safety or serviceability of a given component. Finally, conventional condition indicators, such as NBI component CR or element-level CS, rely on VI and evaluate the physical condition of elements at a surface level. Most NDE technologies attempt to assess the condition of elements, including subsurface damage, that is not part of the visual assessment of CR and CS.

Among the conventional condition indicators, NBI CR offers an overall view of a component but does not necessarily correlate meaningfully with the outputs generated by most NDE techniques. In essence, NBI CR is a safety indicator that considers the impact of damage on the safety and serviceability of bridge components based on a visual assessment. Element-level CS, although more granular and quantifiable than NBI component CR, still relies on visual evidence. Each of these approaches focuses on damage such as surface cracks, delamination, or other visible physical defects in various forms. In contrast, NDE techniques aim to characterize local material properties and identify material-level deterioration or subsurface damage in bridge components, enabling the detection of deterioration that would likely be missed through VIs.

Considering the limited number of indicators, such as NBI component CR and element-level CS, adopted for assessing bridge component performance, the researchers will briefly discuss the integration of NDE data into these CRs in the following subsections. However, before that discussion, the team will explore the general correlation between NBI component CR and element-level CS using actual data from bridges across the country.

NBI Component CR and Element-Level CS

As part of an ongoing project with FHWA, the research team has been assigned the task of developing conversion profiles to translate component NBI CR into available element-level CS, and vice versa, for bridges on the NHS, using data available up until 2022. This project, which is nearing completion, involves multiple tasks that employ various modeling techniques and data analytics to generate reliable and accurate results. To aid in the current effort, some of the processed data, as well as modeling efforts available from that project, were used to derive customized conversion profiles based on the bridges that shared structural and material attributes similar to the test specimen.[1] The primary objective of this cursory analysis is to illustrate a real data-driven framework that demonstrates the correlation between NBI component CRs and element-level CS.

To narrow down the bridges with characteristics similar to the BEAST specimen, the 621,000 bridges nationwide were reduced to 36,000 bridges based on specific criteria, including the following:

- RC concrete deck element 12 (*Manual for Bridge Element Inspection* (MBEI)) (AASHTO 2019a).
- Concrete CIP deck structure type (NBI item 107) (FHWA 2022).
- Monolithic concrete or no types of wearing surfaces (NBI item 108A) (FHWA 2022).
- No deck protection (NBI item 108C) (FHWA 2022).
- Bridges built or replaced before 1980 (to follow construction and material types used in the specimen subjected to accelerated testing).

[1]Nejad, S., R. Walther, and J. McGormley. n.d. *Selected Methods and Profiles for Conversion of Bridge Component-Level and Element-Level Condition Data*. Washington, DC: Federal Highway Administration. Report in progress.

In the process of converting element-level CS to general component CRs, the researchers chose a decision tree model that provides reliable and accurate results as one of the finalized models. This model underwent retraining using new data that met the aforementioned criteria. Subsequently, the team tested the model against a set of randomly selected blind data (that was not part of the training data), resulting in the following accuracies:

- Accuracy of 51 percent for predicting the same CR as assigned by the inspector (within ±0 CR).
- Accuracy of 94 percent for predicting a CR within ±1 CR of the inspector-assigned rating.

To clarify, the accuracy percentages indicate that, for example, in 51 percent of the RC deck elements, the predicted deck CR (using the conversion profile) matched the rating assigned by the inspector. The accuracy increased to 94 percent when the predicted deck CR fell within ±1 CR of the inspector's rating. For instance, if a bridge deck was rated at 6, a predicted rating ranging from 5 to 7 would be considered accurate. Figure 52 provides a snapshot of a decision tree model. The full decision tree that was developed based on the element data that closely aligns with the geomaterial attributes of the specimen subjected to accelerated testing is provided in appendix B.

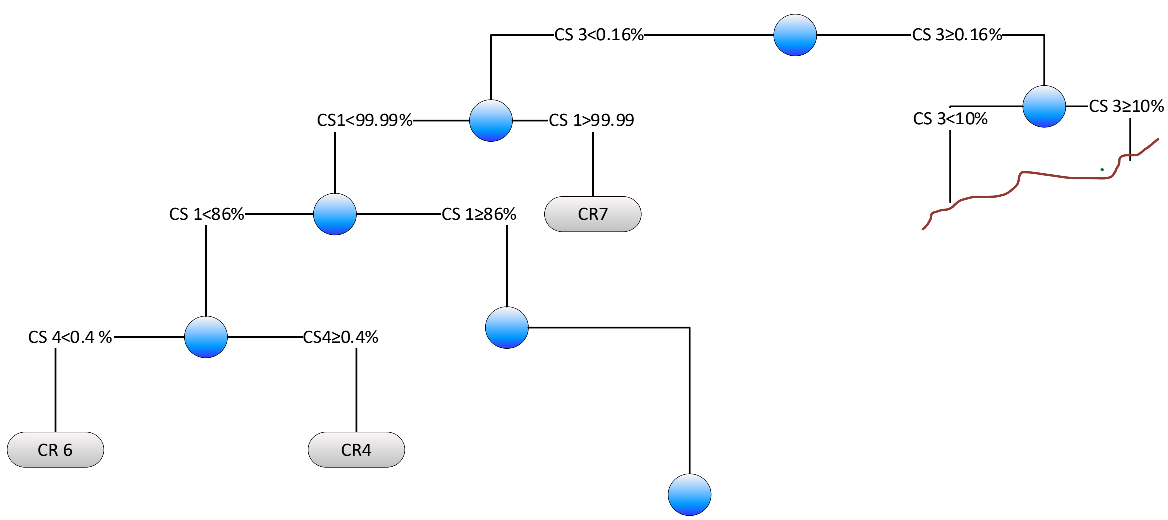

Source: FHWA.

Figure 52. Schematic. Typical decision tree model developed for RC deck.

Alternatively, when converting component general CRs back to element-level CS, the team developed a separate conversion profile specifically for RC deck elements. This profile establishes the average values of CS corresponding to a given component CR. Table 9 presents the conversion table that has been established, linking component CRs to element-level CS.

Table 9. NBI component CR (deck item 58) to element CS (element 12) (MBEI) conversion profile (FHWA 2022; AASHTO 2019a).

Component CR	Element Level CS (percent)			
	CS1	**CS2**	**CS3**	**CS4**
9	98.8	1.2	0.0	0.0
8	93.3	6.5	0.2	0.0
7	74.5	23.4	2.1	0.0
6	52.0	41.5	6.5	0.0
5	38.3	45.5	16.0	0.1
4	29.4	39.9	29.7	1.0
3	27.3	27.3	39.1	6.3

Both profiles show that the correlation between NBI CRs and element-level CS is evidently not significant. In fact, this level of accuracy was achieved when considering single-element components (specifically RC deck elements) in the calculation. However, incorporating multielement components may complicate the situation.

The following section will delve into the role of NDE in defining bridge performance, while subsequent sections (i.e., Proof of Concept—Bridge Accelerated Testing) will explore the potential integration of NDE with other condition information.

ROLE OF NDE IN DEFINING BRIDGE PERFORMANCE

The applicability of NDE techniques in assessing the deck condition is conceptually illustrated in figure 53, which depicts a typical sequence of corrosion-induced delamination and spalling. The damage mechanism of corrosion progresses to delamination and eventually spalling in a complex and gradual manner over time.

Certain NDE technologies are effective for assessing the deterioration mechanism of corrosion, while other NDE technologies are effective for detecting and assessing the resulting damage modes of delamination and spalling. As shown in figure 53, technologies such as GPR, HCP, and ER are most effective in detecting the deterioration mechanism of corrosion, which precedes delamination and spalling. NDE technologies such as IE, USW, and IRT are effective later in the deterioration process, when corrosion processes manifest in physical damage of delamination and spalling. Consequently, these different types of NDE technologies should be understood to have different objectives, and their effectiveness needs to be analyzed differently.

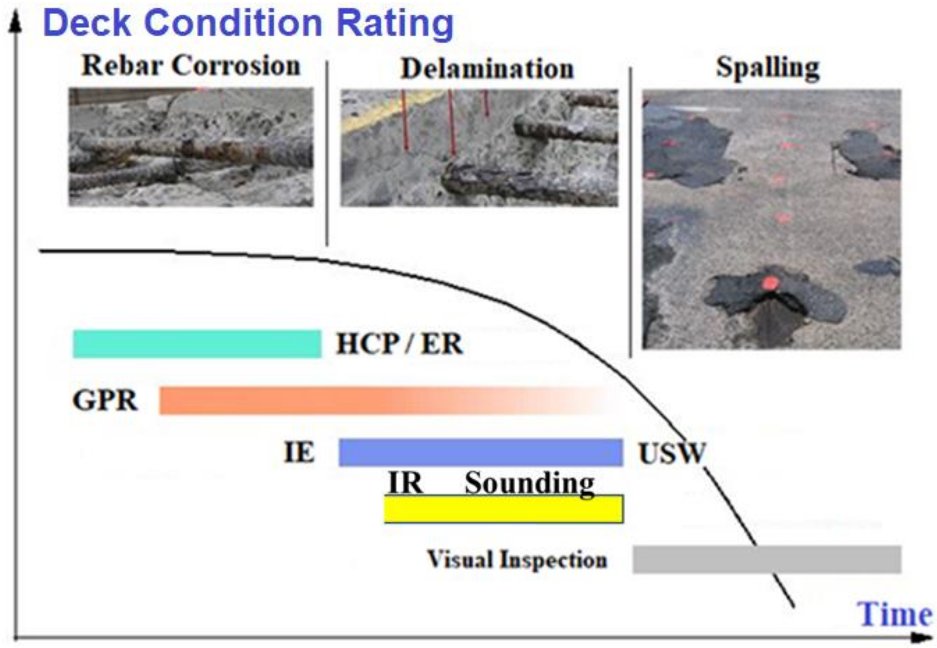

© 2011 Iowa Department of Transportation. Modified by FHWA (see Acknowledgments section).
IR = infrared.

Figure 53. Illustration. Corrosion-induced bridge deck deterioration versus NDE technologies (Gucunski et al. 2011).

PNDE techniques focus on the assessment of the deterioration mechanism of corrosion. The objective of PNDE technologies is to assess the electrochemical properties of the material, such as chloride concentration, ionic diffusivity, and moisture content of the concrete, each of which affects the electromagnetic properties of the material (e.g., resistivity, permittivity). These properties are proactive indicators of the corrosive environment that drives the deterioration mechanism and, therefore, can act as predictors of future damage evolving from corrosion.

Corrosion damage of the steel reinforcing bar causes an internal expansion, since the various forms of iron oxides formed by the electrochemical corrosion process are larger in volume than the ferritic steel from which they are formed. This reaction leads to the formation of cracking planes or delamination within the deck due to the expansive forces generated by corrosion byproducts (i.e., iron oxides). During this stage, DNDE techniques like sounding, IE, IR, and USW can quantify the level of physical damage to the element, surpassing the capabilities of conventional VI techniques. As cracking and corrosion progress, delamination extends to the concrete surface, resulting in spalling and visible physical damage to the element.

While VI (which determines NBI component CRs and element-level CS) and NDE techniques both assess the condition of the structural element, these two assessment strategies appear complementary in nature. CRs primarily describe the surface condition of elements, whereas NDE assessment primarily evaluates the subsurface condition or the potential for subsurface deterioration, as mentioned in the preceding paragraphs. As a result, the level of correlation between NDE assessment and VI can vary, depending on the element and the nature of the specific NDE technique employed. For example, PNDE technologies by their nature are intended to assess the corrosive environment in the RC, which obviously cannot be assessed through VI or by sounding. Consequently, PNDE technologies show poor correlation with VI or sounding.

DNDE technologies detect subsurface damage and, as such, also will not correlate well with VI but should correlate to some extent with sounding. However, because the transition from delamination to spalling is to some degree a stochastic process and occurs progressively over time, some broad correlation between DNDE technologies and VI can be expected. This assertion is because, over time, some portion of previously subsurface damage will have manifested in spalling that can be detected by VI. DNDE technologies will detect the areas of subsurface damage that have not yet progressed to spalling. In this way, the DNDE technologies complement VI and improve the quality of the condition assessment by revealing those areas of physical damage that VI cannot detect.

As previously discussed in the Fundamental Differences section, element-level CS provides more quantifiable measures compared to NBI component CRs. Figure 54 schematically illustrates how bridge inspectors typically assign CS compared with the actual performance of a bridge deck. For the primary deterioration mechanism of corrosion, damage associated with CS2 is either subsurface (delamination), or small spalls less than 1 inch in depth or 6 inches in diameter. Typically, corrosion-induced spalling is greater than 1 inch in depth and greater than 6 inches in diameter, and, as such, CS2 is unlikely to be present in most cases. As a result, when the element is in good condition, CS1 is assigned, whereas CS3 is assigned when visible damage is present. In essence, both CS1 and CS3 can have wide interpretations, resulting in a lack of accuracy and resolution.

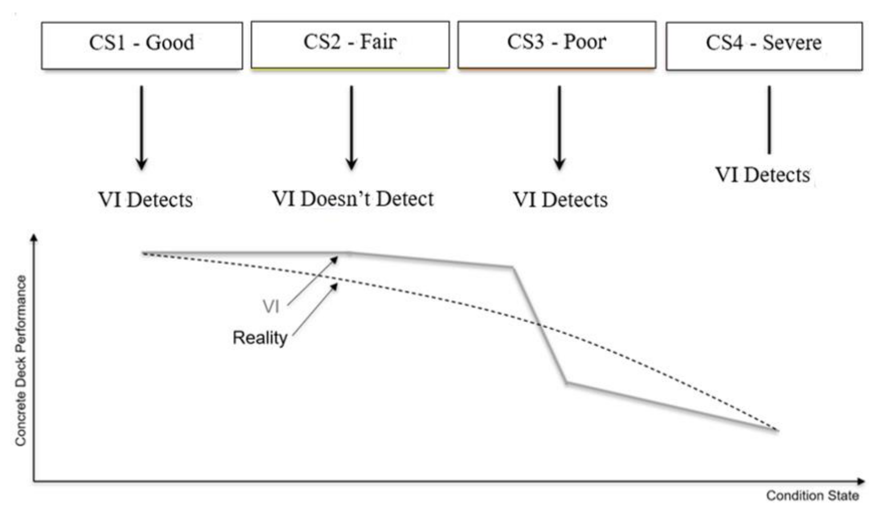

Source: FHWA.

Figure 54. Graph. Conceptual correlation of VI and element-level CS.

After reviewing the sample defects shown in table 10, taken from the MBEI visual guide, evidence shows that determining certain defect types around CS2 can be challenging (AASHTO 2019a). When correlating with NBI component CRs, as depicted in figure 54, this phenomenon leads to a significant drop in CR, as only lower CRs (e.g., ≤5) allow for such large defects (comparable to CS3), while middle and higher CRs (e.g., ≥6) tend to avoid significant visual damages (resulting in the assignment of CS1 or CS2).

Table 10. Samples from MBEI visual guide for different defect types of RC deck (AASHTO 2019a).

CS1–Good	CS2–Fair	CS3–Poor	CS4–Severe
Defect 1080–delamination or spall or patched areas			—
Defect 1090–exposed rebar		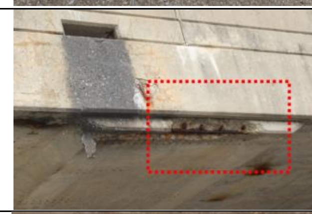	—
Defect 1120–Efflorescence or rust staining	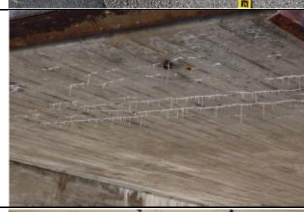		—
Defect 1190–abrasion or wear			—
Defect 1130–cracking (width)		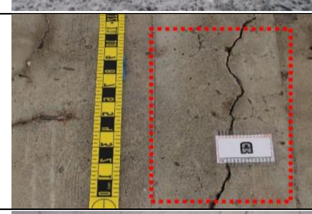	—
Defect 1130–cracking (pattern)	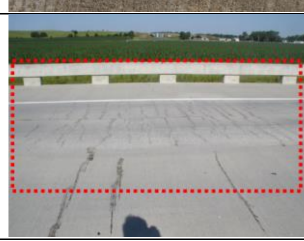		—

—No data.

Furthermore, figure 55 illustrates the conceptual correlation between NDE and element-level CS. Based on the team's extensive experience from multiple bridge assessment projects where both NDE and VIs were conducted simultaneously, and in conjunction with the CS definitions provided by MBEI for RC decks, the following observations have been made (AASHTO 2019a):

- Techniques like GPR are used (by some State DOTs) to check concrete quality, precise reinforcement placement, and accurate thickness measurement during the initial stages of constructing an RC deck. The overall condition of the deck has a direct impact on the time-in-state of its elements across different CSs, making the employment of GPR and other methods desirable to ensure optimal construction practices and enhance the deck's long-term performance.

- Inspectors primarily detect CS1 or CS3 and CS4 and often overlook CS2 due to the challenge of visually detecting subsurface defects.

- The application of NDE for CS1, in most cases, does not seem beneficial according to the definition provided by MBEI (AASHTO 2019a). CS1 allows for minor visual defects on the RC deck that are detectable with the naked eye. No internal defects are permitted for CS1. On the contrary, a visual observation that would classify a structure as CS1 might overlook underlying (nonvisible) damage, whereas detection through NDE could reveal issues that would lower the rating.

- NDE techniques would be advantageous in accurately quantifying CS2, where the defects are located at the subsurface level, which is particularly true when considering the use of ER and HCP to determine corrosion activity before damage has manifested. On reviewing the defect types for RC decks, such damages typically manifest as internal delamination.

- The application of NDE would not be beneficial for identifying CS3 and CS4, as the damage is predominantly at the surface level (e.g., spalled deck with exposed rebar and some degree of section loss), which can be visually detectable and quantifiable by the naked eye. Any internal defects resulting from corrosion have already reached the surface.

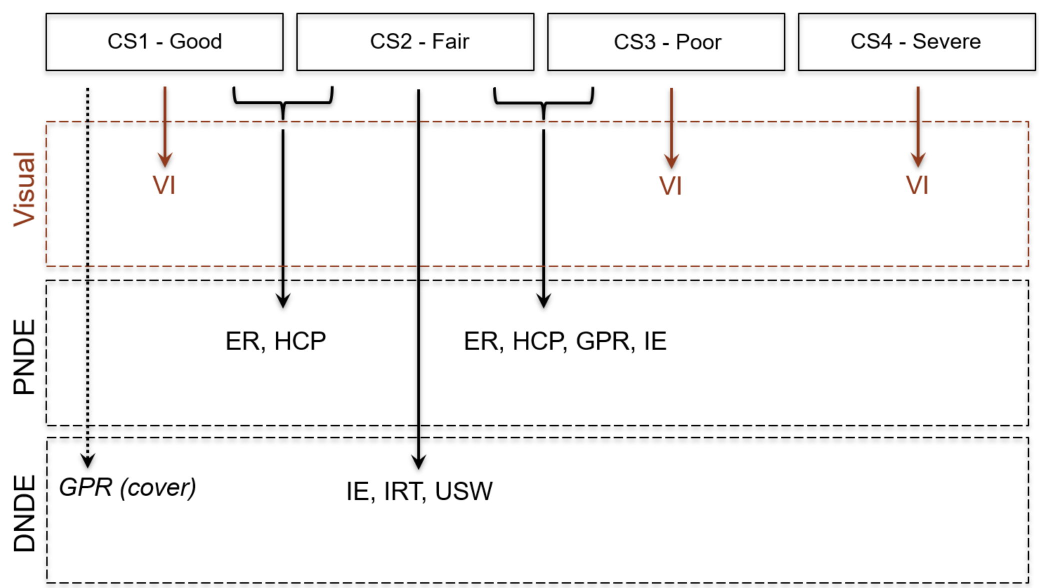

Source: FHWA.

Figure 55. Graph. Proposed integration of NDE techniques and element-level CS.

After conducting a comprehensive analysis of RC decks, the researchers determined that NDE techniques can be most effectively employed during the transition from CS1 to CS2, as illustrated in figure 55. The current definitions by the MBEI assume an absence of internal defects and near-perfect surface conditions when assigning CS1 to RC decks (AASHTO 2019a).

However, the evolution of microcracking from service demands, combined with the pore structure of the concrete, provides pathways for corrosive agents (water, chlorides, and oxygen) to infiltrate the deck and reach the reinforcing rebar. This process results in a corrosive environment in the concrete that initiates a chemical reaction at the rebar level, leading to corrosion and expansion of the steel within the concrete. During this critical phase of corrosion initiation and progression, PNDE technologies such as ER, GPR, or HCP can play a pivotal role in accurately assessing the corrosion potential and forecasting the onset of physical subsurface damage (i.e., CS2). The transitional period from CS1 to CS2, as indicated in figure 55, necessitates the utilization of PNDE technologies to forecast the onset of corrosion damage (CS2). At this stage in the progression, CS2 can be quantified using DNDE technologies, as shown schematically in figure 55.

During the transition from CS2 to CS3, the progression of deterioration from subsurface layers of concrete to the surface is influenced by a combination of various factors, such as traffic loading, freeze–thaw cycles, material quality, etc. Once the subsurface damage extends to the surface, the concrete cover is separated, and spalls become visible. At this stage the portions of the affected deck are rated as CS3 due to visible damage. As depicted in figure 55, the level of corrosion activity plays a pivotal role in determining the transition from CS2 to CS3, and, therefore, PNDE technologies can contribute to forecasting this transition. Using PNDE techniques at this stage allows for estimating the remaining service life of the deck in the future damage-based CS3 and CS4.

A more corrosive environment, indicated by more negative HCP values and relatively lower ER values, will undoubtedly result in a higher percentage of spalling and a reduced remaining service life. Therefore, techniques such as the NDE factor for asset management deterioration modeling (proposed by the authors in a separate ongoing project sponsored by FHWA[2]) could be implemented at this stage to enhance the service life models using the data provided by PNDE.

Certain DNDE technologies can provide some insights regarding the onset of spalling. For example, IE typically responds differently (typically showing a lower resonant frequency) as subsurface damage develops toward the spalling stage, providing some indication that an area of delamination that is currently CS2 has progressed significantly toward CS3.

PROOF OF CONCEPT—BRIDGE ACCELERATED TESTING

During phase I of the bridge accelerated testing experiment, 14 sets of NDE data were collected. Table 3 in chapter 2 presents the cumulative live-load cycles and cumulative freeze–thaw cycles for each date that data were collected. The table also shows when VI surveys were conducted and the CR assigned, when core samples were removed from the model deck for analysis, when

---

2Green, T. Nejad, S., R. Walther, G. Washer, M. Averso, P.D. Thompson, n.d. *Current Practices and Policies of State Highway Agency Bridge and Tunnel Units on the Use of Deployment-Ready NDE Technologies in Complementing Bridge and Tunnel Safety Inspections*. Washington, DC: Federal Highway Administration. Report in progress.

different types of NDE data were collected (IE, USW, ER, GPR, HCP, and IRT), and when HD images were captured.

Due to the shortage of visual condition assessments (two surveys) conducted during the testing, four certified bridge inspectors independently reviewed HD images of the deck captured at different times to assign NBI CR and element-level CS. The results from this independent assignment, along with the condition information provided by Rutgers (conducted twice by an on-site bridge inspector), are presented in figure 56 and figure 57 for further comparison. The plots indicate significant variability in the assignment of CS, whereas less variability is observed in the assignment of CR. This variation aligns with the inspection results conducted by Washer et al. (2014).

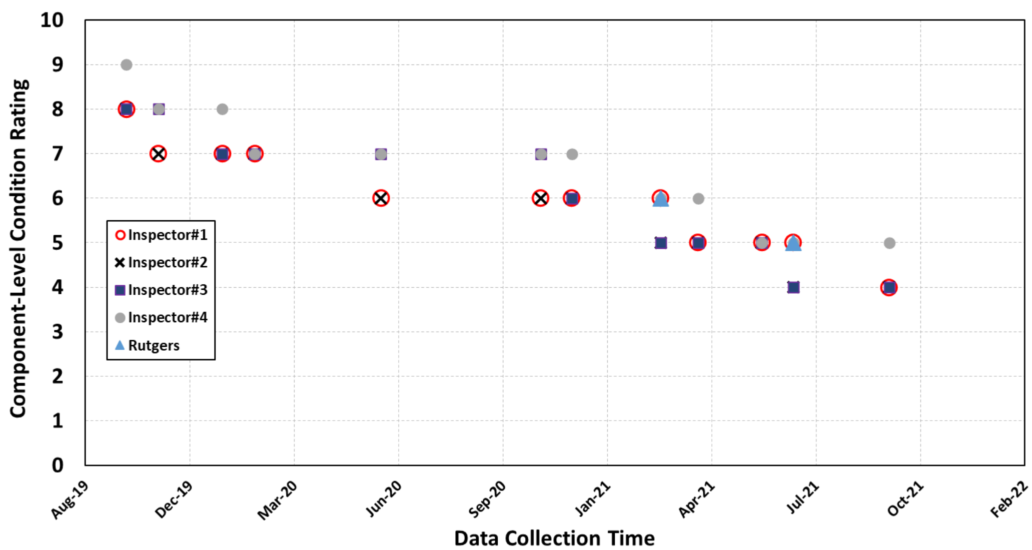

Source: FHWA.

Figure 56. Graph. Assignment of NBI component CR for the deck by multiple certified inspectors.

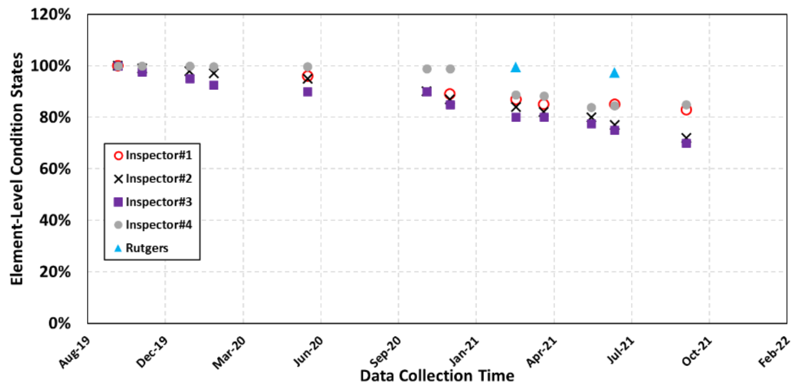

Source: FHWA.

A. Element CS1.

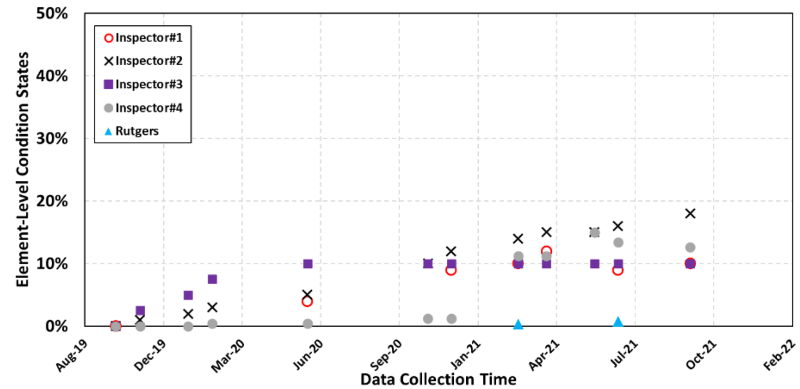

Source: FHWA.

B. Element CS2.

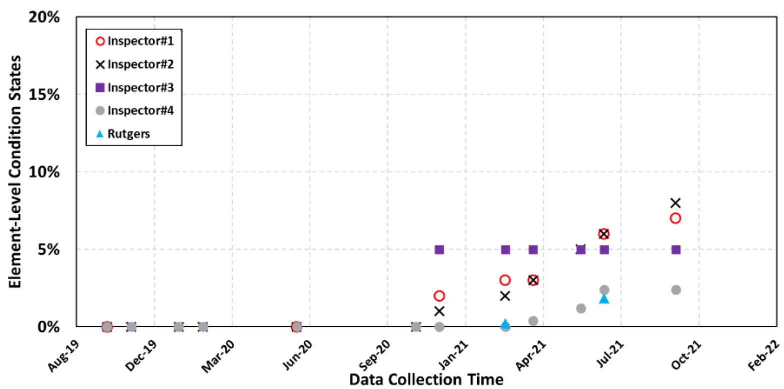

Source: FHWA.

C. Element CS3.

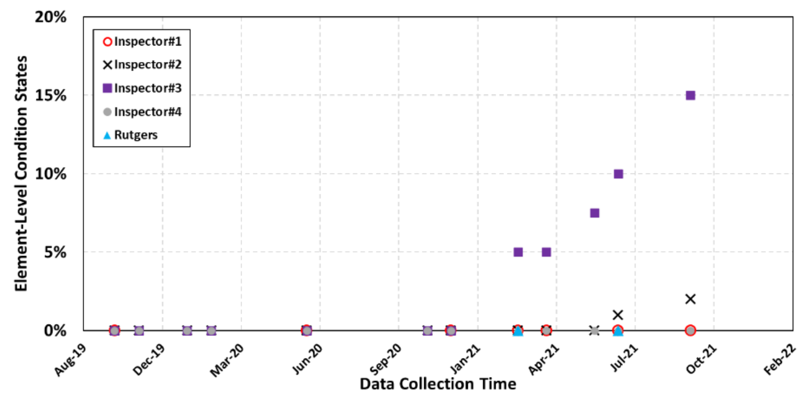

Source: FHWA.

D. Element CS4.

Figure 57. Graphs. Assignment of element-level CS for the deck by multiple certified inspectors.

Initial NDE Analysis

This subsection of the report discusses the preliminary assessment of the NDE results provided to the research team. To further explore the fabrication issue that arose during construction of the deck, which is described in chapter 2, figure 58 presents a contour plot of cover depth measured by GPR. Similar to the concave shape in the transverse direction imparted by the paving machine, a concave shape is also observable in the longitudinal direction.

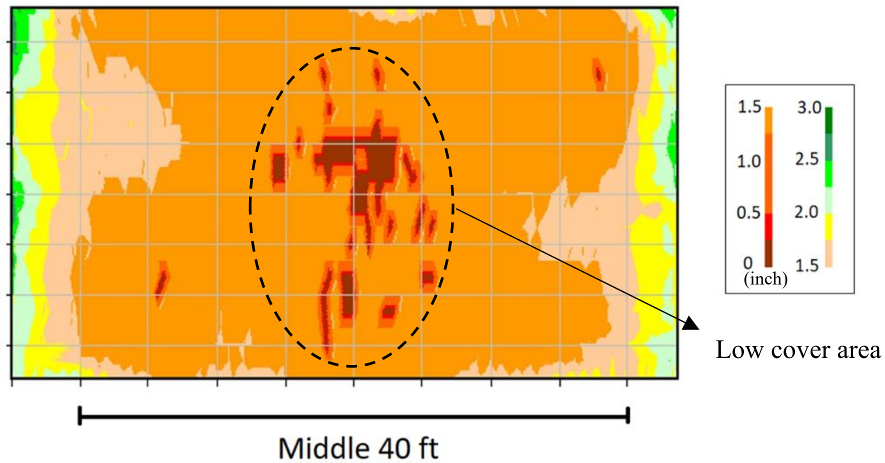

Source: FHWA.

Figure 58. Heat map. Cover depth contour plot for the deck specimen.

This variable cover depth posed significant challenges in analyzing the NDE results, as much of the damage occurred in areas with low concrete cover. Additionally, the deck was subject to unusually high moisture levels compared to an in-service bridge deck, which significantly impacted the results obtained using PNDE technologies. To mitigate some of the low cover issues, the deck was segmented into two primary sections to improve cover uniformity. As shown in figure 58, the deck was divided into an interior section with low cover (40 ft in the middle) and exterior sections with normal cover (5 ft on each side). This segmentation resulted in changes to the average and standard deviation of the cover depth from 1.47 inches and 0.26 inch overall, to 1.34 inches and 0.08 inch in the interior low-cover section, and to 1.76 inches and 0.25 inch in the exterior normal cover sections, respectively.

In chapter 2, the ROC reliability analysis revealed that HCP demonstrated the most consistent results among the applied PNDE techniques compared to the results from DNDE technologies, particularly in areas of the deck with low cover and surface spalling. On the other hand, IE results were influenced by the experimental conditions, but subjectively the IE data were deemed more likely to provide accurate and reliable results due to their smaller effects from surface spalling compared to USW.

Previous research efforts have also demonstrated the high reliability of IE technologies (Sultan 2017; Sultan and Washer 2018). Notably, the IE-index was the only ground truth technology that produced an AUC greater than 0.5 (using ROC analysis) compared to all other NDE technologies used. A minimum AUC of 0.5 indicates that the model has no discrimination capacity to distinguish between positive and negative class instances. Essentially, this value suggests that the model's predictions are no better than random guessing. Therefore, the researchers assumed that the IE-index offers the most reliable representation of physical damage in the deck based on the data from accelerated testing (compared with other technologies). Consequently, the comparison between HCP and IE-index provides the most comprehensive assessment of the effectiveness of NDE technologies for linking NDE results to bridge deck performance.

Qualitative Assessment of NDE Data

The implementation of multiround data collection enables the monitoring of bridge deck conditions over time, allowing for the evaluation of both corrosion and damage progression phases. However, proper analysis of time-lapsed data necessitates the repeatability and consistency of periodic NDE measurements. One primary challenge lies in the environmental variations that can significantly impact NDE measurements, particularly for electrical and electromagnetic-based technologies such as ER, HCP, and GPR. These technologies are sensitive to environmental factors, such as humidity resulting from rainfall or snowfall, as well as the presence of residual roadway salt. In contrast, stress-wave-based NDE techniques like IE or USW exhibit less environmental sensitivity, as their measurements primarily depend on mechanical properties of the concrete material.

In theory, PNDE technologies are intended to assist in characterizing the corrosivity of the bridge deck environment, providing insights into chloride concentration, diffusivity, and moisture levels. Once the corrosive environment reaches a certain level, DNDE technologies can detect resulting damage and provide a more accurate characterization of the current bridge condition compared to conventional VI techniques. To assess the applicability of this theory in the accelerated testing experiment, the team chronologically plotted 10 latest sets of contour data from phase I, as shown in figure 59 for IE (condition level: good, fair, poor, and serious) and HCP tests, using a consistent contour scale for each NDE technology.

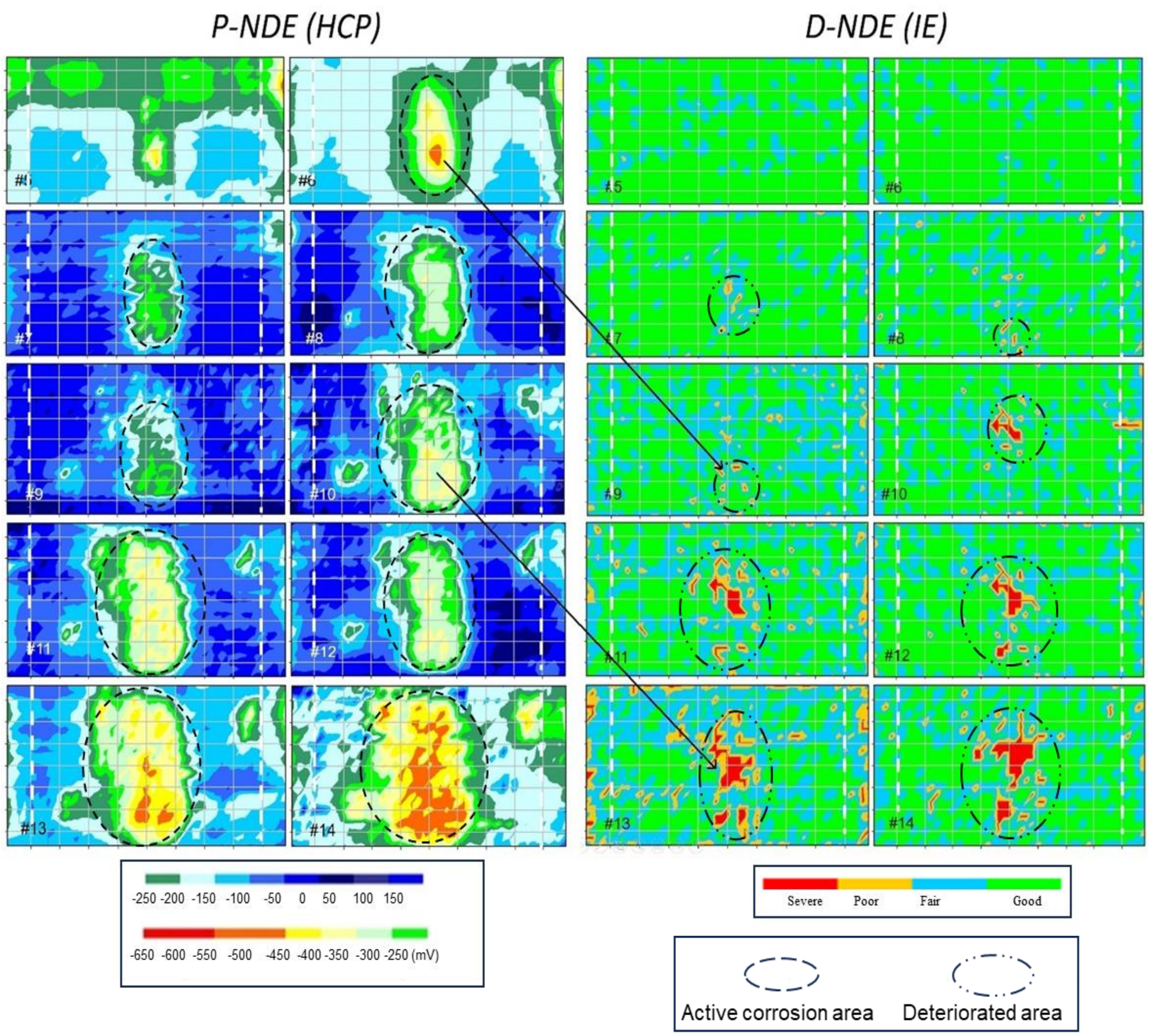

Source: FHWA.

Figure 59. Heat map. Comparison of chronological contour plots for IE and HCP.

A visual comparison of the two contour sets reveals that while HCP identified regions with varying levels of corrosivity in the middle sections of the deck, no other technology had yet detected any signs of damage. As corrosion progressed rapidly and subsurface delamination accumulated, the physical damage became apparent in subsequent rounds of data collection. To scale back the accelerated testing time of the experiment to align with actual in-service bridges, each round of data collection (approximately 200,000 cycles of live load) was compared with the typical truck traffic volume passing bridges in New Jersey and Pennsylvania.

Using the average (median) daily truck traffic (ADTT), the 200,000 cycles of live load correspond to an in-service life of approximately 1.3 yr for Pennsylvania bridges and 2.5 yr for New Jersey bridges. The methodology for scaling the ADTT between accelerated testing live-load and in-service bridges is discussed in chapter 5. In the case of figure 59, HCP identified the corrosive environment three to four rounds ahead of physical damage, which roughly translates to 4–5 yr for a typical Pennsylvania bridge and 8–10 yr for a typical New Jersey bridge. Alternatively, using the median freeze–thaw cycles reported by the InfoBridge web portal

(FHWA n.d.a.), the 30 cycles of freeze–thaw for three rounds of data collection periods (roughly 10 cycles per each data collection period) correspond to an in-service life of approximately 7–8 mo for bridges in the Mid-Atlantic region (Pennsylvania, New Jersey, Delaware, Maryland, Virginia, West Virginia), 18 mo for the Northwest region (Oregon, Washington), and 24 mo for bridges in the Gulf region (Florida, Texas, Alabama, Georgia, Louisiana, Mississippi, New Mexico).

Importantly, the observed physical damage in the middle portions of the deck occurred earlier than the typical t_p (typically 5–10 yr for an uncoated RC deck for in-service bridges), primarily due to low concrete cover, high brine concentration, and excessive loading. Comparing the definitions of NBI CR and element-level CS shows a potential correlation between NBI CR and element-level CS where damage is visually measurable. Based on the qualitative observations made thus far, PNDE can possibly be deployed as a leading indicator of deck corrosiveness. If this is confirmed, the researchers recommend another round of DNDE testing in the next 2–3 yr to investigate the progression of corrosion. If slight damage (due to subsurface delamination) is observed, preventive interventions can be implemented.

However, quantitatively correlating NBI CR and NDE results is not advisable, as the primary objective of NBI CR is to ensure the serviceability and overall safety of bridge components, while NDE is primarily focused on the performance and long-term serviceability of bridge components. Nonetheless, a rational quantitative correlation between element-level CS and NDE can be performed, considering their shared goal of providing a more detailed assessment of multiple bridge elements. The following subsection investigates the quantitative correlation between NDE and element-level CS.

Quantitative Assessment of NDE Data

The team conducted an analysis to verify the concept that the application of NDE can aid in assigning element-level CS2 accurately. The analysis consisted of comparing results from a typical DNDE technology, a typical PNDE technology, and VI results. In general, the NDE data from accelerated testing was shown in chapter 2 to have limited reliability based on ROC analysis for a variety of reasons, including the unusual nature of the deck cover variability and the test conditions implemented, such as periodic wetting of the deck. Consequently, the most effective way to analyze the overall concept of using NDE data to improve the quality (i.e., accuracy) of element-level data was to select technologies with the best apparent performance to represent the two different types of NDE technologies: namely, DNDE and PNDE.

The researchers used IE to analyze results from technologies intended to detect subsurface damage (i.e., delamination) such as sounding, mobile sounding, or IRT. IE was selected to represent this type of NDE technology because it showed positive correlation with other technologies in the previous analysis conducted as part of this project and is known to provide reliable results in systematic tests (Sultan and Washer 2018). HCP was used to represent PNDE technologies such as ER or GPR that analyze electromagnetic properties of concrete. HCP was selected to represent this class of technologies because it showed positive correlation in a previous analysis conducted as part of this research.

Figure 60 illustrates the area quantity of the deck based on the assignment of IE, HCP, and visual inspection values for the interior 40 ft (80 percent of deck area equal to 900 ft^2) of the deck length. In this plot, the quantity obtained using the IE device is indicated by circle symbols. The IE quantity was calculated based on the region of the deck designated as poor and serious according to the interpretation of the shape of the frequency spectrum (FHWA InfoTechnology (FHWA n.d.c.)), as presented conceptually in figure 2 in chapter 2. In this approach, the overall shape of the frequency spectrum is analyzed and correlated to damage severity. The designation of serious is assigned to areas where spalling is imminent, and the designation of poor is assigned to areas containing damage, but spalling is not imminent. In general terms, a designation of serious represents large, shallow defects that respond with lower frequency resonance associated with flexural waves (i.e., “drumhead” effect). A designation of poor is assigned where thickness resonance is present, resulting in increased resonance frequencies (relative to an intact portion of the deck). For this study, the IE results in terms of poor and serious were provided by the Rutgers research team.

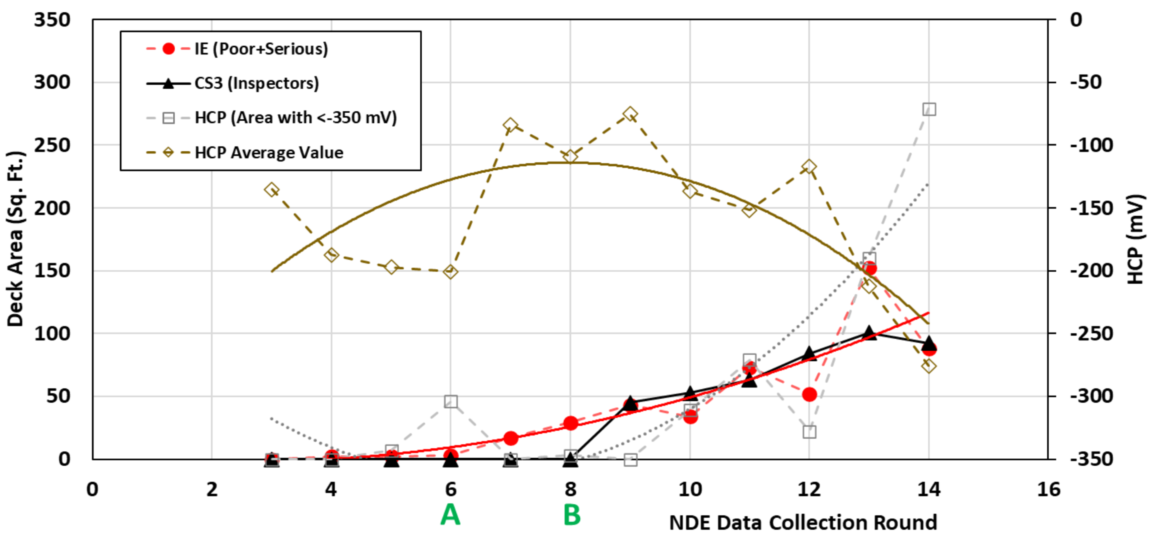

Source: FHWA.

Figure 60. Graph. Middle portion of the deck (40 ft).

The figure also includes the CS3 quantities from VI shown as triangle symbols. These data represent the average CS quantities (in ft^2) as reported by four certified bridge inspectors and one of the researchers from the University of Missouri, based on a review of the HD images captured at each inspection interval.

HCP data are presented in two different formats. Area quantities were determined from locations on the deck where the HCP result was less than −350 mV. These data are shown as open square symbols plotted using the left ordinate (ft^2) of figure 60. The HCP data were also analyzed in terms of the average HCP value (mV) for the entire portion of the deck being analyzed. These data are plotted against the right ordinate, which shows the average HCP values in millivolts. The raw data are shown (diamond symbols) and a curve fitted to the data (solid line at the top of the graph). The first and second rounds of NDE data collection were linked to the deck’s curing time and were, therefore, excluded from the plot.

The CS2 descriptions for typical RC structures primarily focus on surface deterioration. "Delamination" is the only subsurface damage mentioned in the descriptions for both CS2 and CS3. Without hammer sounding or another NDE technology, VI alone would not typically detect this deterioration. As a result, a typical bridge deck inspection without hammer sounding would only assess the surface of the deck, and the CS2 quantity would include only surface deterioration. For the tested bridge deck, the areas classified as CS2 primarily consisted of scaling, where the cement paste had eroded, revealing the aggregate.

In figure 60, CS3 data reported by inspectors generally relate to spalls on the deck surface with a depth of at least 1 inch. Due to the low cover (≤1 inch) in the middle portion of the bridge, as illustrated in figure 58, subsurface damage quickly propagates toward the surface, resulting in spalling. Many of these spalled areas revealed reinforcing bars in the concrete. Considering that the concrete cover over reinforcing bars of most bridge decks is typically 1.5 inches or greater, a visual assessment of the spalls would suggest that these areas have a depth exceeding 1 inch, which is the threshold distinguishing CS2 from CS3. Hence, inspectors assessed these areas as CS3.

If the bridge had typical cover thickness (≥1.5 inches), these areas would likely remain intact for a longer period compared to that observed in the test data, and the areas would develop visible spalls much later. However, in the data from the accelerated testing, the areas of subsurface delamination quickly resulted in spalls, leading to the classification of CS3. Therefore, the CS3 areas can be used to assess those areas previously classified as CS2. For instance, figure 60 demonstrates that IE results began indicating the development of subsurface damage at the sixth monitoring interval (point A). These areas of subsurface damage were later identified by the inspector two monitoring intervals later (point B). These data illustrate that the IE results served as a leading indicator (i.e., CS2) of the approaching deterioration in the form of spalls (CS3). The observed trend in the data suggests that new areas of subsurface damage are emerging while existing areas of subsurface damage are advancing toward spalling. This trend is evident in both the VI results and the IE results, which display an increasing pattern in subsequent intervals, as expected.

In the sections of the deck where the cover depth is appropriate, as depicted in figure 61, the IE results indicate the development of subsurface damage toward the latter monitoring intervals. Since the cover depth is within the typical range, these subsurface damage areas had not yet manifested as spalled regions.

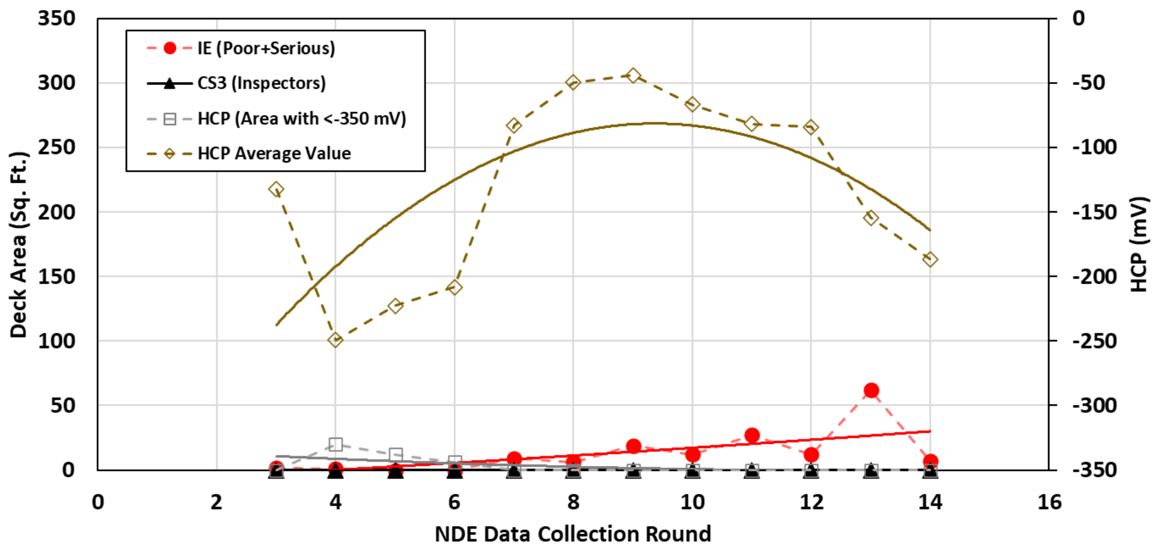

Source: FHWA.

Figure 61. Graph. End portions of the deck (5 ft from each side).

Worth noting is the fact that the HCP data align with this analysis. When comparing the rates and magnitudes of changes in the HCP data, whether in terms of average values (mV) or areas (ft^2), these data consistently indicate that the portions of the deck with appropriate cover experience damage much later in time compared to the sections with low cover. Also, the comparison of IE and HCP contours presented in figure 59 for both the low cover and normal cover sections illustrates that the data are in line with the areas of low cover, which deteriorate at a significantly faster rate than the areas with typical cover.

In an alternative interpretation of the NDE results, figure 62 presents the outcomes from the middle section of the deck specimen. The figure displays the results obtained from IE, HCP, and multiple CS quantities assigned by inspectors, allowing for a comprehensive comparison. To establish a clear relationship and sequence of multiple events, the researchers have labeled significant events in the progression of damage in the deck sequentially in the figure. Point 0 (zero) represents the initiation of damage with further progression labeled with letters A–E, as shown in the figure.

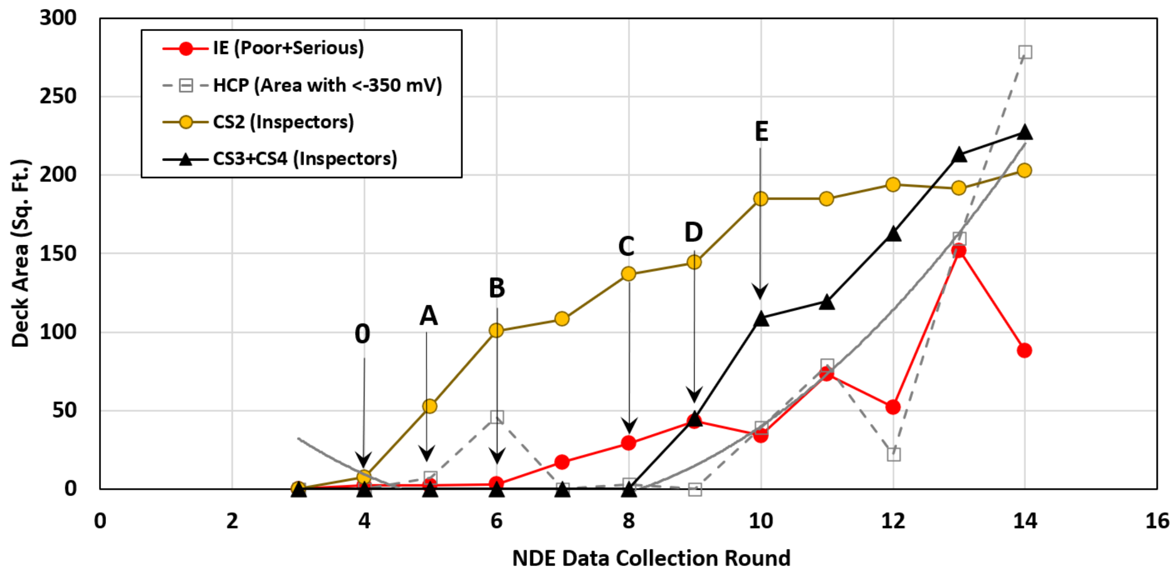

Source: FHWA.
0 = typical surface scaling picked by inspector; A = HCP first inflection; B = IE first inflection; C = first physical damage picked by inspector; D = HCP second inflection; E = IE second inflection.

Figure 62. Graph. Middle portion of the deck (40 ft) with inspection data.

Event 0 represents the initial observation of deck scaling detected by inspectors. This inspection occurred after the bridge had undergone the first round of approximately 185,000 live-load cycles and eight cycles of freeze–thaws. Moving to event A, one round later, HCP showed indications of highly corrosive areas (≤–350 mV) where no internal or surface defects had been detected by VI or IE. However, HCP measurements carry a high noise ratio, making them susceptible to a lack of sufficient accuracy. The quantity of CS2 exhibits a linear increase primarily associated with the scaling of the surface due to increased live-load cycles and freeze−thaw damage.

By the sixth round, denoted as event B, which includes the accumulation of 35 cycles of freeze-thaw and more than 570,000 live-load cycles, IE revealed varying levels of subsurface delamination, categorized as deep (poor) and shallow (serious). The linear increase in the quantity of CS2 continued due to scaling effects. Subsequently, in the eighth round (event C), inspectors detected the first instances of physical damage (CS3+CS4). At this point, the deck had been subjected to 914,000 live-load cycles and 48 freeze–thaw cycles. With the use of median ADTT as a scaling metric, the 914,000 live-load cycles roughly correspond to 6 and 11 yr of traffic exposure for a typical bridge in Pennsylvania and New Jersey, respectively.

In the following ninth round, referred to as event D, HCP exhibited a second inflection point with a consistent increase in subsequent data collection periods. Physical damage (identified by inspectors as CS3 and CS4) continued to grow due to the extent of subsurface delamination. Starting from the 10th round, denoted as event E, IE demonstrated its second inflection point, indicating larger subsurface delamination closer to the deck surface. By this data collection period, the deck had been exposed to 132,000 live-load cycles and 70 freeze–thaw cycles. At this stage, subsurface delamination, primarily due to low cover, begins to spall, and exposed reinforcing bars become evident. The rate of assigned CS3 and CS4 continued to increase, while additional assignments of CS2 (surface scaling) nearly ceased.

The researchers would have liked to have more data collections available to study the ratio of HCP and IE against multiple CS quantity ratios. Considering the low cover issue in the middle of the deck, the team anticipated that higher rates of HCP (≤–350 mV) and IE (poor and serious) quantities, along with an increased level of lower CS assignments, would have been observed if the testing had been continued.

CONCLUSION

The integration of NDE technologies with conventional performance indicators of bridge deck has been explored, revealing both significant benefits and notable challenges. The team assessed the correlation between NDE and conventional performance indicators (i.e., element-level CS) both qualitatively and quantitatively throughout the lifecycle of the specimen used for accelerated testing. The researchers demonstrated that NDE provides a more detailed assessment of bridge deck conditions that enable the early detection of issues not visible through traditional inspections. This report provides approaches for integrating these data into contemporary asset management and conventional performance indicators, particularly element-level CS. This capability is crucial for preemptive interventions, potentially extending the lifespan of bridge structure and offering cost-effective solutions for maintenance and safety. Conclusively, the research shows how the data from the accelerated testing specimen can be used within the broader context of performance reporting, primarily with element-level CS.

However, the adoption of NDE into routine bridge maintenance practices faces obstacles. The absence of standardized protocols for the collection and interpretation of NDE data presents a challenge. Additionally, the effectiveness of NDE techniques is influenced by various factors, including environmental conditions and the subjective nature of data analysis. These challenges necessitate a concerted effort to overcome.

CHAPTER 4. SERVICE LIFE MODELING

INTRODUCTION

As described in chapters 2 and 3, the researchers analyzed NDE data obtained from experimental accelerated testing of a model deck section at the BEAST facility at Rutgers University to investigate the use of NDE to improve the accuracy of performance evaluation and service life predictions for RC bridge decks through evaluation of the tested deck specimen. To that extent, the team performed mechanistic service life analyses to model deterioration of the deck specimen caused by chloride-induced corrosion of the reinforcing steel and, in particular, used the NDE data to properly define the model attributes.

The researchers performed modeling using the team's in-house service life modeling software, CASLE. This proprietary modeling software uses a probabilistic modeling approach, based on the principles outlined in *fib Bulletin 34*: *Model Code for Service Life Design* (Schiessl et al. 2006), to simulate chloride ingress through concrete and to estimate the percentage of an element's surface area affected by subsurface corrosion initiation and associated damage (i.e., delamination, cracking, and spalling). To further validate the integrability of NDE data into mechanistic-level service life prediction, the research team examined a previous project using the NDE assessment of two in-service bridges as outlined in a subsequent section (Comparison Field Study—In-Service Iowa Bridges) (ElBatanouny et al. 2022). The comparison case study discussed herein comprises two bridges examined by the researchers as part of a research project sponsored by the Iowa Highway Research Board (IHRB) and the Iowa DOT (ElBatanouny et al. 2022).

DEVELOPMENT OF SERVICE LIFE MODEL

Chloride-Induced Corrosion of Reinforcing Steel

Carbon steel corrodes readily in moist atmospheric environments by reacting with water and oxygen to form iron oxide, or rust. In RC, however, carbon steel reinforcement is protected from corrosion by the surrounding concrete. The concrete provides chemical protection of the steel through its highly alkaline pore solution (pH typically 12–14), which stabilizes the steel surface by producing a "passive film" or "passivating layer" that impedes corrosion. Depassivation, or deterioration of the passive film, can occur either by an excess of chloride ions or by reduction of pH, such as by carbonation of the concrete. Corrosion is set to initiate either when a threshold of chloride concentration is reached, or when the pH of the concrete is reduced at the bar depth, respectively.

Chloride-induced corrosion is the most common form of corrosion in RC bridge decks. In these elements, chloride is most often introduced into RC by diffusion from the environment (e.g., from deicing chemicals applied to the bridge deck). Chloride may also be introduced from admixtures or salt-contaminated mixing water or aggregates used during mixing. The rate of chloride ingress through the concrete is a complex function of the concrete mixture design, the age of the structure, environmental conditions (such as temperature, moisture exposure, etc.), and the presence of sealers or protective coatings on the surface of the bridge deck. Cracks and other damage in the concrete arising from material degradation or loading can provide pathways to the reinforcing bar with higher rates of chloride ingress than in nearby sound concrete.

When the concentration of chloride at the surface of the steel reinforcing reaches a critical "threshold" value, localized corrosion can initiate, typically forming pits on the steel's surface. The critical chloride concentration at which corrosion initiates is a distribution that depends on several factors, including the interfacial properties of the steel and concrete, the pH of the pore solution in the concrete, and the electrochemical potential of the steel (Bertolini et al. 2013). Above a minimum concentration of approximately 0.2 percent chloride by weight of cement, corrosion of uncoated carbon steel in uncarbonated concrete becomes possible, and a high probability of initiation occurs when concentration exceeds 0.5 percent chloride by weight of cement. The threshold may be lower in concrete affected by carbonation. Corrosion risk is generally increased by greater chloride content, higher moisture content, and lower concrete resistivity. Corrosion often proceeds rapidly at cracks in concrete due to high local moisture, chloride concentrations, and oxygen availability.

Corrosion products build up on the surface of the reinforcing steel after corrosion initiates and gradually increases in volume, eventually generating sufficient tensile stresses within the concrete to initiate cracking, delamination, and spalling of the cover concrete. A typical t_p for chloride-induced corrosion to initiate cracking, spalling, and delamination over uncoated carbon reinforcing steel is approximately 5 yr, but this time may be significantly shorter in elements subject to elevated temperatures, high concentrations of chloride ions, and cyclic wetting and drying.

Conceptual Approach to Modeling Chloride-Induced Corrosion

Corrosion-related deterioration is modeled as a two-stage process consisting of the initiation time (t_i), which is the time elapsed before corrosion initiates, and the t_p, which is the time elapsed between when corrosion begins and sufficient buildup of corrosion products occurs to cause damage in the form of cracks, delamination, and spalls. This concept is illustrated in figure 63. The rates of chloride ingress and damage propagation experienced by specimens in accelerated exposure testing can be relatively high compared to rates experienced by a typical bridge deck because accelerated exposure testing relies on amplified exposure conditions, such as high chloride ion concentrations, cyclic wetting and drying, cyclic elevated temperatures, and freezing and thawing. The performed service life modeling attempted to account for these factors.

The timing of chloride-related corrosion initiation in an RC structure is governed by the rate at which chloride moves through the concrete and accumulates at the bar surface. Chloride transport through sound concrete can occur through several means, including diffusion (caused by a concentration gradient), capillary absorption (driven by wetting and drying), and permeation (driven by pressure gradients). Chloride ingress in a typical bridge deck element will largely occur via diffusion, with a small percentage of the uptake near the surface driven by capillary absorption and permeation (typically occurring between zero and one-half inch in depth). Service life modeling performed by the research team considered only diffusion-based transport.

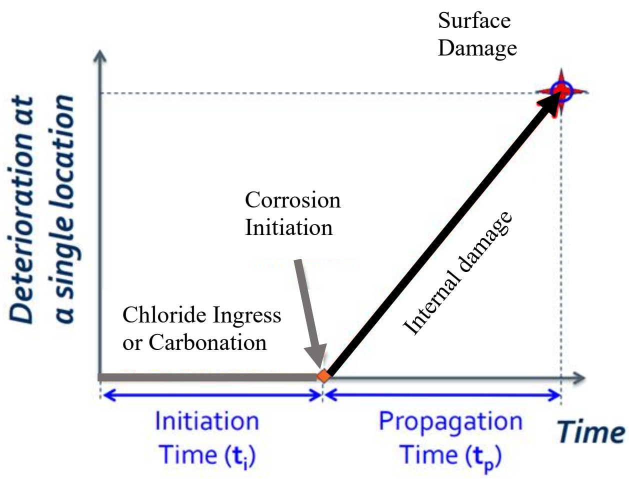

Source: FHWA.

Figure 63. Graph. Corrosion sequence.

The driving force for a diffusion-based transport mechanism is the concentration of chloride at the surface of the element, C_s. Chloride diffusion through concrete can be described by Fick's second law of diffusion:

$$\frac{\partial C}{\partial t} = D_a \frac{\partial^2 C}{\partial x^2} \tag{5}$$

Where:

C = chloride concentration at a depth x from the concrete surface at time t.
D_a = apparent chloride diffusion coefficient of the concrete.

If C_s and D_a are assumed to be constants over time, then the concentration $C(x,t)$ can be represented by a closed-form equation:

$$C(x,t) = C_s - (C_s - C_0)\,\mathrm{erf}\left(\frac{x}{2\sqrt{D_a t}}\right) \tag{6}$$

Where:

C_0 = initial (background) chloride concentration of the concrete.
erf = Gaussian error function.

In the case of accelerated exposure samples, neither C_s nor D_a is constant with time. The chloride exposure is periodic over the testing period and varies in average concentration and application rate (figure 64). The D_a is a time-dependent property of concrete that typically decreases over time due to hydration of the cementitious materials and varies proportionally with ambient temperature. As such, a closed-form solution to Fick's second law of diffusion is not adequate for modeling deterioration of the decks. Instead, a finite difference solution approach based on a

Crank–Nicholson discretization (Chapra and Canale 2002) is employed by CASLE to allow for variation of the chloride exposure (C_s) and concrete properties with time ($C_s(t)$ and $D_a(t)$, respectively).

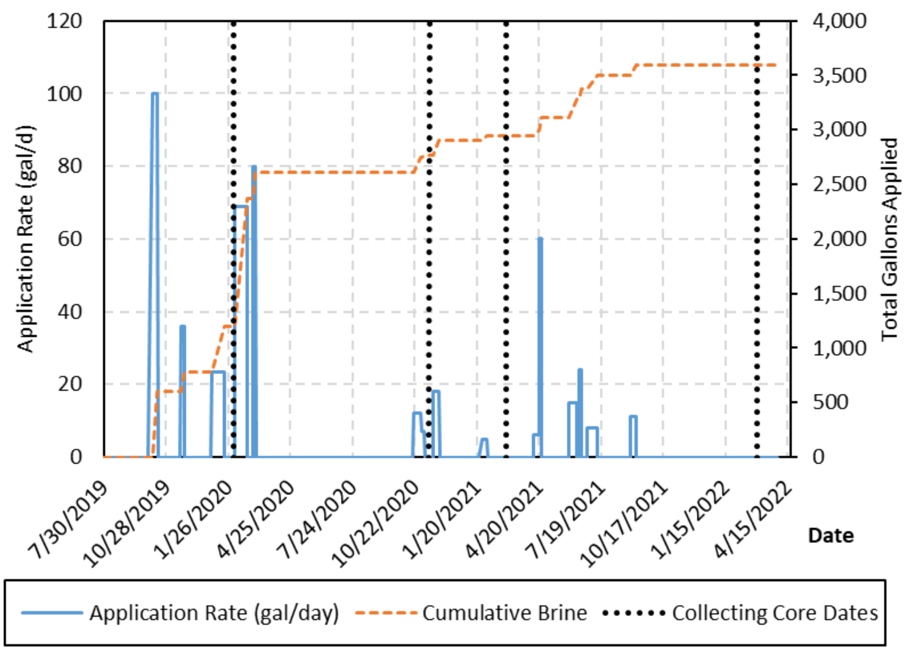

Source: FHWA.
Note: Cores were sampled by Rutgers at dates shown at the dotted lines.

Figure 64. Graph. Brine application rate for the deck specimen between July 2019 and April 2022.

FULL-SCALE ACCELERATED BRIDGE TESTING—BEAST SPECIMEN

Development of Model Inputs

The research team performed service life modeling of the deck specimen tested at the BEAST facility using inputs obtained from a combination of NDE techniques and core sampling. In consideration of the variability inherent in concrete elements, the team used a full probabilistic modeling approach. This approach determines how much concrete surface area is affected by corrosion-related damage based on statistical distributions of the key parameters. This approach recognizes that corrosion is a local process that can develop at multiple locations over time.

Parameters for the model can be conceptually separated into exposures (loads) and resistances to corrosion, as follows:

- "Exposure" parameters include the C_s as a function of time and the ambient temperature as a function of time. Exposure-related input parameters were based on records provided to the researchers by Rutgers and on conditions observed from laboratory testing of the extracted cores (performed by others).

- “Resistance” parameters include the concrete cover, the D_a as a function of time, and the chloride initiation threshold for the reinforcing steel. Resistance-related input parameters were based on a combination of GPR data (cover), core sampling (D_a), and literature values (e.g., chloride initiation threshold).

- The t_p was modeled as a constant value calibrated based on comparison of the model outputs to IE data. The team assumed for modeling purposes that the deterioration identified by IE was all attributed to chloride-induced corrosion of the reinforcing steel; other deterioration mechanisms were not considered.

Exposure Parameters

Primary exposures relevant to chloride-induced corrosion of the deck specimen include periodic brine application (chloride exposure) and ambient temperature cycling (temperature).

Chloride Exposure

The deck was reportedly exposed to a 6-percent brine solution at periodic intervals, as shown in figure 65. Brine exposures began on October 9, 2019, when the deck was 99 d of age, with an initial application rate of 100 gal/d. The brine application rate was reduced for subsequent exposure periods and typically ranged between 5 and 60 gal/d. Exposures were paused in March 2020 due to the COVID-19 pandemic and resumed on October 20, 2020. Due to the two distinct exposure periods and the varying application rates, chloride exposures for service life modeling were modeled in three stages, with stage 1 consisting of an initial exposure period between October 9, 2019, and March 5, 2020; stage 2 representing a pause in exposure between March 6, 2020, and October 19, 2020, during which no chloride was applied; and stage 3 consisting of a second exposure period starting October 20, 2020. A constant (average) chloride exposure was modeled for each interval.

The CASLE service life model considers the surface exposure in units of parts per million (ppm) chloride by weight of concrete. Due to the varying brine application rate, the team determined that the most effective method for estimating the C_s for each exposure period in these units was to fit chloride profiles to the acid-soluble chloride concentrations measured by Rutgers on cores sampled at the intervals shown by the dashed line in figure 65 and summarized in table 11.

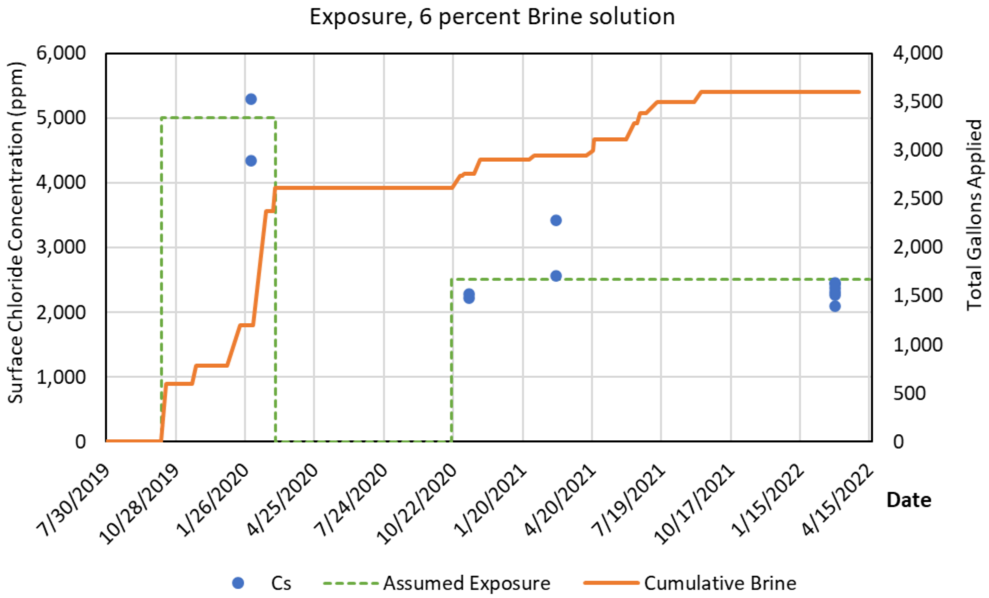

Source: FHWA.

Figure 65. Graph. Modeled chloride exposures compared to the cumulative brine applied to the deck specimen and the estimated C_s based on chloride profiles measured on cores.

Table 11. Cores sampled from deck specimen (subjected to accelerated testing) and used for development of service life model inputs.

Date	Age of Deck (days)	Total Brine Applied (gallons)	Number of Cores Sampled
February 3, 2020	216	1,200	2
November 11–12, 2020	498–499	2,760	2
March 4, 2021	611	2,930	2
March 2, 2022	974	3,595	6

Acid-soluble chloride profiles were reportedly obtained by profile-grinding each 3-inch-diameter core at 11 to 13 different depths ranging between 0.02 and 1.92 inches from the surface. Using the core samples taken from the bridge specimen, a parameter fitting based on Fick's second law of diffusion was performed to estimate the exposure C_s and the apparent 28-d diffusion coefficient of the concrete (D_{28}). The fitted chloride profiles are shown in appendix C, and the estimated surface concentrations of chloride are shown in figure 65. Based on the fitted chloride profiles, the research team assumed the average chloride exposure during the first exposure interval was 5,000 ppm chloride by weight of concrete, and the average chloride exposure during the second exposure interval was 2,500 ppm chloride by weight of concrete. The chloride concentration in each interval was modeled as a normally distributed variable centered around the average value for the interval and having a coefficient of variation of 15 percent.

Temperature

Rutgers monitored temperatures at multiple locations on the deck specimen throughout the study period. While exposure temperatures were cycled in short intervals to simulate freezing and thawing exposures, the longer term temperatures of the deck trended more broadly with variations of the seasonal outdoor temperature, as shown in figure 66. Because chloride diffusion is a typically slow process, chloride is less likely to be influenced by the rapid freeze-thaw temperature cycling and is more likely to be influenced by the more gradual, seasonal temperature changes represented by the 15-d averages shown in the figure. As such, the research team modeled the deck temperature as a sine-like function based on the 15-d average temperatures.

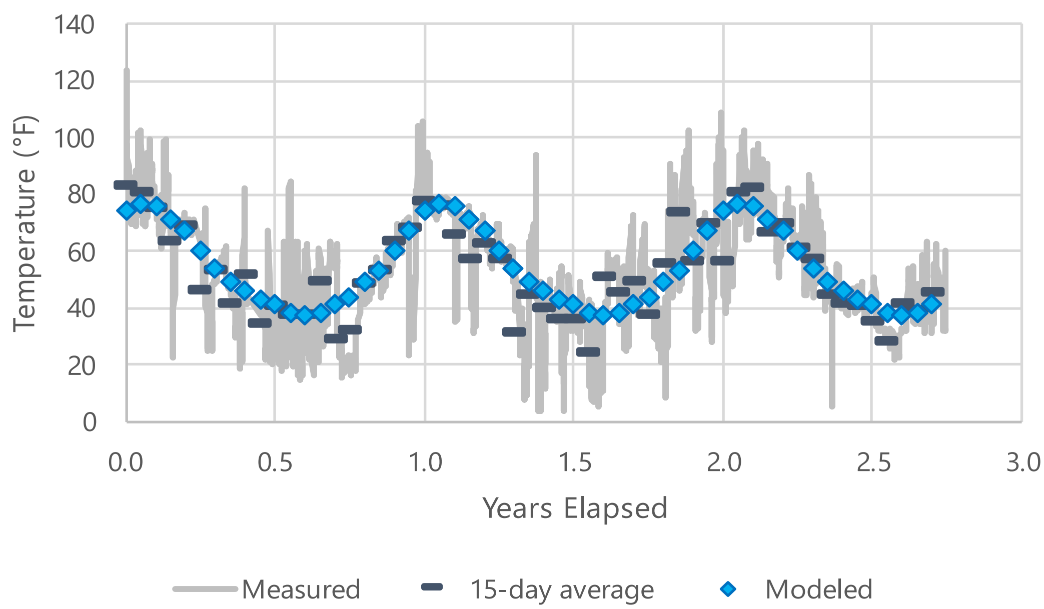

Source: FHWA.

Figure 66. Graph. Measured temperature in the deck specimen and modeled exposure temperature.

Resistance Parameters

Resistance of the deck specimen to chloride-induced corrosion is a function of the concrete cover to the reinforcing bars, the D_a as a function of time, and the chloride threshold (C_t) of the reinforcing steel.

Concrete Cover

The depth of concrete cover is crucial to reliable service life modeling. NDE can provide accurate measurements of cover depth when properly calibrated. Rutgers performed GPR surveys of the deck on October 1, 2019, to obtain measurements of the concrete cover before the start of the accelerated exposure protocol. During this evaluation, the researchers observed that the formwork had shifted during concrete placement, resulting in shallower cover in the middle 40 ft of the deck and deeper cover in the outer 5 ft at each end (figure 67). The researchers fit separate statistical distributions to the two populations of data for service life modeling, and results of modeling are therefore based on an area-weighted average of simulations performed for each region of the deck (referred to in the modeling cases as the "middle 40 ft" and the "outer 5 ft"). As shown in figure 68, the team assumed the two populations were represented by lognormal distributions centered around 1.34 inches and 1.76 inches, with standard deviations of 0.08 and 0.25 inch, respectively.

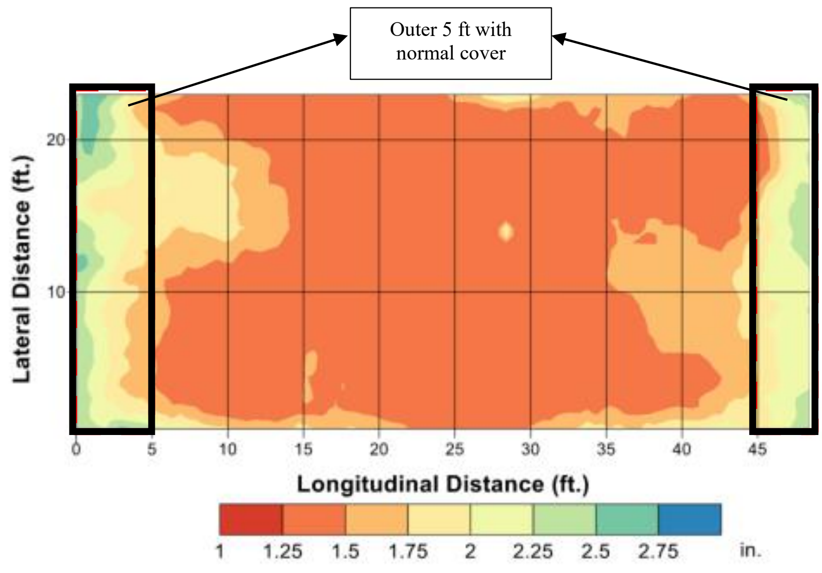

Source: FHWA.
Note: The cover measured in the outer 5 ft at each end (outlined) was deeper than cover measured in the interior 40 ft.

Figure 67. Heat map. Depth of concrete cover (in inches) measured by GPR in the deck specimen.

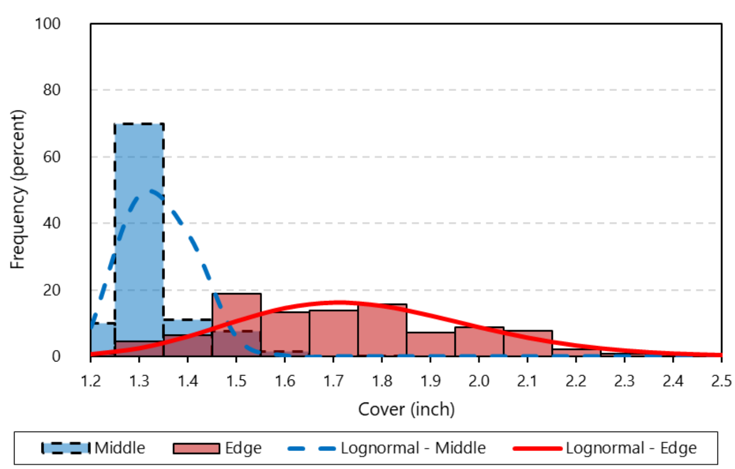

Source: FHWA.

Figure 68. Graph. Histogram with lognormal fits of measured cover over reinforcing steel located in the middle 40 ft of the deck and in the outer 5 ft at each end of the deck.

Apparent Diffusion Coefficient

In models of typical RC structures, CASLE assumes that the D_a through concrete decreases exponentially with time according to the following equation (ACI Committee 365 2017):

$$D(t,m) = D_{28}\left(\frac{28\text{ days}}{t}\right)^{m} \tag{7}$$

Where:

- D_{28} = apparent diffusion coefficient of the concrete at a reference age of 28 d.
- t = age of the concrete (in days).
- m = aging factor that accounts for the reduction in chloride diffusion with time due to ongoing cement hydration.

For concrete mixtures containing only portland cement (i.e., no supplementary cementitious materials (SCMs)), m is assumed to be equal to 0.20 (ACI Committee 365 2017). Exposure to elevated temperature for extended periods of time can cause the concrete to age at a more rapid rate than that captured by the aging factor of 0.2. However, based on the temperature profiles shown in figure 66, the team expects aging of the deck concrete due to cement hydration to follow a similar time-dependency as for conventional structures.

Materials degradation occurring under the accelerated exposure protocol may also result in a change in the diffusion coefficient of the concrete over time. The researchers observed the deck specimen undergoing materials degradation in the form of surface scaling and spalling (figure 69), which occurred over a large percentage of the deck surface area. While some spalling may be associated with corrosion of the reinforcing steel, the visual appearance of this deterioration suggests an additional root cause for the observed deterioration, such as deicer salt scaling, calcium oxychloride formation, or some other form of physical or chemical attack on the concrete. Identification of the root cause of this deterioration was outside the scope of the investigation; however, the visual appearance of the concrete suggests that this deterioration mechanism may result in an increase in the D_a over time. Such an increase would not be accounted for in the simple exponential function typically applied to conventional RC structures. Therefore, the researchers considered an additional materials degradation factor, n, to be added to the aging exponent to implicitly account for the impact of accelerated concrete deterioration on chloride transport through the deck:

$$\begin{aligned} D_{combined}(t,m,n) &= D_{28}\left(\frac{28\text{ days}}{t}\right)^{m+n} \\ &= D'_{28}\left(\frac{28\ days}{t}\right)^{m} \text{ for } D'_{28} = D_{28}\left(\frac{28\text{ days}}{t}\right)^{n} \end{aligned} \tag{8}$$

Where $D_{combined}$ is the diffusion coefficient of the concrete over time as a combined function of both material aging and material degradation.

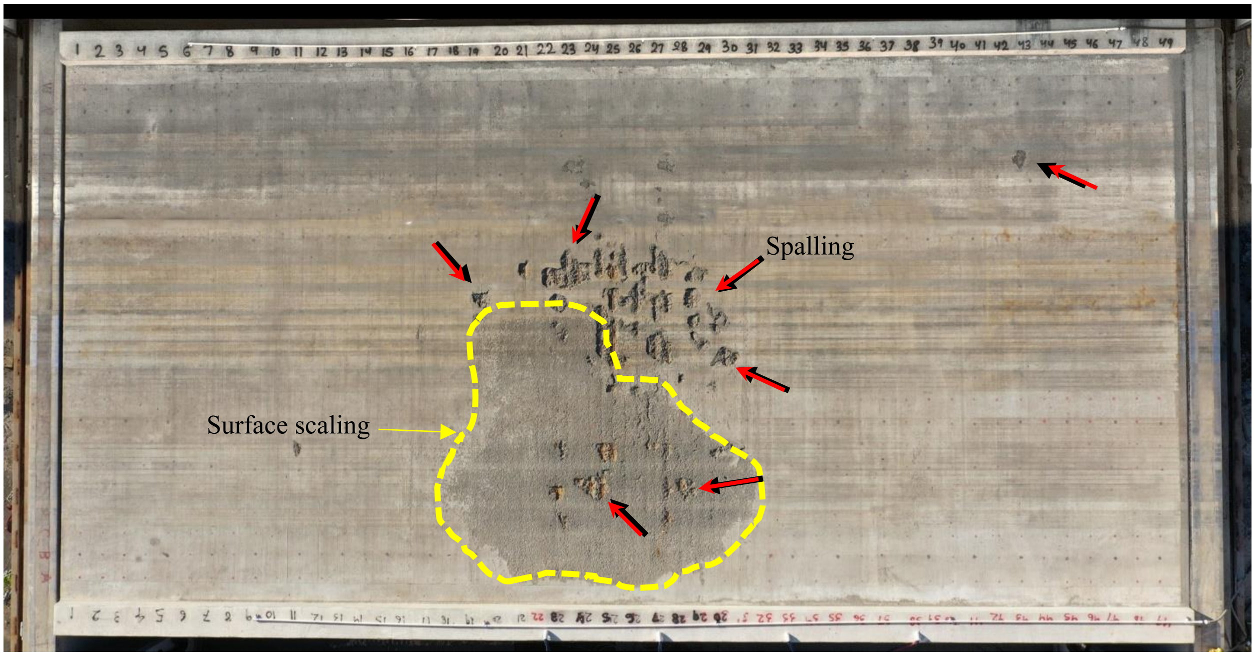

Note: Dashed circle shows surface scaling; arrows show spalling.

Figure 69. Photo. Surface scaling and spalling of deck specimen as observed on October 20, 2021.

D_{28} was calculated based on chloride profiles obtained by Rutgers on cores of uncracked concrete exposed to varying rates of brine solution application for a period of 329 d, starting at an age of 56 d. A 6-percent brine solution was always applied to the deck specimen; however, the application rate varied. Chloride profiles and their numerical fits are presented in appendix C. The average D_{28} estimated in this way was 0.217 in^2/yr, with a standard deviation of 0.056 in^2/yr.[3] D_{28} was assumed to vary over the surface of the element according to a normal distribution with a mean and standard deviation equal to the values obtained from these cores.

The materials degradation factor, n, was determined based on the D_{28}, D'_{28}, estimated from cores sampled at each exposure period. The CASLE module used to calculate these D_a values assumed a single aging factor of 0.20 to account for cement hydration. Therefore, the team expects the changes in the fitted D'_{28} values over time to follow an exponential decay function, with a coefficient equal to the materials degradation factor n. Based on the results shown in figure 70, the materials degradation factor n was estimated to be equal to −0.71. The negative sign on the exponent indicates that the concrete is becoming less resistant to chloride ingress over time due to materials degradation.

[3]Note: This estimate differs from the average D_a estimated by Rutgers using a closed-form solution to Fick's second law of diffusion. The average D_a estimated by the closed-form solution to Fick's second law represents an average over the entire exposure duration (i.e., 329 d) rather than the instantaneous value at an age of 28 d, which is used for the service life modeling approach described herein.

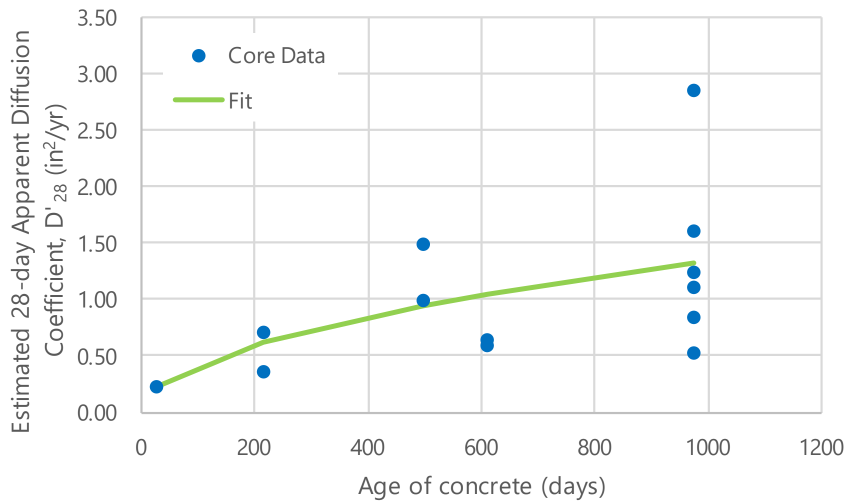

Source: FHWA.

Figure 70. Graph. Change in the estimated D_{28} with time as a function of concrete age and materials degradation factor, n.

Impact of Cracking

Cracking that develops in concrete elements can permit moisture and chloride ions to access the reinforcement more easily and can trigger early-age corrosion. For models of typical RC bridge decks, CASLE considers the effect of cracking by modeling concrete in the vicinity of cracks as having a higher diffusion coefficient (on the order of 0.8 in^2/yr), and the remainder of the concrete having a lower diffusion coefficient for sound concrete. Because detailed crack mapping to document crack locations and widths was not performed during the accelerated testing study, the researchers reviewed high-resolution photographs of the deck on three dates—November 29, 2019, February 24, 2020, and November 6, 2020—to assess the change in crack frequency over time.

Table 12 summarizes the observations. Cracks were generally difficult to resolve in the photographs but were observed infrequently. Moreover, the frequency of cracking observed decreased over time, likely because of superficial cracks wearing away as the surface scaling advanced. On the date showing the most extensive cracking, cracks were observed to cover just 33 total linear ft of the deck, equivalent to a crack frequency of less than 0.03 ft/ft^2 of area; at this frequency, the impact of cracking can be considered to have a negligible impact on predicted service life and was, therefore, not modeled explicitly. However, the researchers did observe that surface scaling affected a large and increasing percentage of the deck area throughout this period. While surface scaling has been considered implicitly in the materials degradation factor described earlier in this section, the root cause of the surface scaling has not been identified and may not be fully captured by the cores tested to determine this materials degradation factor. This limitation is discussed further in the following subsections.

Table 12. Damage progression with time, estimated based on high-resolution photographs.

Damage	11/26/2019	2/24/2020	11/6/2020
Total length of cracking (ft)	33	25	None observed
Total area of surface scaling (ft^2)	14.4	22.6	55.4
Surface area affected by scaling (percent)	1.3	2.0	4.9

C_t

For uncoated, black, reinforcing steel embedded in portland cement concrete, the researchers assumed that the C_t for corrosion initiation was represented by a beta distribution with a mean of 0.48 percent by weight cement, a standard deviation of 0.15 percent by weight of cement, and lower and upper bounds of 0.2 and 2.0 percent by weight of cement, respectively (*fib Bulletin 34* (Schiessl et al. 2006)). These parameters can be converted to units of ppm by weight of concrete for modeling based on the equivalent cement content (700 lbs/yd^3) and the unit weight (145 lbs/ft^3, assumed) of the concrete mixture.

Summary of Model Inputs

Table 13 summarizes the service life modeling inputs. The team considered C_s, cover depth, D_a, and C_t as randomly distributed variables over the surface of the deck specimen with probability distributions summarized in the table. All other parameters were modeled deterministically, meaning that they took on a single value for each modeling case (although in the case of temperature, that value could still vary as a function of time). The team performed a Monte Carlo simulation to account for the interaction between the distributions of the variables considered. In total, 1,000 iterations were performed to estimate the percentage of the deck surface area affected by corrosion initiation and propagation with time.

Table 13. Summary of model input parameters.

Parameter	Probability Distribution	Value
C_s (ppm)	Normal	Stage 0 (07/02/19 to 10/08/19)—M: 0; SD: 0 Stage 1 (10/09/19 to 03/05/20)—M: 5,000; SD: 750 Stage 2 (03/06/20 to 10/19/20)—M: 0; SD: 0 Stage 3 (10/20/20 and later)—M: 2,500; SD: 375
Temperature (°F)	Deterministic (varies with time)	See figure 66
Cover depth (inches)	Lognormal	Middle 40 ft—M: 1.34; SD: 0.08 Outer 5 ft—M: 1.76; SD: 0.25
D_{28} (in^2/yr)	Normal	M: 0.217; SD: 0.056
Aging factor m	Deterministic	M: 0.20
Damage factor n	Deterministic	M: −0.71
C_t (ppm)	Beta	M: 858; SD: 268; LL: 358; UL: 3,576
t_p (yr)	Deterministic	Determined based on model calibration

M = mean; SD = standard deviation; LL = lower limit; UL = upper limit.

Results and Discussion of Accelerated Testing Study

Figure 71 shows the service life model projections for the projected percentages of the deck specimen surface exhibiting corrosion initiation and damage over the simulated exposure period. The team used this model to predict the time to corrosion initiation, while NDE data (primarily IE) was used to inform the t_p estimates (time after initiation until surface damage, i.e., cracking and spalling, appeared). The predicted percentage of surface area with corrosion initiation was evaluated against the area indicated by HCP measurements to have a high probability of active corrosion as discussed in the following paragraphs. Figure 71 shows the model projections alongside relevant NDE data used for model calibration and validation.

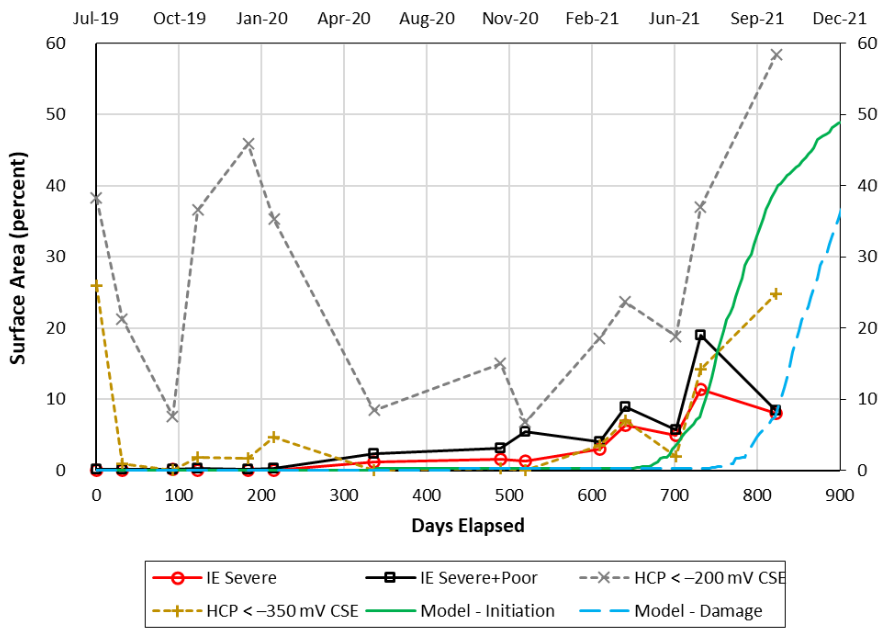

Source: FHWA.

Figure 71. Graph. Comparison of model projections to NDE data obtained from IE and HCP measurements.

The predicted percentage of corrosion initiation appeared to align well with the HCP measured by Rutgers. Per ASTM International (2015) C876 standard, a greater than 90-percent probability exists of active corrosion occurring in areas of RC elements where HCPs are more negative than −350 mV, as measured with a reference copper-copper sulfate electrode (CSE), and less than a 10-percent probability of active corrosion occurring in areas where HCPs are less negative than −200 mV CSE. The predicted percentage of corrosion initiation in the deck specimen follows closely with the HCP data and is in general agreement with the HCP limits for which corrosion initiation is likely to be indicated (less than or equal to −350 mV CSE), validating the approach used for prediction of corrosion initiation in the deck. Therefore, accounting for surface damage using the materials degradation factor appears to provide a reasonable basis for predicting service life under accelerated testing.

The predicted percentage of corrosion damage is based on the time to initiation plus an assumed t_p. In analysis of existing structures under standard exposure conditions, the t_p for uncoated black reinforcing steel is usually modeled as between 5 and 10 yr but can be calibrated based on damage observed on the structure. The t_p for corrosion-related damage for the deck was calibrated based on the percentage of IE results indicating poor or severe deterioration of the bridge deck surface area. As described in chapter 2, a condition of poor is assigned for cases where the dominant IE frequency response is associated with the shallow delamination, and cases of low-frequency response associated with the flexural mode of a delamination are assigned a condition of severe. The modeled damage prediction curve was found to match the IE data most closely when a t_p of 0.25 yr (3 mo) was assumed. This t_p is significantly shorter than the 5- to 10-yr t_p more commonly observed on bridge deck structures. While some acceleration of corrosion-related damage was likely occurring in the deck due to the aggressive exposure conditions, the IE data used for model calibration were also likely affected by deterioration that was not strictly related to chloride-induced corrosion. The surface scaling observed on the bridge deck is not likely to have been the result of chloride-induced corrosion but may have an impact on the observed IE results. Consequently, the corrosion t_p estimated by application of IE to adjust the anticipated propagation period is likely conservative with respect to the actual occurrence of corrosion-related deterioration of the deck.

COMPARISON FIELD STUDY—IN-SERVICE IOWA BRIDGES

Introduction to Companion Study

This section details the study conducted to explore the integration of NDE into service life models developed for in-service bridges. A key objective was to determine the existence of correlations between NDE data, NBI condition data, and service life models. The study specifically focused on two in-service bridges, aiming to conduct a thorough analysis of NDE and service life data, and to compare these findings with standard NBI data. The research team had previously surveyed these bridges as part of a distinct past project, although the service life models in question were developed under the current project. More comprehensive details regarding the team's surveys are available in the team's report for the Iowa DOT, with a summary provided in the following subsections (ElBatanouny et al. 2022).

Structure Description

The team selected two structures located in Iowa as sample bridge decks for this study. To make the comparison less complex, the team selected structures with similar characteristics of deck specimen as that at the BEAST facility. The structures have RC bridge decks that carry interstate traffic. Both structures are of generally similar construction to the specimen built at the BEAST facility; they both have uncoated (black bar) reinforcement and were exposed to deicing agents. A brief description of each structure and its NBI CRs are described in the following subsections.

Jasper County Bridge

The Jasper County bridge is located on eastbound I–80 in Iowa. The bridge is two lanes, runs east to west, and is 134 ft 2 inches long and 40 ft wide. The original plans for the bridge were dated 1959, and construction was completed in 1962. The plans for a concrete overlay were dated 1980, and the project was completed in 1982.

Linn County Bridge

The Linn County bridge is located on 8th Street NE over I–380. The bridge is two lanes, runs east to west, and is 264 ft 6 inches long and 30 ft wide. The original plans for the bridge were dated July 1971, and construction was completed in 1972. The plans for a concrete overlay project were dated 1994, and construction was completed in January 1998.

NBI Data

The researchers compared the NBI component-level CR and element-level CS data from the InfoBridge website (FHWA n.d.a.) to the results of the teams' indepth surveys, specifically the NDE and service life modeling findings. Figure 72 and table 14 and table 15 summarize the results.

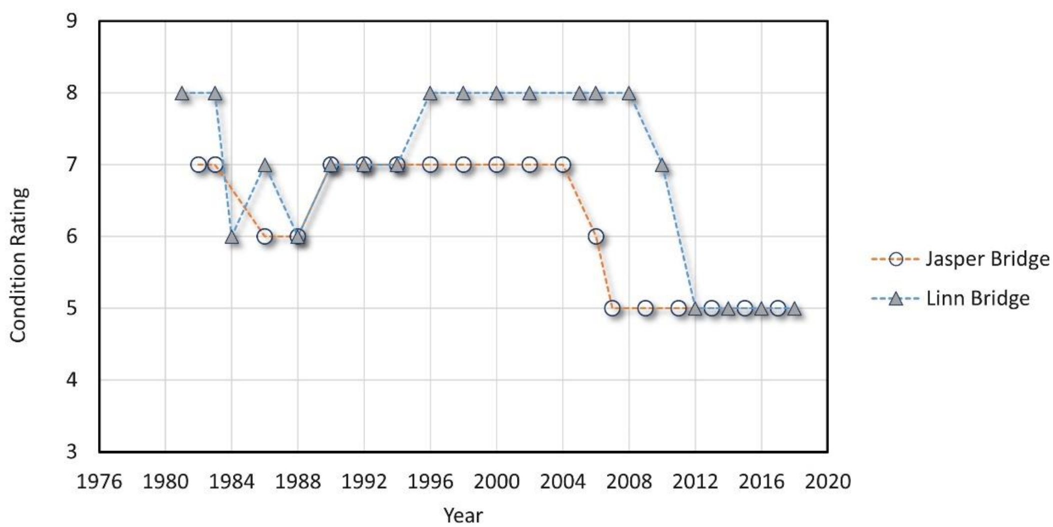

Source: FHWA.

Figure 72. Graph. CR history for two bridge decks in Iowa (FHWA n.d.a.).

Table 14. Element-level deck CS data—Jasper bridge (FHWA n.d.a.).

Year	Element Number	Element Name	Unit	Total Quantity (SF)	CS1 (SF (%))	CS2 (SF (%))	CS3 (SF (%))	CS4 (SF)	HI (%)
2019	12	RC deck	SF	8,952	7,720 (86)	1,232 (13)	0	0	95.46
2019	510	Wearing surfaces	SF	8,040	4,442 (55)	3,576 (44)	22 (<1)	0	85.14

SF = square feet; HI = health index

Table 15. Element-level deck CS data—Linn bridge (FHWA n.d.a.).

Year	Element Number	Element Name	Unit	Total Quantity (SF)	CS1 (SF (%))	CS2 (SF (%))	CS3 (SF (%))	CS4 (SF)	HI (%)
2019	12	RC deck	SF	6,302	6,137 (97)	140 (2)	25 (<1)	0	99
2019	510	Wearing surfaces	SF	5,480	5,229 (95)	251 (4)	0	0	98.49

Previous Investigations

In 2019, the researchers performed an indepth investigation on behalf of Iowa DOT to predict future performance of various bridges after surface treatments (ElBatanouny et al. 2022). The inspections, which included NDE and material sampling, were performed after removal of the wearing surfaces. The findings of the investigation were reported to the IHRB.

Field Summary

The researchers performed indepth evaluations of the bridges that included chain dragging, material sampling, GPR reinforcement cover surveys, and HCP surveys performed over select areas of the two bridge decks. The team performed GPR surveys via line scans conducted at 2-ft intervals across the width of the lane in each inspection area. HCPs were measured along the same lines using a rolling half-cell probe equipped with a reference CCSE; readings were taken every 6 inches. NDE was performed after removal (i.e., scarification) of the existing overlay and a portion of the top region of cover concrete and before application of a polyester polymer concrete (PPC) overlay. The findings of these various methods were synthesized into a service life model for each deck.

The acoustic sounding after overall removal identified areas of damage in the deck where the concrete over the reinforcement had delaminated, which most often results from corrosion. In contrast, HCP measures the areas of probable corrosion activity, which does not necessarily mean that concrete delamination has occurred.

Table 16 summarizes the damage in the concrete deck, which shows the results from the element-level survey based primarily on VI of the surfaces of the deck. Since the concrete deck had an overlay, the top surface of the deck element was not observable; thus, the recorded condition was that of the wearing surface element (i.e., the overlay). The CS data for the deck element were based on observable damage in the soffit of the deck and any areas where the wearing surface was sufficiently damaged to reveal damage in the deck element. The element-level results for the wearing surface were a combination of cracking, spalling, and patches in the overlay. The element-level results do not correlate with the NDE results for the deck because the VI result documents different damage modes than the NDE results. The element-level results record visible surface features such as spalling, cracking, and patches, whereas the NDE results show subsurface corrosion damage within the deck. Thus, the deck element, wearing surface element, and NDE results each provide different information regarding the condition of the deck, such that a combination of these three types of data provides a more holistic view of the current condition of the deck.

Table 16 shows the quantities of HCP measurements that indicate a high probability of active corrosion at the time of measurement as percentages. Measured values were compared to the criteria for the numeric magnitude technique provided in appendix XI of ASTM International (2015) C876 standard, except that the range for active corrosion was increased from −350 mV to −300 mV based on the experience for the Linn County bridge. These bridge data were based on interpretation of the contour plots consistent with the potential difference technique from the same standard. The quantity of "active corrosion" based on the HCP data is greater than the quantity of delaminated concrete. This result could be expected for areas of active corrosion that have not yet propagated damage. The team compared results from sounding and HCP surveys to the service life model results for damage and initiation, respectively.

Table 16. Summary of NDE findings related to deck condition.

Bridge	Deck Routine Element-Level Inspection Result (%)	Overlay Routine Element-Level Inspection Result (%)	Delamination (% Total Surface Based on Sounding)	Active Corrosion Sites Based on HCP (% Total Surface)
Jasper	13	44	10	24
Linn	2	4	22	29*

*Based on contour plots, the lower bound for the range of active corrosion was adjusted from −350 to −300 mV CSE.

GPR surveys were used to determine cover depth distribution. For the Linn County bridge, reinforcement cover was, on average, 3.17 inches with a 0.36-inch standard deviation. For the Jasper County bridge, reinforced cover was, on average, 2.37 inches with a 0.36-inch standard deviation. These values include the overlay that was removed before the researchers' investigation; that is, the thickness of the overlay was added to the GPR measurements for the purpose of developing service life model inputs. The average and statistical variation of cover depth were inputs to the service life modeling.

Figure 73 and figure 74 are delamination NDE data maps for each bridge. These figures show a plan view of each bridge deck with outlines indicating areas of delamination detected by sounding. A portion of each deck shows a contour map indicating the HCP results and the scanning lines labeled A through G where GPR scans were performed for the purpose of determining the cover depth. An *x–y* plot below each plan view figure indicates the cover depth measured by GPR along a few of the scan lines. These plots are helpful in visualizing the extent of corrosion in the discussed bridge deck.

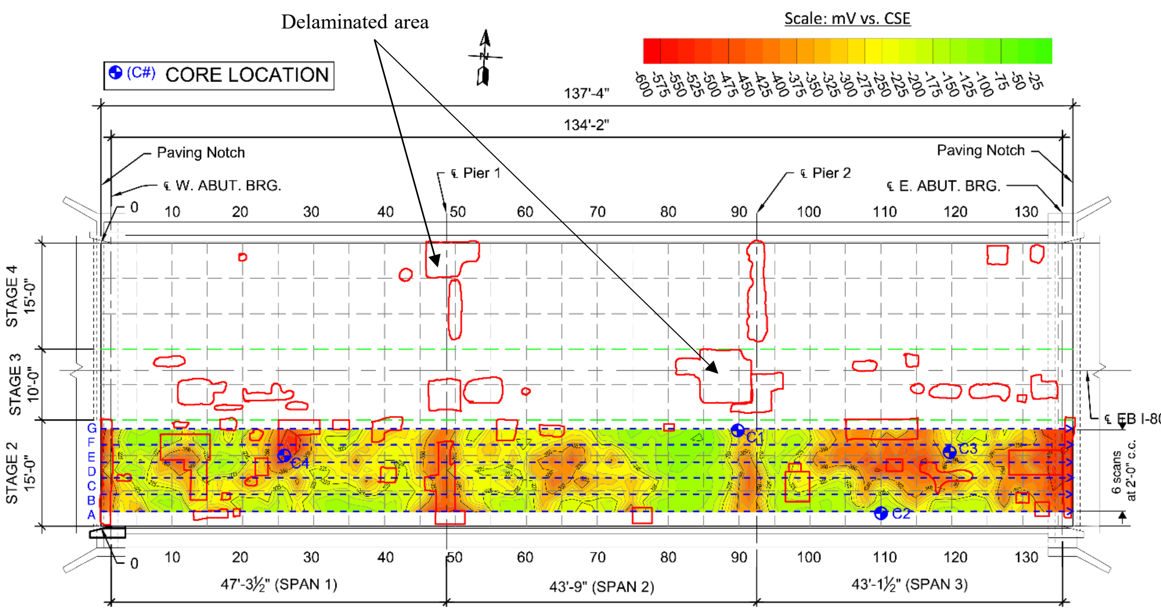

Note: delaminated areas are circled.

A. Delaminated areas overlaid over HCP contour.

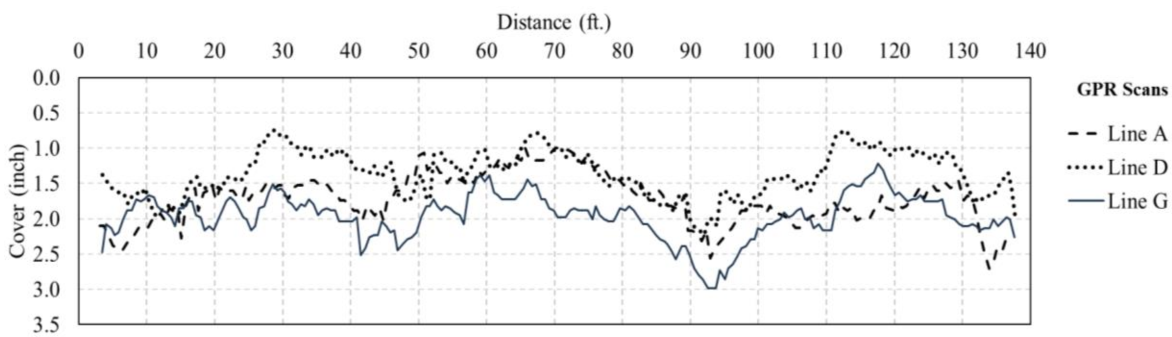

B. Concrete cover for GPR scans A through G.

Figure 73. Graphs. Jasper County bridge (ElBatanouny at al. 2022).

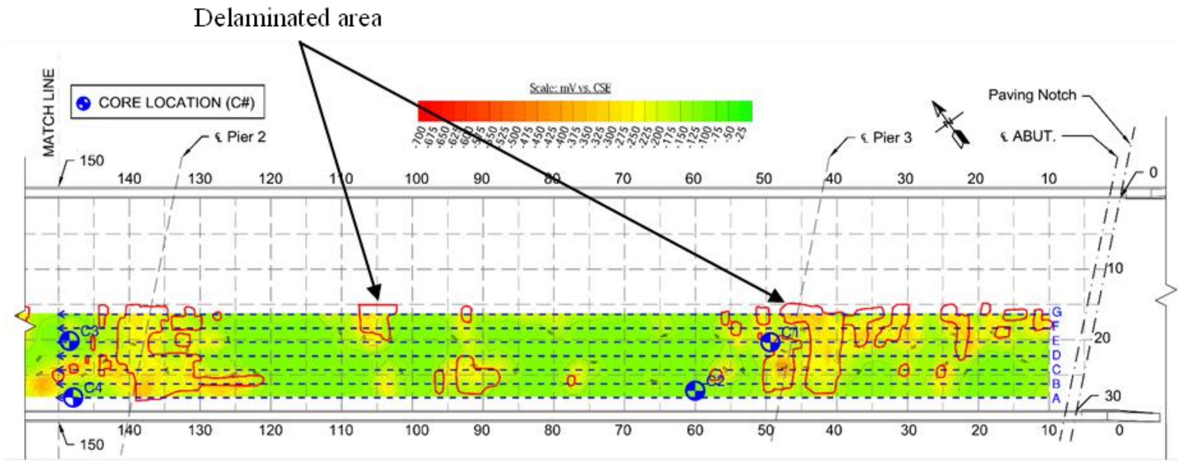

© 2024 WJE.
Note: delaminated areas are circled.

A. Delaminated areas overlaid over HCP contour.

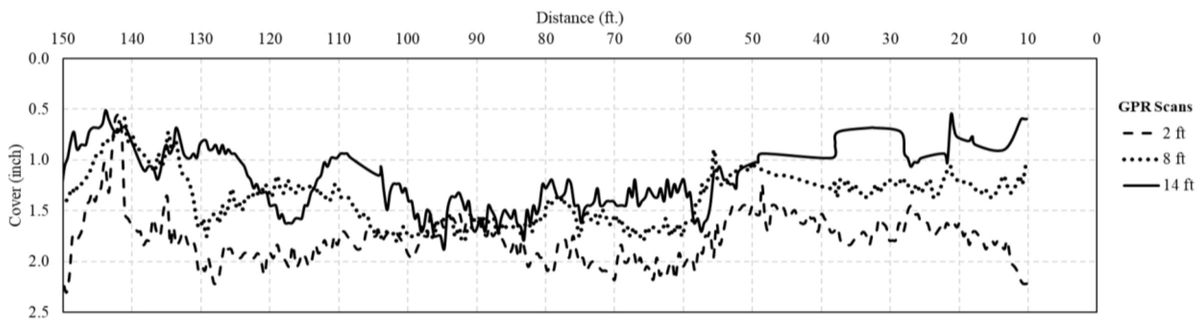

© 2024 WJE.

B. Concrete cover for GPR scans A through G.

Figure 74. Graphs. Linn County bridge (ElBatanouny at al. 2022).

Service Life Summary

The research team formulated the service life model inputs based on previous work on two Iowa bridge decks, as well as on the field inspection results (ElBatanouny et al. 2022). Appendix D summarizes the inputs used for the modeling. The primary inputs are chloride transport properties and reinforcement cover. The outputs can be either time until corrosion initiation or time until damage propagation; t_p was assumed to be a constant value of 10 yr. The modeling was performed for the period 1972 through 2026 based on the input data. The team then analyzed these data by comparing the modeling results to field inspection results from 2019 when sounding, HCP surveys, and GPR scans were performed.

Table 17 gives the findings from the service life modeling for 2019. The table shows the percentage of deck area where initiation of corrosion is predicted by the model and the area of damage based on the initiation prediction and assuming a t_p of 10 yr. The model results indicate that, in 2019, the predicted areas of damage in the Jasper and Linn decks were 12 percent and 17 percent, respectively. These data can be compared with the field survey results shown in table 16 that indicate measured damage of 10 percent and 22 percent for Jasper and Linn decks, respectively.

Table 17. Results for 2019 from service life modeling for the sample bridge decks.

Bridge	Predicted Corrosion-Related Damage (% Deck Total Surface Area)	Predicted Corrosion Initiation (% Deck Total Surface Area)
Jasper	12	24
Linn	17	28

Table 17 indicates that, for 24 percent and 28 percent of the deck area of the Jasper and Linn decks, respectively, initiation of corrosion is predicted. HCP survey results in table 16 indicate corresponding field-measured values of 24 percent and 29 percent, respectively. These data indicate relatively close correlation between the NDE results for the subject bridges and the predictive model. In this way, the NDE data provide a benchmark for the model accuracy based on historical performance of the decks.

These data can be placed in context with historical and future performance to illustrate how NDE results can provide a benchmark for service life modeling. The time-based model outputs are compared with the 2019 NDE surveys in figure 75 (Linn) and figure 76 (Jasper), which show model results from 1972 through 2026. In the figures, the dashed line is the predicted area of corrosion initiation, and the solid line shows the predicted area of damage based on the model. The abscissa is shown on the left and records the area of damage (percent) from 0 percent at the top to 30 percent at the ordinate. The results from the 2019 NDE surveys are shown as individual points on the curve. The modeling results at those points are also shown.

The amounts of damage predicted by the models and those identified during sounding had generally good agreement. These values are shown by solid lines and plot markers. Furthermore, the level of corrosion initiation predicted by the model (shown by dashed lines) agrees with the findings from the HCP surveys (shown by plot markers).

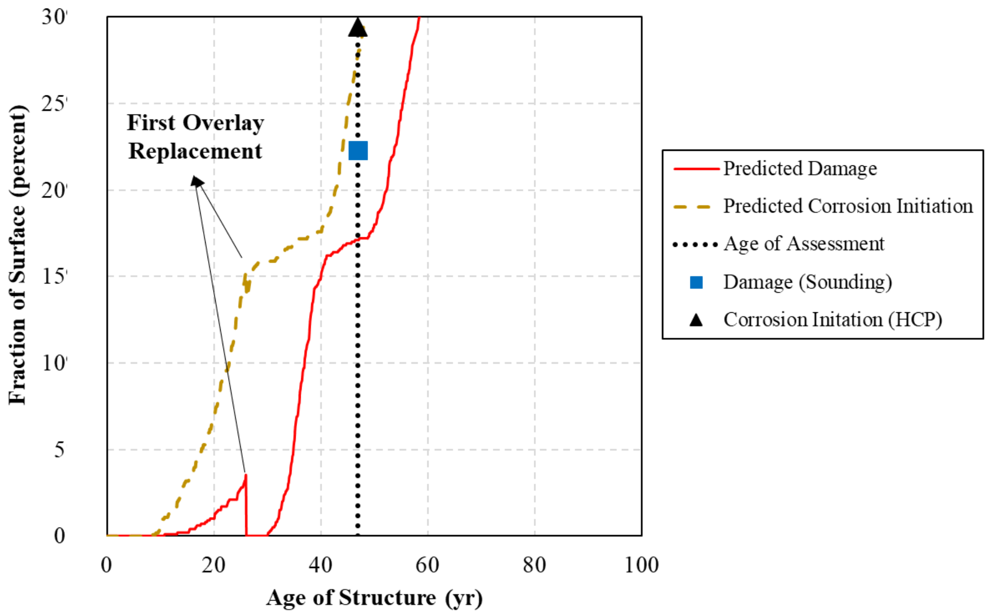

Source: FHWA.

Figure 75. Graph. Service life model results—Linn County bridge.

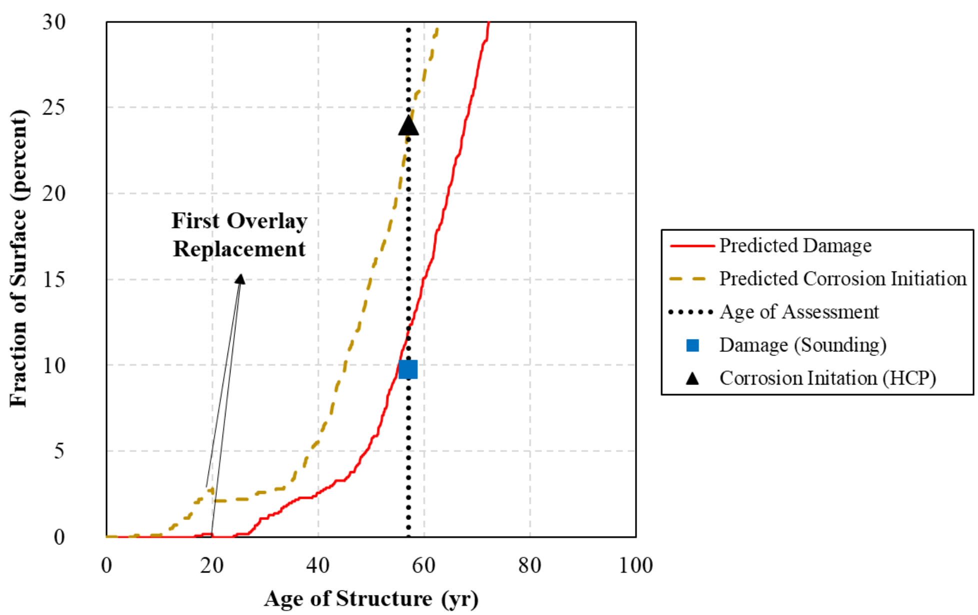

Source: FHWA.

Figure 76. Graph. Service life model results—Jasper County bridge.

Results and Discussion of Field Study

The findings from the NDE and service life modeling were compared to the NBI data, as shown in figure 77 and figure 78, for Linn County and Jasper County bridges, respectively. The NBI CRs are plotted against the left *y*-axis. Service life model predictions, indicated by "SVL," as well as results from NDE, are plotted against the right *y*-axis. The element-level CSs for the wearing surface ("510-Wearing Surface CS>=2") are also plotted, with the damage percentage relative to the right *y*-axis. However, CS data points do not correlate well with the levels of damage identified from sounding, likely because the wearing surface rating includes other factors such as cracking and abrasion.

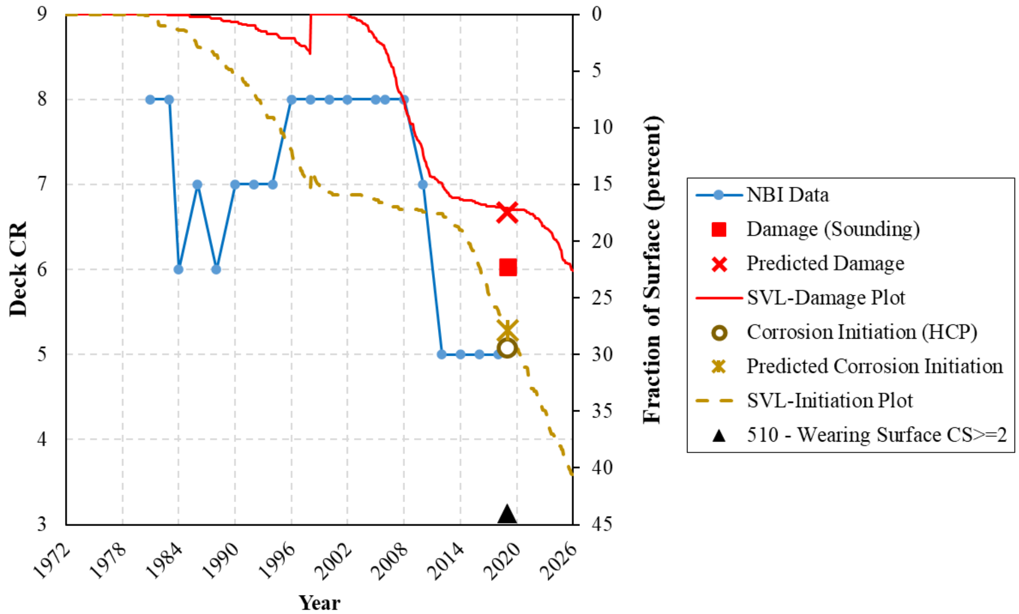

Source: FHWA.

Figure 77. Graph. Comparison between service life model, NDE, and NBI CR—Linn County bridge.

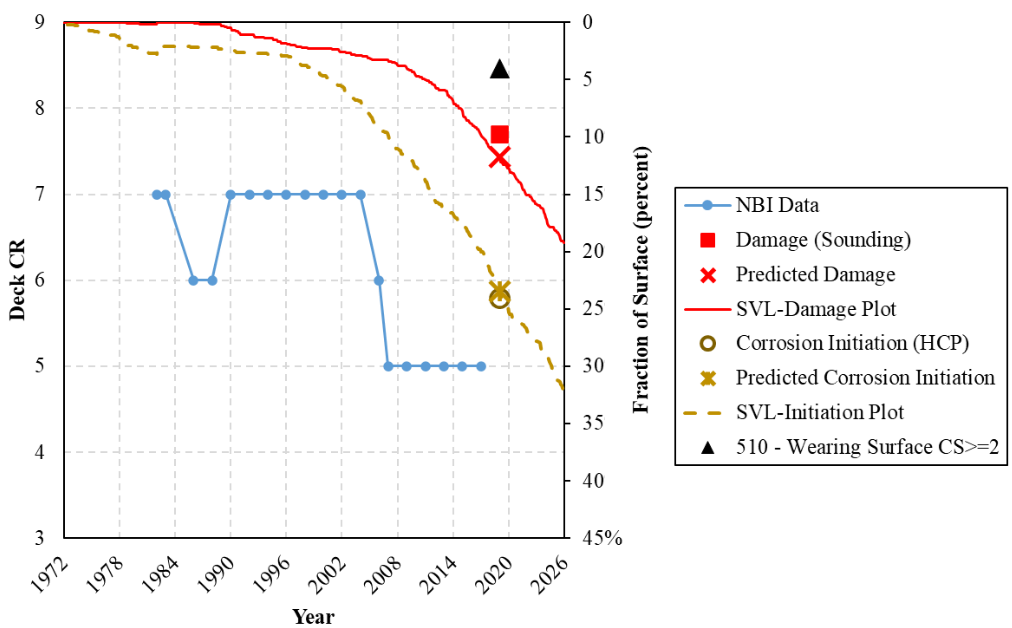

Source: FHWA.

Figure 78. Graph. Comparison between service life model, NDE, and NBI CR—Jasper County bridge.

The researchers established an approximate correlation of the axis range for NBI CR from 3 to 9 to an associated cumulative damage range from 0 percent to 30 percent based on an internal ongoing research project. Using these correlated scales, figure 79 and figure 80 show similar comparisons of model predictions to NBI ratings and indepth survey results, omitting the CS data. The result provides a good means to compare NBI ratings to damage level.

As previously discussed in the section titled Service Life Summary, the team found a good correlation between damage detected by sounding and damage predicted by the service life model. Similarly, the team also observed a good correlation between active corrosion measured by HCP and corrosion predicted by the service life model. Since NBI data cannot show the corrosion condition in fine resolution, the service life modeling and NDE data show that additional information about the deck can be gained.

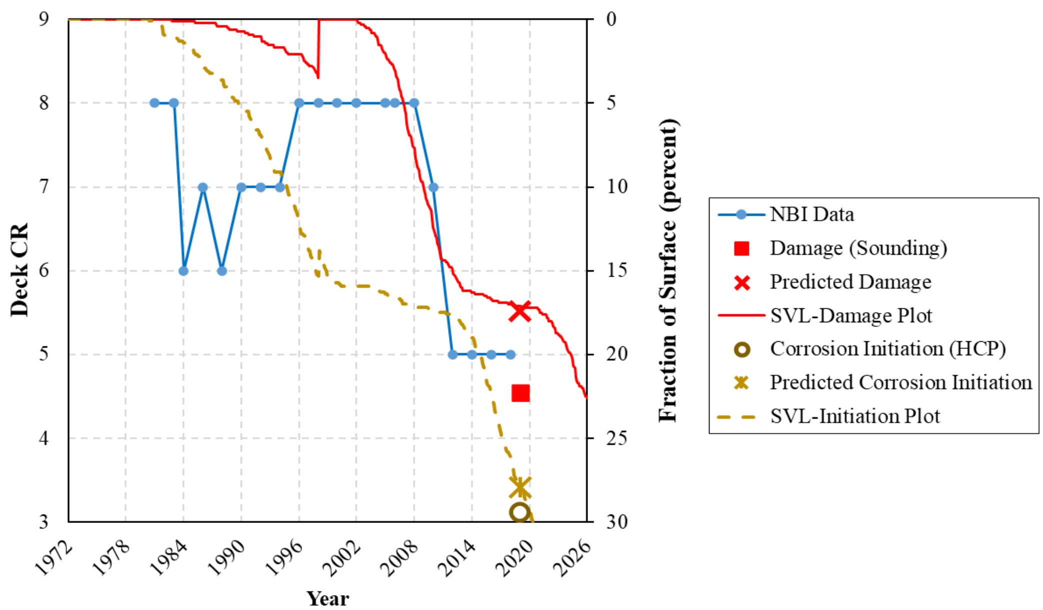

Source: FHWA.

Figure 79. Graph. Comparison between service life model, NDE, and NBI CR—Linn.

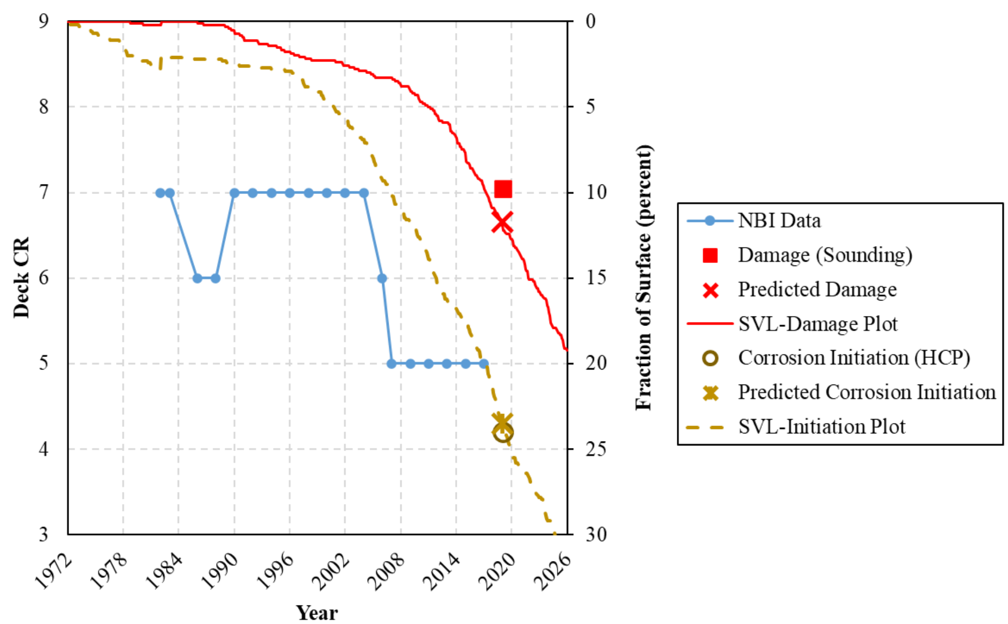

Source: FHWA.

Figure 80. Graph. Comparison between service life model, NDE, and NBI CR—Jasper.

CONCLUSIONS AND RECOMMENDATIONS

Summary of Findings

The service life model developed in CASLE for the deck specimen subject to accelerated testing adequately modeled the ingress of chloride ions into the concrete and subsequent initiation of corrosion in the reinforcing steel. NDE played an important role in defining some of the input parameters, including the use of GPR for determining concrete cover, and IE for determining the t_p. NDE, specifically HCP, was also used to verify the overall predicted percentage of surface area with corrosion initiation. NDE becomes especially useful in the propagation stage of deterioration, where no broadly accepted mechanistic model exists to predict rate of damage accumulation. VI is insufficient to characterize the degree of damage induced by corrosion. Traditionally, practitioners have used chain drag and hammer sounding to quantify accumulated damage and have used material testing to quantify the corrosion environment, but these methods are subject to the skill, experience, and even quality of hearing of the inspector, as well as noise from the surrounding environment. Adaptations of the concept into more sophisticated IE or automated acoustic sounding methods could make such assessments more efficient and objective. The NDE approaches described herein for the deck can be applied to in-service bridge decks to ensure representative service life models and performance evaluation. Further findings specific to the model developed for the deck specimen subject to accelerated testing and recommendations for future test refinements are described in the following paragraphs.

The exposure protocol during the accelerated testing did not appear to accelerate the aging of concrete due to cement hydration but did appear to introduce materials degradation that affected the rate of chloride ingress. The root cause of the materials degradation was not identified in the course of the study but appeared to result in surface scaling and spalling not typically observed in conventional RC bridge decks at the scale observed in the deck subject to accelerated testing. This materials degradation, therefore, appears to be unique to the accelerated exposure conditions for the tested deck and can be accounted for by considering an exponential materials degradation factor to describe the change in the D_a with time. Considering a materials degradation factor in future service life modeling will facilitate decoupling the impact of the accelerated materials damage on the predicted service life of bridge deck(s) tested in an accelerated testing condition but may require further analysis of the root cause of this deterioration. By decoupling the impact of accelerated damage within the simulation, service life estimates can be developed for real bridge decks represented by the deck specimen subject to accelerated testing.

The CASLE service life model used for this analysis is limited to predicting damage due to corrosion of reinforcing steel. Other well-established modeling approaches were not found that collectively consider deterioration caused by live loading, freezing and thawing, or other materials degradation. As such, the corrosion t_p "calibrated" for the deck specimen based on IE data is likely conservative, since the IE data are affected by both corrosion-related deterioration and other deterioration of the deck. However, for a goal of predicting the service life of in-place bridge decks based on simulations in the accelerated testing, such analyses can rely on corrosion t_p values for real, in-place structures. Corrosion propagation depends on local environmental conditions (e.g., temperature, moisture exposure) of an in-service bridge deck, accurate representation of which is not possible under the accelerated testing protocol, nor is it intended. However, PNDE of in-service bridge decks, including GPR cover surveys, HCP measurements, and DNDE technology such as IE, supplemented by core sampling, provide the necessary information for evaluating and predicting their performance.

Recommendations

The use of NDE and service life modeling provided additional information compared to the sole use of NBI inspection data for condition assessment of bridge decks. Without high-quality NDE data (e.g., sounding and cover surveys), the current condition of the structure cannot be accurately characterized, and the future performance (through development of service life models) cannot be reasonably estimated. Furthermore, NDE, through HCP corrosion testing, provides further insight into areas with active corrosion beyond what has manifested as damage. To that extent, the following are recommendations for future bridge inspections:

- Perform HCP testing to quantify active corrosion in addition to delamination surveys for structures with uncoated reinforcement.

- Perform service life modeling for in-service structures and new construction to better understand actual and expected performance. These models can be correlated with CR data.

- Expand the collection of CS data for decks to differentiate wear- and abrasion-related deterioration from corrosion-related delamination to better characterize corrosion condition.

CHAPTER 5. DETERIORATION MODELING

INTRODUCTION

Bridges—crucial components of transportation infrastructure—undergo continuous wear and tear over time. Predicting the deterioration of bridges is of paramount importance to ensure their safety and longevity. Indeed, accurately predicting future conditions is a key input to effective preservation, maintenance, and rehabilitation decisionmaking for bridge owners. One prominent approach to this challenge is the use of deterioration models. This approach relies on historical data from bridges that share similar characteristics and exposure conditions to provide a macrolevel understanding of bridge performance. This model then can be used to forecast the transition of the bridge deck from a new or good condition to a progressively poorer condition over time.

Since these deterioration models are typically trained by a network of bridge inventory, some coupled uncertainties are present within the interpretation of a deterioration model for a given bridge. The deterioration model often generates the mean result derived from the benchmark data and does not necessarily encompass different characteristics of individual bridges. This situation could be improved by introducing new knowledge gained from external attributes influencing the structure. Data collected through a campaign of detailed VI, structural monitoring, and NDE is an example of performance-specific information that could play a significant role in modifying the prognosis of remaining service life.

The researchers investigated the development of deterioration models specific to the deck specimen subjected to accelerated testing. Furthermore, the team thoroughly examined the implementation of NDE to enhance the accuracy of performance evaluation for bridge decks via the assessment of the results from accelerated testing.

LITERATURE REVIEW

Several deterioration models have been created to describe the deterioration phenomena using input from bridge inspection data to assist decisionmakers in predicting the future condition of a network of facilities (Agrawal, Kawaguchi, and Chen 2010). Researchers have routinely practiced three different approaches to simulate bridge deterioration: deterministic, probabilistic (or stochastic), and AI/ML. A review of the technical literature reveals that each technique has its own advantages and disadvantages that eventually lead to partial success in providing practical responses for deterioration modeling purposes.

Deterministic models technically correlate age or a limited number of other parameters with the component's condition using a simple mathematical formulation, such as the mean, standard deviation, and regression (Liu 2013). Despite the ease of model development and interpretation, deterministic models do not account for the stochastic characteristics of bridge deterioration process nor consider the effects of unobserved explanatory variables (Jiang, Saito, and Sinha 1988).

By contrast with deterministic models, probabilistic deterioration models view bridge deterioration as a stochastic process being affected by various external parameters. Stochastic duration models have been established by several studies to predict sound bridge deterioration models (Mishalani and Madanat 2002; Agrawal, Kawaguchi, and Chen 2010; Sobanjo, Mtenga, and Rambo-Roddenberry 2010; Nasrollahi and Washer 2014). These investigations successfully implemented different probabilistic methodologies to simulate the deterioration phenomena for multiple bridge components. The probabilistic models rely on transition probabilities to capture the nature of the evolution of CSs from one discrete time point to the next. These models rely on sophisticated probabilistic methodologies, such as Cox proportional hazards survival analysis, Weibull model, or Markov chain theory. These methodologies enable them to generate forecasts pertaining to the condition of various bridge components throughout their operational lifespan, as well as provide comprehensive projections for overall bridge conditions and performance metrics at the network level.

Survival analysis is a particularly valuable tool in this context, as it accommodates situations where duration data may be incomplete or subject to censoring, which presents a distinct advantage over traditional statistical methodologies. Despite the obvious advantages of being able to capture uncertainties, these models suffer from underlying limitations. Several issues include difficulties in estimating transition probabilities, incomplete capture of various explanatory variables, complex computations, lack of historical condition data for training, and data censorship.

Alternatively, AI/ML models have also been proposed. AI/ML models use modern computer techniques to automate the intelligent data “learning” process of bridge deterioration behaviors, such as artificial neural networks (Bu et al. 2012; Tokdemir, Ayvalik, and Mohammadi 2000). These techniques are mostly inspired by natural rules and present solutions based on experience and development of various discriminators. Despite the novelties, major drawbacks prevent these models from creating sufficient knowledge and transparency. As a result, those models act as black boxes and cannot explicitly provide a transparent function correlating the output to the given inputs. The computations must be conducted in an a priori format that requires significant trial-and-error operations. In essence, the consequences of the limitations associated with the various methods discussed in the preceding paragraphs will directly lead to poor predictions of future infrastructure conditions, thus compromising maintenance and rehabilitation decisionmaking.

FHWA initiated the LTBP Program to address some of the major issues and thoroughly investigate the performance of highway bridges (FHWA n.d.d.). The main goals of the LTBP Program are to identify and prioritize the most critical bridge performance issues, to collect data on those issues, and use that data to achieve a detailed understanding of bridge deterioration and performance. The products of the LTBP Program include a large bridge database accompanied by a collection of data-driven, decisionmaking tools based on predictive models (FHWA n.d.a.).

A key product of the LTBP Program, the InfoBridge (FHWA n.d.a.), serves as a central repository for all field data collected through the LTBP Program and contains additional bridge performance-related data mined from existing sources, such as the NBI, national weather data, traffic data, and other data sources. InfoBridge is also equipped with the “condition forecast” module to predict the future behavior of different bridge components using a variety of deterioration models, including base model (as a deterministic model), survival (as probabilistic model), and ML (as an AI/ML model). The models from this module have been primarily derived from bridge samples with similar characteristics to the deck specimen at the BEAST facility.

DETERIORATION MODELING IMPLEMENTATION

In developing data-driven deterioration models, a need exists for historical data collected over an extended period. However, little or no information is available in the literature to address data collection from a bridge specimen subjected to accelerated aging. As such, this research project sought to study how data collected during accelerated aging can be incorporated into existing modeling methodologies, and how these data function in the context of a deterioration model built specifically for the tested deck specimen. Historical data (NBI component-level CR and CS) associated with similar deck types from sources such as FHWA's InfoBridge (FHWA n.d.a.) were used to validate the deterioration model being developed for the deck specimen.

In doing so, the researchers assessed four deterioration models and compared them against the data from the accelerated testing specimen. Three of the models defined the performance of the deck in terms of NBI deck CR based on a 0–9 scale. The fourth deterioration model established the performance of the deck on the basis of element-level CS using a continuous scale (0–100 percent) for four CSs. Each modeling type is thoroughly discussed in the following subsections.

Deterministic—Base Model

The base models in InfoBridge (FHWA n.d.a.) are deterministic statistical models that are easy to understand and implement. With base models, the research team computed historical time durations for each bridge component (i.e., deck, superstructure, and substructure) of each bridge group from the training subsets of the NBI data. These historical time durations were applied to bridges of the same type to forecast their CRs for the deck, superstructure, and substructure. Base models have been developed for bridges with CIP decks and three types of superstructures: steel girder, prestressed concrete girder, and concrete slab. Since the deck specimen subjected to accelerated testing is a multigirder steel composite with CIP concrete deck, the base model associated with similar girder and deck type was extracted from InfoBridge. No other features, such as climatic zones, traffic volume, or route classification, were incorporated during the original model development. The base model in the InfoBridge was trained based on 11,892 bridges that met the following criteria:

- At least 30 yr of NBI data.
- No increase in deck CR.
- No historical data discontinuity (e.g., inspection data missing from the historical record).

In the context of bridge asset management, "time-in-condition" refers to the duration that a specific bridge component has spent in a particular CR. The time-in-condition statistics computed on the basis of 11,892 bridges were used to create bridge component lifecycle predictions for bridge components. Statistics, including lower bound, upper bound, mean, and median of the time-in-condition, are calculated based on the 25th, 50th, and the 75th percentiles of the dataset for each CR. Once computed, the time-in-condition for all ratings (3 through 9) were combined to create the primary base model for a representative bridge rated at 9. The lifecycle prediction stopped at CR3. The researchers assumed that reaching CR3 would trigger rehabilitation or replacement projects, and, consequently, forecasting beyond that level would be futile. Figure 81 plots the base model for an Iowa bridge with similar characteristics to the deck specimen subjected to accelerated testing at the BEAST facility.

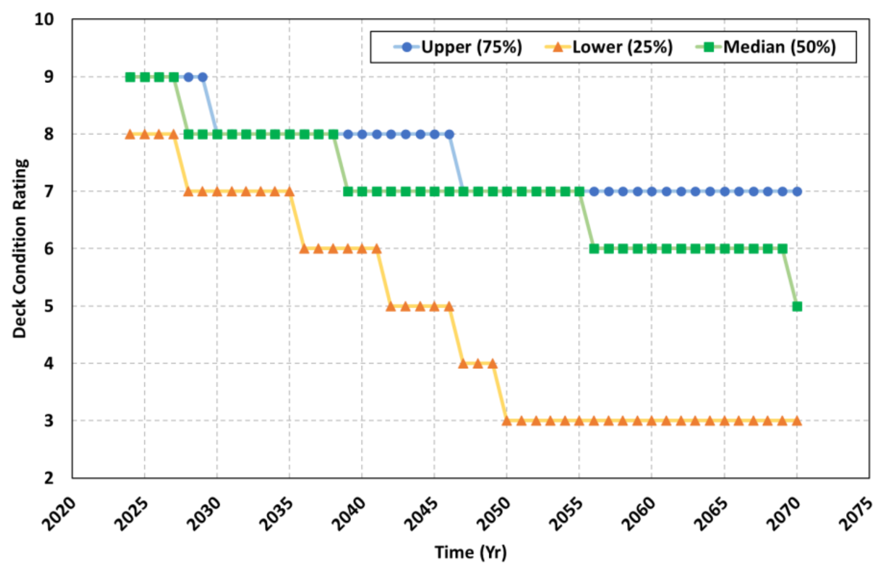

Source: FHWA.

Figure 81. Graph. Sample base model developed for a representative bridge in Iowa with structural similarity to the deck specimen subjected to accelerated testing.

Probabilistic—Survival Model

The probabilistic models in InfoBridge (FHWA n.d.a.) are established based on a survival-based model to forecast the performance of a given bridge according to the overall network performance. These models rely on a probabilistic methodology combining survival analysis and Markov chain theory. They are designed to generate predictions for the condition of bridge components throughout their lifespan and overall forecasts for bridge conditions and performance measures at the network level. Survival analysis can account for incompletely recorded durations when analyzing data based on periods. This feature grants an advantage over alternative statistical methodologies.

The proportional hazards model (PHM) for bridge deterioration relied on survival analysis applied to the continuous durations observed in each CR, as per the NBI inspection records. The foundation of the network performance lies in the PHMs for the deck, superstructure, and substructure components of bridges, as well as culverts. In crafting these component deterioration models, the researchers employed the semiparametric Cox PHM. This model aided in creating multivariable survival functions and determining PHM hazard ratios for each CR. These PHM results were subsequently used to compute structure-specific Markov chain transition probability matrices. These matrices played a pivotal role in formulating lifecycle models for the deterioration of bridge components.

The deterioration of bridge components is a stochastic process that varies widely for several factors, including design attributes, construction quality, highway class, traffic loading, environmental factors, age, and maintenance history. While many of these important factors are generally not captured by available data, such as construction quality, certain attributes could be quantified using available data sources. The probabilistic models in InfoBridge (FHWA n.d.a.) were originally established based on many attributes, including the following:

- Design and material types (primarily for superstructure).
- Deck type.
- Modeling variables (as applicable):
    - Span type.
    - Number of spans.
    - Maximum span length.
    - Age.
    - Skew.
    - Year originally built or reconstructed.
    - Wearing surface type.
    - Deck membrane type.
    - Deck protection system.
    - Functional class.
    - Average daily traffic (ADT).
    - ADTT.
- Environmental conditions:
    - Number of snowfalls.
    - Number of freeze–thaw cycles.

To identify the representative bridge(s) that match the primary characteristics of the deck specimen subjected to accelerated testing, the team performed a query in InfoBridge (FHWA n.d.a.). The query filters were associated with matching the deck specimen's structural characteristics as well as the modeling variables listed in the preceding list. Figure 82 plots the survival model developed for an Iowa bridge with similar characteristics of the deck specimen subjected to accelerated testing. Note that while the base model is restricted to the discrete categorical CR (i.e., whole number) values, the survival model treats CR as a continuum over the range of whole number CRs.

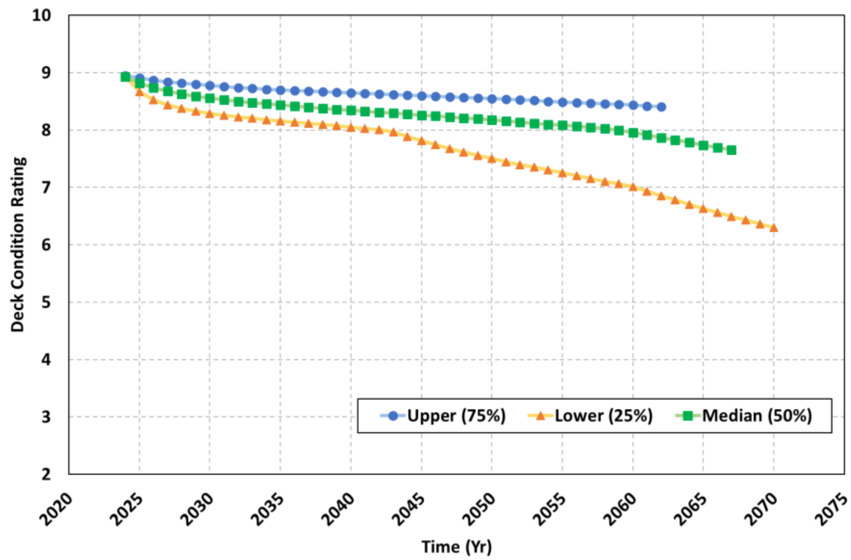

Source: FHWA.

Figure 82. Graph. Sample survival model developed for a representative bridge in Iowa with structural similarity to the deck specimen subjected to accelerated testing.

AI/ML—Deep-Learning Method

AI/ML models are among the strong tools used to develop bridge deterioration models to forecast CRs of bridge components. The ML model in InfoBridge (FHWA n.d.a.) was constructed by combining historical bridge CR ratings from the NBI with climate data. The research methodology used involves a deep-learning-assisted approach to bridge deterioration modeling (Liu and Zhang 2020).

Deep learning is a type of ML technique that enables computational models with multiple layers to grasp intricate and high-dimensional datasets. In the context of condition forecasting, these data representations correspond to the statistical relationships or patterns that elucidate how various factors impact the deterioration of bridge components. The original modeling process took into account 24 different factors, including variables like traffic volumes, construction materials, and climate elements. To identify the representative bridge(s) that match(es) the primary characteristics of the tested deck specimen, the team performed a query in InfoBridge (FHWA n.d.a.). The query filters were associated with matching the deck specimen's structural characteristics as well as many modeling variables, including span type, number of spans, maximum span length, age, skew, year originally built or reconstructed, wearing surface type, deck membrane, and deck protection, among others. Figure 83 plots the survival model developed for an Iowa bridge based on the bridges with similar characteristics of the deck specimen subjected to accelerated testing. Like the base (deterministic) model, outputs are discrete categorical CRs represented at the 25th, 50th, and 75th percentiles.

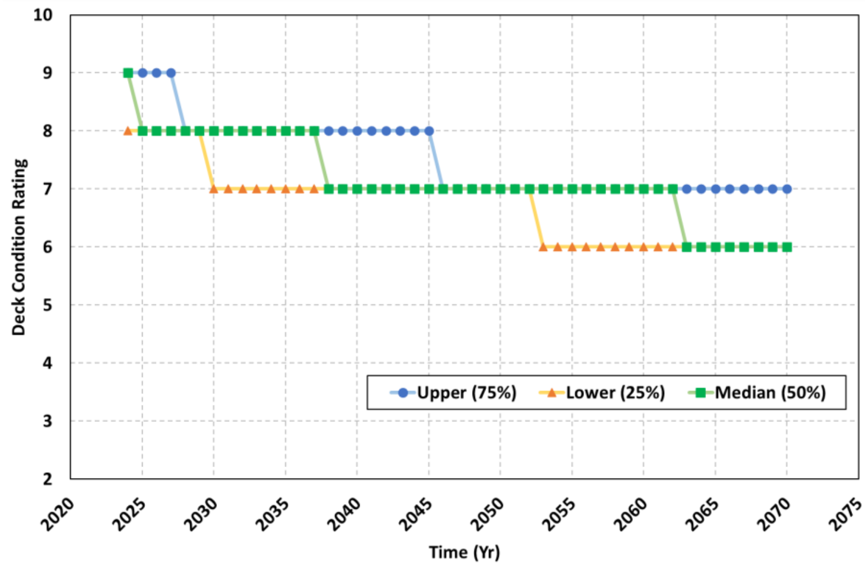

Source: FHWA.

Figure 83. Graph. Sample ML developed for a representative bridge in Iowa with structural similarity to the deck specimen subjected to accelerated testing.

Probabilistic—Element-Level Markov Model

General NBI CRs are assigned to major bridge components, including deck, superstructure, and substructure, as well as culverts. The CRs assigned during inspections use a 0–9 scale based on the severity, extent, and effect of the deterioration on strength or serviceability, with 0 being the lowest or worst condition and 9 the best. These ratings provide a consistent standard for the collection of bridge and culvert data but lack granularity to support refined maintenance, preservation, rehabilitation, and replacement decisionmaking that include economic considerations. To that end, element-level data collection for bridges was introduced nationally and standardized in the 1990s by AASHTO's *Guide for Commonly Recognized (CoRE) Structural Elements* and more recently the MBEI (AASHTO 1997, 2019a). The guide was introduced to support refined condition and needs assessment and asset management modeling, analysis, and decisionmaking. For reference, the AASHTO MBEI defines CS1 as good, CS2 as fair, CS3 as poor, and CS4 as severe (AASHTO 2019a).

Starting in 2014, States that were not collecting element data began collecting it for bridges on the NHS (which comprises roughly 24 percent of highway bridges nationwide) for reporting to the NBI. Although the element-level data became available in 2014 for a fraction of bridges nationwide, the temporal range of data is not yet sufficient for developing purely data-driven deterioration models, in which the performance of a bridge is defined on the basis of element-level CSs (0–100 percent for CS1 through CS4). That said, a few researchers have studied the available data to extract useful enough information to enable development of such models. For instance, Thompson (2021) recently developed an open-source, long-range renewal planning module for transportation structures. Using bridge management data and models, the platform produces a network-level 10-yr spending plan, with forecasts of condition and performance, based on an optimized selection of preservation, rehabilitation, and reconstruction activities. Bridge element-level CSs play a key role in defining the future performance of bridges on this platform. The time-in-state for RC bridge deck was estimated to be 13.5, 14.5, and 22.5 yr for CS1, CS2, and CS3, respectively, using this platform (Thompson 2021).

Using a Markov model to develop deterioration curves, the team used the above-mentioned time-in-state values to calculate transition probabilities between CSs. The deterioration curve was created using predefined Markov-modeling relationships: CS1 can only become a CS1 or CS2, CS2 can only become a CS2 or CS3, and CS3 can only become CS3 or CS4. Figure 84 plots the Markov deterioration model developed for different CSs of a RC deck that was similar to the tested deck specimen.

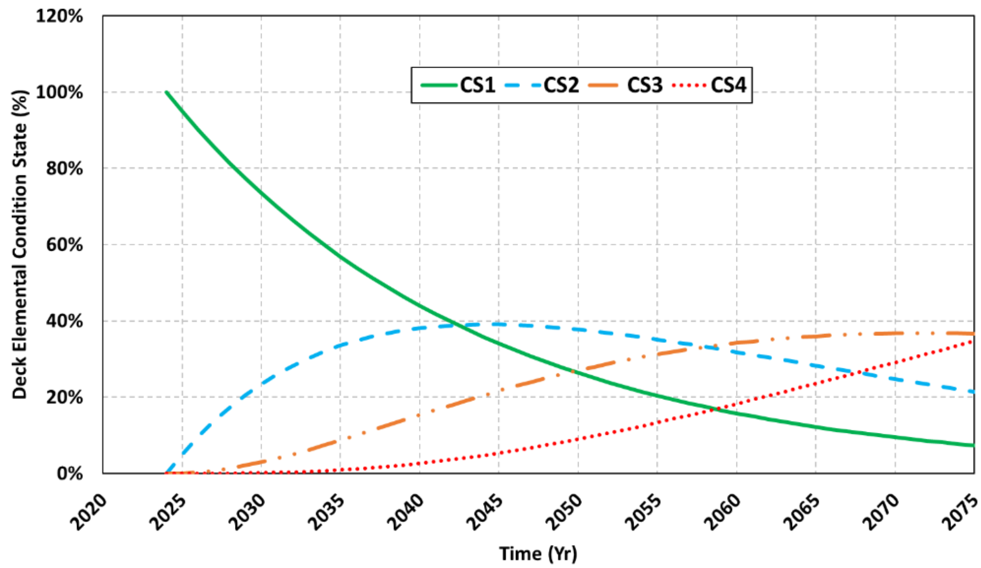

Source: FHWA.

Figure 84. Graph. Sample probabilistic element-level deterioration model developed for a representative bridge in New Jersey with structural similarity to the deck specimen subjected to accelerated testing.

SCALING BEAST PREDICTION MODEL TO AN ACTUAL IN-SERVICE BRIDGE

The BEAST facility uses a two-axle wheel carriage to apply a 50-kip load to the deck specimen under study. The wheel carriage traverses the specimen to simulate vehicle loading on a bridge deck. To relate this accelerated loading regime to typical loading patterns for in-service bridges, the team found it necessary to develop a process for scaling the BEAST data to match in-service bridges. This section discusses the processes undertaken to scale the BEAST data.

A load equivalency factor (LEF) in bridge design is used to quantify the cumulative effect of different types of vehicle loads on a bridge's structural integrity and durability. The LEF is typically used to convert different types of vehicles and their axle loads into an equivalent number of standard load repetitions. This process allows engineers to assess the impact of a mix of vehicles (see figure 122 in appendix E) on a bridge's fatigue life and structural deterioration. For example, a heavy truck with a high axle load has a greater impact on a bridge's fatigue life compared to a passenger car with a much lower axle load. The LEF provides a way to express this difference in terms of equivalent repetitions of a standard load.

A LEF can be used to measure how quickly the tested deck specimen deteriorates compared to regular highway and bridge surfaces under fatigue conditions. LEF represents the damage proportion of a single pass of a truck with any axle configuration to that of a single axle carrying 18,000 lbs of load. The acceleration of deterioration can be determined by comparing a standard traffic and truck mixture to a single pass of the BEAST carriage on the deck. This approach considers both the distribution of truck classes and their configurations, considering axle and load distributions. For conciseness, the details of LEF computation are listed in appendix E.

The LEF for the BEAST carriage is 9.07. Using the LEF calculation presented in appendix E, along with the proportion estimation for each vehicle class, results in a composite LEF of 1.42 for the discussed traffic blend. This value signifies that a solitary traversal of the BEAST carriage imparts approximately 6.4 times the damage of a single pass by an average truck (which is a representative of the traffic blend). One day of BEAST operation, encompassing 13,000 carriage passes, is likened to approximately 83,000 passes of an average truck.

To establish a connection between the level of truck traffic and the resulting damage on in-service bridges, the team analyzed historical truck traffic data for different bridge populations. The researchers examined three levels of bridge populations specifically. The first level focused on bridges in New Jersey, where the BEAST facility is located. At a broader level, bridges were studied within the mid-Atlantic cluster, encompassing six States: New Jersey, Pennsylvania, Delaware, Virginia, West Virginia, and Maryland in the northeast region of the country. Finally, bridges across the entire Nation were grouped to extract truck traffic data. Since the deck specimen width at the BEAST facility is equivalent to that of a two-lane bridge, the team only considered two-lane bridges for analysis at all three population levels. Consequently, distributing the ADTT between different lanes was not needed. In calculating the equivalent single-axle load (ESAL), which is a computational component of the LEF methodology, no growth rate was factored in when scaling the ADTT.

Figure 85 depicts the frequency histogram of ADTT for two-lane bridges in New Jersey. The 50th percentile (median) and 95th percentile values were found to be around 165 and 1,405, respectively. Assuming that a single traversal of the BEAST carriage imparts approximately 6.4 times the damage of a single pass by an average truck, the 2 million cycles of live load at the end of the phase I experiment would roughly equate to 213 and 25 yr of an in-service bridge with ADTT values of 165 and 1,405, respectively. Given that two-lane bridges are likely situated in low truck traffic areas, considering the upper bound of the 95th percentile for scaling the timing between BEAST and an actual in-service bridge seems reasonable. Table 18 provides the conversion between BEAST live-load volume and ADTT values calculated based on different populations of bridges. A review of the 95th percentile values underscores the significant ability of the BEAST facility to accelerate load-induced deterioration relative to actual traffic mixtures, ranging from low to high traffic conditions.

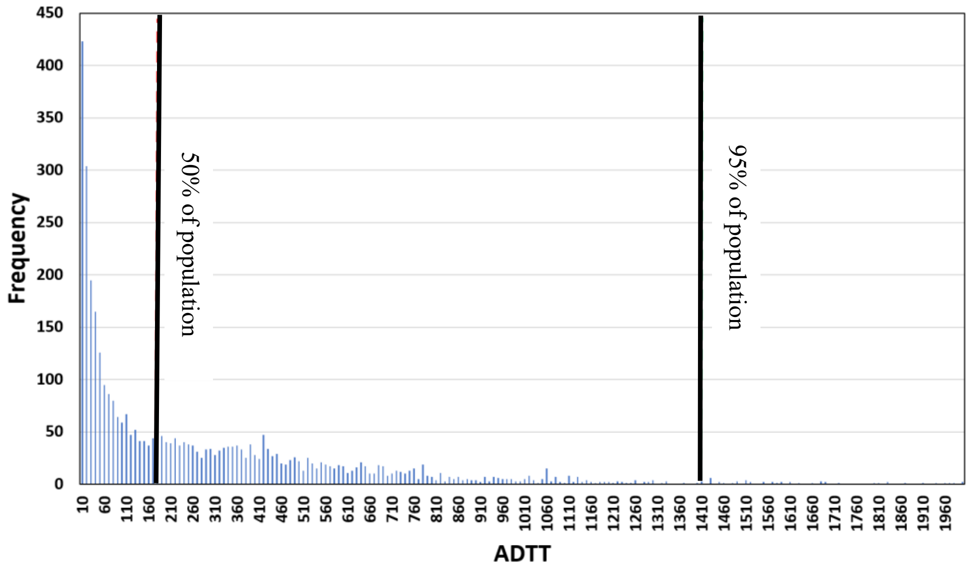

Source: FHWA.

Figure 85. Graph. Frequency histogram of ADT for two-lane bridges in New Jersey.

Table 18. Summary of truck traffic conversion between accelerated testing and an in-service bridge.

Traffic	New Jersey	Mid-Atlantic	United States
95-percent ADTT	1,405	2,865	2,310
Time in service (2 million cycles) (yr)	25	12	15

Alternatively, the estimated number of in-service years for an actual bridge, in terms of a single day of BEAST operation with 13,000 carriage passes, is summarized as follows. The 2 million cycles for the entire duration of the phase I experiment results in nearly 151 d of BEAST operation. Therefore, 1 d of BEAST operation is equivalent to 60, 30, and 36 d of an in-service bridge located in New Jersey, the mid-Atlantic, or nationwide, respectively (assuming two-lane bridges at the 95th percentile).

In addition to evaluating the live-load effects, one of the objectives of the accelerated testing was to comprehend the long-term performance of bare RC bridge decks under realistic environmental conditions. Two environmental loadings were applied, as follows:

- Temperature fluctuations were applied to simulate both freeze–thaw and hot–dry cycles on the bridge specimen. The research team anticipated that the tests would impose a minimum of 280 freeze-thaw cycles (0 °F to 50 °F) over a 9-mo duration. However, factors during the testing caused these targets to be adjusted downward to only 85 freeze-thaw cycles.
- The application of 6-percent brine solution to the bridge specimen aimed to simulate common winter maintenance practices. A brine solution containing up to 18-percent salt (NaCl) could be deployed during any phase of the accelerated testing.

Figure 86 and figure 87 illustrate the frequency histogram of annual freeze–thaw and snowfall cycles, respectively, for bridges in New Jersey. The snowfall cycle serves as an indirect indicator of deicing applications on an actual bridge. The figures indicate the 50th and 95th percentiles for both plots.

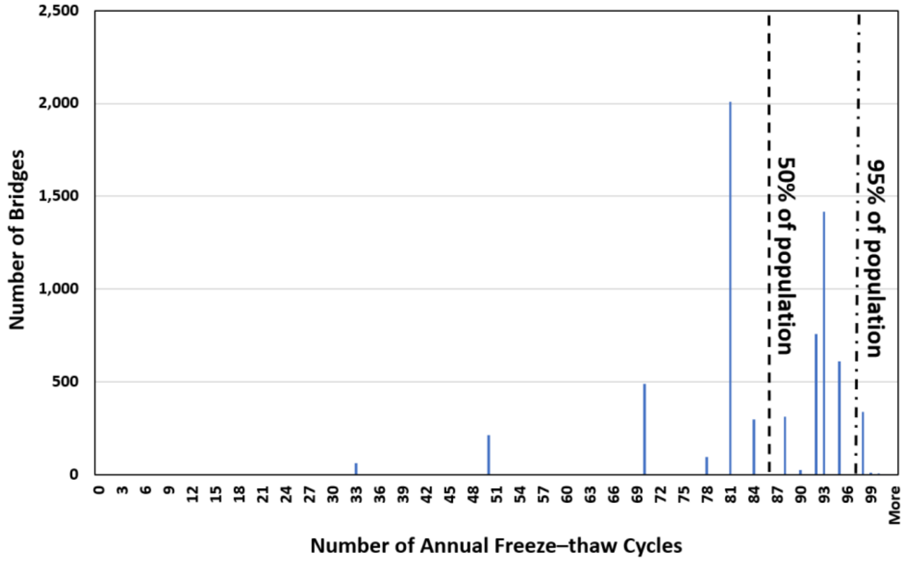

Source: FHWA.

Figure 86. Graph. Frequency histogram of annual freeze–thaw cycles in New Jersey.

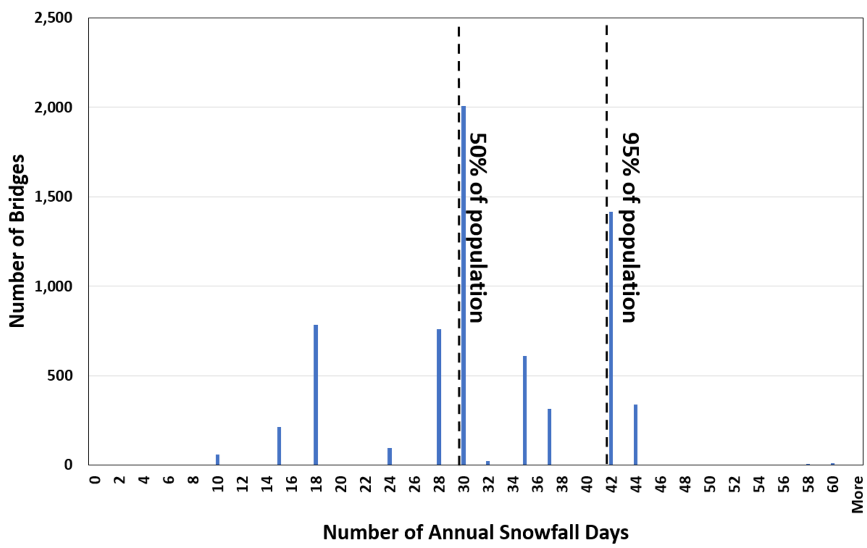

Source: FHWA.

Figure 87. Graph. Frequency histogram of annual snowfall days in New Jersey.

Table 19 summarizes the three levels of bridge populations that were specifically examined to determine the median (50-percent) and 95-percent freeze–thaw cycles. Given the small number of the freeze–thaw cycles, which was equivalent to only a few months or up to a few years of service based on different geographical regions nationwide, no scaling between the experimental timing and an in-service bridge could be established for the phase I testing period.

Table 19. Summary of freeze-thaw cycle conversion between accelerated testing and an in-service bridge.

Freeze–Thaw Cycles	New Jersey	Mid-Atlantic*	North-West*	Gulf*
Annual number	107	50	21	15
At BEAST scale**	10 mo	20 mo	4 yr	6 yr

*Regions were adapted from LTBP-defined regions (mid-Atlantic: Pennsylvania, New Jersey, Delaware, Maryland, Virginia, West Virginia; North-West: Oregon, Washington; Gulf: Alabama, Florida, Georgia, Louisiana, Mississippi, New Mexico, Texas) (FHWA n.d.d.).
**Calculated based on 85 cycles/yr.

Moreover, the team noted that some surface scaling on the deck specimen may be attributed to deicer scaling caused by freezing and thawing of the concrete surface following exposure to the brine solution. Scaling is a progressive form of concrete deterioration that can occur when saturated concrete surfaces undergo freezing and thawing cycles, with greater severity in the presence of deicing salts. Although deicer scaling is not typically a deterioration mechanism for bridge decks, the team observed ponding on the surface of the deck specimen, which could facilitate deterioration through subsequent freezing and thawing cycles. Taking measures to reduce the potential for ponding on the top surface of the deck specimens could make the freezing and thawing exposures more representative of existing bridge deck structures.

Furthermore, the freeze–thaw cycling was generally not accelerated. Introducing more frequent freeze–thaw cycling as part of the exposure protocol could help accelerate deterioration mechanisms. For instance, an analogous approach to the ASTM International (1997) C666 test, where concrete specimens are cycled between 0 and 40 °F several times per day, could be adopted in the accelerated testing protocol. However, correlations would need to be established between the simulated exposure and field conditions.

DEVELOPMENT OF DETERIORATION MODELS FOR ACCELERATED TESTING

In developing deterioration model(s) for the deck specimen subject to accelerated testing, the researchers conducted a comprehensive search using the InfoBridge platform (FHWA n.d.a.) to identify bridges with characteristics closely resembling the accelerated test specimen in terms of configuration, materials, and external loading attributes. The team ultimately selected six bridges with the highest similarity to the deck specimen for assessing the proposed deterioration models. A representative deterioration model was developed for the six in-service test bridges. The representative deterioration models were developed for the selected bridges, which share the same (or similar) deck type, deck protection (black versus epoxy-coated reinforcement) type, length, width, number of lanes and span, superstructure type, traffic, and environmental loading.

Figure 88 through figure 90 plot the representative deterioration curves for the deck specimen subject to accelerated testing (in terms of deck component-level CR) using deterministic, probabilistic (survival), and ML approaches, respectively. Each figure includes three curves, including the lower bound, upper bound, and median of the time-in-condition based on the 25th, 50th, and 75th percentiles of the dataset for each CR. Similarly, figure 91 plots the representative deterioration curves for the deck specimen subject to accelerated testing (in terms of deck element-level CS) using the survival modeling approach. In these deterioration curves, the vertical and horizontal axes demonstrate the deck's performance in terms of NBI deck CR and

CS and in-service years, respectively. The horizontal axis in these plots follows the expected real-life (i.e., not accelerated) years of operation of a typical highway bridge under real environmental and traffic conditions.

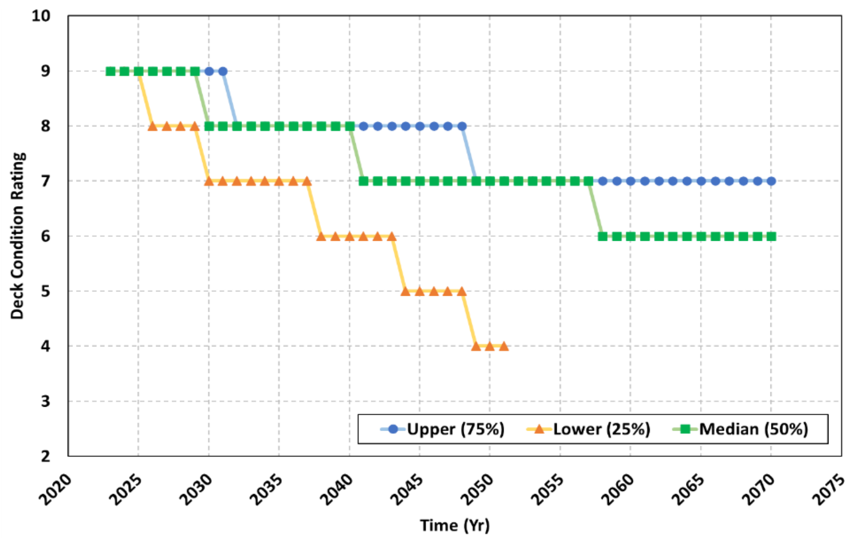

Source: FHWA.

Figure 88. Graph. Representative basic model developed for the deck specimen subject to accelerated testing.

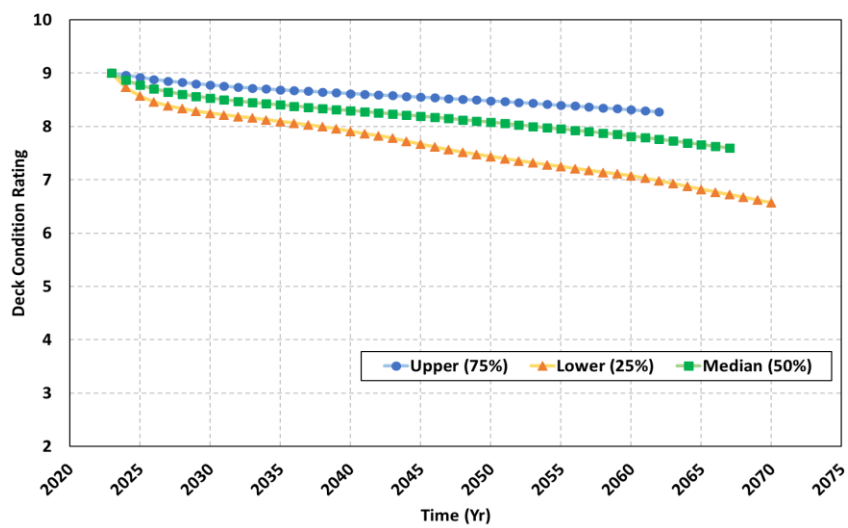

Source: FHWA.

Figure 89. Graph. Representative survival model developed for the deck specimen subject to accelerated testing.

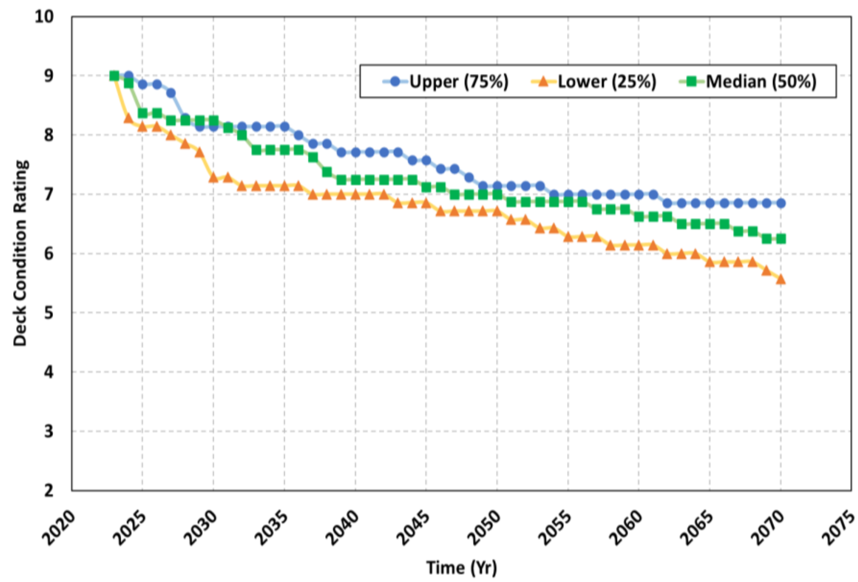

Source: FHWA.

Figure 90. Graph. Representative deep-learning model developed for the deck specimen subject to accelerated testing.

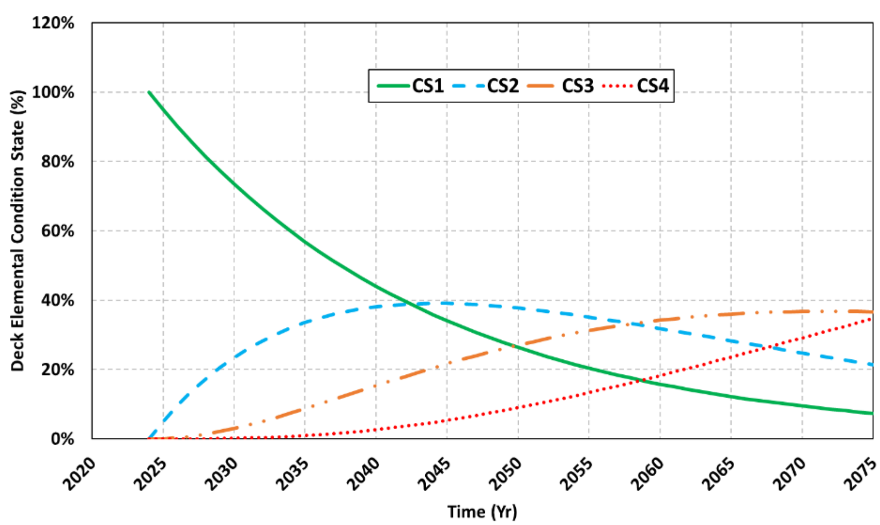

Source: FHWA.

Figure 91. Graph. Representative survival model developed for the deck specimen subject to accelerated testing (deck element-level CS).

As discussed in chapter 2, the time scale for the accelerated testing is compressed and does not follow the normal in-service operational life of a typical highway bridge. The team addressed this issue by using the ADTT data as a scaling factor to expand the compressed timing of accelerated testing and align it with the operational life of an in-service typical highway bridge. Figure 92 through figure 94 show plots of the deterioration curves for the deck specimen subject to accelerated testing using the converted in-service years listed in table 18 on the horizontal axis. For example, in scaling the BEAST timing to similar New Jersey bridges, the team determined that it would take 25 yr for a representative bridge on a typical roadway in New

Jersey to experience the 2 million cycles of truck traffic that was imposed on the BEAST specimen.

During the commissioning of the accelerated testing, 14 datasets of VI and NDE data were collected periodically. The inspection data, indicated by black plus symbols, were the averages of four inspection assignments conducted by four experienced bridge inspectors who reviewed HD photos of the deck specimen. The deck's initial condition was not assumed to be CR9 by all inspectors, but the fitted black solid line in the graphs was set to start at CR9. The first two datasets were ignored in this analysis as they were collected when the deck specimen was still in curing mode and no live load was yet imposed on the specimen. The timing of data collection was determined using the live-load cycles at each period. Figure 92 incorporates a secondary vertical axis depicting the ADTT volume. The live loads applied to the accelerated deck specimen were selected to match the life expectancy of a representative bridge in New Jersey. The vertical dashed lines indicate the 14 data collection occasions conducted throughout the accelerated testing period. The subsequent plots omit the vertical dashed lines and secondary vertical axis for conciseness and visual clarity. Additionally, black plus symbols in the plots represent VI data collected at various intervals during the testing of the deck specimen. A solid black line is fitted to the VI data to compare the behavior of the deck specimen subject to accelerated testing with deterioration curves derived from similar bridges exposed to similar environmental conditions.

In figure 92 through figure 94, considering the lower performance of the deck specimen subject to accelerated testing, deterioration curves associated with the 25th percentile of the datasets were included. Among the different deterioration curves calculated using deterministic, survival, and deep-learning methods, the deck specimen's performance fell below the lower bounds (25th percentile of the datasets) for all three curves, closely aligning with the deterministic model developed based on New Jersey data.

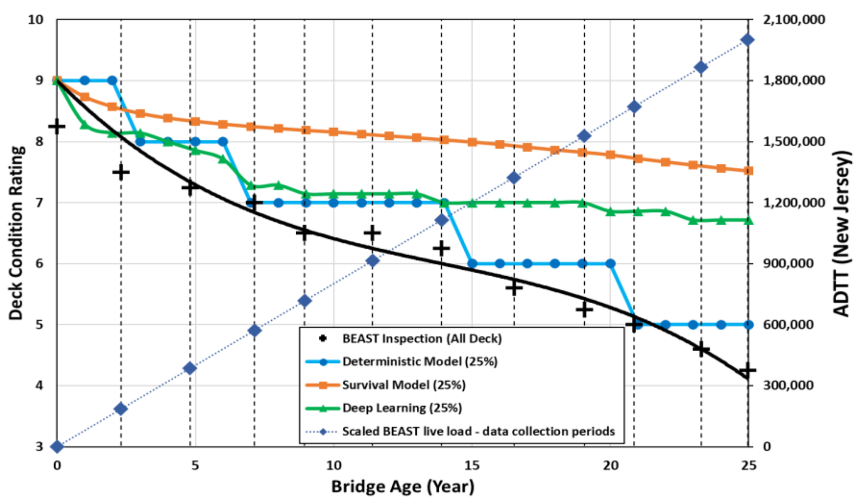

Source: FHWA.

Figure 92. Graph. Deck specimen (subject to accelerated testing) versus representative models (lower bound) using New Jersey truck traffic data as scaling factor for time.

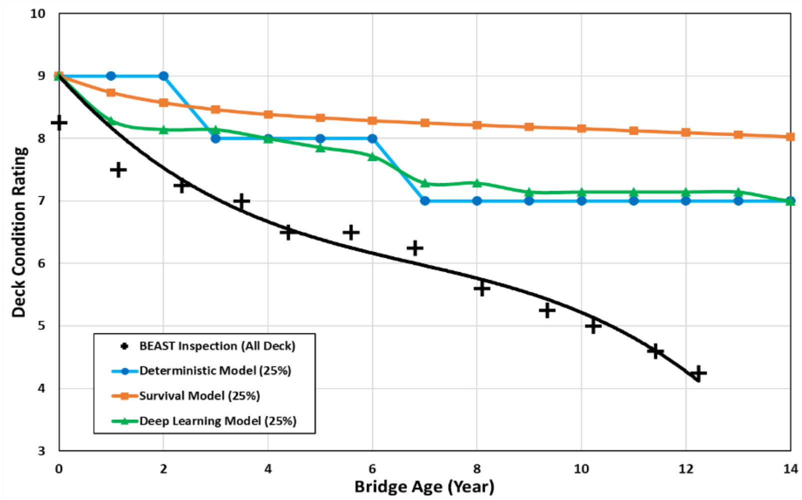

Source: FHWA.

Figure 93. Graph. Deck specimen (subject to accelerated testing) versus representative models (lower bound) using mid-Atlantic truck traffic data as scaling factor for time.

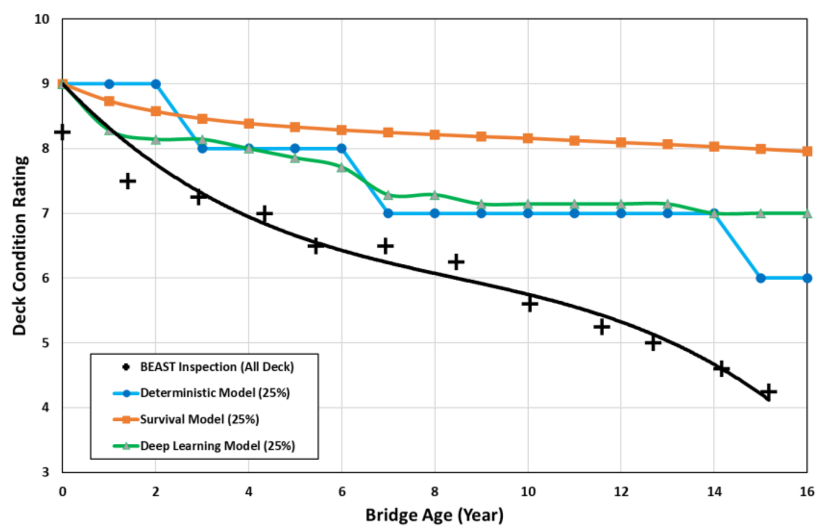

Source: FHWA.

Figure 94. Graph. Deck specimen (subject to accelerated testing) versus representative models (lower bound) using nationwide truck traffic data as scaling factor for time.

To accurately estimate the current and future performance of a concrete deck, determining the thickness of the concrete cover over the reinforcement is essential. GPR can provide accurate measurements of the actual concrete cover. Rutgers performed GPR surveys of the deck specimen to obtain measurements of the concrete cover before the start of the accelerated exposure protocol. During this evaluation, the researchers observed that the formwork had shifted during concrete placement, resulting in shallower cover in the middle 40 ft of the slab and deeper cover in the outer 5 ft on each end (figure 67), referred to as the “middle 40 ft” and the “outer 5 ft.” Two populations were assumed to be represented by lognormal distributions centered around 1.34 inches and 1.76 inches, respectively, with standard deviations of 0.08 and 0.25 inch, respectively. Recognizing the significant difference between cover depths, figure 95 and figure 96 distinctly illustrate the performance of the middle and outer edges of the deck, respectively. In this case, the inspectors were instructed to assign ratings separately for the middle and outer edges of the deck. In creating these figures, the research team used the deterioration curves for the deck specimen subject to accelerated testing using the converted in-service years for New Jersey (depicted in figure 92).

For the middle 40 ft with low cover depth, the deterministic model closely aligns with the inspection curve developed based on the 25th percentile of the data, using New Jersey's ADTT as the scaling conversion factor. However, the probabilistic and AI/ML models exhibited overperformance in representing the deck specimen (subject to accelerated testing) performance compared to VI results. In the case of outer edges with normal cover depth, both the 25th and 50th percentile curves were plotted. Here, the deck specimen's performance fell between the 25th and 50th percentile models, with the closest proximity to the deterministic model developed based on the 25th percentile dataset.

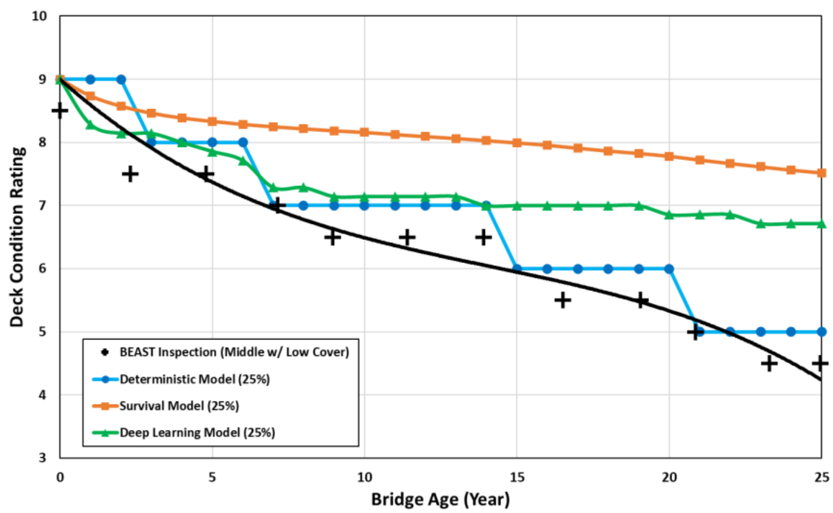

Source: FHWA.

Figure 95. Graph. Deck specimen (subject to accelerated testing) versus representative models (lower bound) using New Jersey truck traffic data as scaling factor for time—middle 40 ft of the slab is considered.

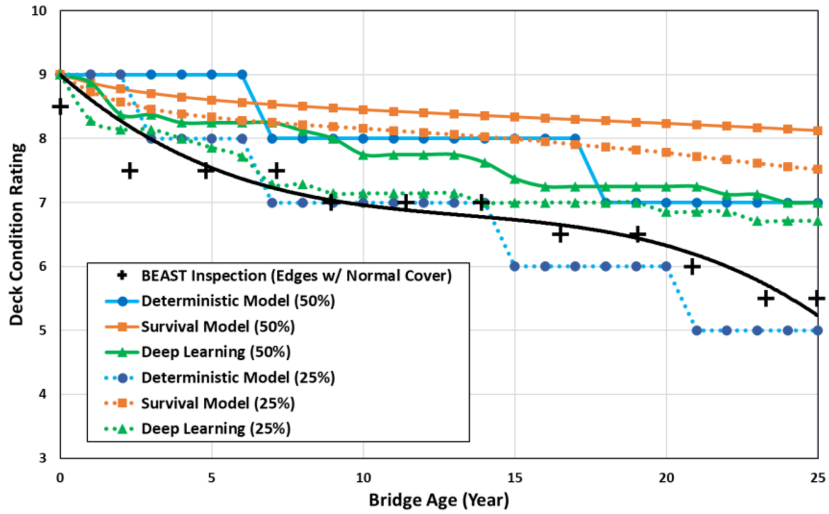

Source: FHWA.

Figure 96. Graph. Deck specimen (subject to accelerated testing) versus representative models (lower bound and median) using New Jersey truck traffic data as scaling factor for time—outer 5 ft (from each of left and right edges) of the slab is considered.

Similar to the deterioration curves developed based on deck CR (NBI item 58 (FHWA 2022)), Markovian element-level CS deterioration models have been formulated and illustrated in figure 97 through figure 99. These figures use the truck traffic level in New Jersey, the mid-Atlantic region, and the Nation as the conversion factor between the accelerated test timing and a representative in-service bridge, respectively.

In each figure, four curves (represented by solid lines) associated with CS1 through CS4 for element-level inspections of the accelerated bridge specimen were assigned, using live-load traffic as the conversion factor to scale the time axis. Additionally, four curves (represented by dashed lines) were developed using a Markov model, applying the time-in-state values reported by Struplan (Thompson 2021) to calculate transition probabilities between CSs. Across all three conversion scales, the deck specimen's performance consistently surpassed the Markovian model, previously developed based on extended time-in-state values.

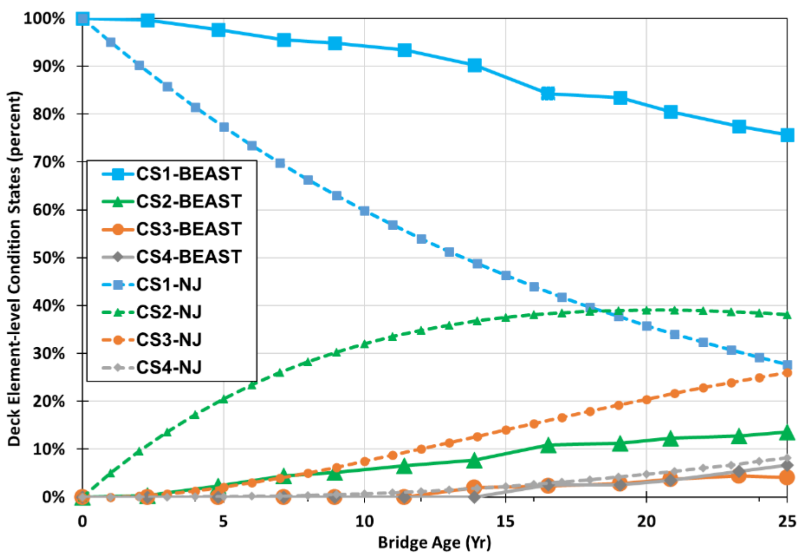

Source: FHWA.

Figure 97. Graph. Element-level presentation of deck specimen (subject to accelerated testing) versus representative models using New Jersey truck traffic data as scaling factor for time.

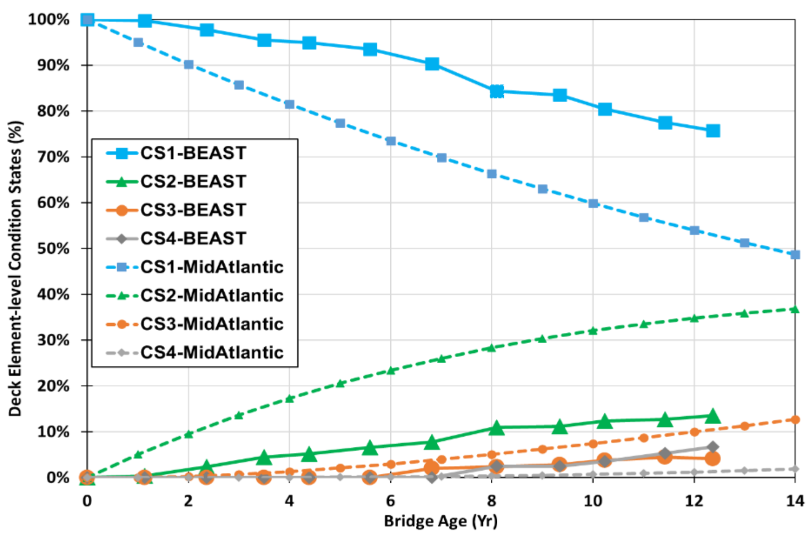

Source: FHWA.

Figure 98. Graph. Element-level presentation of deck specimen (subject to accelerated testing) versus representative models using mid-Atlantic truck traffic data as scaling factor for time.

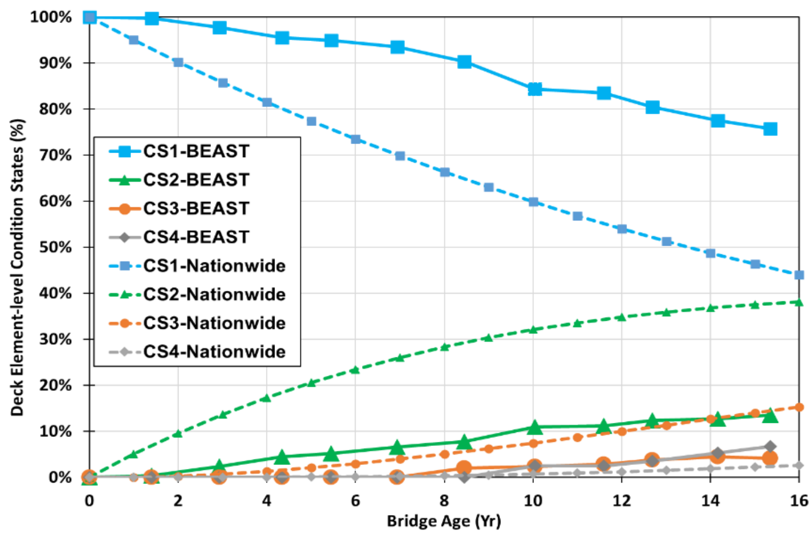

Source: FHWA.

Figure 99. Graph. Element-level presentation of deck specimen (subject to accelerated testing) versus representative models using nationwide truck traffic data as scaling factor for time.

NDE INTEGRATION

For bridge owners, the ability to predict the future conditions of the bridge deck is key for effective maintenance and rehabilitation decisionmaking. For this reason, objectively assessing the condition of bridge decks is important. Therefore, developing approaches capable of quantifying the condition of the bridge deck in terms of condition maps and indexes is vital. One goal of this research study was to process the NDE data in tandem with the CRs such that the findings offer additional input on the change rate in the condition and demonstrate how condition maps from NDE data can be used to develop more realistic bridge deterioration models. One way to implement such a system could be the development of an equivalency factor that allows VI findings to be refined through the application of various NDE methods, where weighting factors are applied to each method based on its ability to give greater or lesser confidence to the current visual method of determining CRs.

The researchers adapted the condition index methodology proposed by Gucunski et al. (2016) to analyze the NDE data collected from the accelerated testing experimentation. Both PNDE and DNDE technologies were applied to the deck specimen subject to accelerated testing. The PNDE technologies included ER, HCP, and GPR, while the DNDE technologies included IE and USW. The NDE Condition Index subsection in chapter 2 summarizes the methodology taken to determine condition indexes proposed by Gucunski et al. (2016).

The methodology was applied to the collected NDE data based on the ranges provided in table 4 in chapter 2. As shown in the table, NDE results were assigned qualitive categories of low/good through high/serious. For PNDE technologies, low indicates a low potential for deterioration and high indicates elevated potential for deterioration at a particular location or area. For example, HCP measurements showing potential less than −350 mV indicate a high potential for deterioration. For DNDE technologies, good indicates DNDE results did not detect damage and the material is intact, and serious indicates DNDE results show damage at a particular location or area. For example, an IE measurement of 1 indicates intact material, and 4 indicates a subsurface delamination is detected in that measurement. These data were input to the weighted sum equations proposed by Gucunski et al. (2016) and shown in table 4 in chapter 2.

The results are shown in figure 100. One advantage of calculating a condition index is that it provides a weighted average of NDE measurements across the entire deck area and computes a single representative index number for the deck. This situation is analogous to an NBI component CR that assesses the overall deck condition using a single value on a scale of 0 through 9. This measurement facilitates comparison between the NDE results and the component CR, with some limitations as discussed in the following paragraphs.

In mapping a single representative value for NDE, understanding that the application of a weighted average in the condition index calculation would not be justifiable if one small area had a severe defect while the rest of the deck was in a sound condition is important. For instance, for a given deck with a small area of spalling but otherwise in nearly new condition, a rating greater than 7 (described as having some minor problems present) will not typically be assigned. However, the same deck would receive a score of 99 percent for the IE condition index. Keeping this limitation in mind, the researchers explore the applicability of the NDE condition index and its potential correlation with bridge performance in the following paragraphs.

Based on the findings of the condition index approach, no significant correlation between the methods is evident. The GPR amplitude indicates an index of 100 percent, while the ER indicates an index of 0 percent; thus, these methods show little sensitivity to changes in the condition index within the framework of this experiment and the NDE data collected. Based on the ranges defined by their corresponding equations, the results in figure 100 show that condition indexes for ER and GPR amplitude did not change. In fact, the ER measurements from the accelerated testing were always less than 40 kΩ·cm, resulting in a condition index equal to 0. In the case of GPR amplitude, the opposite was observed, and all the measured GPR signal attenuations were greater than −15 dB (defined by Gucunski et al. 2016), resulting in a condition index equal to 100. The trends of the DNDE results were generally similar to each other except during the early stages of the specimen testing. The remaining PNDE technology, HCP, showed an initial drop early in the service life of the deck specimen, followed by an increase to a trend roughly similar to that of the DNDE technologies. Assuming the condition decreases with time, then some weak correlation between condition index and NDE measurements is present.

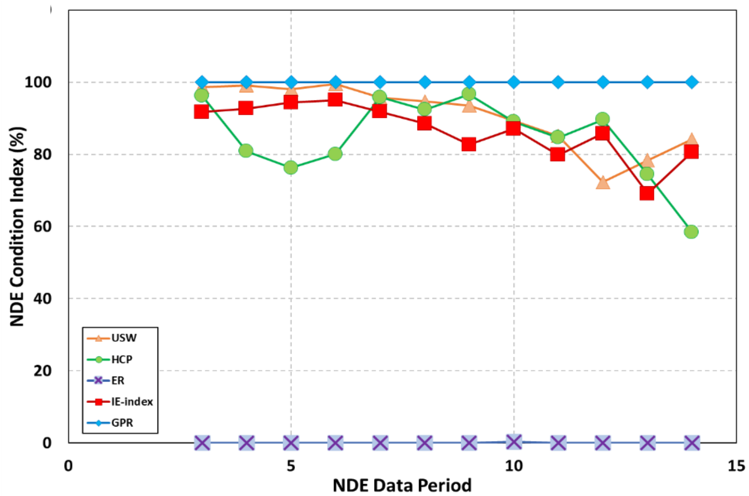

Source: FHWA.

Figure 100. Graph. NDE condition index for IE, HCP, ER, USW, and GPR amplitude.

Considering the above-mentioned observation along with the indepth reliability assessment of NDE results (performed in chapter 2), HCP, IE, and USW showed the highest consistency among the PNDE and DNDE technologies. Therefore, IE, USW, and HCP techniques were selected for further assessment.

To conduct a comprehensive analysis and comparison between the NDE results and CR and deterioration models, figure 101 through figure 103 were generated to illustrate the computed condition indexes for IE, USW, and HCP techniques, respectively, compared with a representative in-service deck. In figure 101, the left ordinate shows the CR based on VI using the converted in-service years for New Jersey and the results from the deterministic, deep-learning, and survival models. The deterioration curves associated with deep learning and survival were eliminated from figure 102 and figure 103 for visual clarity. Each figure incorporates a secondary ordinate (on the right side) that shows the condition indexes for IE, USW, and HCP.

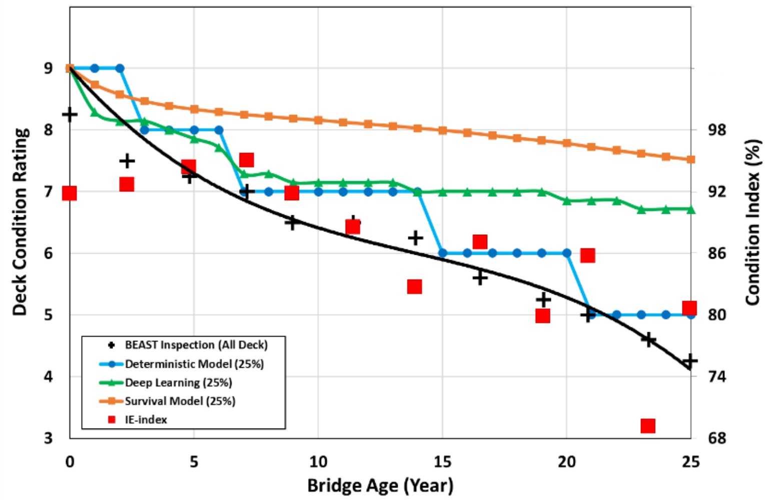

Source: FHWA.

Figure 101. Graph. Deck CR and IE condition index compared to a representative in-service bridge age.

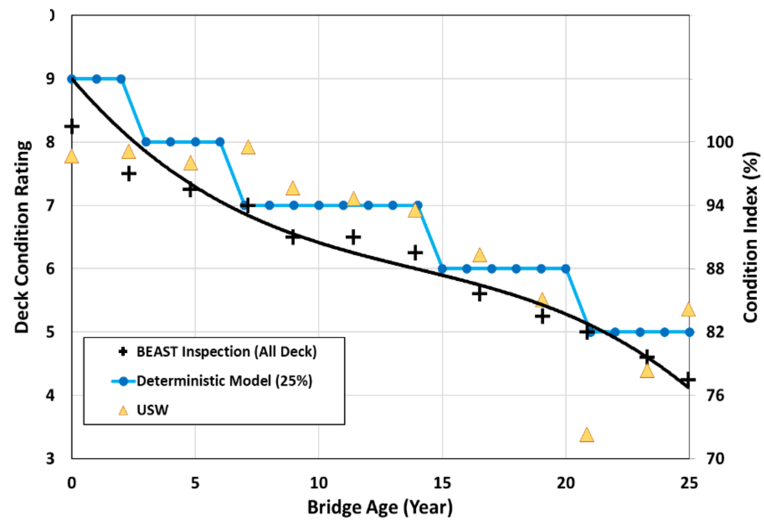

Source: FHWA.

Figure 102. Graph. Deck CR and USW condition index compared to a representative in-service bridge age.

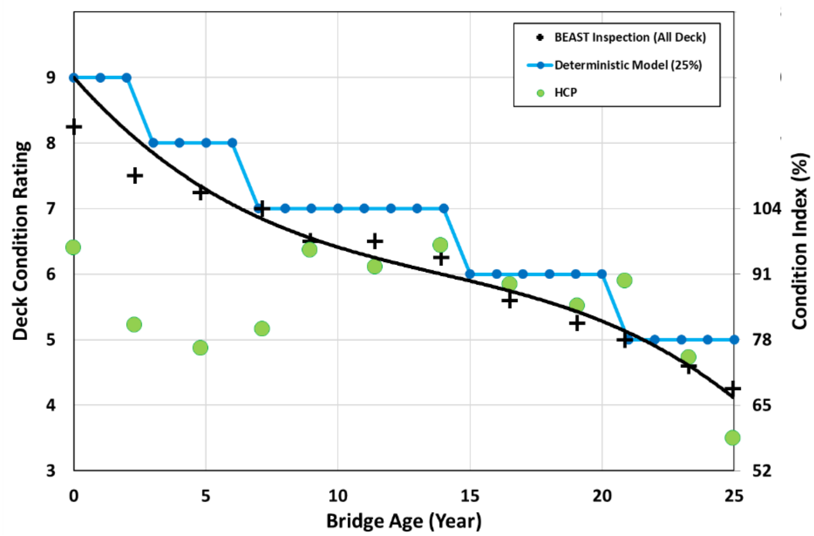

Source: FHWA.

Figure 103. Graph. Deck CR and HCP condition index compared to a representative in-service bridge age.

In the creation of these figures, the researchers gave careful consideration to aligning the scales of the secondary ordinate with the CR and deterioration curves, depicted by the primary vertical axis on the left. The ordinate has different ranges in each figure so as to present the NDE index values in close proximity to the CR data. In fact, the absolute values of the indexes vary significantly from one to another. This adjustment enabled the qualitative establishment of baselines, facilitating the conversion of NDE data to deck performance and vice versa.

Ideally, a condition index of 100 percent should perfectly correspond to a deck CR of 9. However, using this subjective axis scaling did not result in a linear correlation between the CR and the condition index. This discrepancy is expected due to the inherent differences between these two indicators. The primary focus here was to establish the minimum baseline thresholds between the two. To achieve this, the right ordinate was adjusted to accomplish two objectives: to align the overall shape of the deck deterioration models (developed based on the left ordinate, which is shown by solid black lines in figure 101 through figure 106), and to ensure the minimum thresholds of both indicators match. In most cases, however, this approach resulted in a mismatch at the upper end of the scales, where the CR of 9 and the condition index of 100 percent do not align perfectly.

For example, the figures clearly illustrate that for IE condition indexes of 90 and greater, the deck specimen subject to accelerated testing consistently receives ratings of 7 and higher. Conversely, when the IE condition index drops to 80 percent, the corresponding CR for the test specimen decreases to 5. A parallel correlation can be observed for USW condition indexes of 90 and greater, where the deck specimen consistently achieves ratings of 7 and greater. However, with a reduction in the USW condition index to 80 percent, the CR experiences a decline of two points, settling at 5.

In the case of HCP, the initial four data collections yielded abnormal readings, likely influenced by curing and surface moisture associated with the original construction. Specifically, the section of the deck above the stay-in-place formwork introduced higher electrical connection to the reinforcement, leading to significantly negative potential (voltage) readings. Excluding these initial four HCP readings, figure 103 clearly illustrates that the HCP condition indexes never exceeded values of 96 percent. Even when it reached 96 percent, the deck was already rated somewhere between 6 and 7. The comparison from this set of available data suggests that HCP is not effective in differentiating among ratings 7 or above (they all represent "good," or readings ≥ –200-mV CSE). Ratings between 5 and 6 correlated with HCP condition indexes in the range of 75–90 percent and further decreased to CR 4 when the HCP condition index fell below 75 percent.

In a manner analogous to the NDE condition index, figure 104 through figure 106 illustrate the computed defect indexes for IE, USW, and HCP techniques. A defect map, as defined herein, categorizes the deck into two primary states (indexes): healthy and defective areas. Figure 107 showcases a sample defect map developed for HCP, where the bridge defect ratio represents the percentage of defective regions relative to the entire bridge area. Unlike the condition index, which defines the qualitative categories for NDE results, the defect index has only two categories of defective or sound. The defect index takes into account areas deemed defective by IE, USW, or HCP techniques and divides that area by the total area of the deck. For HCP, defective areas are regions with active corrosion (HCP less than −350 mV, range defined by ASTM International (2015) C876), and for IE, defective areas are regions with progressed (poor condition) or deep shallow delamination (severe condition).

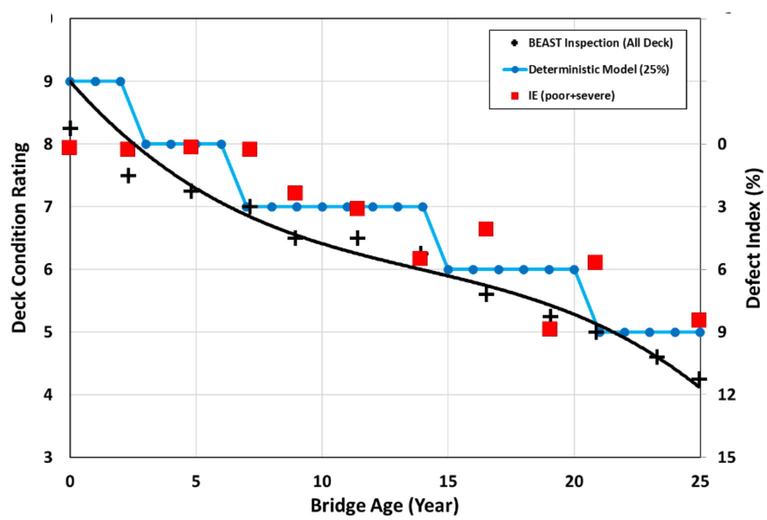

Source: FHWA.

Figure 104. Graph. Deck CR and IE defect index compared to a representative in-service bridge age.

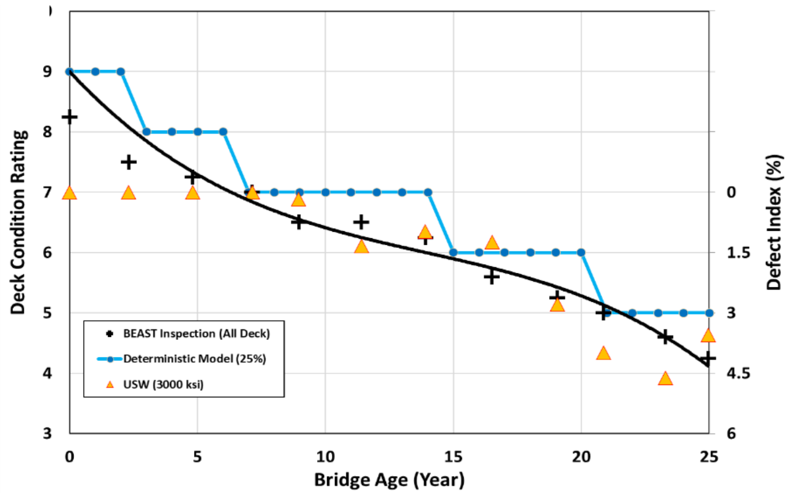

Source: FHWA.

Figure 105. Graph. Deck CR and USW defect index compared to a representative in-service bridge age.

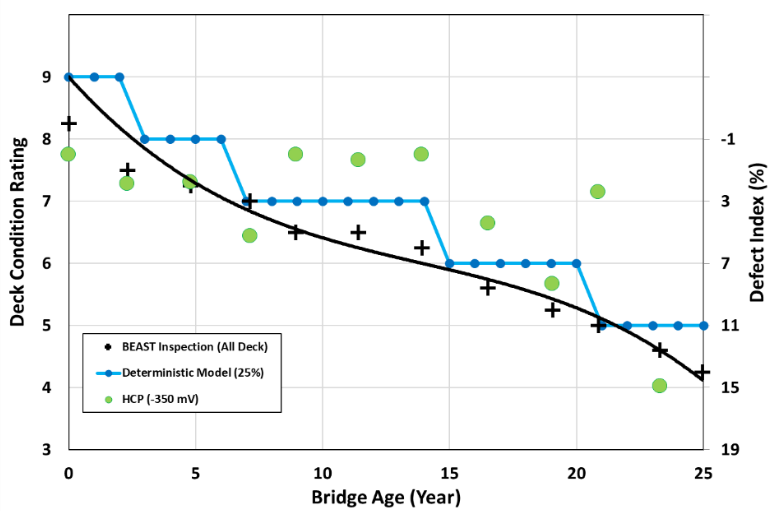

Source: FHWA.

Figure 106. Graph. Deck CR and HCP defect index compared to a representative in-service bridge age.

Source: FHWA.
Note: Black and gray represent the unhealthy and healthy sections of deck, respectively.

A. Defect heat map.

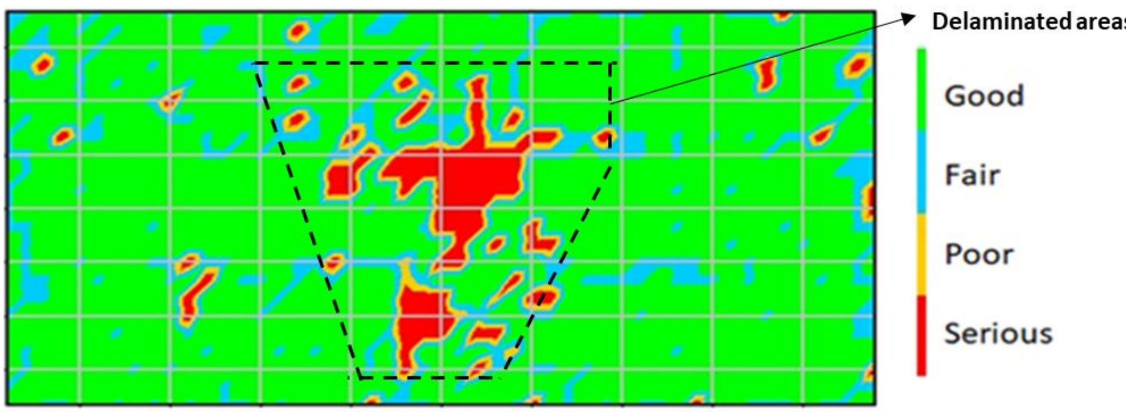

Source: FHWA.

B. Colored heat map.

Figure 107. Heat maps. Deck specimen's IE.

In the instance of USW, defective areas are assumed to be regions with a concrete elastic modulus less than 3,000 ksi. While the concrete deck with design and in situ compressive strengths exceeding 4,000 ksi and 4,500 ksi, respectively, may exhibit a low elastic modulus (i.e., <3,000 ksi), this value is often indicative of the presence of delamination or cracking and does not necessarily reflect the actual concrete elastic modulus at the test location.

Each figure incorporates a secondary ordinate (on the right side), presenting defect indexes for IE, USW, and HCP. These figures were created using the deterioration curves developed for deck specimens subject to accelerated testing, using the converted in-service years for New Jersey. The deterioration curves associated with deep learning and survival were eliminated from these figures for visual clarity. Similar to condition index plots, the researchers aligned the scales of the secondary axis with the NBI CR and deterioration curves on the primary vertical axis, allowing for qualitative baselines and the conversion of NDE data to deck performance and vice versa. Unlike the condition index, the defect index increases, not decreases, as the deck deteriorates.

Figure 104 illustrates that for IE defect indexes of 5 percent and less, the deck specimen consistently receives ratings of 7 and greater. However, with an increase in the IE defect index to 10 percent, the corresponding CR for the deck VI dropped to 5. Any defect index greater than 10 percent correlated with a CR of 4 or less. The researchers observed a parallel, albeit more sensitive, correlation for USW defect indexes of 1 percent and less, where the deck specimen consistently achieved a CR of 7 and greater. However, with an increase in the USW condition index to 2 percent, the condition based on VI dropped to CR6. Subsequent increases of the defect index to 3 percent and beyond correlated with CR dropping to 5 and 4, respectively. In the case of HCP, defect indexes of 5 percent and less correlated with the deck VI assessment of CR7 and greater. However, with an increase of the HCP defect index to 10 percent, the CR experiences a decline of 2 points, settling at 5. Any defect index beyond 10 percent correlated with a visual assessment of CR4 or less.

Table 20 provides a summarized overview of the qualitative correlations between NDE condition indexes, NDE defect indexes, and deck CRs, offering a comprehensive reference for interpreting the findings. This approach enhances the understanding of how NDE results align with established CR and deterioration models, providing valuable insights into the overall performance of the bridge deck. However, both condition and defect index qualitative conversions were only achieved by reviewing data from accelerated testing and are established on a limited dataset. That said, the methodology established here to derive the conversion table was designed to serve as a framework with the potential to be expanded to a broader range of bridge types. Further extensive research studies on various bridges with different deck types, geometries, and environmental factors are needed to validate the extent of similar qualitative conversions. The intention here is to highlight the value of NDE and how it complements existing performance measurements, such as NBI component or element-level conditions. While CRs are integral to bridge asset management systems and are not envisioned by the practice to be superseded by other metrics, the discrete changes in CRs offer little insight into the condition change rate, which is continuously changing over time. Therefore, NDE data need to be complementary to the CRs.

Table 20. Qualitatively established NDE condition and defect index thresholds versus NBI deck CR using data from accelerated testing.

NBI Deck Rating	NDE Condition Index (%)			NDE Defect Index (%)		
	IE	USW	HCP	IE	USW	HCP
≥7	>90	>90	>96	<5	<1	<5
6	>80	>80	>90	<10	<2	<10
5			>75		<3	
≤4	<80	<80	<75	>10	>3	>10

Note: The thresholds are derived based on limited data from the deck specimen subject to accelerated testing. NDE condition index and defect index have descending and ascending trends as bridge deteriorates, respectively.

In the preceding paragraphs, the NBI component-level CR served as the primary indicator of the deck's performance, along with associated deterioration models. To further examine the correlation between NDE and deck performance data, element-level CSs were introduced as an alternative metric. Figure 108 illustrates the element-level CSs (CS1–CS4) plotted using the deck's VI (solid lines), Markovian deterioration curves (dashed lines), and IE data (markers). The Markovian curves were drawn using New Jersey traffic data for scaling.

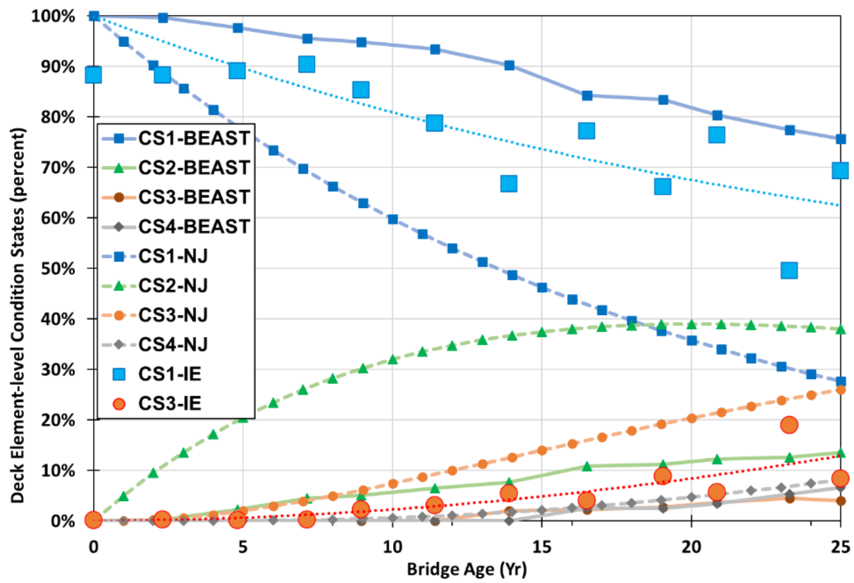

Source: FHWA.

Figure 108. Graph. Deck specimen's element-level CSs.

The element-level CSs generally describe the condition of the subject material (i.e., steel, concrete) as good (CS1), fair (CS2), poor (CS3), or severe (CS4). Using the definitions by the MBEI, specific descriptions of the type of defect in the material are also provided in table 21 (AASHTO 2019a). The primary corrosion-related defect for bridge decks is defect element 1080, delamination, spall, or patched area. The CS definitions for the defect element 1080, delamination, and spalling, are shown in table 21. As shown in the table, CS2 is used to describe areas of delamination and shallow spalls less than 6 inches in diameter. CS3 is used to describe spalls of greater than 6 inches in diameter. For the deck specimen, which had areas of low cover and accelerated loadings, the team found that subsurface areas of delamination propagated to spalls quickly. Consequently, areas of delamination detected by IE were categorized as CS3 in the analysis.

Table 21. Definition of delamination or spall or patched area defect (1080) (AASHTO 2019a).

Defects	CS1 GOOD	CS2 FAIR	CS3 POOR	CS4 SEVERE
Delamination or Spall or Patched Area (1080)	None.	Delaminated. Spall 1 in. or less deep or 6 in. or less in diameter. Patched area that is sound.	Spall greater than 1 in. deep or greater than 6 in. diameter. Patched area that is unsound or showing distress. Does not warrant structural review.	The condition warrants a structural review to determine the effect on strength or serviceability of the element or bridge.

As depicted in figure 108, a notable disparity exists between VI and CSs predicted by deterioration models. VI assesses much smaller proportions of the deck were deteriorating over time compared to the predicted CSs derived from the deterioration model using New Jersey's network-level data. However, incorporating NDE data as an alternative measure reveals that the actual damage in the deck is in greater proportions compared with VI, and smaller proportions compared with deterioration models.

This observation serves as a compelling example of how NDE data can more accurately reflect the deck's condition by indicating both surface and subsurface damage, a capability lacking in VI at the element level. This outcome results in the NDE data indicating greater proportions of the deck in CS3 compared with VI. Conversely, NDE data indicate the deck's overperformance compared to predictions from a network-level deterioration model. Considering that these deterioration models form the backbone of BMSs for calculating bridge LCCs, the additional data provided by NDE can help improve the quality of the forecasted deck performance by more accurately characterizing the extent of damage present at periodic condition assessment intervals. These data, in turn, will improve the quality of the forecast from deterioration modeling, such as when Bayesian updating is used in maintaining a deterioration model in a BMS. In other words, the updating of, for example, transition probabilities in a Markov or Weibull model like that used in AASHTOWare™ Bridge Management with periodic inspection results will more accurately reflect the actual deterioration (AASHTO 2022). This finding can lead to significant cost savings when rehabilitation, repair, or replacement decisions are made more effectively using better quality data. This dual benefit of NDE usage showcases its effectiveness in portraying the actual condition of a bridge deck compared to typical bridge inspections or predicted deterioration models.

SUMMARY AND CONCLUSION

The team explored the development and implementation of data-driven deterioration models for bridge decks using data captured from accelerated testing. Deterministic, probabilistic (survival), and AI/ML methods were used to predict bridge deck deterioration. The team also conducted a comparative analysis of traditional deterministic and probabilistic models against advanced survival and AI/ML models. Comparison of model outcomes with the NDE data suggests that the predictive capabilities of deterioration models can be enhanced with NDE to offer a nuanced view of bridge deck conditions at each stage of aging.

This chapter describes the qualitative correlations between NDE condition indexes, NDE defect indexes, and deck CRs, offering the following conclusions:

- Deck CR7 and above correlate with an NDE condition index of greater than 90 percent for IE and USW techniques, and greater than 96 percent for HCP techniques. Conversely, deck CR4 and below correspond with an NDE condition index of less than 80 percent for IE and USW and less than 75 percent for HCP techniques. Deck CR6 and CR5 correspond with intermittent values.

- Deck CR7 and above correlate with an NDE defect index of less than 5 percent for IE and HCP techniques, and less than 1 percent for USW techniques. Alternatively, deck CR4 and below correspond with an NDE defect index of greater than 10 percent for IE and HCP, and greater than 3 percent for USW techniques. Deck CR6 and CR5 correspond with intermittent values.

The analysis has deepened the understanding of how NDE results correlate with established CR and deterioration models, offering critical insights into the overall performance of the bridge decks. However, acknowledging that these conversions of condition and defect indexes are solely derived from data collected from a single accelerated testing and therefore rely on a limited dataset is important. These correlation studies serve as an initial framework for the application of NDE data to a wider variety of bridge types encompassing varying deck types, geometries, and environmental conditions.

The application of NDE data offers insights into the condition of bridge decks that can support effective maintenance and rehabilitation decisionmaking. The results presented in this report demonstrate an improvement in the accuracy and reliability of deterioration predictions when NDE data are integrated with traditional condition assessment methods, including VI. The findings affirm the indispensable value of NDE in bridging the gap between conventional assessment techniques and the dynamic requirements of contemporary bridge management.

Future research should aim at expanding the scope of NDE integration to encompass a broader spectrum of bridge types and conditions, further refining model precision. Additionally, further development of AI/ML models to interpret complex data patterns and predict deterioration more accurately is needed. Emphasis should also be placed on the development of comprehensive BMSs that fully leverage the predictive power of NDE-enhanced deterioration models. The ultimate goal is to craft intelligent, data-driven frameworks that support proactive decisionmaking, minimize LCCs, and ensure the longevity and reliability of bridge infrastructures.

APPENDIX A. FULL TIME-LAPSED CONTOUR PLOTS FOR NDE DATA COLLECTED FROM THE ACCELERATED TESTING (PHASE I)

Figure 109 through figure 115 present the contour plots for all 14 datasets from the accelerated testing.

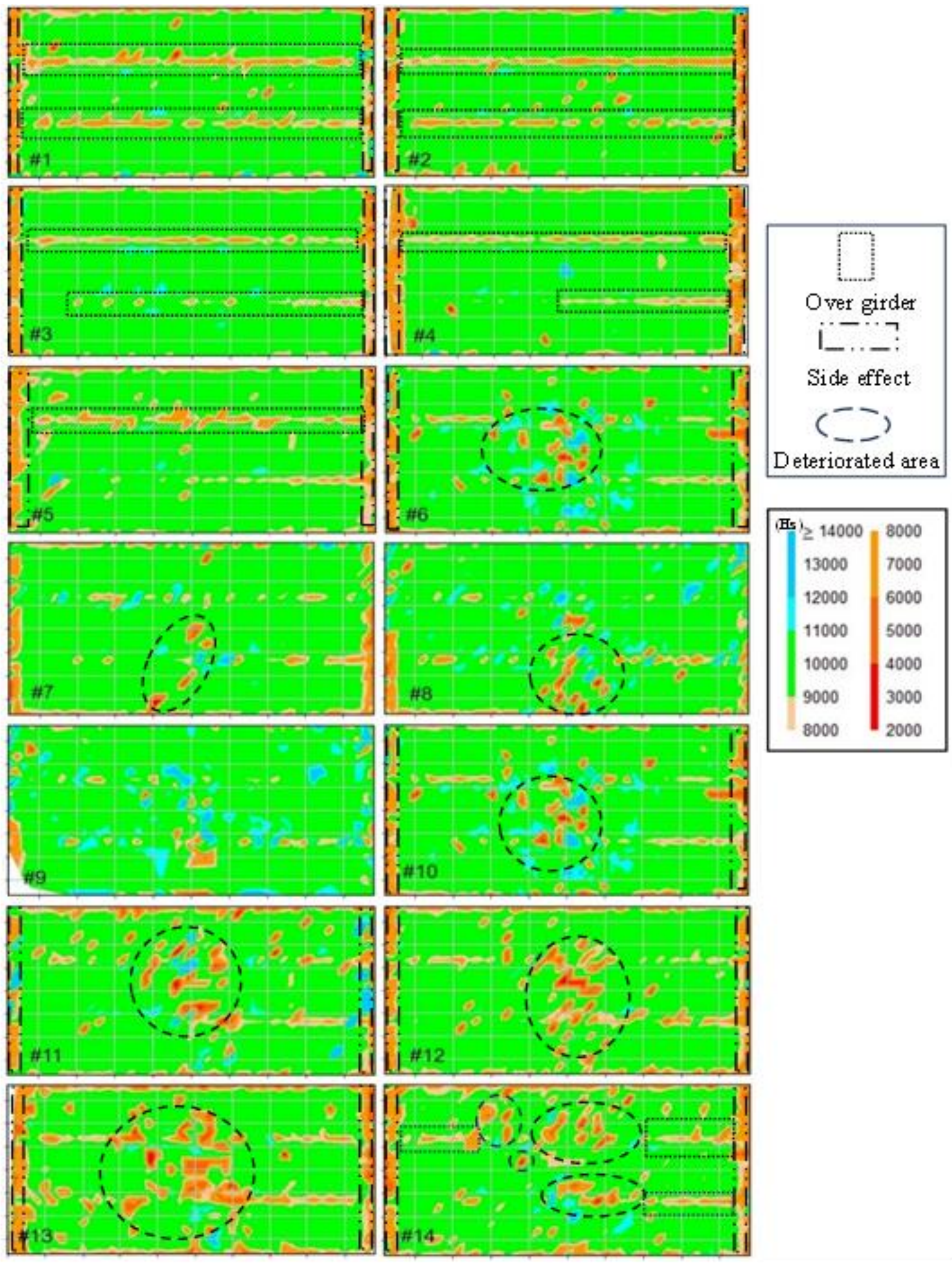

Source: FHWA.

Figure 109. Heat map. IE-dominant frequency contours.

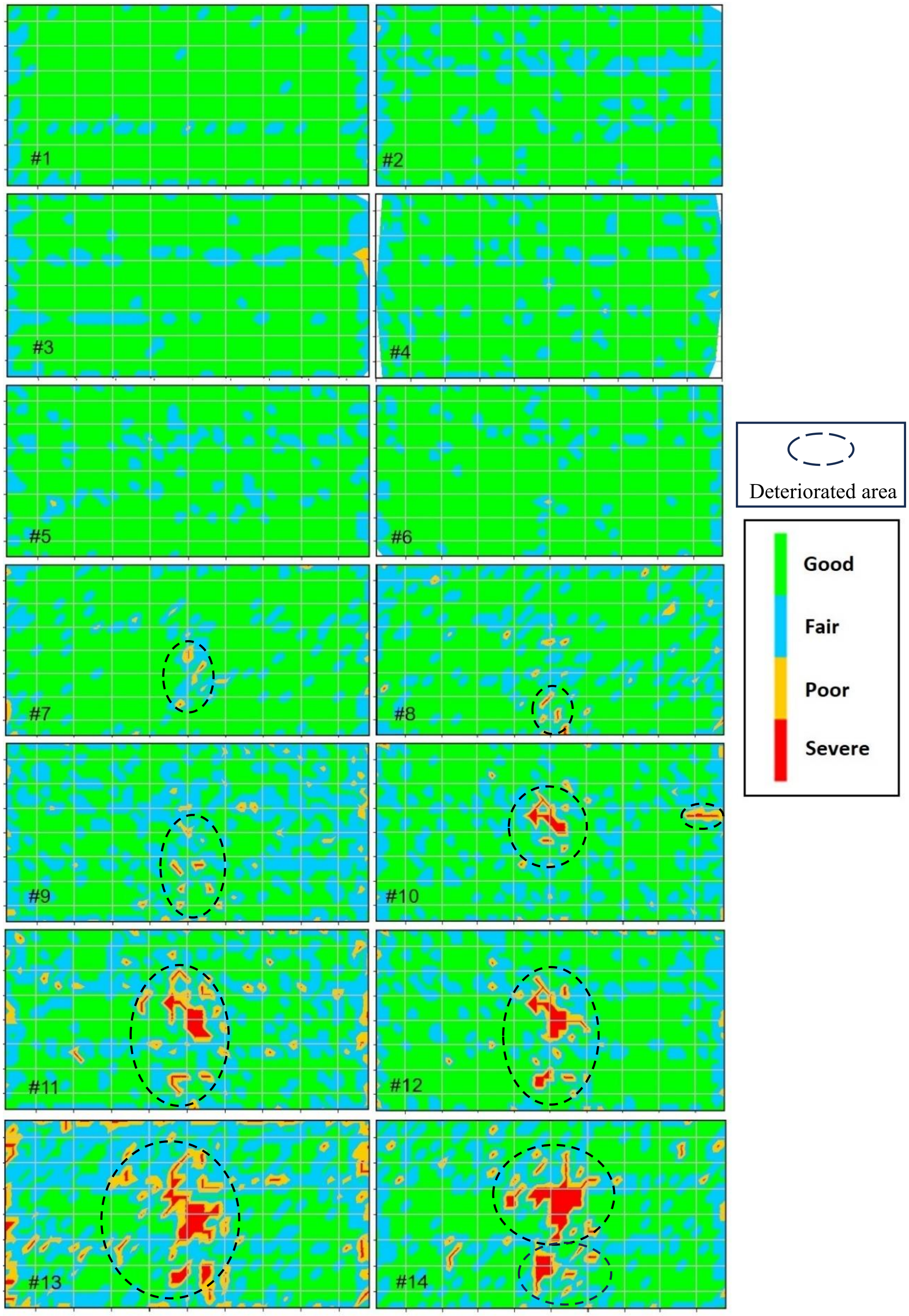

Source: FHWA.

Figure 110. Heat map. IE-index contours.

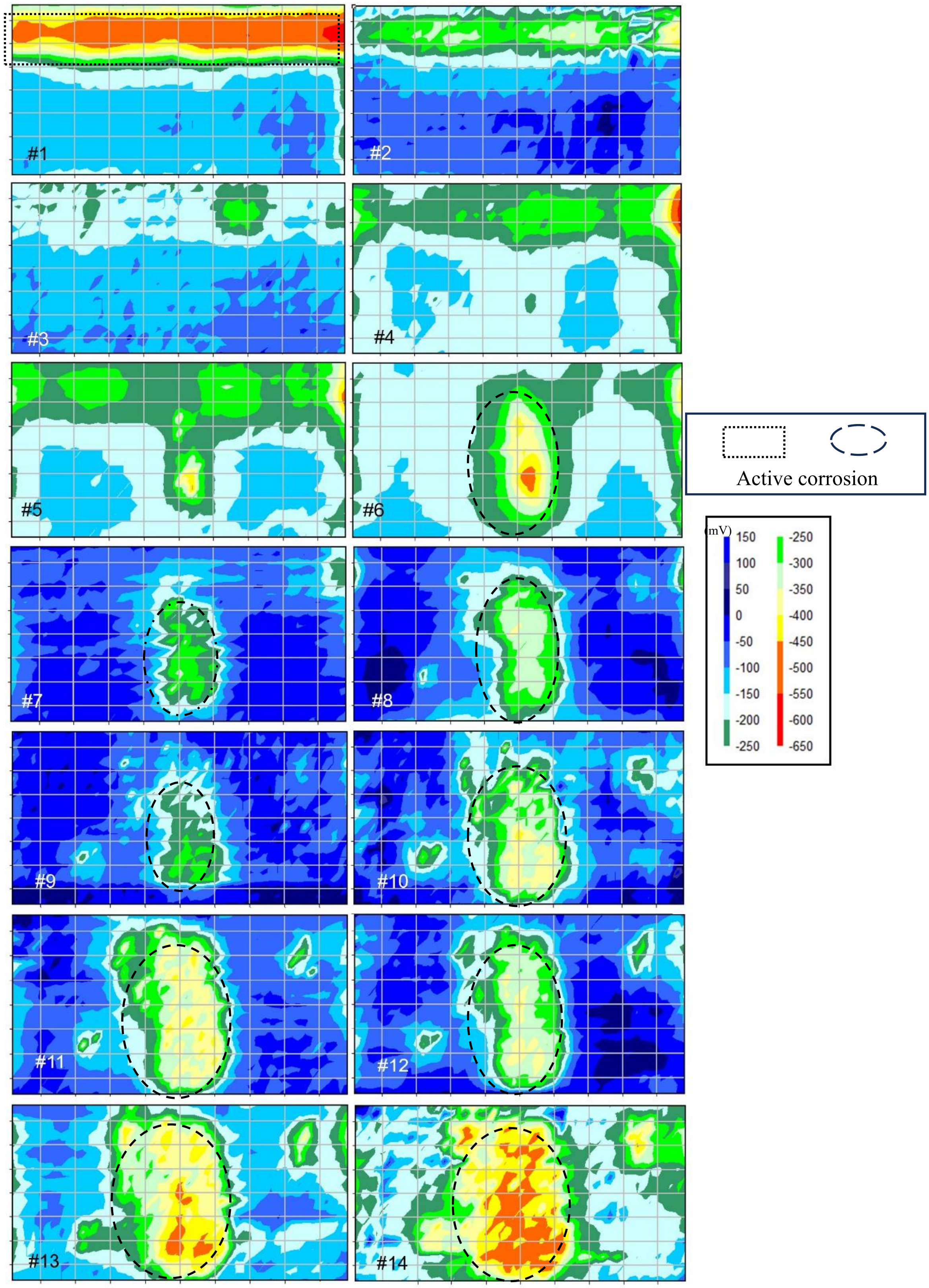

Source: FHWA.

Figure 111. Heat map. HCP contours.

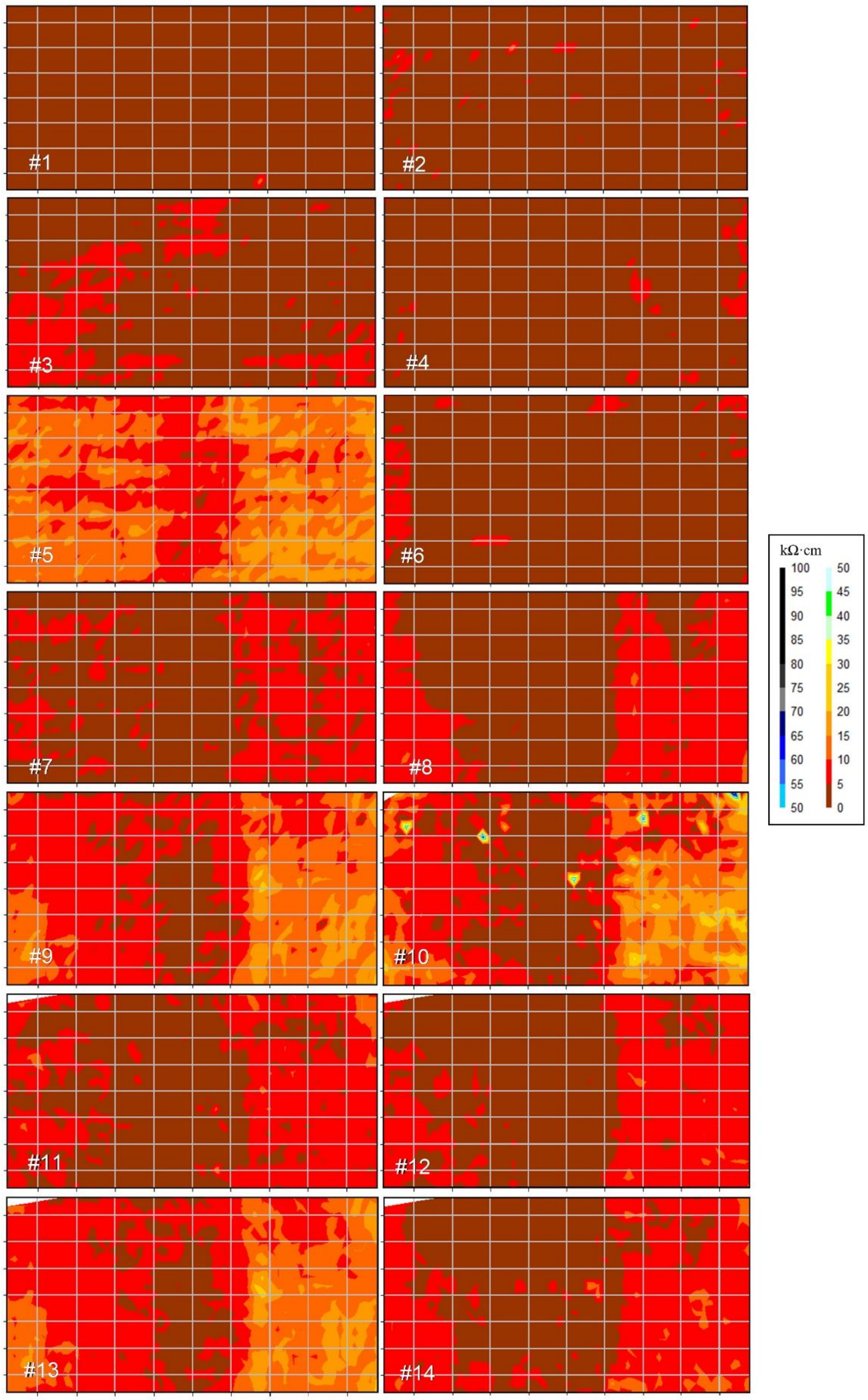

Source: FHWA.

Figure 112. Heat map. ER contours.

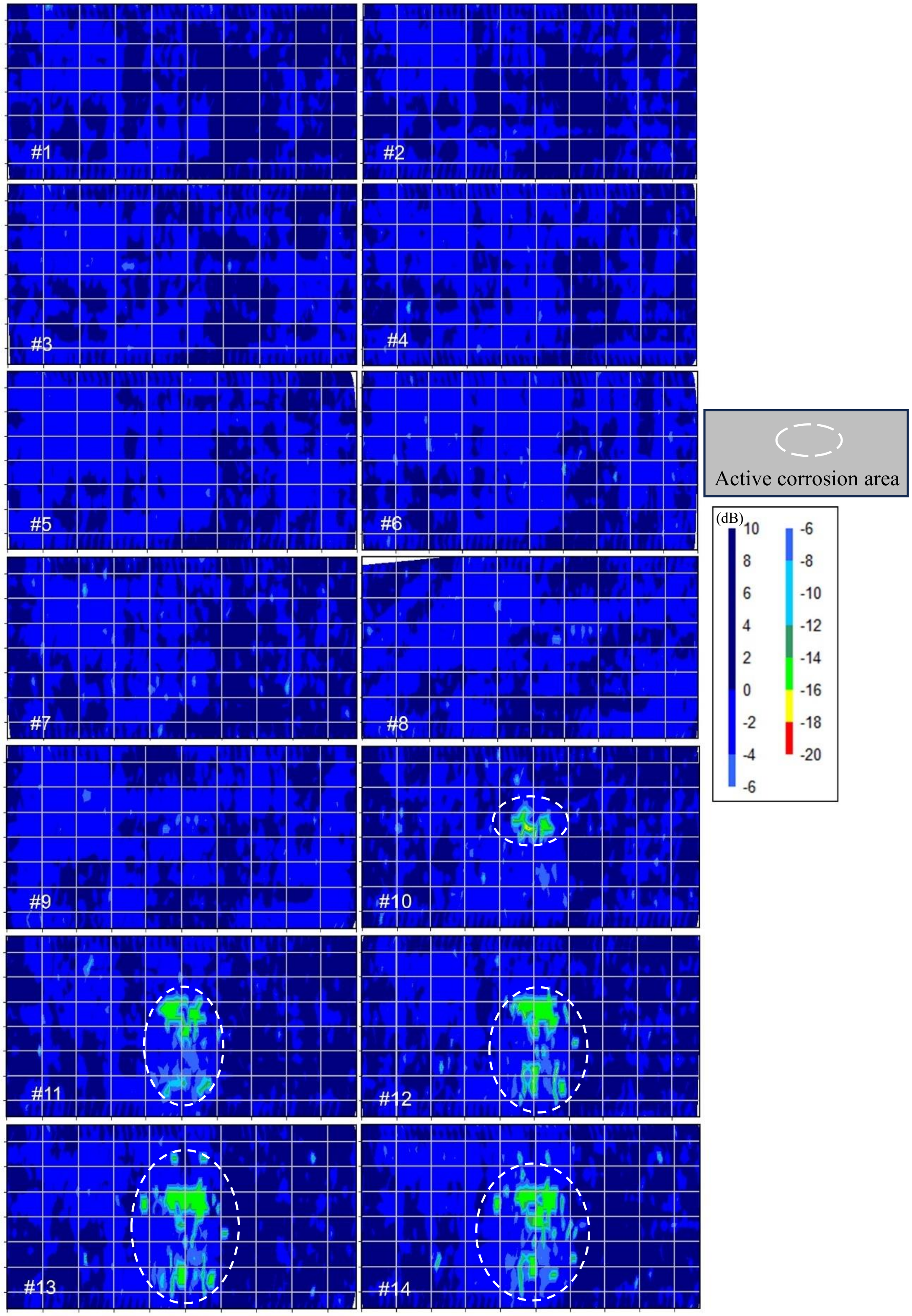

Source: FHWA.

Figure 113. Heat map. GPR-amplitude contours.

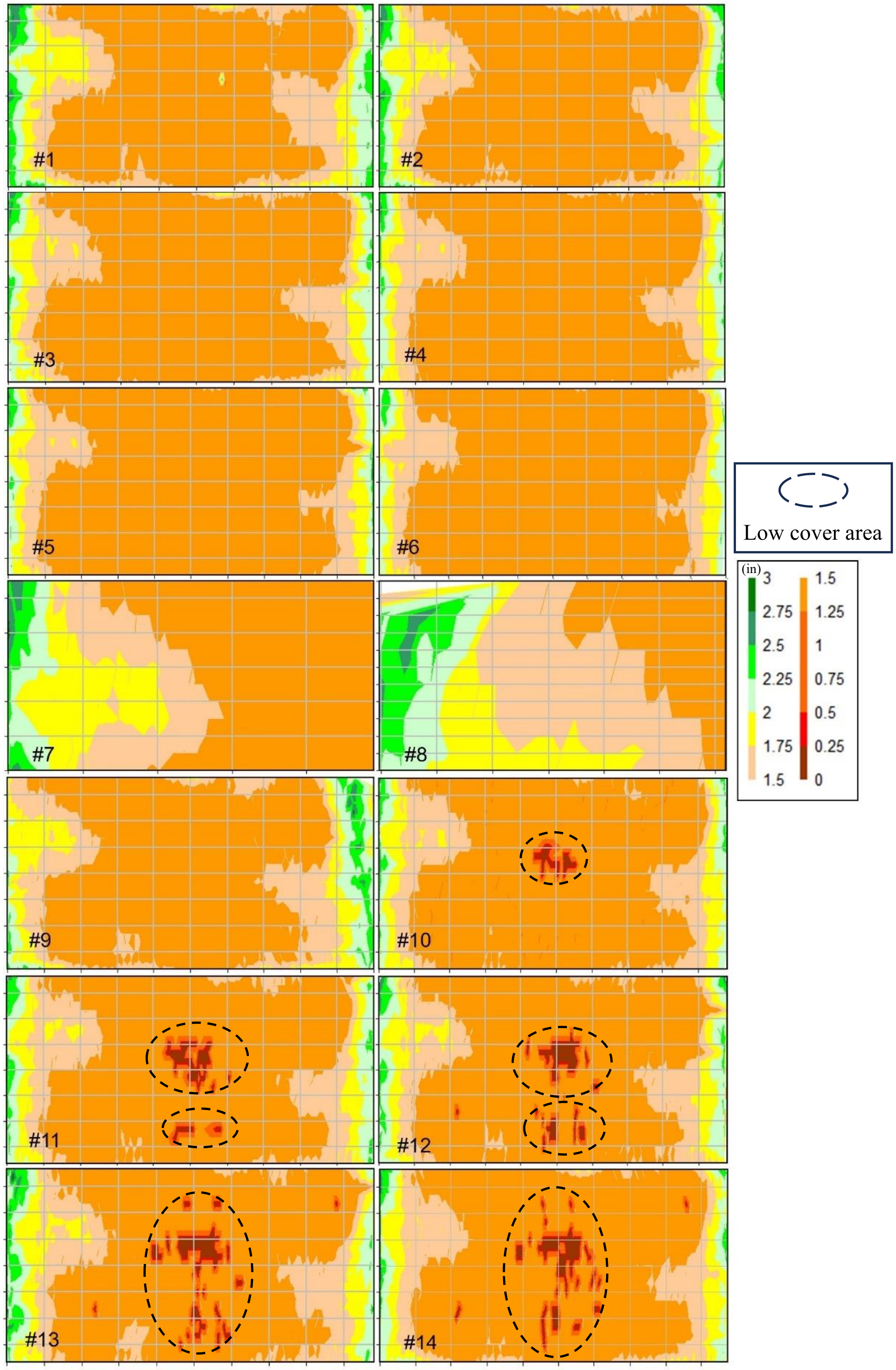

Source: FHWA.

Figure 114. Heat map. Cover depth contours.

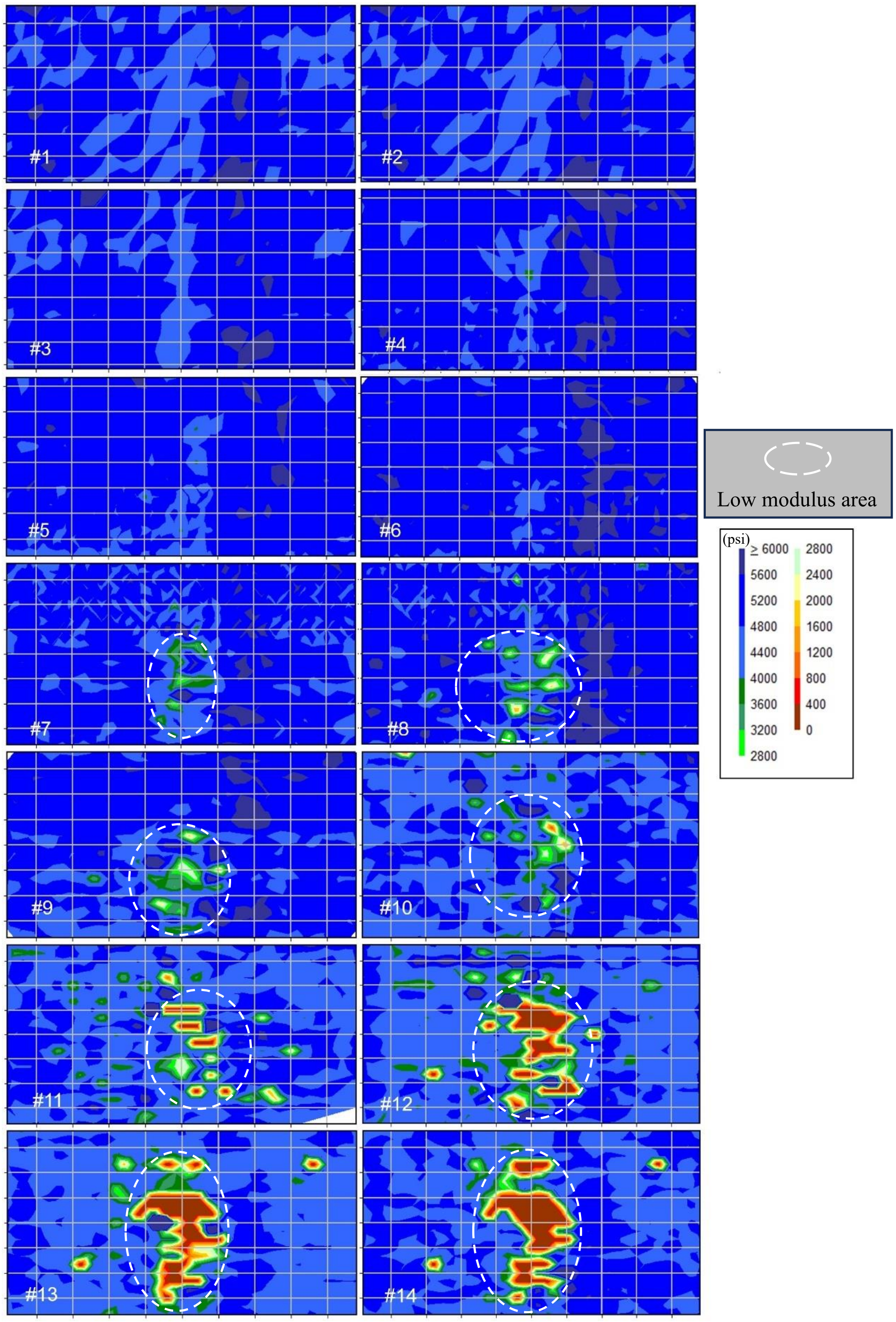

Source: FHWA.

Figure 115. Heat map. Elastic modulus contours.

APPENDIX B. CLASSIFICATION TREE

The classification tree (figure 116), represented in the form of a visual classification tree, is provided to facilitate the conversion of element-level CSs to component-level CRs for an RC deck. In the following decision trees, *x1*, *x2*, *x3*, and *x4* correspond to CS1 through CS4 percentages, respectively. The threshold values at the tree nodes should not be rounded. The outcome at the end of each branch determines the NBI component CR.

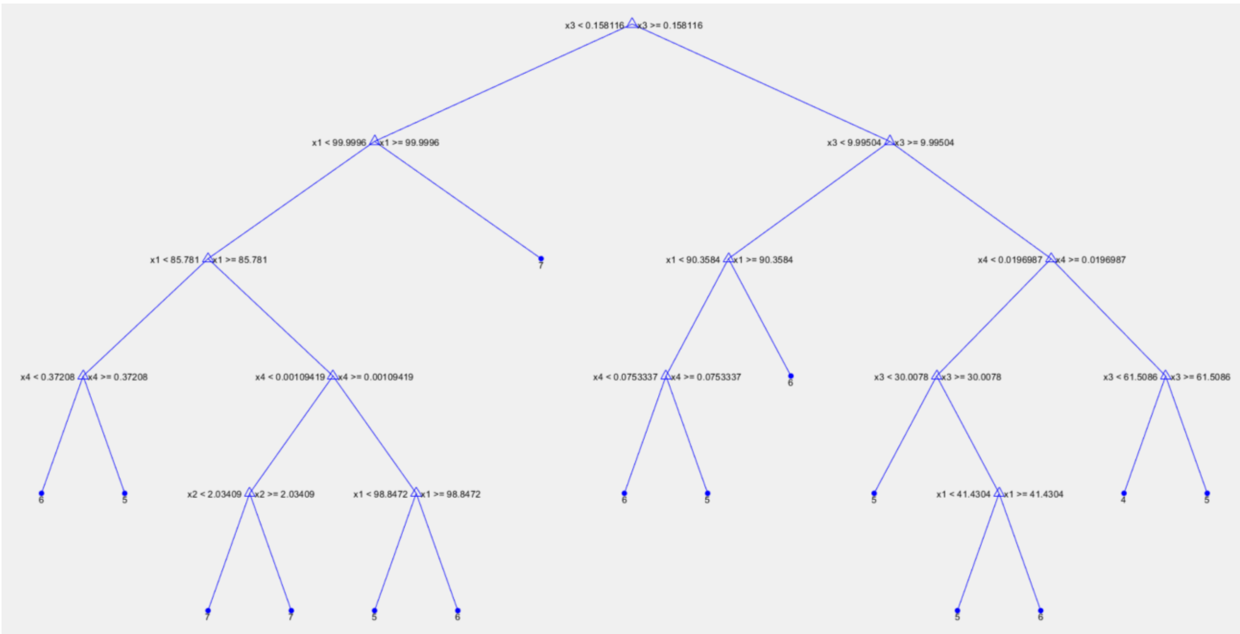

Source: FHWA.

Figure 116. Flowchart. Decision classification tree for the conversion of element-level CSs to component-level CRs for an RC deck.

APPENDIX C. CHLORIDE PROFILES

The chloride profiles from the specimen subjected to the accelerated testing and their numerical fits are presented in figure 117 through figure 121 and summarized in table 22.

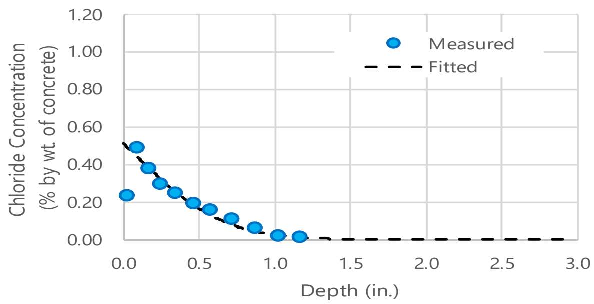

Source: FHWA.

A. Uncracked sample ponding in 1.5-percent solution.

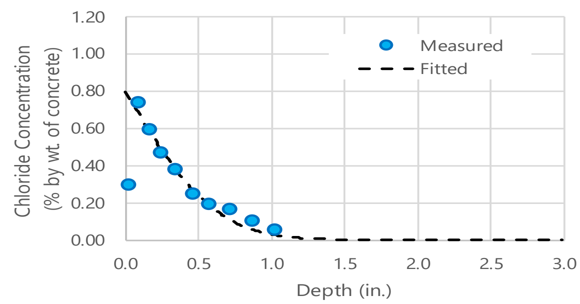

Source: FHWA.

B. Uncracked sample ponding in 3-percent solution.

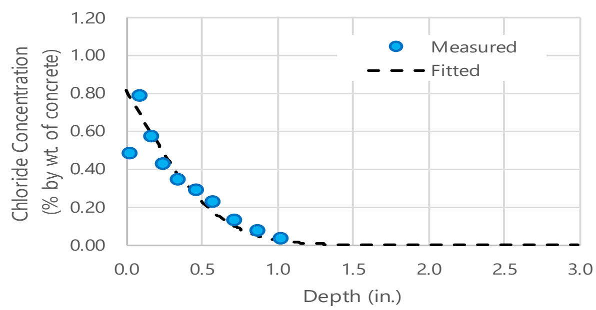

Source: FHWA.

C. Uncracked sample ponding in 4.5-percent solution.

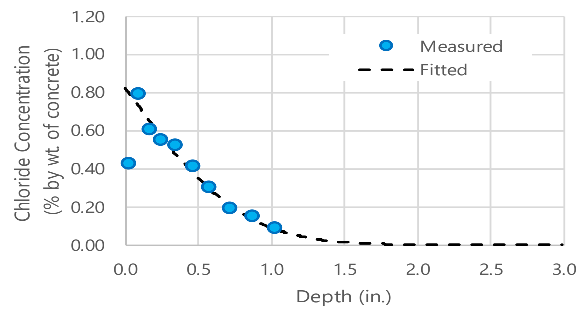

Source: FHWA.

D. Uncracked sample ponding in 6-percent solution.

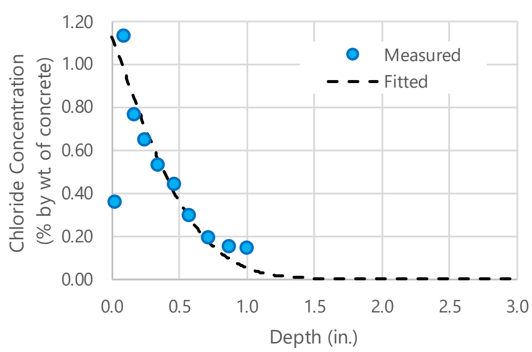

Source: FHWA.

E. Uncracked sample ponding in 9-percent solution.

Figure 117. Graphs. Measured and fitted chloride profiles for cores of uncracked concrete tested after 329 d of exposure to brine solutions of varying application rates, starting at an age of 99 d.

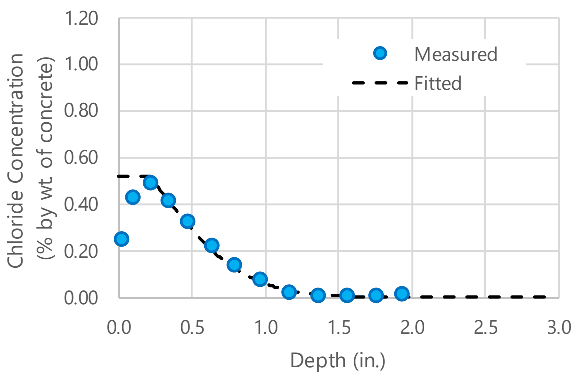

Source: FHWA.

A. H2-L2.

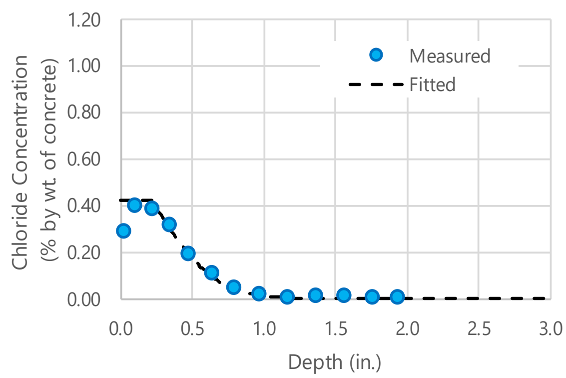

Source: FHWA.

B. H6-Fix.

Note: Capillary action due to a wetting and drying front is evident in these cores and is indicated by a peak chloride concentration measured at a depth interior to the concrete.

Figure 118. Graphs. Measured and fitted chloride profiles for cores sampled from accelerated bridge deck on February 3, 2020 (at an age of 216 d).

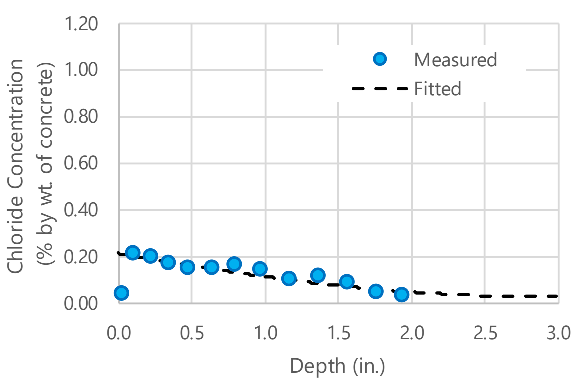

Source: FHWA.

A. H4-18.

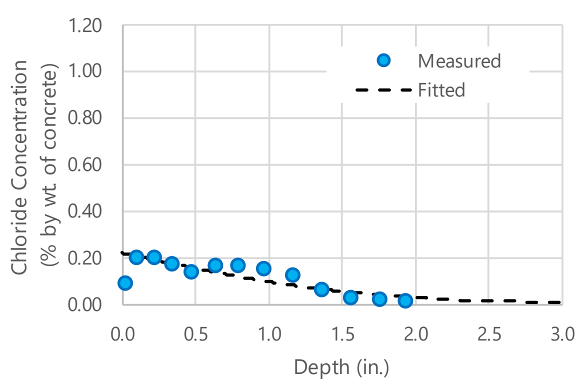

Source: FHWA.

B. H6-46.

Note: While limited capillary action was evident in the near surface region of these cores, it was not included in the fitted chloride profiles.

Figure 119. Graphs. Measured and fitted chloride profiles for cores sampled from deck specimen on November 11 and 12, 2020 (at ages of 498 d and 499 d, respectively).

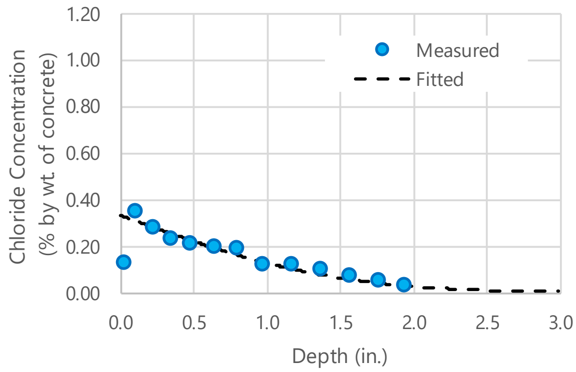

Source: FHWA.

A. H5-18.

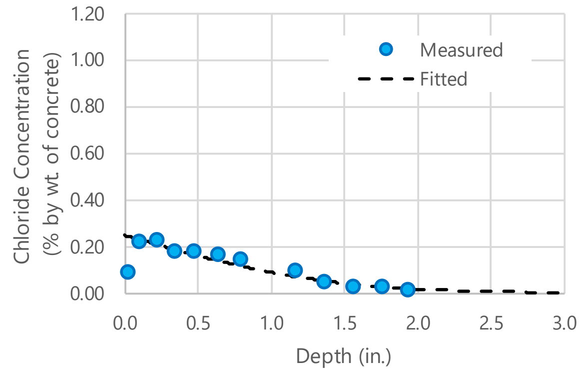

Source: FHWA.

B. H6-fix (3-21).

Note: While limited capillary action was evident in the near surface region of these cores, it was not included in the fitted chloride profiles.

Figure 120. Graphs. Measured and fitted chloride profiles for cores sampled from the deck specimen on March 4, 2021 (at an age of 611 d).

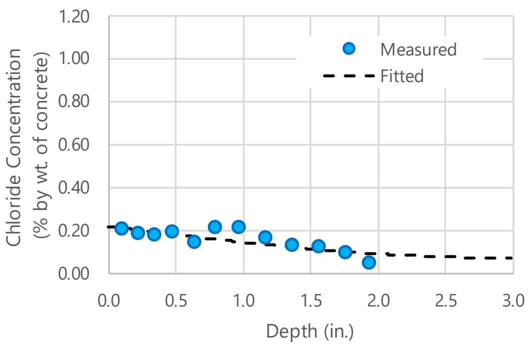

Source: FHWA.

A. 17×9.

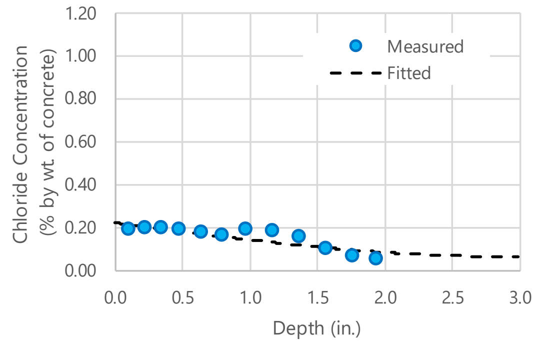

Source: FHWA.

B. 11×17.

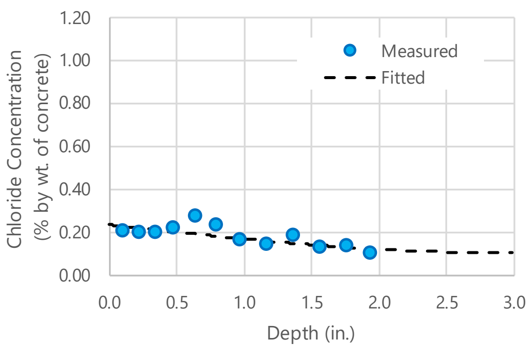

Source: FHWA.

C. 25×22.

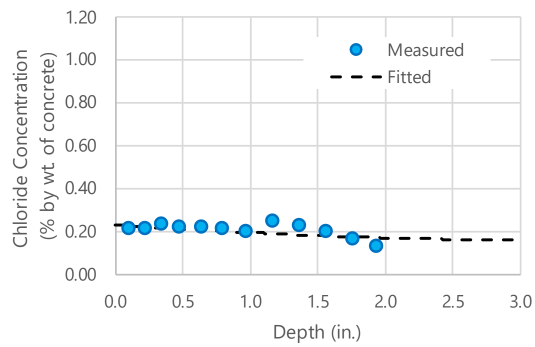

Source: FHWA.

D. 20×17.

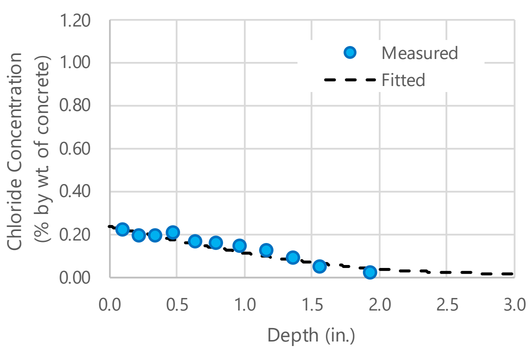

Source: FHWA.

E. 40×7.

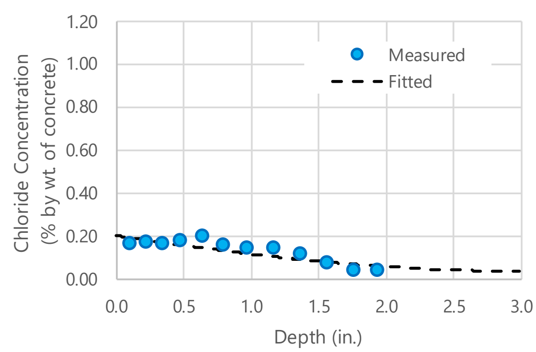

Source: FHWA.

F. 5×4.

Note: Chloride profiles are flatter than for other sampling dates, indicating that chloride ions have penetrated deeper into the concrete at this age.

Figure 121. Graphs. Measured and fitted chloride profiles for cores sampled from test deck on March 2, 2022 (at an age of 974 d).

Table 22. Summary of chloride profile results.

Core ID	Chloride Exposure	Sampling Date	Age at Sampling (days)	Total Exposure Duration (days)	Estimated D_{28} (in²/yr)	Estimated C_s (ppm)
Laboratory Cylinders						
1.5 UC	Ponding in 1.5% brine solution	3/6/2020	385	329	0.206	0.520
3.0 UC	Ponding in 3.0% brine solution	3/6/2020	385	329	0.188	0.804
4.5 UC	Ponding in 4.5% brine solution	3/6/2020	385	329	0.173	0.823
6.0 UC	Ponding in 6.0% brine solution	3/6/2020	385	329	0.315	0.830
9.0 UC	Ponding in 9.0% brine solution	3/6/2020	385	329	0.203	1.140
BEAST Cores						
H2-L2	1,200-gal total brine	2/3/2020	216	117	1.074	0.528
H6-Fix (2020)	1,200-gal total brine	2/3/2020	216	117	0.539	0.435
H4-18	2,760-gal total brine	11/11/2020	498	399	2.645	0.222
H6-46	2,760-gal total brine	11/12/2020	499	400	1.775	0.229
H5-18	2,930-gal total brine	3/4/2021	611	512	1.202	0.342
H6-Fix (3/21)	2,930-gal total brine	3/4/2021	611	512	1.081	0.257
17x9	3,595-gal total brine	3/2/2022	974	875	2.515	0.227
10x17	3,595-gal total brine	3/2/2022	974	875	2.264	0.231
25x22	3,595-gal total brine	3/2/2022	974	875	3.259	0.244
27x17	3,595-gal total brine	3/2/2022	974	875	5.811	0.237
40x7	3,595-gal total brine	3/2/2022	974	875	1.081	0.245
5x4	3,595-gal total brine	3/2/2022	974	875	1.703	0.210

UC = uncracked sample.

APPENDIX D. SERVICE LIFE MODEL INPUT PARAMETERS

Table 23 and table 24 show the values input into the service life model for the Jasper and Linn County, IA, case study bridges, respectively.

Table 23. Service life model inputs—Jasper County bridge.

Parameter	Value	
General		
Total deck thickness (inches)	7.75	
Overlay thickness (inches)	1.75	
Deck age at initial HPC overlay application (yr)	20	
Deck age at new overlay application (yr)	57 (if applied)	
Surface damage at end of service (percent)	25	
Material		
Transport Properties		
Apparent D_{28} (normal distribution) (in^2/yr)	Deck concrete—M: 0.30; SD: 0.08	Overlay—M: 0.35; SD: 0.09
Diffusion decay parameter (i.e., aging factor)	Deck concrete—0.20	Overlay—0.32
Exposure Conditions		
Mean annual temperature (°F)	49.2	
C_s (normal distribution) (ppm)	M: 4,500; SD: 900	
Buildup time (yr)	5	
Depth of convection zone (beta distribution) (inches)	M: 0.22; SD: 0.35; LL: 0; UL: 2	
Reinforcing Properties		
Cover depth (normal distribution) (inches)	M: 3.27; SD: 0.36	
Critical C_t (beta distribution) (ppm)	M: 749; SD: 234; LL: 312; UL:3,121	
t_p (normal distribution) (yr)	M: 10; SD: 2.5	

HPC = high-performance concrete.

Table 24. Service life model inputs—Linn County bridge.

Parameter	Value		
General			
Total deck thickness (inches)	9.5		
Overlay thickness (inches)	1.75		
Deck age at initial HPC overlay application (yr)	26		
Deck age at new overlay application (yr)	47 (if applied)		
Surface damage at end of service (percent)	25		
Transport Properties			
Apparent D_{28} (normal distribution) (in^2/yr)	Deck concrete—M: 0.32; SD: 0.08	HPC overlay—M: 0.35; SD: 0.09	PPC overlay—M: 0.002; SD: 0.09
Diffusion decay parameter (i.e., aging factor)	Deck concrete—0.20	HPC overlay—0.32	PPC overlay—See equation 1 of ElBatanouny et al. (2022)
Exposure Conditions			
Mean annual temperature (°F)	47.5		
C_s (normal distribution) (ppm)	M: 4,500; SD: 900		
Buildup time (yr)	5		
Depth of convection zone (beta distribution) (inches)	M: 0.22; SD: 0.35; LL: 0; UL:2		
Reinforcing Properties			
Cover depth (normal distribution) (inches)	M: 3.17; SD: 0.36		
Critical C_t (beta distribution) (ppm)	M: 749; SD: 234; LL: 312; UL: 3,121		
t_p (normal distribution) (yr)	M: 10; SD: 2.5		

APPENDIX E. LEF METHODOLOGY

To implement the LEF methodology, the team computed the ESAL value, which is primarily a measure that quantifies the impact of trucks with different axle setups and weight distributions on a pavement or a bridge, compared to standard single-axle trucks, each carrying 18,000 lbs. Calculating the ESAL for each vehicle class considering both the axle arrangement and the vehicle's weight is crucial. One major element of ESAL corresponds to the computation of LEF for each axle configuration or vehicle type, and then aggregating these data across different configurations to estimate the ESAL.

The LEFs established by AASHTO's Bridge Design Specification are contingent on various factors, including axle arrangement and spacing, slab depth, and terminal serviceability, among others (AASHTO 2020). Table 25 provides LEF factors for rigid pavement, given that the deck specimen at the BEAST facility is constructed with concrete. The BEAST carriage is categorized as a tandem axle with a load of 50 kips. The maximum reported axle load matches the 50 kips carried by the BEAST carriage.

Table 25. Typical LEFs.

Axle Type	Axle Load (kips)	LEF
Single	2	0.0002
	10	0.082
	14	0.341
	18	1
	20	1.57
	30	8.28
Tandem	2	0.0001
	10	0.013
	14	0.048
	18	0.133
	20	0.206
	30	1.14
	34	1.92
	40	3.74
	50	9.07

To start with the calculation of ESAL, table 26 lists the single pass of BEAST equivalency for each vehicle class at various load scenarios. This table is adopted from SUDAS 2023 (Iowa SUDAS 2023) and considered a variety of loading scenarios for classes 6 through 9 (figure 122) such as empty, half, or fully loaded (FHWA 2014). Since classes 3 and below pertain to regular cars and class 10 and above correspond to special and nonfrequent trucks, those were eliminated from analysis.

Table 26. Estimation of vehicle LEFs by class (distribution adopted from Iowa SUDAS 2023).

Vehicle	Load Scenario	Vehicle Weight (lb)	Axle Type	Axle Load (percent)	Axle Load (lb)	ESAL Rigid per Axle	Vehicle LEF
Class 4	Fully loaded	25,000	Front single	36	9,000	0.1072	0.870
			Rear single	64	16,000	0.7624	
Class 5	Fully loaded	20,000	Front single	32.5	6,500	0.0581	0.455
			Rear single	67.5	13,500	0.3967	
Class 6	Empty	22,000	Front single	32	7,040	0.0653	0.186
			Rear tandem	68	14,960	0.1211	
	Fully loaded	46,000	Front single	32	14,720	0.5513	2.351
			Rear tandem	68	31,280	1.7998	
Class 8	Empty	24,000	Front single	37.5	9,000	0.1072	0.189
			Rear tandem	37.5	9,000	0.0298	
			Trailer single	25	6,000	0.0525	
	50-percent loaded	44,000	Front single	22	9,680	0.1301	0.894
			Rear tandem	50	22,000	0.4805	
			Trailer single	28	12,320	0.2837	
	Fully loaded	64,000	Front single	15.63	10,000	0.1429	4.449
			Rear tandem	53.13	3,4000	2.4633	
			Trailer single	31.25	20,000	1.8429	
Class 9	Empty	36,000	Front single	30.56	11,000	0.1922	0.338
			Rear tandem	38.89	14,000	0.0974	
			Trailer tandem	30.56	11,000	0.0480	
	50-percent loaded	58,000	Front single	19.83	11,500	0.2230	1.410
			Rear tandem	41.38	24,000	0.6648	
			Trailer tandem	38.79	22,500	0.5224	
	Fully loaded	80,000	Front single	15	12,000	0.2584	5.185
			Rear tandem	42.50	34,000	2.4633	
			Trailer tandem	42.50	34,000	2.4633	

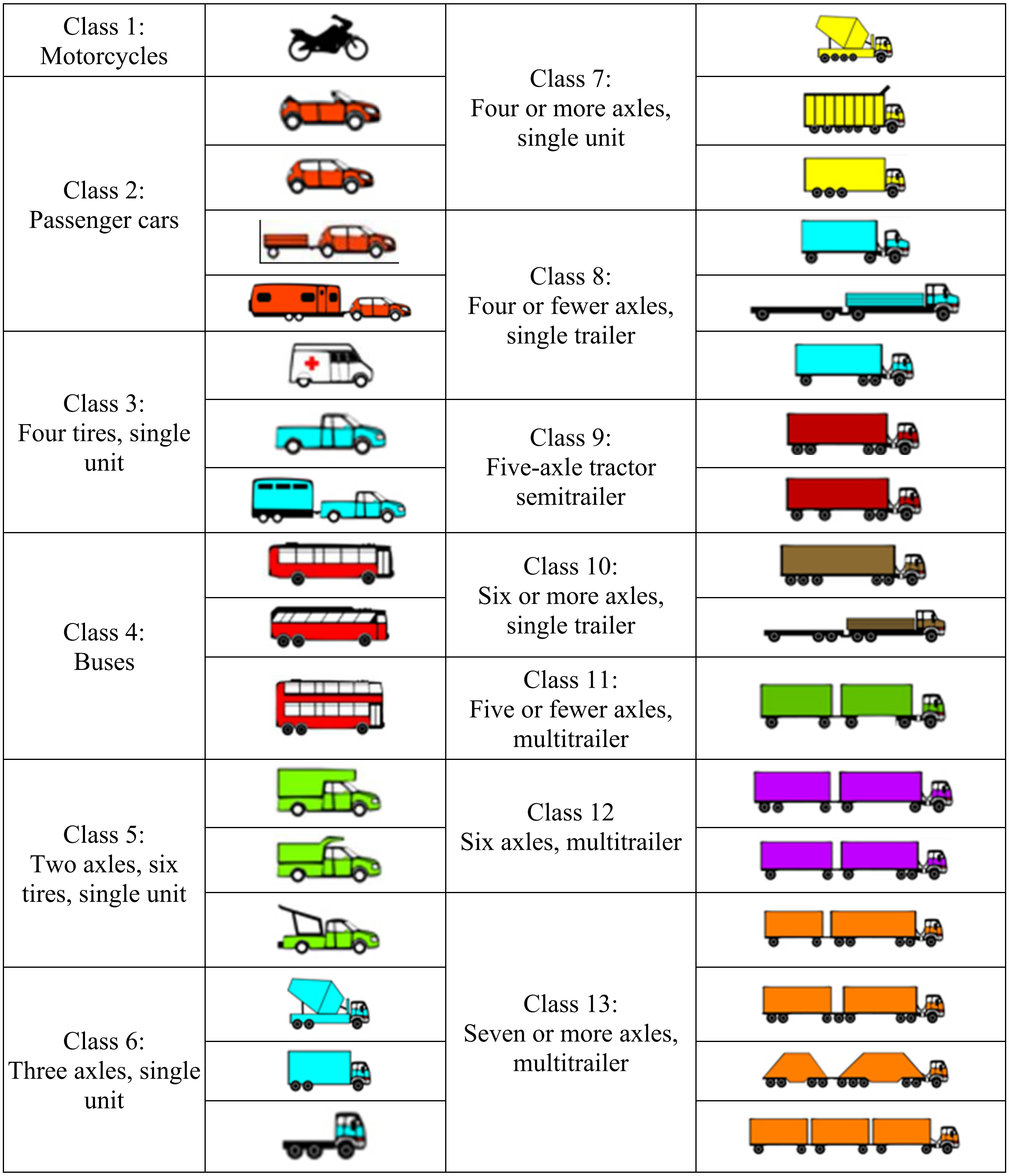

Source: FHWA.

Figure 122. Chart. Vehicle classification according to FHWA (2014).

Weigh-in-motion (WIM) data are a valuable tool in illustrating how the BEAST's impact aligns with real-world traffic behavior. By analyzing WIM data, effectively gauging how the loads and axle configurations of actual vehicles compare to the simulated effects of the BEAST was possible. This information provided a concrete understanding of the BEAST's equivalency in relation to traffic patterns on bridges. The available WIM data from in-pavement sensors for December 2021 obtained from the New Jersey Department of Transportation (NJDOT) was used to determine the traffic mixture by vehicle class and ADTT (WIM data (NJDOT 2017)). WIM data were obtained for the southbound direction on the John A Lynch Senior Memorial Bridge over the Raritan River between New Brunswick and Piscataway Townships in New Jersey. Adopted from a relevant study conducted by Rutgers University, trucks are assumed not to exit the route after the WIM site, and all proceed in the southbound direction. This case represents a high ADTT scenario of about 2,013 trucks of classes 4–9, except class 7. Weekends and low-traffic days around the holiday were excluded from the average. Table 27 shows the obtained proportion of each vehicle class.

Table 27. Proportion of each vehicle class of the ADTT from Site 18D.

Class Type	Proportion of Vehicle Class from Site (percent)
Class 4	7
Class 5	40
Class 6	10
Class 8	4
Class 9	39

The WIM data offer insights into vehicle classes but do not specify weights for each class. Therefore, a logical allocation of weights can be carried out using various truckload scenarios. Zhou et al. (2020) proposed a typical example of weight distribution of three or more axle trucks on the basis of class type, including the following:

- Class 4: Fully loaded.
- Class 5: Fully loaded.
- Class 6: 50-percent fully loaded and 50-percent empty.
- Class 8: 40-percent empty, 20-percent half-full, and 40-percent fully loaded.
- Class 9: 40-percent empty, 20-percent half-full, and 40-percent fully loaded.

Table 28 shows the combined distribution of vehicle weights, after applying the weight distribution and the vehicle class proportions presented in table 27.

Table 28. Calculated LEF for BEAST carriage.

Class	LEF	Distribution Within Class	Class Distribution
4	0.870	1.0	7
5	0.455	1.0	40
6	0.186	0.5	10
6	2.351	0.5	
8	0.189	0.4	4
8	0.894	0.2	
8	4.449	0.4	
9	0.338	0.4	39
9	1.410	0.2	
9	5.185	0.4	
LEF			1.42

According to table 25, the LEF for the BEAST carriage is 9.07. Using the LEF calculation presented in table 26, along with the proportion estimation for each vehicle class, results in a composite LEF of 1.42 for this traffic blend. This value signifies that a solitary traversal of the BEAST carriage imparts approximately 6.4 times the damage of a single pass by an average truck (which is a representative of the traffic blend). One day of BEAST operation, encompassing 13,000 carriage passes, can be likened to approximately 83,000 passes of an average truck.

ACKNOWLEDGMENTS

The original images in figure 2, figure 3, figure 4, and figure 6 are the copyright property of National Academy of Sciences and were modified to clearly show the details of each NDE technology to be understandable by visually impaired readers.

Figure 53 is the copyrighted property of the Iowa DOT. The labels have been modified for conciseness.

The original image in figure 10 is the copyright property of Rutgers, the State University of New Jersey and was modified to remove a product name.

Figure 73 and figure 74 are the copyrighted property of WJE and have been modified for color compliance.

Assistance from Dr. John Braley at Rutgers University in providing NDE data and essential information throughout the project execution is greatly appreciated.

REFERENCES

AASHTO. 1997. *AASHTO Guide for Commonly Recognized (CoRe) Structural Elements.* Washington, DC: American Association of State Highway and Transportation Officials.

AASHTO. 2019a. *Manual for Bridge Element Inspection*, 2nd edition. Washington, DC: American Association of State Highway and Transportation Officials.

AASHTO. 2019b. *Standard Method of Test for Surface Resistivity Indication of Concrete's Ability to Resist Chloride Ion Penetration*. *T358.* Washington, DC: American Association of State Highway and Transportation Officials.

AASHTO. 2020. *AASHTO LRFD Bridge Design Specifications*, 9th edition. Washington, DC: American Association of State Highway and Transportation Officials.

AASHTO. 2022. *AASHTOWare Bridge Management (BrM), Version 6.7*. Washington, DC: American Association of State Highway and Transportation Officials

ACI Committee 228. 2013. *Nondestructive Test Methods for Evaluation of Concrete in Structures*. ACI 228.2R-98. Farmington Hills, MI: American Concrete Institute.

ACI Committee 365. 2017. *Report on Service-Life Prediction.* ACI 365.1R-17. Farmington Hills, MI: American Concrete Institute.

Agrawal, A.K., A. Kawaguchi, and Z. Chen. 2010. "Deterioration Rates of Typical Bridge Elements in New York." *Journal of Bridge Engineering* 15, no. 4: 419–429.

ASTM International. 1997. *Standard Test Method for Resistance of Concrete to Rapid Freezing and Thawing*. ASTM C666. West Conshohocken, PA: ASTM International.

ASTM International. 2008. *Standard Test Method for Evaluating Asphalt-Covered Concrete Bridge Decks Using Ground Penetrating Radar*. ASTM D6087-08. West Conshohocken, PA: ASTM International.

ASTM International. 2012. *Standard Test Method for Field Measurement of Soil Resistivity Using the Wenner Four-Electrode Method*. ASTM G57-06(2012). West Conshohocken, PA: ASTM International.

ASTM International. 2013. *Standard Test Method for Detecting Delaminations in Bridge Decks Using Infrared Thermography*. ASTM D4788-03. West Conshohocken, PA: ASTM International.

ASTM International. 2015. *Standard Test Method for Corrosion Potentials of Uncoated Reinforcing Steel in Concrete*. ASTM C876-15. West Conshohocken, PA: ASTM International.

ASTM International. 2020. *Standard Specification for Deformed and Plain Carbon-Steel Bars for Concrete Reinforcement*. ASTM A615/A615M-20. West Conshohocken, PA: ASTM International.

ASTM International. 2021. *Standard Specification for Portland Cement*. ASTM C150/C150M-21. West Conshohocken, PA: ASTM International.

ASTM International. 2022a. *Standard Test Method for Determining the Apparent Chloride Diffusion Coefficient of Cementitious Mixtures by Bulk Diffusion*. ASTM C1556-22. West Conshohocken, PA: ASTM International.

ASTM International. 2022b. *Standard Test Method for Measuring the P-Wave Speed and the Thickness of Concrete Plates Using the Impact-Echo Method*. ASTM C1383-15. West Conshohocken, PA: ASTM International.

Babanajad, S., Y. Bai, H. Wenzel, M. Wenzel, H. Parvardeh, A. Rezvani, R. Zobel, F. Moon, and A. Maher. 2018. "Life Cycle Assessment Framework for the U.S. Bridge Inventory." *Transportation Research Record* 2672, no. 12: 82–92.

Bertolini, L., B. Elsener, P. Pedeferri, E. Redaelli, and R. B. Polder. 2013. *Corrosion of Steel in Concrete: Prevention, Diagnosis, Repair.* 2nd edition. Weinheim, Germany: Wiley-VCH.

Broomfield, J. P. 2007. *Corrosion of Steel in Concrete*, 2nd edition. New York, NY: Taylor and Francis.

Bu, G., J. Lee, H. Guan, M. Blumenstein, and Y.-C. Loo. 2012. "Performance Prediction of Concrete Elements in Bridge Substructures using Integrated Deterioration Method." In: *IABSE Congress Report*. Zurich, Switzerland: International Association for Bridge and Structural Engineering, vol. 18, no. 33, p. 108–115.

Chapra, S. C., and R. P. Canale. 2002. *Numerical Methods for Engineers*, 4th edition. New York, NY: McGraw-Hill.

ElBatanouny, M. K., E. I. Wagner, K. A. Hawkins, and P. D. Krauss. 2022. *TR-772: Performance Evaluation of Polyester Polymer Concrete Overlays*. Ames, IA: Iowa Department of Transportation.

FHWA. 2014**.** "Traffic Monitoring Guide" (web page). https://www.fhwa.dot.gov/policyinformation/tmguide/tmg_2013/vehicle-types.cfm, last accessed October 18, 2024.

FHWA. 2022. *Specifications for the National Bridge Inventory (SNBI).* Report No. FHWA-HIF-22-017. Washington, DC: Federal Highway Administration.

FHWA. n.d.a. "LTBP InfoBridge™" (web page). https://infobridge.fhwa.dot.gov/Home/, last accessed August 8, 2024.

FHWA. n.d.b. “LTBP InfoBridge™ Library” (web page). https://infobridge.fhwa.dot.gov/Page/protocols, last accessed July 24, 2024.

FHWA. n.d.c. “LTBP InfoTechnology™” (web page). https://infotechnology.fhwa.dot.gov, last accessed July 19, 2024.

FHWA. n.d.d. “Long-Term Bridge Performance (LTBP) Program (web page). https://highways.dot.gov/research/long-term-infrastructure-performance/ltbp/long-term-bridge-performance, last accessed October 18, 2024.

Gucunski, N., A. Imani, F. Romero, S. Nazarian, D. Yuan, H. Wiggenhauser, P. Shokouhi, A. Taffe, and D. Kutrubes. 2013. *Nondestructive Testing to Identify Concrete Bridge Deck Deterioration*. Report No. S2-Ro6A-RR-1. Washington, DC: Transportation Research Board.

Gucunski, N., B. Pailes, J. Kim, H. Azari, and K. Dinh. 2016. “Capture and Quantification of Deterioration Progression in Concrete Bridge Decks through Periodical NDE Surveys.” *Journal of Infrastructure Systems* 23, no. 1: B4016005.

Gucunski, N., F. Romero, S. Kruschwitz, R. Feldmann, and H. Parvardeh. 2011. *Comprehensive Bridge Deck Deterioration Mapping of Nine Bridges by Nondestructive Evaluation Technologies.* Project No. SPR-NDEB(90)-8H-00. Ames, IA: Iowa Department of Transportation.

Hearn, G., and H. S. Shim. 1998. “Integration of Bridge Management Systems and Nondestructive Evaluations.” *Journal of Infrastructure Systems* 4, no. 2: 49–55.

Iowa SUDAS. 2023. “Pavement Thickness Design.” In *SUDAS Design Manual, 2023 Ed*. Ames, IA: Iowa Department of Transportation, chapt. 5F.

Jiang, Y., M. Saito, and K. C. Sinha. 1988. “Bridge Performance Prediction Model Using the Markov Chain.” *Transportation Research Record* 1180: 25–32.

Liu, H. T. 2013. “Adaptive Optimization Methods in System-Level Bridge Management.” Ph.D. dissertation. University of California at Berkeley.

Liu, H., and Y. Zhang. 2020. “Bridge Condition Rating Data Modeling Using Deep Learning Algorithm.” *Structure and Infrastructure Engineering* 16, no. 10: 1447–1460.

Martino, N., K. Maser, R. Birken, and M. Wang. 2014. “Determining Ground Penetrating Radar Amplitude Thresholds for the Corrosion State of Reinforced Concrete Bridge Decks.” *Journal of Environmental and Engineering Geophysics* 19, no. 3: 175–181.

Metz, C. E. 1978. “Basic Principles of ROC Analysis.” *Seminars in Nuclear Medicine* 8, no. 4: 283–298. https://doi.org/10.1016/S0001-2998(78)80014-2, last accessed October 18, 2024.

Mishalani, R. G., and S. M. Madanat. 2002. "Computation of Infrastructure Transition Probabilities Using Stochastic Duration Models." *Journal of Infrastructure Systems* 8, no. 4: 139–148.

Nasrollahi, M., and G. Washer. 2014. "Estimating Inspection Intervals for Bridges Based on Statistical Analysis of National Bridge Inventory Data." *Journal of Bridge Engineering* 20, no. 9: 04014104.

NJDOT. 2016. *Design Manual for Bridges and Structures*, 6th edition. Trenton, NJ: New Jersey DOT.

NJDOT. 2017. "New Jersey Weigh in Motion" (web page). https://www.njtms.org/njwimsite/, last accessed April 26, 2023.

Nockemann, C., H. Heidt, and N. Thomsen. 1991. "Reliability in NDT: ROC Study of Radiographic Weld Inspections." *NDT & E International* 24, no. 5: 235–245.

Nogueira, C. L. 1998. "Application of Nondestructive Evaluation Techniques in Bridge Inspections as a Tool for Bridge Management Systems." Master thesis. University of Colorado, Denver.

Office of the Federal Register, National Archives and Records Administration. 2022. "National Bridge Inspection Standards (NBIS) Final Rule." *Federal Register* 87, no. 88 (May 6, 2022): 27396–27437. Government. U.S. Government Printing Office.

Office of the Federal Register, National Archives and Records Administration. 2012. Pub. L. No. 112–141. *Moving Ahead for Progress in the 21st Century Act*. Government. U.S. Government Printing Office, July 5, 2012.

Rens, K. L., C. L. Nogueira, and D. J. Transue. 2005. "Bridge Management and Nondestructive Evaluation." *Journal of Performance of Constructed Facilities* 19, no. 1: 3–16.

Schiessl, P., P. Bamforth, V. Baroghel-Bouny, G. Corley, M. Faber, J. Forbes, C. Gehlen, et al. 2006. *fib Bulletin No. 34: Model Code for Service Life Design.* Lausanne, Switzerland: fib.

Shin, H., and D. A. Grivas. 2003. "How Accurate is Ground-Penetrating Radar for Bridge Deck Condition Assessment?" *Transportation Research Record* 1845, no. 1: 139–147.

Sobanjo, J., P. Mtenga, and M. Rambo-Roddenberry. 2010. "Reliability-Based Modeling of Bridge Deterioration Hazards." *Journal of Bridge Engineering* 15, no. 6: 671–683.

Sultan, A. A. 2017. "Advancements in Evaluating Reliability of Nondestructive Technologies for The Detection of Subsurface Fracture Damage in R.C. Bridge Decks." Ph.D. dissertation. University of Missouri, Columbia.

Sultan, A. A., and G. A. Washer. 2018. "Comparison of Two Nondestructive Evaluation Technologies for the Condition Assessment of Bridge Decks." *Transportation Research Record,* 2672, no. 41: 113–122.

Thompson, P. 2021. "StruPlan: Open-Source Long-Range Renewal Planning for Transportation Structures." In: *Bridge Safety, Maintenance, Management, Life-Cycle Resilience and Sustainability*. New York, NY: CRC Press.

Tokdemir, O.B., C. Ayvalik, and J. Mohammadi. 2000. "Prediction of Highway Bridge Performance by Artificial Neural Networks and Genetic Algorithms." In: *2000 Proceedings of the 17th International Symposium on Automation and Robotics in Construction (ISARC)*, *Taipei, Taiwan*. Oulu, Finland: International Association for Automation and Robotics in Construction (IAARC), p. 1–8.

Washer, G., M. Nasrollahi, C. Applebury, R. Connor, A. Ciolko, R. Kogler, P. Fish, and D. Forsyth. 2014. *Proposed Guideline for Reliability-Based Bridge Inspection Practices.* NCHRP Project 12-82 (01). Washington, DC: National Cooperative Highway Research Program.

Washer, G., A. Jungnitsch, and S. Nelson. 2015. *TPF-5(247) Interim Report: Field Testing of Hand-Held Infrared Thermography, Phase II.* Report cmr16-007. Jefferson City, MO: Missouri Department of Transportation.

Wenzel, H., R. Veit-Egerer, and M. Widmann. 2013. "Life Cycle Analysis Applied to the New Jersey Case Study." In: *Industrial Safety and Life Cycle Engineering (IRIS)*. Vienna, Austria: VCE Vienna Consulting Engineers ZT GmbH, p. 443–464.

Wikimedia Commons. 2021. "PPV, NPV, Sensitivity, and Specificity." last modified December 2, 2022, 11:26. https://commons.wikimedia.org/wiki/File:PPV,_NPV,_Sensitivity_and_Specificity.pdf, last accessed September 30, 2024.

WJE, Inc. 2024. *CASLE*™ (software).

Zhou, J., T. Li, X. Ye, and X. Shi. 2020. "Safety Assessment of Widened Bridges Considering Uneven Multilane Traffic-Load Modeling: A Case Study in China." *Journal of Bridge Engineering* 25, no. 9: 05020008.

Recycled
Recyclable

Recommended citation: Federal Highway Administration,
Linking NDE Data and Bridge Deck Performance
(Washington, DC: 2025) https://doi.org/10.21949/1521625

HRDI-20/02-25(WEB)E